NATIONAL TECHNICAL UNIVERSITY OF ATHENS
SCHOOL OF NAVAL ARCHITECTURE AND MARINE ENGINEERING

Analysis and Design of Composite-to-Metal Adhesively Bonded Joints

by

Konstantinos N. Anyfantis

PhD thesis

Thesis Supervisor: N.G. Tsouvalis, Associate Professor, NTUA

Athens, February 2012

Στους γονείς μου, Νίκο και Βάσω
Στο κορίτσι μου, Μαργαρίτα

Acknowledgements

Looking back, I am surprised and at the same time very grateful for all I have received throughout these years. It has certainly shaped me as a person and has led me where I am now and where I will be in the near future.

I want first to thank my supervisor Associate Professor Nicholas Tsouvalis not only for being an excellent teacher but for being valuable friend. From the beginning of my PhD studies, he encouraged me to conduct high quality research and I am grateful for his deep intuitions about the evolution of the current Thesis. From my point of view, the most important is that he always was next to me but never in front or behind me.

I also thank Professor Dimitrios I. Pantelis and Professor Vassilios J. Papazoglou, who are the members of my PhD's advisory committee, for their comments and assistance on my PhD thesis.

Additionally, I would like to thank the laboratory technicians Mr. Athanasios Markoulis and Mr. Haris Xanthis for their cooperation and for offering valuable assistance in the experimental activities.

It was a pleasure and honour for me to meet and share my doctoral studies and life with wonderful people like Mr. Elias Chatzidouros, Mr. Ilias Zilakos and Mr. Vassilios Karatzas. I will never forget our fruitful conversations about science and real life. I thank these people from the deepest of my heart.

I also thank Mrs. Mina Ntemagkou for her kind assistance and valuable information she provided to me, which were crucial for the fulfillment of the 8th Chapter.

I would like to thank my parents and my wife for their great encouragement and their boundless support during all years of my PhD studies and in particular during the most difficult period.

Finally, I want to thank all my friends and colleagues who supported me during these years.

Konstantinos N. Anyfantis

Analysis and Design of Adhesively Bonded Joints between Composites and Metals

by
Konstantinos N. Anyfantis

Abstract

This work is based on the development of numerical tools for the computational analysis of engineering structures that involve adhesion problems, that is interface and interphase problems. The proposed numerical tools are implemented within the framework of non-linear Finite Element Methods (FEM) and are developed so as to be utilized by design engineers and researchers for the design and analysis of adhesively bonded joints and composite structures.

Initially, a Progressive Failure Model (PFM) is developed and applied to predict the behaviour of an experimentally tested blade-stiffened panel found in the literature. The developed PFM has been implemented in non-linear finite element analysis procedures under the framework of the commercial software Ansys. Failure initiation and failure propagation as well as the post buckling ultimate attained load have been numerically evaluated. Final failure behaviour of the simulated stiffened panel is due to sudden global failure, as concluded from comparisons between numerical and experimental results being in good agreement.

In the following, particular focus has been given initially in the study of the failure mechanisms that evolve during the pure mode delamination propagation in fiber reinforced composite materials (interface problems) and later in the study of the mixed-mode loading and fracture of adhesively bonded joints (interphase problems). The proposed numerical tools involve novel constitutive relations that describe the aforementioned phenomena and are based on fracture and damage mechanics, in accordance to Cohesive Zone Modeling (CZM) techniques.

Initially, a continuum damage constitutive model is presented for the prediction of the in-plane failure modes of laminated composite materials. In the following, new cohesive laws are developed for the prediction of delamination initiation and propagation under Mode I and Mode II loading and fracture in fibrous laminated composite materials. Having provided numerical predictions of the failure response of composite materials, the next research activity is focused on providing constitutive relations for the predictions of structural adhesively bonded joints. The proposed constitutive relations, are validated with tests conducted on steel-to-steel and steel-to-composite adhesive joint geometries that involve flat adherents. Next, a numerical parametric study, that involves axisymmetric adhesive joints (tubular cases), has been conducted, showing the potential of the proposed numerical tool.

In conclusion, the present PhD thesis provides separate numerical tools that can be combined for the prediction of the failure response of structures that involve composite materials and adhesive joints.

Table of Contents

List of Figures

List of Tables

This page has been intentionally left blank

1. Structural adhesive bonding

1.1 Introduction

Many methods exist for bringing together similar or dissimilar structural materials, in terms of the joining technique utilized. Conventional mechanical joints, such as bolted, pinned or riveted are preferred due to their simplicity and the disassembly ability that they offer for joining metal or composite materials. However, when a mechanical joint is loaded, local damage is induced at the fastener holes due to stress concentrations (da Silva et al., 2011). This fact leads to the structural degradation of a joint and jeopardizes the structural integrity of the assembly structure. The demands for designing lightweight structures without any loss of stiffness and strength have turned many researchers and design engineers to seek for alternate joining methods. Thus, the field of structural adhesive bonding has matured with the development of a wide range of adhesives from the chemical industry. Adhesive bonding is a material joining process in which an adhesive, placed between the adherend surfaces, solidifies to produce an adhesive bond. The reasons why adhesive bonding is so desirable compared to other conventional joining methods (e.g. fastening) have been given by Adams et al., 1997:

1. Often, thinner gage materials can be used with attendant weight and cost savings.
2. The number of production parts can be reduced, whereas the design is more simplified.
3. The need for milling, machining and forming operation of details is reduced.
4. Large area bonds can be made with a minimum work force without special skills.
5. Adhesive bonding provides a high strength to weight ratio with three times higher the shearing force of riveted joints.
6. Improved aerodynamic/hydrodynamic smoothness and visual appearance.
7. Use as a seal, and/or corrosion preventer when joining incompatible materials.
8. Excellent electrical and thermal insulation.
9. Superior fatigue resistance. Adhesively bonded assemblies have shown a fatigue life twenty times better than riveted structures of identical parts.
10. Often, the adhesive is sufficiently flexible to allow for the variations in coefficients of thermal expansion when joining dissimilar materials.

However, it isn't but until the past century that science and industry enabled the development of a wide range of adhesives with the introduction of synthetic polymers. Before then, the only adhesives available were derived from natural sources such as plants and animal collagen.

Adhesive bonding for load-bearing primary structures has been developed only several decades ago and has its roots in the field of aeronautics. In the 1930s, the first synthetic resin glues were produced, followed by epoxies, neoprenes and acrylonitriles during the World War II, where technology advanced under the pressure of improvement of weapons. The first notable application for joining similar adherents is the bonding of plywood laminate in the British wooden Mosquito bomber during World War II. In the meantime, in United States, Narmco developed the Meltbond adhesives in the early 1940's for the consolidated Vultee B-36 bomber. Since those times, the use of structural adhesives has increased steadily and has been adopted for joining similar or dissimilar structural materials (metals, plastics, composites etc.). In modern aviation, many applications can be found in the construction of the F-18 and F-20 fighter aircrafts, where composite panels where adhesively bonded to form the wing skins and control surfaces. Similar applications are found in many types of commercial aircrafts, such as in AIRBUS A380 (see Figure 1.1), where around 46% of the joints are based on adhesive bonding techniques. Also, Boeing 787 and the Airbus A350 contain more than 50% bonded composite structure.

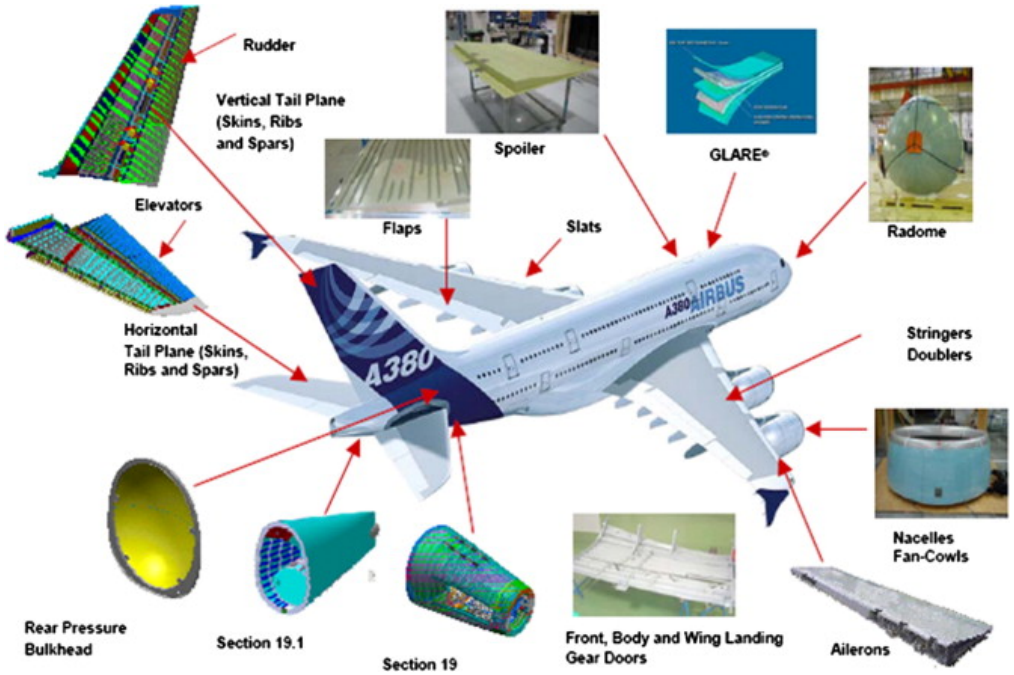

Figure 1.1: Adhesive bonding applications in the new Airbus A380 commercial aircraft (Figure taken from Katsiropoulos et. al. (2011)).

By extrapolating the experience gained from aeronautics, adhesives have been adopted more and more by other industries like the marine industry, wind turbines, piping and civil engineering to mention just a few.

Adhesive bonding has many applications in the construction of wind blades, since most structural parts are composites. Specifically, significant research has been devoted for the design and analysis of the adhesively bonded wind turbine blades, which are constructed in a box section-type with monolithic and sandwich layers. Thus, the blades are constructed in two separate parts and then adhesively assembled to form the aerodynamic shape. Additionally, shear webs are adhesively bonded to the upper and lower shells of the blade, as shown in Figure 1.2.

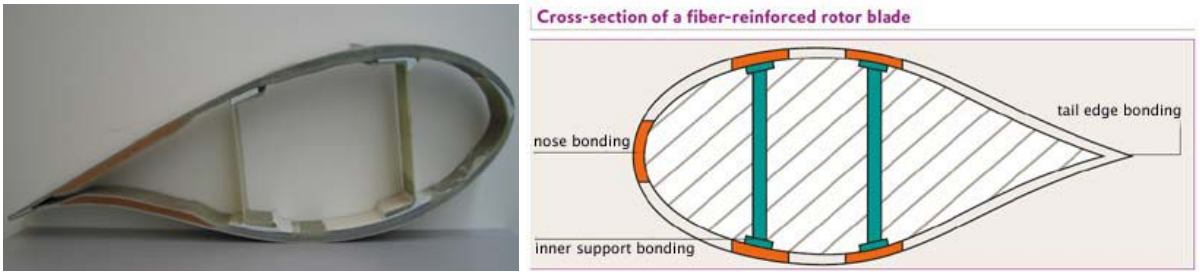

Figure 1.2: Cross section of a wind turbine blade showing adhesively bonded parts (Jensen 2008).

Adhesive bonding has been adopted by the marine industry at the decade of 1980. It has been a field of research by several scientists since then, with the design of adhesive joints in marine structures (deck-to-hull, bulkhead-to-hull joints) gaining the greatest focus. Specific structural parts of a ship, such as superstructures, bulkheads, masts or even the entire deck, may be replaced by composite materials, properly designed and adhesively bonded either to composite or metal parts. Figure 1.3, presents a modern large-scale application where either a composite bulkhead or a composite deck is adhesively bonded to a steel hull.

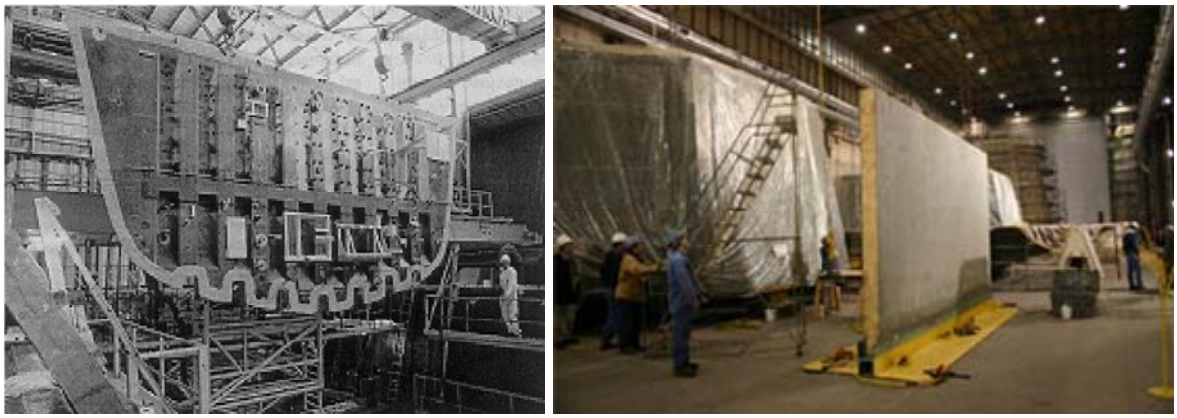

Figure 1.3: Composite bulkhead adhesively bonded to steel hull (left) and composite deck adhesively bonded to steel hull (right).

Additionally, modern adhesive bonding technologies offer many techniques for repairing defected structural elements that have a discontinuity (physical cracks) or have lost part of their stiffness or strength (e.g. corrosion). In most cases, repairing is achieved with the application of supplemental structural materials on and in the vicinity of the defect, with the aid of adhesive materials. The design of each repair, aims at compensating the loss of strength or stiffness owed to the corresponding defect. Thus, patch repair is a very promising technique in marine

applications, where carbon, glass or combined fabric patches are either directly laminated or cured composite patches are adhesively bonded on the cracked or corroded area of metallic parts (i.e. fuel tank, water ballast tank, hull etc.). This technology is advantageous in the marine industry, since the hot work of welding is avoided, minimizing thus the risk of a fire, plus the repair can be done on the spot with no need of dry-docking of the ship. The stripping out of neighboring compartments needed for welding is also avoided. The sealing of the cracks made by adhesive joining is water-tight and it can be performed on complex surface geometries. Repairs of this kind can adapt to any substrate geometry and fit into places where normal welding would not easily reach. The maintenance cost is reduced and the materials used are light, so they are easy to transport and to handle with no need of heavy lifting machinery.

1.2 Adhesive material systems

When selecting an adhesive system for bonding similar or dissimilar materials, one should first consider the factors common to all adhesive bonding applications. The expected end use environment is probably the most important of these considerations. Among the environmental concerns are expected temperature ranges, chemical and UV exposure and possible UL electrical requirements. Other important considerations are the anticipated bond loading and strength requirements of the final application. In most cases, more than one type of adhesive could fulfill the necessary requirements. Each system exhibits characteristic properties that fit particular application needs. In general, structural adhesives can be categorized in 6 groups, that is epoxies, urethanes, acrylics, anaerobics, cyanoacrylates and UV curable adhesives (Adams et al., 1997).

Epoxies are known for their versatility. Their bond strength, electrical conductivity and temperature resistance can be modified to fit almost any specific application needs. Epoxies are made in either one- or two-part formulations. The two-part systems consist of a resin and a hardener, which must be mixed together in strict proportions for maximum bond strength. They can be cured at room or elevated temperatures. One-part epoxies require no mixing; however, they must be cured by heat, usually around 300º F for one hour or more. Heat cured epoxies tend to exhibit greater strength than their mixed counterparts. The two-component systems are more widely used because they can be stored for long periods of time and do not activate until mixed. Unlike other adhesives, epoxies are not solvent based, but cure as the result of a chemical reaction.

Urethanes, also known as polyurethanes, form strong bonds on a variety of substrates. Urethanes are found primarily in applications that require high strength with flexibility. Urethanes are available in both one- and two-part systems. One-part formulations require heat curing while two-part systems may be room temperature cured.

The acrylics used today are second generation or modified acrylic systems. These “improved” acrylics provide many of the same attributes as epoxies and urethanes as well as having the advantage of rarely needing primers. These are one- or two-part systems consisting of

a catalyst primer and the adhesive. Usually, the one-part systems do not need mixing or weighing, greatly simplifying their application.

Anaerobics are one-part thermosetting adhesives whose curing mechanism is triggered by the absence of oxygen. This eliminates the problem of premature curing. Curing occurs at room temperature, and can be speeded by addition of heat or ultraviolet radiation. The cure cycle may be as short as 15 seconds set time and 2–24 hours for full cure. Anaerobics also exhibit the useful property of being easily cleaned from unbonded surfaces after the bondline has set up. Anaerobics are excellent for critical sealing and bonding applications where strength is not critical. Their use is also expanding into the sealing of welds and soldered joints.

Cyanoacrylates are single-part, fast curing "convenience adhesives." With a normal setting time of 2 or 3 seconds and a full cure time of 24 hours at room temperature, these systems are popular in tacking and quick contact assembly operations. The presence of surface moisture, even in limited quantities such as humidity in the air, initiates curing. Cyanoacrylates are highly application specific.

Ultraviolet (UV) curing technology was first developed in the mid 1960s as a method for curing packaging inks. Since then, the technology has advanced and spread into other areas. Adhesives, potting compounds and sealants, as well as inks, are now available with UV curing systems. The rapid cure and other advantages of these systems have made UV curables one of the fastest growing families of adhesives in use today.

1.3 Fabrication of adhesive joints

The fabrication of an adhesive joint assembly is a straightforward procedure that must be followed with extreme caution and concentration, since the quality of an adhesive joint is a key parameter to its structural integrity and its in-service performance. Thus, the fabrication process involves the surface preparation of the bonding surfaces, application of the primer, application of the adhesive, assembly of the various components to be joined and finally the curing of the adhesive joint.

The preparation of the surfaces to be adhesively bonded will largely determine the success or failure of the bonded joint. The purpose of surface preparation is to ensure that after the adhesive is applied, it will wet the surface of the adhered and not what appears to be the surface. The apparent surface could be a layer of oil, grease, film or some other contaminant. One basic consequence of the surface treatment is the enhancement of the degree of mechanical interlocking (see Figure 1.4) between adhesive polymers and substrates, which seems to increase the strength of the joint (Anyfantis and Tsouvalis, 2009; Bishop, 2005). Roughening the surfaces of the adherents can be achieved either by mechanical or by chemical methods. Since when using a chemical treatment method, immersion of the substrates into a chemical solution is inevitable, it is impractical to apply such a method to the large scale structures incorporated in

the marine industry. Surface roughness is one of the major parameters that control the state of the adhesion achieved by chemical or mechanical surface treatments.

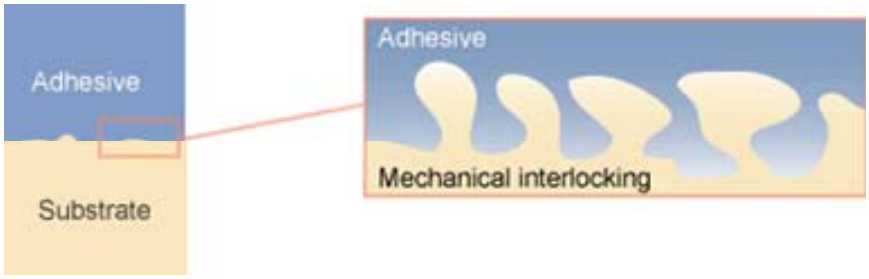

Figure 1.4: Mechanical interlocking arises from the flow of the adhesive into the pores and interstices of the materials according to the theory of adhesion.

In the framework of mechanical treatment methods, polishing and grit blasting are the most common techniques utilized for roughening the adherend surfaces. In fact, grit-blasting can be applied only on the bonding surfaces of metal adherents while polishing is applied to the composite surfaces. According to Harris & Beevers (1999), grit blasting is a very promising technique because it introduces chemical changes on the surfaces of the adherents, which in turn affect the strength and the structural integrity of the joint. Nevertheless, there is a value of the surface roughness which is optimum for the strength of the adhesion. The value of the surface roughness does not only affect the strength of the adhesive-adherend interface, but also has a profound and critical influence on the stresses near this interface (Morais et al., 2007). The process of adhesion is in itself a subject of considerable research, as are the joint failure modes (Shalid and Hashim, 2002).

In real life applications a low viscosity primer usually is applied, in one or more coats, by spraying or brushing. Primer may provide flexibility, shock resistance and peel resistance for improved strength characteristics. Primers may also be used to wet or penetrate the adherend better than the adhesive itself or to protect a treated surface of a substrate prior to the application of adhesive.

After the primer has dried, the adhesive is applied, usually in liquid or paste form (thixotropic). Adhesives may be applied manually by roller, brush, extrusion and flow, and trowel, semi automatically with spray guns or high pressure extrusion guns; automatically by machine methods that are usually geared for mass production of a particular component.

If the adhesive contains a solvent, most of it must be removed before the joint is closed. Evaporation of the solvent may be done at room temperature or be speeded up by moderate heating with infrared lamps or a hot air oven. After the solvent has been removed, the coated parts should be immediately mated before the tack life of the adhesive expires. Arrangements should be made for positioning the components for mating and for holding them in place while the assembly cures. Assembly fixtures ranging from simple jigs or locating rivets, pins etc., to self contained equipment (which also includes provision for applying pressure, heat or both) are

used for positioning. Special tapes may be used (for many applications) to position the components and also to provide adequate pressure.

Those adhesives where bond must meet higher requirements of strength, heat resistance or both need be cured or set. Curing may be achieved by heat alone, pressure alone or by a combined process.

1.4 Loading and fracture in bonded structures

It is of great importance not only to describe but also to understand the types of loading stresses involved in adhesively bonded structures. Apart from the materials involved, the design configuration of an adhesive joint depends on the loading stresses developed within the joint. In adhesive bonded joints between similar or dissimilar adherents, five basic types of loading stresses are common: tension, compression, shear and cleavage or peel as illustrated in

Figure **1.5**.

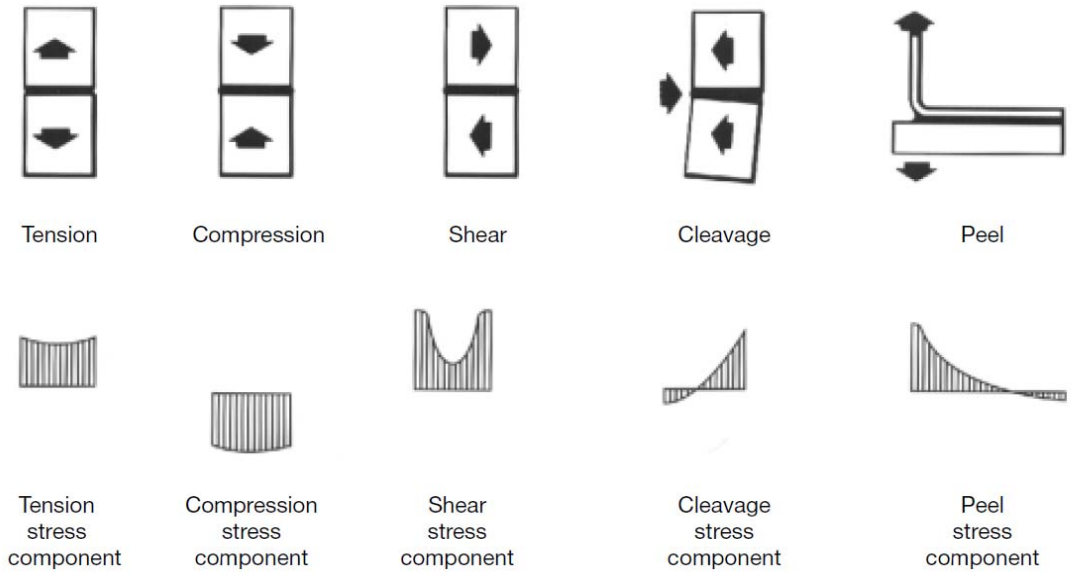

Figure 1.5: Types of loading stresses in bonded structures.

Tensile stresses develop when the forces acting perpendicular to the plane of the joint are distributed over the entire bonded area and at the free surfaces of the adherents. Adhesive joints perform well to tensile loading, while the entire adhesive contributes to the strength of the joint. Unfortunately, in practical applications, loads are hardly ever purely axial but cleavage or peel stresses tend to develop due to the eccentricity of the loading. In order to design a joint to carry pure tension loads, it is of great importance to introduce specific constrains by not allowing cleavage stresses to develop.

On the other hand, compressive loads are the opposite of tensile, as they also act perpendicularly to the plane of the joint, but tend to bring the adherents closer and reduce the

adhesive thickness. As for the tensile loads, it is important to keep the loads aligned so that purely compressive stresses develop within the adhesive. Due to the high compressive strength of most adhesives, a joint loaded in compression is not likely to fail, although it may crack at weak spots because of uneven stress distribution. In fact, a joint loaded in pure compression hardly needs structural adhesive bonding of any sort. If the compression force is high enough and there is no movement of the adherents, the adherents will maintain a relative position between each other.

Adhesives are generally strongest when stressed in shear, while the entire bonded area contributes to the strength of the joint. Shear stresses result when forces act in the plane of the adhesive trying to separate the adherents. Joints dependent upon the adhesive's shear strength are relatively easy to manufacture and are commonly used. Most joint configurations are designed at a manner that all types of loading, exerted to the adherents, conclude to shear loading of the adhesive. On the other hand, cleavage and peel stresses tend to be catastrophic for the joint, in a way that they are totally undesirable.

Cleavage occurs when forces act at one end of a rigid bonded assembly and tend to split the adherents apart. Peel stresses are much alike cleavage but apply to a joint when one or both of the adherents are flexible. Joints loaded in peel or cleavage provide much lower strength than joints loaded in shear because the stress is concentrated on only a very small area of the total bond. Peel stresses are confined in a very thin line at the edge of the bond, so the remainder of the bonded area makes no contribution to the strength of the joint.

When an adhesive joint is stressed either under pure tension, compression, shear, peel and cleavage loading or combined, the loads are being transferred from one substrate to the other through the adhesive and via the adherend/adhesive interface. Thus, fracture of adhesive joints is located at the weakest point of the structure and is usually divided into two types: usually at either the interface of the adhesive and the adherend (interfacial or adhesive failure) or inside the adhesive itself (cohesive failure), since adhesives usually are less strong than the adherents, as shown in Figure 1.6. In many practical applications the crack path is oscillatory, i.e. travelling from one interface to its opposite by cracking the bulk adhesive.

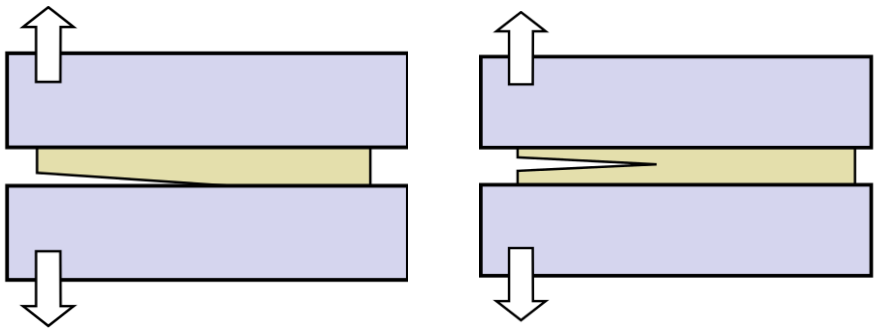

(a) (b)

Figure 1.6: Adhesive or interfacial failure (a) and cohesive failure (b) of an adhesive joint

1.5 Adhesive joint geometries

The butt joint design configuration is based on the ability of the adhesive to withstand tension stresses developed by the tension loading of the adherents. The simplest joint to make is the plain butt joint (see Figure 1.7), Adams et al. (1997). The major drawback in using butt joints is their inability to withstand bending forces because the adhesive would then experience cleavage stresses. Another drawback is the difficulty to align the two adherents during the manufacturing process of the butt joint. Butt joints in general are not used when composite-to-metal or composite-to-composite thin skins are involved.

Figure 1.7: The plain butt joint.

If the adherents are too thick to design simple over-lap joints, the butt joint can be improved by redesigning it in a number of ways. Any modification of the simple butt joint is oriented towards reducing cleavage effects caused by side loading.

Thus, Baker and Hart (1957) introduced the scarf butt joint (see Figure 1.8), a more practical adhesive joint between similar or dissimilar adherents, which keeps the axis of loading in line with the joint and does not require a major machining operation. Hart-Smith (1973) is the pioneer of the development of scarf joints and lap-stepped joints between metal and composite adherents for astronautic and aeronautic applications. Since Hart-Smith (1973), several researchers have been focused on stepped-lap butt joints and scarf joints between dissimilar adherents. Ikegami et al. (1990) and Sato and Ikegami (1992) conducted a further investigation on the strength of scarf joints by feeding several researchers to work on the optimization of scarf and stepped-lap butt joints between dissimilar adherents.

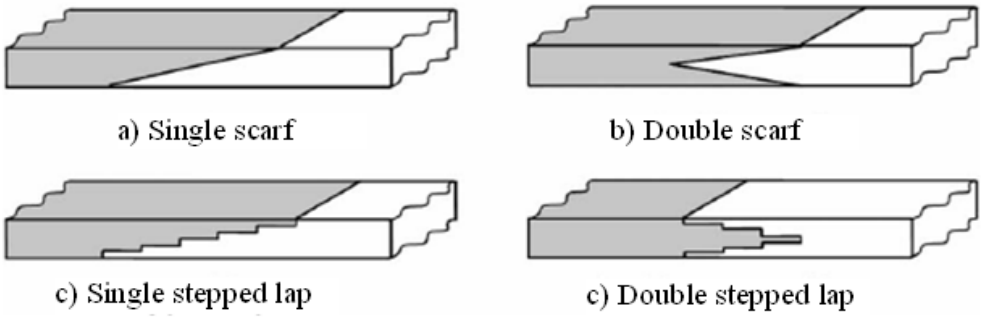

Figure 1.8: Scarf and stepped butt type joints.

Dance and Kellar (2004) patented the “comeld joint” in order to bring together FRP and metals by enhancing the performance of the stepped lap joint. He proposed a special surface treatment technique of the metal by using a power beam to create protrusions and cavities in the metal onto which the composite is laid and cured. According to Smith (1990) the comeld joint failed at a much higher load than a common double stepped lap joint when stainless steel was

used as the metal adherend, by offering a significant advantage in joint design. Investigating the utilization of butt joints for thick adherents made from dissimilar materials (composite-to-steel), Dvorak et al. (2001) suggested a promising configuration illustrated in Figure 1.9. Dvorak's results show that adhesively bonded tongue-and-groove joints between steel and composite plates loaded in monotonically increasing longitudinal tension are stronger than conventional strap joints, even in relatively thin plates. However, the complex manufacturing process of the proggles on the steel adherend exhibits a drawback in this innovative type of joint.

Melogranaa et al. (2003) based upon Dvorak's results, conducted a parametric experimental study in an effort to redesign the tongue and groove joint, by optimizing configuration between thin carbon fiber laminates and steel. This research promotes the utilization of thin composite and metal adherents for tongue and groove joints in marine applications, while Melogranna leads to the conclusion that the tongue-and-groove joints with large aspect ratio (length to width: 2) tongues were stronger than the conventional single lap joints.

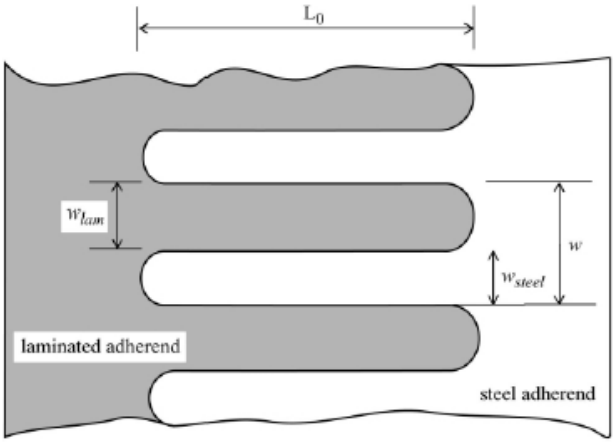

Figure 1.9: The tongue and groove butt joint proposed by Dvorak et al. (2001).

Lap joints are the most commonly used as adhesive joints between dissimilar adherents (composite and metal), because they are simple to manufacture, are applicable to thin adherents (skin or sheet) and most of all, they stress the adhesive in a way that it is stressed in shear. However, the single lap joint causes the adhesive to be stressed not only in shear. In this design the adherents are offset and the loading forces are not in-line, as illustrated in Figure 1.10. This eccentricity leads to the development of bending moments and as a result cleavage stresses that develop at the ends of the joint seriously impairs the efficiency of the joint, Adams et al. (1997).

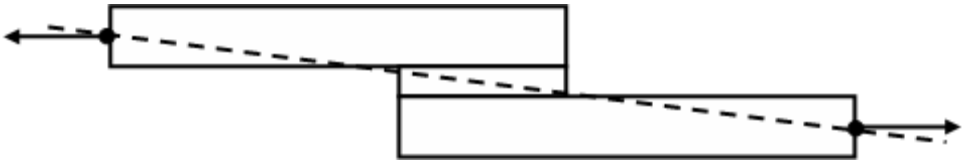

Figure 1.10: Schematic presentation of a single lap joint.

The need to redesign an overlap joint so as to reduce peel stresses at the edges of the overlap area and the manufacturing difficulty to enhance the joint with a spew fillet led to the tapered lap joint. According to Oterkus et al. (2006), there is a strong relation between the taper angle and overlap length regarding to the linear or the non-linear behaviour of the joint. But an optimization of both can lead to very efficient joint design. The latest research on design optimization of single lap joint by combining spew fillets and/or tapered ends is that of Deng and Lee (2008). According to the authors, the results show that the combination of an inside taper in the plate and a triangular fillet give the most reduction in the maximum interfacial stresses of about 30%.

Furthermore, Zeng and Sun (2001) first introduced the wavy-lap joint. According to the authors, this new design not only avoids the load eccentricity but also allows the development of compressive stress at the joint's end of the overlap section. Tong and Steven (1999) pointed out the existence of a positive normal stress (peel) at the end of the overlap region of the ordinary single-lap joint, which is critical for the adhesive. Referring to Adams et al. (1997), they pointed out that adhesives have good strength to compressive and shear loading, but when the peel or cleavage is considered, their performance is poor. Therefore, by changing the stress field from tensile to compressive at the overlap area, the adhesive efficiency is increased and as a consequence the overall joint performance will be better.

An alternative configuration of the single lap joint is the joggle lap joint (Figure 1.11). This joint poses the easiest method of bringing loads into alignment and it can be used for effectively bonding composite-to-composite or composite-to-metal. Also, it provides a free aligned surface to which it is easy to apply pressure. Unless gross distortion causes peel and cleavage, normal structural loads will induce compressive forces in the critical regions and premature failure will be avoided, Lees (1986).

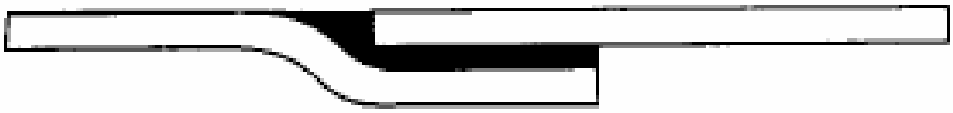

Figure 1.11: The joggle-lap joint.

After the introduction of the joggle-lap joint a new generation known as single strap (or lap) and double strap (or lap) joints has been introduced. A step beyond single lap joints, strap and double lap joints are designed to keep the operating loads aligned and are generally used when overlap joints are impractical because of adherend thickness, Adams et al. (1997). As the single strap joint, see Figure 1.12, is subjected to tension, a non uniform stress field is developed within the joint and the adherents, Shenoi and Wellicome (1993). The through thickness and along the bond line variation of shear and tensile stresses causes a severe deformation of the single strap joint.

Figure 1.12: The single strap joint.

To overcome the susceptibility of premature failure due to cleavage and peel stresses in the single strap joint, the double strap joint has been introduced by Hart-Smith (1973), Figure 1.13a. This type of joint is preferred if a substantial load-bearing capacity is required. This may be enhanced by focusing on the geometry of the joint, especially important if untoughened adhesives must be used. Chamfering to give the tapered double strap joint, (see Figure 1.13b) improves joint strength; the greater compliance of the tapered tip reduces stress concentration at the edge of the joint and thereby reduces any tendency towards peel and cleavage failure, Hart-Smith (1973).

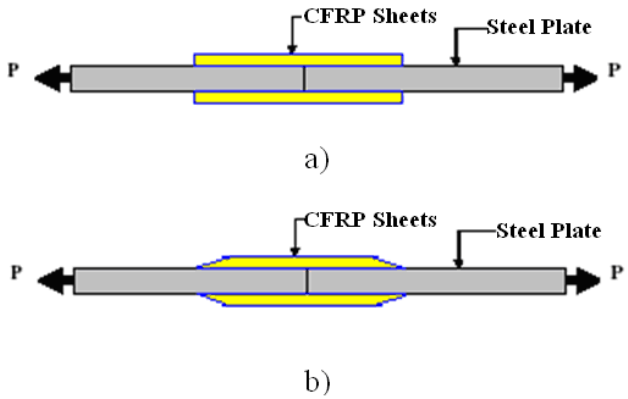

Figure 1.13: a) Double Strap Joint (DSJ) b) DSJ with tapered edges.

The employment of single strap or double strap joints in marine applications took a giant leap forward with the introduction of the patch repair technology of cracked plates (e.g. hull, deck), see Figure 1.14.

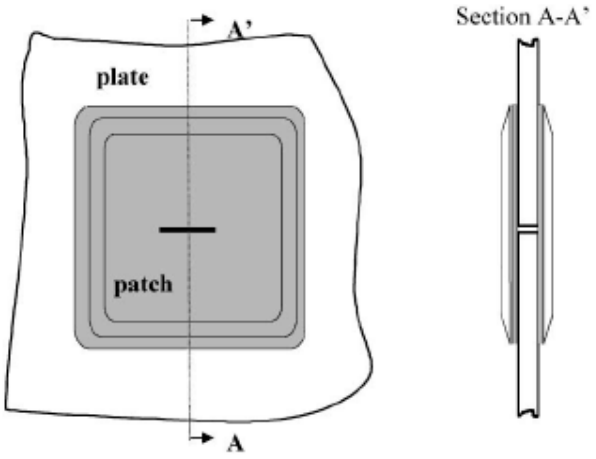

Figure 1.14: Patch repair of cracked steel plates.

Acquiring information from the relevant field of aeronautics, (Baker, 1988 and Rose, 1988), patch repair of cracked steel plates in naval structures is more and more applied as referred by Clifford et al. (2002). Grabovac et al. (2009) present a real application case of a patch repair in an aluminium superstructure using a modified vinylester resin as adhesive. The repair exhibited outstanding results even after 15-year operational time. The importance of the single or double strap joints is that of being implemented as models for efficiently analyzing patch repairs.

The double lap joint presented in Figure 1.15, points out a configuration of bringing together composites and metal, by balancing the load, Hart-Smith (1973). It is well known that the behaviour of the composites is highly anisotropic in respect of both stiffness and strength. In the fiber direction, unidirectional composites can be very strong and stiff, whereas the transverse and shear properties are much lower. This makes the composite adherents vulnerable at the interlaminar plane. Like shear stresses, peel stresses peak at the ends of the overlap and can induce composite failures due to the low transverse tensile strength, da Silva and Adams (2007). This has turned several researchers to the study of the best configuration between dissimilar adherents (e.g. composite-to-metal).

Figure 1.15: The double lap joint.

Tsouvalis and Karatzas (2011) proposed a novel adhesive joint configuration based on a butt - double lap geometry. This simple concept composite-to-metal joint can be simply and easily manufactured using even conventional manufacturing methods of composite materials. The authors have showed that their proposed joint yields comparable strengths to those attained from the double strap steel-to-composite joints and superior to the strength of other novel concept steel-to-composite joints, either with CFRP or with GFRP.

Joining large sandwich components to steel or aluminum structures is a reliable and economical way but a very demanding task. After conducting several numerical and experimental studies, Hentinen et al. (1997) concluded that the overlaminated joint is more efficient compared to a bolted joint. Furthermore, Clifford et al. (2002) examined the mechanical response of a prototype joint (see Figure 1.16) between a glass-fiber reinforced polymer sandwich superstructure and a steel hull formed via resin infusion and subsequently modified the joint configuration to improve performance through a combined modelling and mechanical testing.

Cao and Grenesdt (2003) based their research on Cliffords' (Clifford et al., 2002) design concept by pointing out a new lighter and stronger joint between sandwich panels and steel plates. They stated that, by moving the edge of the steel further away from the area of high stress concentrations in the joint, a lighter joint was obtained. The limited number of tests suggested

that the new joint design was stronger. Neither the new joint nor the reference joint broke completely even after very large deformations, as the authors state.

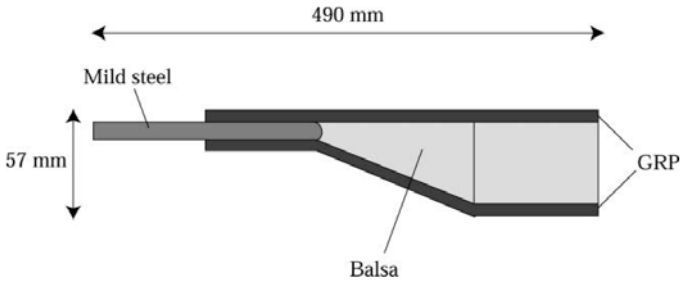

Figure 1.16: Joint proposed by Clifford et al. (2002).

Two different techniques to join a composite skin/foam core sandwich to a steel section were developed and tested to failure by Cao and Grenesdt (2004). One joint was based on bonding and bolting, whereas the other used perforated steel flanges which were embedded and co-infused with the glass fiber skins, (see Figure 1.17). Both joint concepts were relatively simple to manufacture, although the co-infused perforated joint was the simpler. This joint was also lighter and stronger than the bonded-bolted joint. The strengths of the specimens with joints were approximately 90% of that of composite skin/foam core reference beams made of the same materials. However, the failures never occurred at the joints, but typically where the composite skin thicknesses were locally increased. This thickness increase resulted in some skin waviness and an associated reduction of compression strength.

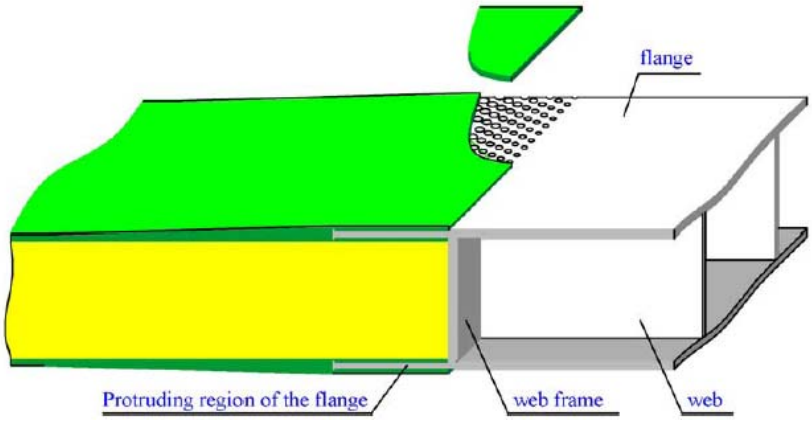

Figure 1.17: Joint configuration proposed by Cao and Grenesdt (2004).

1.6 Advances in adhesive bonding technology

Pires et al. (2003) used two different structural adhesives (DP490 and ESP110) in the same overlapped region to bond single lap joints. The strains to failure were on average 5.3% for the DP490 and 2% for the ESP110. The initial Young's modulus of the ESP110 adhesive is higher than that of the DP490 adhesive, 5.9 GPa compared with 1.8 GPa, and its cohesive

strength is also higher. They have showed that the use of a bi-adhesive system was advantageous to the joint; the more flexible the adhesive, the more uniform the stress distribution in single lap joints and the smaller the stress concentration. Yan et al. (2007) used elastic finite element methods to investigate the effect of parallel slots, at the adherents of aluminum single lap joints, on the stress distribution at the mid-bondline. Particularly, they have conducted a parametric study based on the variation of the length and depth of the slots. They have shown that the peak stress in mid-bondline decreased markedly with the existence of two parallel slots located in the outside of the adherend, with respect to the middle part of the lap zone, as well as that the original low stress in this zone of the joint increases. The stress level in the middle part of the overlap zone is higher than that of the normal joint. For the peel stress, the peak stress changed markedly from positive to negative at the left end of the lap zone and it is of benefit to restrict the harmful effect of the peel stress on the joint. Also, when a high elastic modulus adhesive is used, the stress in the middle part of the joint increases while the stress concentration at the point near the end of the lap zone decreased, so that the peak stress decreases markedly.

A field of increasing research is the welding of metals to fibre reinforced polymers. To this end an innovative method to produce hybrid joints for multi-material components with the use of ultrasonic welding technology was investigated by Balle et al. (2009) for the joining of a thin plate of aluminium alloy to CFRP. The ultrasonic welding technology is an innovative method to produce hybrid joints for multi-material components. Results demonstrated that after the welding the carbon fibers are almost perfectly surrounded by the aluminium alloy developing both an intermolecular contact and a mechanical interlocking, however the complexity of the process as well as the fact that so far 3 mm thick substrates can be joined presents a significant drawback.

The use of shape memory alloys for the improvement in the performance of composite patch repairs of metallic structures is investigated by Khalili et al. (2010). NiTi wires between plies were embedded in kevlar/epoxy patches that were positioned in notched and unnotched plates. Tensile, bending and impact loading were performed for different patch configurations. Results showed the beneficial effect of the shape memory alloy to the patch performance.

In the context of designing more auspicious hybrid joints, the formation of a fibre-friendly fixation through “cold-metal transfer” in the metal substrate is investigated by Ucsnik et al. (2010). In particular different shaped extrusions in a particular pattern were formed in the area of the metal that is to be bonded with a Carbon epoxy substrate for the creation of double lap shear joints for tensile testing. The fashioned metal to composite joints exhibited a great increase of the failure load and strain compared to traditional double lap shear joints.

A novel approach for joining CFRP to aluminium is presented by Möller et al. (2010). This approach consists of a fabric of carbon fibres and titanium wires which is then thermally joined to the aluminum substrate with the use of laser beam welding. The process is used in such a way that only the aluminium structure is molten creating a brazed bond to the titanium wire structure. Subsequently the fabric is immersed with the matrix material and an integral CFRP aluminium structure is formed. It was shown that a good wetting of the titanium structure can be obtained

and static tensile tests demonstrated that this approach is in principle suitable to produce load-bearing joints.

A direction of increasing research is based on the utilization of Carbon Nano Tubes (CNTs) for increasing the performance of adhesive joints or for aiding health monitoring techniques.

Faulkner et al. (2011) investigated the use of CNTs as an epoxy adhesive additive for adhesive joints between steel–composite interfaces and composite–composite interfaces. The study also examined the effect of CNT functionalization to improve CNT dispersion and thus improve joint strength. It is shown for both steel–composite and composite–composite adhesive joints that the dispersion of MWCNTs in the adhesive can improve fracture properties.

Burkholder et al. (2009) have shown that Mode I testing determined a modest significant increase in G_{Ic} due to CNT reinforcement with no difference in crack propagation behavior. However, Mode II testing indicated a significant increase in G_{IIc} due to CNT reinforcement.

Hsiao et al. (2003) utilized different weight fractions of MWCNTs dispersed in epoxy to produce toughened adhesives. The reinforced adhesives were used to bond the graphite fibre/epoxy composite adherents. Their shear strength was experimentally measured through single lap joint tests. They have showed that by adding 5 wt% MCNT in the epoxy adhesive, the average shear strength of the adhesion is improved by 45.6% (±5.6%).

The use of carbon nanotubes network was evaluated in the work of Lim et al. (2011) for the damage monitoring of adhesively bonded hybrid composite-to-metal joints. Towards this end, conductive networks of carbon nanotubes were introduced to the composite substrate as well as the epoxy adhesive. By measuring the resistance signals during quasi-static and cyclic tensile loading, the extent of damage and the type of failure mechanism of the joint was identified, thus proving that by selectively modifying the surface conductivity of a composite substrate and/or the adhesive, creates an efficient method for the detection of damage.

2. Analysis of Adhesive Joints

2.1 Introduction

Bonded joints are frequently expected to sustain static or cyclic loads for considerable periods of time without any adverse effect on the load-bearing capacity of the structure. A lack of suitable material models and failure criteria has resulted in a tendency to 'overdesign' adhesive joints. Safety considerations often require that adhesively bonded structures, particularly those employed in primary load-bearing applications, include mechanical fasteners (e.g. bolts) as an additional safety precaution. These practices result in heavier and more costly components. The development of reliable design and predictive methodologies can be expected to result in more efficient use of adhesives. In order to design structural joints in engineering structures, it is necessary to be able to analyze them. This means to determine stresses and strains under a given loading, and to predict the probable points of failure. There are two basic mathematical approaches for the analyses of adhesively bonded joints: closed-form analyses (analytical methods) and numerical methods (i.e. finite element or FE analyses). Differential equations are derived by applying a physical principle such as conservation of mass, momentum or energy. These equations govern the kinematic and mechanical behaviour of general bodies. The analysis of adhesively bonded joints started 70 years ago with the simple closed-from model of Volkersen (1938) that considers the adhesive and adherents as elastic, and that the adhesive deforms only in shear. The equilibrium equation of a single lap joint led to a simple governing differential equation with a simple algebraic solution. However, the analysis of adhesive joints can be highly complex if composite adherents are used, the adhesive deforms plastically or if there is an adhesive fillet. In those cases, several differential equations of high complexity might be obtained (non-linear and nonhomogeneous). For those cases, numerical methods are more adequate.

2.2 Analytical and semi-empirical solutions

It is well known that analytical methods is an important means to identify effective critical parameters, and thus closed form solutions, particularly the simple explicit ones, are

valuable in the preliminary design stage. Therefore, considerable efforts have been devoted to the development of theoretical and analytical methods for studying adhesively bonded joints. The simplest analysis considers one of the most common joints that can be found in practice, the single-lap joint (SLJ), Adams et al. (1997). In this analysis, the adhesive is considered to deform only in shear and the adherents to be rigid. The adhesive shear stress (τ) is constant over the overlap length, as shown in Figure 2.1, and is given by $\tau = P/bl$, where P is the applied load, b is the joint width and l is the overlap length. The value of the shear stress can be interpreted as the average shear stress acting on the adhesive layer.

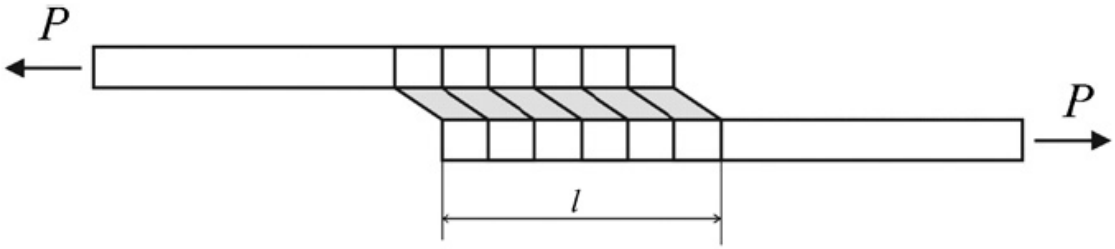

Figure 2.1: Deformations in single – lap joints with rigid adherents.

According to da Silva et al. (2009), this analysis is not very realistic due to many simplifications, but is still the basis for quoting adhesive shear strength in many test situations such as ASTM and ISO standards (Tong and Steven, 1999).

For a single lap joint in tension, Volkersen (1938) pioneered the stress analysis using a shear lag model, in which it was assumed that adhesive layer experiences only shear straining and adherents only undergo longitudinal deformation. The tensile stress in the upper adherent is maximum at A (see Figure 2.2) and decreases to zero at B (free edge), so the strain must progressively reduce from A to B.

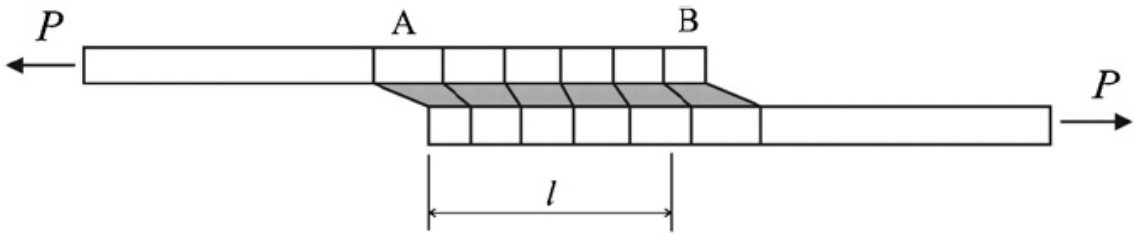

Figure 2.2: Deformations in single – lap joints with elastic adherents.

The reduction of the strain in the adherents along the overlap and the continuity of the adhesive/adherent interface cause a non-uniform shear strain (and stress) distribution in the adhesive layer. A serious drawback connected to the theory of Volkersen is that it neglects the eccentricity in the applied load, as depicted in Figure 2.3, which is caused by the non-symmetric geometry of single-lap joints. The eccentricity serves to introduce bending moments in the adherents, which in turn lead to bending deformations of the adherents. De Bruyne (1944)

adapted Volkersen's single-lap theory for the double lap joints. De Bruyne modelled the adherents as bars which are allowed to deform in the longitudinal direction, uniformly through the thickness of the adherents. The adhesive layer was considered to be a shear spring carrying only the shear stresses needed to transfer the longitudinal forces from the inner to the outer adherents.

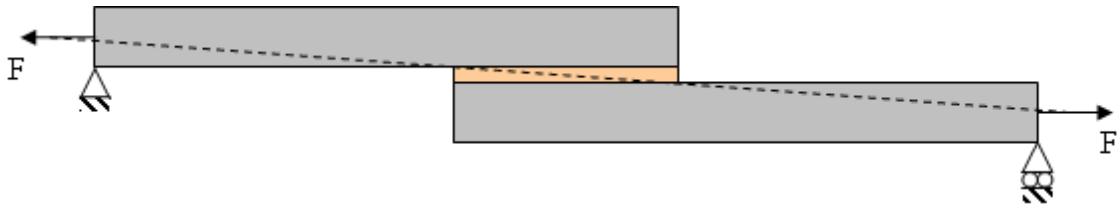

Figure 2.3: The eccentricity of the SLJ loaded in tension.

Goland and Reissner (1944) made a significant contribution by taking into account the adherent bending and adhesive peeling effects as well as adherent's large deflection (see Figure 2.4) in a two-step and decoupled approach. Their work has been widely used and evaluated experimentally and numerically by many investigators.

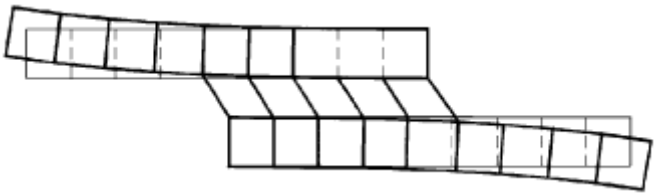

Figure 2.4: Deformations in single – lap joints predicted with Goland and Reissners's model.

Hart-Smith (1973) proposed an improved model which removes the lumped overlap (assumed by Goland and Reissner analysis) restriction by treating the adherents as beams on an elastic foundation, and provided stress solutions for linear elastic and elastic plastic adhesives. Hart-Smith has also applied his theory on composite laminated adherents, by validating his results with respective numerical and experimental studies. There is no doubt that the earlier work done by Volkersen (1938) and Goland and Reisner (1944) was a big step forward in the stress analysis of adhesively bonded joints. But according to da Silva et al. (2011) their work has several limitations: They do not account for variations of the adhesive stresses through the thickness direction, especially the interface which are important when failure occurs close to the interface. The authors also support that the peak shear stress occurs at the ends of the overlap, which violates the stress-free condition, as presented in Figure 2.5. Analyses that ignore the stress free condition overestimate the stress at the ends of the overlap and tend to give conservative failure load predictions. Ojalvo and Eidinoff (1978) used Hart-Smith's formulation, while Chen and Cheng (1983), and Crocombe and Adams (1981) adopted Goland and Reissner's formulation. Ojalvo and Eidinoff (1978) used a more complete strain/displacement equation for

the adhesive layer to investigate the influence of adhesive thickness on the stress distribution. There are also several attempts to extend or advance their work by including more factors.

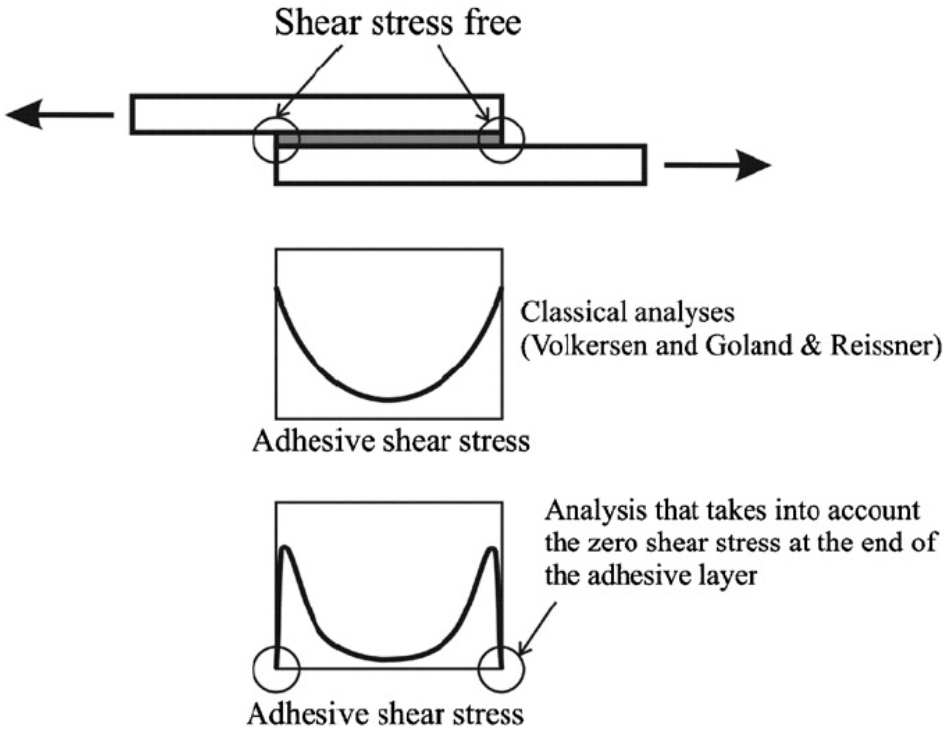

Figure 2.5: Adhesive shear stress distribution when the stress free condition at the ends of the overlap is verified.

Oplinger (1994) attempted to improve the solution of Hart-Smith (1973) by considering large deflections of the overlap coupled with the adhesive shear stress. Tsai et al. (1998) improved theoretical solutions of Volkersen/De Bruyne's and Goland and Reissner's for double lap and single lap adhesive joints, respectively. This study is based on the assumption of linear shear stress distributions through the thickness of the adherents. Jalali and Taheri (1998), Hart-Smith (1973), Tsai et al. (1998), Frostig et al. (1999), Mortensen and Thomsen (2002), Yang et al. (2004) and Zou et al. (2004) have also made contributions to theoretical analysis for adhesively bonded joints incorporating composite or steel adherents. It is noted from the above literature references that, the Euler beam theory has been widely used to model adherents and the case of coupling the peel strain with large overlap deflections has not been considered.

Zou et al. (2004) present a robust analytical tool for joint design. This tool is based on the classical laminated plate theory in conjunction with an adhesive interface constitutive model for balanced composite joints subjected to in-plane and out-of-plane loads. According to the author, this so promising tool can be easily extended to the application of various joint configurations (single lap, single strap etc.). Luo and Tong (2007) presented closed-form solutions that predict accurate edge moment and adhesive stresses for an isotropic SLJ. His study is also based on the use of Euler beam theory. However, the analysis of adhesive joints can be highly complex if composite adherents are used, the adhesive deforms plastically or if there is an adhesive fillet. In

those cases, several differential equations of high complexity might be obtained (non-linear and non-homogeneous). For those cases, numerical methods are more adequate.

2.3 Numerical solutions

The Finite Element Method (FEM), the Boundary Element Method (BEM) and the Finite Difference Method (FDM) are the three major numerical methods for solving partial differential equations in science and engineering. The FEM is by far the most common technique used in the context of adhesively bonded joints. One of the first reasons for the use of the FE method was to assess the influence of the spew fillet. The joint rotation and the adherents and adhesive plasticity are other aspects that are easier to treat with a FEM analysis. The study of Adams and Harris (1984) is one of the first FE analyses taking into account these three aspects.

The use of the BEM is still very limited in the analysis of adhesive joints. Vable (2008) explains why boundary elements can be useful for analyzing adhesive joints. The BEM has been used for the analysis of metallic structures repaired by composites (patch-repair). Salgado and Aliabadi (1995) and Liu et al. (2007) utilized the BEM to analyze cracked sheets, in which the patch and the cracked sheet were modeled using boundary elements and the adhesive was simulated as shear springs. However, these studies are focused on the cracked plate rather than on the adhesive bond. Cavallini et al. (2006) presented a boundary element technique for modeling an adhesively bonded structural joint. The formulation allowed the analysis of general lay-up laminates such as the Glare material.

The FD method is especially used for solving complex governing differential equations in closed-form models, that are usually non-linear and non-homogeneous. Öchsner (2011) refers that the major advantage of the FDM is the simple computer implementation of the procedures. The main disadvantages are the expected complications for the simulation of boundary conditions for complex shaped geometries and the difficult attainment of symmetry of the stiffness matrix. For these reasons, the FDM is only applied to simple geometries.

The finite element method is obviously treated in more detail due to its importance, and several approaches to failure analysis are treated with continuum mechanics, fracture mechanics and the more recent damage mechanics and extended finite element method (XFEM). The FE method is a numerical analysis procedure that provides an approximate solution to problems in various fields of engineering. Ashcroft (2011) gives a description of the method applied to adhesive joints.

2.3.1 Continuum mechanics approach

In the continuum mechanics approach, the maximum values of stress, strain or strain energy, predicted by the FE analyses, are usually used in the failure criterion and are compared with the corresponding material allowable values. Initially, the maximum principal stresses were

proposed for very brittle materials whose failure mode is at right angles to the direction of maximum principal stress. This criterion ignores all the other principal stresses, even though they are not nil. Establishing the failure modes in lap joints bonded with brittle adhesives, Adams et al. (1997) have extensively used this criterion to predict joint strength with success. However, because of the singularity of stresses at re-entrant corners of joints, the stresses depend on the mesh size used and how close to the singular points the stresses are taken. Values of stresses calculated at Gauss points near the singularity or extrapolation of Gauss point values to the singularity were, in fact, used. Therefore, care must be taken when using this criterion. Although the criterion is sensitive to the mesh size used, the physical insight into the failure process is very clear, as the maximum principal stress is the most responsible for the failure of joints bonded with brittle adhesives.

Von Mises proposed a yield criterion, which states that a material yields under multi-axial stresses when its distortion energy reaches a critical value. Such a criterion has been used by Ikegami et al. (1990) to study the strength of scarf joints between glass fiber composites and metals. It should be noted that this criterion is more applicable to material yielding than strength. Shear stresses have been extensively used to predict lap joint strength, especially in closed-form analyses, considering a limiting maximum shear stress equal to the bulk adhesive shear strength. These are also described here for a complete description of the continuum mechanics approach. Greenwood (1969) used the maximum shear stress calculated by Goland and Reissner's analysis (Goland and Reissner 1944) to predict joint strength. The Engineering Sciences Data Unit (ESDU 1979) implemented this criterion into a commercial package. More recently, John et al. (1991) used shear stresses together with a critical distance to predict the strength of double lap joints. Lee and Lee (1992) also used the maximum shear stress in tubular joints. da Silva et al. (2009a, b) showed for single lap joints that this criterion is only valid for brittle adhesives and short overlaps. This approach ignores the normal stresses existing in lap joints and therefore it overestimates the joint strength.

When ductile adhesives are used, criteria based on stresses are not appropriate because joints can still endure large loads after adhesive yielding. For ductile adhesives, Adams and Harris (1984) used the maximum principal strain as failure criterion for predicting the joint strength. This criterion can also predict the failure mode. However, it is equally sensitive to the mesh size, as previously discussed for the maximum principal stress approach. Hart-Smith (1973) proposed that the maximum shear strain might be used as a failure criterion when plastic deformation was apparent. da Silva et al. (2009c) implemented this criterion and others into a commercial package. da Silva et al. (2009a, b) have shown, for single lap joints, that the maximum shear strain criterion is very accurate for ductile adhesives. Crocombe (1989) studied the failure of cracked and un-cracked specimens under various modes of loading and used a critical peel stress at a distance from the singularity with some success. An alternative method was also proposed to use an effective stress, matched to the uniaxial bulk strength, at a distance. However, it was found for the latter criterion that the critical distance at which it should be

applied varied with different modes of loading because of the change in the plastic zone size. No general criterion for a given adhesive was presented. There is no real physical justification for these criteria applied at a distance, and many of them are dependent on parameters such as the adhesive thickness t_a, which means that no general criterion of failure is available within these methods. The strain energy is the area under the stress-strain curve. Therefore, both stress and strain criteria can be related to strain energy. However, it should be noted that criteria based on strain energy take account of all the stress and strain components. As a result, they are more suitable as a failure criterion than either stresses or strains alone.

Plastic energy density has also been used as a failure criterion (Adams and Harris 1987), being similar to the total strain energy criterion but it only takes the plastic part of the deformation into account. Zhao et al. (2011) applied a criterion whereby if the average plastic energy density over a certain distance within the single lap joint reached a critical value, then the joint was deemed to have failed. The specific energy is not so sensitive to the size of the integration zone, as it is 'averaged' over an area (2D analyses) or volume (3D analyses). It is common knowledge that the accuracy of the FE approach is more reliable when it is interpreted as an average, rather than in a pointwise sense. The integration region is usually chosen as a whole element for numerical convenience. In Zhao et al. (2011), the value of adhesive thickness t_a was used for integration and the predictions compared very well with the experimental results for a ductile adhesive. In the analysis of lap joints, Crocombe (1989) found that, for largely ductile adhesives, the whole overlap yielded before failure. A new failure criterion was then proposed based on the yielding of adhesive in the whole overlap. Once a path of yielding was found in the overlap with a given load, the joint was thought to be failed. Such a criterion is useful for very ductile adhesives in which the adhesive bond cannot support any larger load once it yields globally. However, it should be noted that the adhesives need to be extremely ductile (more than 20% of failure strain in shear) for the whole adhesive bond to yield before final failure (Adams et al., 1997; da Silva et al., 2008). Also, this criterion is only applicable to lap joints. Unfortunately, for certain geometric conditions, joints tend to fail before the whole adhesive bond yields. It should be realized that all the above criteria are applicable to continuous structures only. They run into difficulty when defects occur or more than one material is present, since stresses or strains are not well defined at the singular points. As a result, new criteria or modified versions of the above criteria need to be developed.

2.3.2 Fracture mechanics approach

Continuum mechanics assumes that the structure and its material are continuous. Defects or two materials with re-entrant corners obviously are not consistent with such an assumption. Consequently, continuum mechanics gives no solution at these singular points resulting in stress or strain singularities. Cracks are the most common defect in structures, for which fracture mechanics has been developed. In fracture mechanics, it is well accepted that stresses calculated

by using continuum mechanics are singular (infinite) at the crack tip. The reason why singularities exist is explained as follows. Figure 2.6 shows stresses around the tip of a sharp crack in an infinitely large plate given by continuum mechanics.

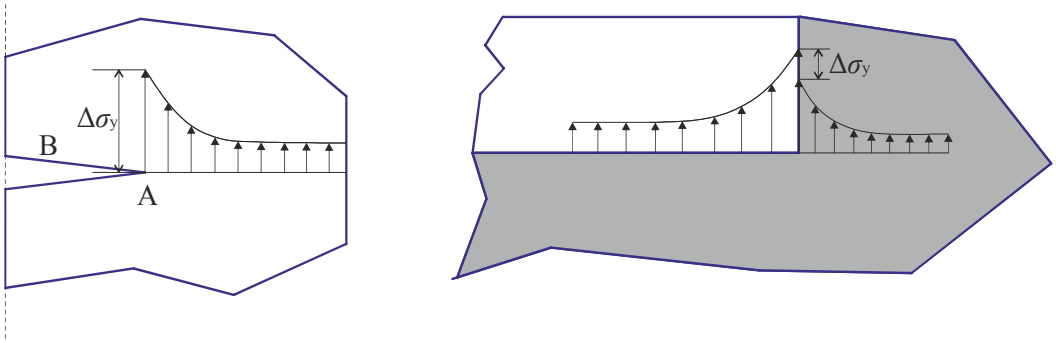

(a) (b)

Figure 2.6: Stress discontinuity around (a) a crack tip and (b) a re-entrant corner.

Physically, the y-stresses, σ_y, at the crack tip A must be finite (instead of infinite as theory predicts). However, σ_y stresses into the crack and away from the tip of the crack (shown as B in Figure 2.6) are nil because of the free surfaces. Consequently, a discontinuity of σ_y is apparent at point A unless σ_y is zero there. Such a stress distribution cannot be accommodated in continuum mechanics, which requires all the stresses to be continuous. As a result, stresses at the crack tip are not defined (being infinite). With current theories on mechanics, such a singularity always exists when the crack angle is <180°. This result was found by Williams (1959) for stress singularities in a wedged notch. This argument is also applicable to the stress singularity in two materials bonded together with a re-entrant corner. Actually, the stress discontinuity still exists, although the free surfaces do not exist. For ductile materials, a large amount of material yielding occurs and the crack may propagate stably before final failure. Thus, linear elastic fracture mechanics (LEFM) does not work anymore for such materials. The HRR (Hutchinson Rice Rosengreen) solution developed by Hutchinson (1968) and by Rice and Rosengren (1968) has, however, been extensively used in ductile fracture. Another important parameter governing failure is the so-called crack tip opening displacement (Dugdale, 1960). However, a strain singularity still exists for ductile materials, even though the stress singularity has disappeared. Fracture mechanics has been successfully applied to many engineering problems in recent years.

The damage tolerance design concept, originally adopted in the aircraft industry, was based mainly on the well-established concept of LEFM, and it has gradually gained ground in other engineering fields. Many studies dealing with adhesive joints use the strain energy release rate, G, and respective critical value or fracture toughness, G_c (O'Brien et al., 2003; Cheuk et al., 2005; Shahin and Taheri, 2008) instead of stress intensity factors because these are not easily determinable when the crack grows at or near to an interface. However, the fracture of adhesive joints inherently takes place under mixed mode because of the varying properties between different materials and the complex stress system. Failure criteria for mixed mode fracture can be

developed in a way analogous to the classical failure criteria, although the fracture surface (or envelope) concept must be introduced. Various mathematical surface functions have been proposed to fit the experimental results, such as the 3D criterion (Dillard et al., 2009):

$$\left(\frac{G_{\mathrm{I}}}{G_{\mathrm{Ic}}}\right)^{\alpha}+\left(\frac{G_{\mathrm{II}}}{G_{\mathrm{IIc}}}\right)^{\beta}+\left(\frac{G_{\mathrm{III}}}{G_{\mathrm{IIIc}}}\right)^{\gamma}=1 \tag{2.1}$$

where G_{I}, G_{II} and G_{III} are the energy release rates at Mode I, II and III fracture, respectively. The linear energetic criterion ($\alpha = \beta = \gamma = 1$) and the quadratic one ($\alpha = \beta = \gamma = 2$) are the most commonly used. The law parameters may be chosen to best fit the experimental data, or they may be prescribed based on some assumed relationship. Alternate forms for fracture envelope criteria have also been proposed (Kinloch, 1987; Hashemi et al., 1989; Charalambides et al., 1992). In all cases, the failure surface can be made to match experimental results very closely, by including additional constants.

On the other hand, cracks are more prone to develop at the bi-material interface because of the existence of stress concentrations at that area (Goyal et al., 2008) and thus be responsible for the total failure of the adhesive joint. The Virtual Crack Closure Technique (VCCT) has been utilized for the numerical simulation of the failure behaviour of adhesive joints (Panigrahi and Pradhan, 2007; Zhang et al., 2010; Sun and Yang, 2004). According to this method, the internal nodal forces are calculated at the crack tip together with the relative displacements of the adjacent nodes. These magnitudes are used for the calculation of the energy release rate (G_i, i = I, II or III), which is further compared with the experimentally measured fracture toughness (G_{ic}, i = I, II or III) of the material system. Crack propagation then occurs if the energy release rate magnitude is greater than the G_{ic} magnitude. This method is valid within the framework of Linear Elastic Fracture Mechanics (LEFM) and thus it is not appropriate in numerical predictions of adhesive joints with ductile adhesives.

Fracture mechanics can thus be used to predict joint strength or residual strength if there is a crack tip or a known and calibrated singularity (Clarke and McGregor, 1993). When materials deform plastically, the LEFM concepts have to be extended into elasto-plastic fracture mechanics. The *J*-integral proposed by Rice and Rosengren (1968) is suited to deal with these problems. The analytical definition of the *J*-integral is given by Rice as an energy line integral:

$$J=\int_{C} w\mathrm{d}x_2-T_j\frac{\partial u_j}{\partial x_1}\mathrm{d}S \tag{2.2}$$

where C denotes a curve surrounding the crack tip, the variable S indicates the arc length, w is the energy density, T_j is the traction vector, u_j is the displacement vector and x_1 - x_2 is the coordinate system. The integral path can be arbitrary provided that it travels from one of the crack surfaces to another counter-clockwise and it encloses the crack tip. The *J*-integral approach

has been used by a variety of researchers to predict the joint strength of cracked adhesive joints with good results (Choupani, 2008; Sørensen and Jacobsen, 2003; Banea et al., 2010). Nonetheless, for ductile adhesives the value of G_c is not independent of the joint geometry (Kinloch and Shaw, 1981). This is mainly because the adherents restrict the development of the yield zone in the adhesive bond, making G_c a function of joint geometry.

The major advantage of the path-independence of the *J*-integral in homogeneous materials disappears due to the interface length dependence and practice of using far field stresses and strains to calculate *J* is no longer possible. Under these conditions, the *J*-integral must be extrapolated against interface length to a point so that a great deal of mesh refinement is required. In real joints, the bondline is usually very thin and the two interfaces with the adherents will interact with each other. The interference of different singular sources so closely sited (thin bondlines) makes numerical extrapolation very difficult. If an integral path includes both interfaces, some singular effects will offset each other and the accuracy is then doubtful. Therefore, the parameter *J* may not be used as a strength criterion for joints without a pre-crack. Moreover, failure modes are extremely complicated in the area of stress or strain concentrations. Therefore, if fracture mechanics is to be used for ductile adhesives, the process will be prohibitive: first it needs to be determined when and where a crack with a reasonable size initiates. Then, this crack has to propagate stably and be arrested. Next, a new crack at another place may initiate and propagate into an unstable one, causing catastrophic failure. This process is very difficult to simulate because the crack sizes and positions are very difficult to determine. Furthermore, such a process will involve a large amount of computing time with very fine mesh, and the mesh shifting and releasing involved in crack propagation will be very difficult to perform.

2.3.3 Damage mechanics - Cohesive Zone Modeling approach

Advanced modeling techniques are thus required that comprise accurate failure predictions, surpassing the aforementioned limitations associated to the continuum and fracture mechanics approaches, to effectively model damage evolution within a material or structure with bonded components. Structural damage during loading can be found in the form of micro-cracks over a finite volume or interfacial region between bonded components, such that load transfer is locally reduced, globally resulting on a drop of applied load for a given value of applied displacement to the structure. Figure 2.7 shows a typical uni-axial σ-ε diagram up to failure for a ductile material or structure.

A FE model built solely with solid continuum elements comprising the elastic and plastic constitutive behaviours of each one of the materials, wrongly gives as modeling output the abcd' curve because of generalized plasticization without damage evolution, while a damage and failure based model can actually provide the real abcd curve, by allowing damage to grow

through the simulation of material stiffness degradation between point c (damage onset) and point *d* (complete failure).

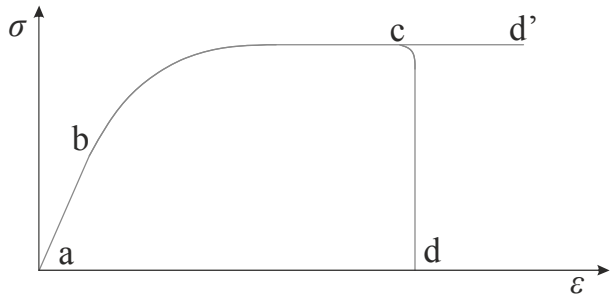

Figure 2.7: Typical uni-axial *σ*-*ε* response of a ductile material or structure.

Damage mechanics permits the simulation of step-by-step damage and fracture at a pre-defined crack path or arbitrarily within a finite region up to complete structural failure (Duan et al., 2004). However, this is still an innovative field under intense development, regarding more accurate modeling techniques, reliable and simple parameter determination methods, increase of robustness and elimination of convergence issues and it is also under heavy implementation in commercial FE software packages such as ABAQUS® (Campilho et al., 2011a).

The available techniques for damage modeling can be separated into local or continuum approaches. In the local approach, damage is confined to a zero volume line or a surface, allowing the simulation of an interfacial failure between materials, e.g. between the adhesive bond and the adherent (Yang et al., 2001), the interlaminar failure of stacked composites (Turon et al., 2007a) or the interface between solid phases of materials (Chandra et al., 2002). By the continuum approach, the damage is modeled over a finite region, within solid finite elements of structures to simulate a bulk failure (Song et al., 2006) or along an adhesive bond to model a cohesive fracture of the adhesive bond (Kafkalidis and Thouless, 2002).

The use of cohesive zone models (CZM's) coupled to conventional FE analyses is the most widespread method of predicting static or fatigue damage uptake in structures (Tvergaard and Hutchinson, 1992; Tvergaard and Hutchinson, 1993; Yang et al., 1999; Yang et al., 2000; Yang and Thouless, 2001; Campilho et al., 2005; Campilho et al., 2007).

CZM's are based on the assumption that one or multiple fracture interfaces/regions can be artificially introduced in structures, in which damage growth is allowed by the introduction of a possible discontinuity in the displacement field. The technique consists of the establishment of traction-separation laws (addressed as CZM laws) to model interfaces or finite regions. The CZM laws are established between paired nodes of cohesive elements, and they can be used to connect superimposed nodes of elements representing different materials or different plies in composites, to simulate a zero thickness interface (local approach; Figure 2.8a), or they can be applied directly between two non-contacting materials to simulate a thin strip of finite thickness between them, e.g. to simulate an adhesive bond (continuum approach; Figure 2.8b). A few works on CZM techniques use the local approach (Campilho et al., 2005, Turon et al., 2007a). With this

methodology, the plastic dissipations of the adhesive bond are simulated by the solid finite elements, whilst the applicability of cohesive elements is restricted to damage growth simulation (Figure 2.8a).

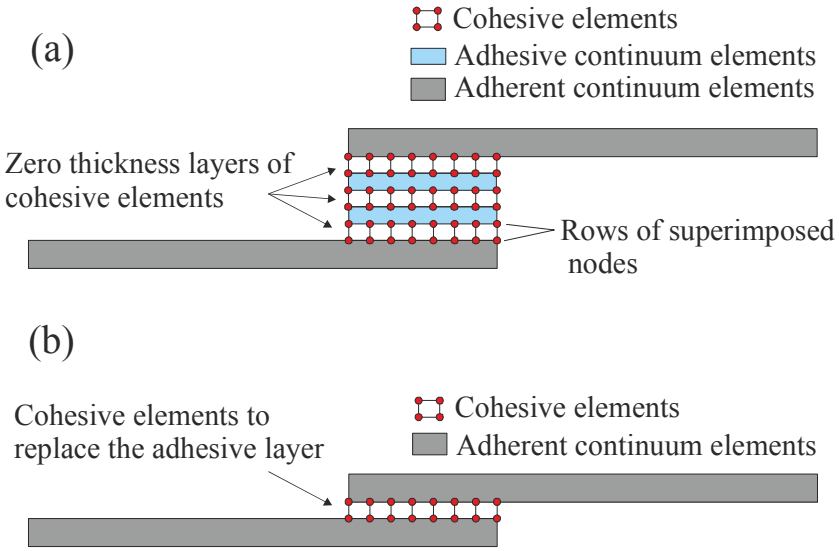

Figure 2.8: Cohesive elements to simulate zero thickness failure paths - local approach (a) and to model thin adhesive bond between the adherents-continuum approach (b) in an adhesive bond.

Although the computer implementation of LEFM techniques endured great success some decades ago, they are restricted to small-scale yielding beyond the crack tip. Since for modern toughened adhesives the plastic zones developing along the adhesive bond can be larger than the adherents thickness (Ji et al., 2010), a large effort was undertaken beginning in the late 1950s/early 1960s by Dugdale (1960). The concept of cohesive zone was proposed to describe damage under static loads at the cohesive process zone ahead of the apparent crack tip, which can be understood as a phenomenon of microvoids formation that grows with the increase of the load, forming thin fibrils until the crack appears (see Figure 2.9).

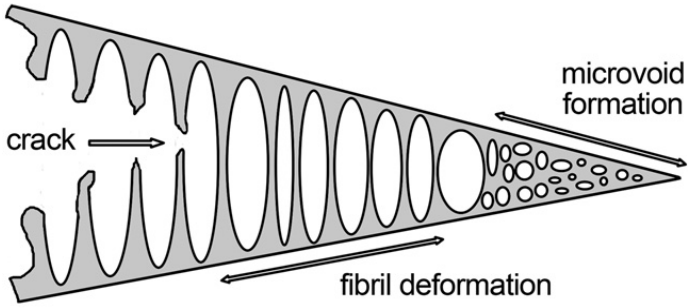

Figure 2.9: Formation of the process zone ahead of the crack in thin polymeric ductile adhesive layers.

2.3.3.1 Cohesive laws

The constitutive relation of cohesive elements is described by cohesive laws, that relate the tractions σ with the corresponding separations δ (relative displacements between the two crack

faces, i.e. between the two planes of the cohesive elements) i.e. traction–separation or T-S laws, σ-δ. The concept of a cohesive law is that the stress along the crack faces of the process zone can be described by a traction-separation law in Mode I, II and III loading and fracture (see Figure 2.10).

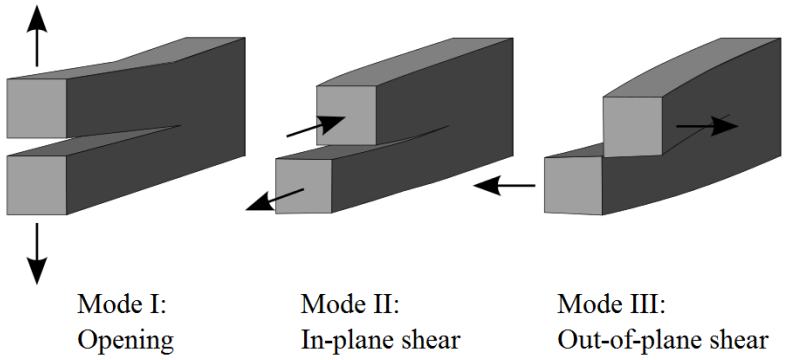

Figure 2.10: Basic loading and fracture modes of an adhesive joint.

The local normal stress σ_I and the local shear stress σ_{II} inside the process zone are functions of the local normal crack opening δ_I and tangential sliding δ_{II}. This can be written as:

$$\sigma_I = \sigma_I(\delta_I, \delta_{II}) \quad \text{and} \quad \sigma_{II} = \sigma_{II}(\delta_I, \delta_{II}) \tag{2.3}$$

According to Sørensen and Kirkegaard (2006), the evaluation of the path-independent J-integral along a path around the fracture process zone yields:

$$J = \int_0^{\delta_I^*} \sigma_I(\delta_I, \delta_{II})\,\mathrm{d}\delta_I + \int_0^{\delta_{II}^*} \sigma_{II}(\delta_I, \delta_{II})\,\mathrm{d}\delta_{II} \tag{2.4}$$

with δ_I^* and δ_{II}^* defined as the normal opening and tangential sliding displacement at the pre-crack tip, as shown in Figure 2.11.

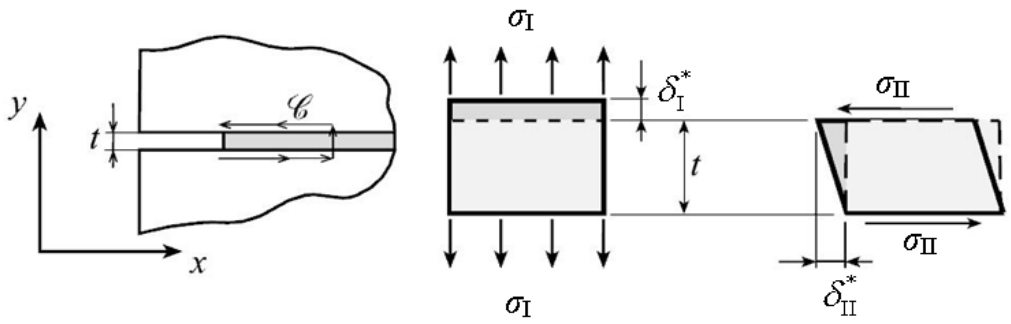

Figure 2.11: Basic deformation modes of an adhesive layer with thickness t under normal stress σ_I and shear stress σ_{II}.

When $\delta_{\mathrm{I}}^{*} \neq 0$ and $\delta_{\mathrm{II}}^{*} = 0$, a situation called pure normal opening or Mode I (see Figure 2.11), the second integral of the Equation (2.4) $J = \int_0^{\delta_{\mathrm{I}}^{*}} \sigma_{\mathrm{I}}(\delta_{\mathrm{I}}, \delta_{\mathrm{II}})\,\mathrm{d}\delta_{\mathrm{I}} + \int_0^{\delta_{\mathrm{II}}^{*}} \sigma_{\mathrm{II}}(\delta_{\mathrm{I}}, \delta_{\mathrm{II}})\,\mathrm{d}\delta_{\mathrm{II}}$ turns to zero, and the equation now yields:

$$\sigma_{\mathrm{I}}(\delta_{\mathrm{I}}^{*}) = \frac{\partial J}{\partial \delta_{\mathrm{I}}^{*}} \tag{2.5}$$

and the pure Mode I cohesive law is derived by differentiation. Respectively, the pure Mode II cohesive law can be derived when only tangential opening is present, meaning that $\delta_{\mathrm{I}}^{*} = 0$, from the following equation:

$$\sigma_{\mathrm{II}}(\delta_{\mathrm{II}}^{*}) = \frac{\partial J}{\partial \delta_{\mathrm{II}}^{*}} \tag{2.6}$$

As it can be seen, it is assumed that the local cohesive stresses depend on the local opening displacement but not on the crack opening history. This means that there is no interaction between the pure Mode I and pure Mode II cohesive law and that the normal cohesive stresses do not depend on the tangential crack opening and that the shear stresses do not depend on the normal crack opening.

$$\sigma_{\mathrm{I}} = \sigma_{\mathrm{I}}(\delta_{\mathrm{I}}) \qquad \text{and} \qquad \sigma_{\mathrm{II}} = \sigma_{\mathrm{II}}(\delta_{\mathrm{II}}) \tag{2.7}$$

This leads to the ability to measure pure mode cohesive laws under mixed mode loading by measuring both the normal and tangential crack opening.

In general, a cohesive law is described by two parts, a traction strengthening part and a traction softening part, either of which may be linear or non-linear, as shown in Figure 2.12. In CZM techniques, the two approaches that can be used regarding the cohesive law type are the intrinsic and the extrinsic approach (Kubair and Geubelle, 2003).

In the intrinsic approach, the tractions, starting from the origin, have a hardening (rising) part that denotes an increasing resistance of the cohesive surface to separation. The slope of this part of the cohesive law controls the stiffness of the cohesive area modelled. At a given separation δ_0, the cohesive traction reaches a maximum value σ_c, corresponding to the cohesive strength. After that point, the traction–separation curve follows a softening (decreasing) path associated with the failure process. Tractions are being reduced until δ reaches a critical value δ_c, from which point onwards tractions are set to zero, thus leading to the creation of a traction–free surface (i.e. a physical crack). The energy release rate is the key parameter in the formulation of a cohesive law, since the area under the traction–separation curve corresponds to the fracture toughness G_c of the adhesive joint system. This approach was first introduced within the context of finite element methods by Needleman (Needleman, 1987), who used a polynomial form for

the traction–separation law in the modelling of void nucleation associated with particle debonding.

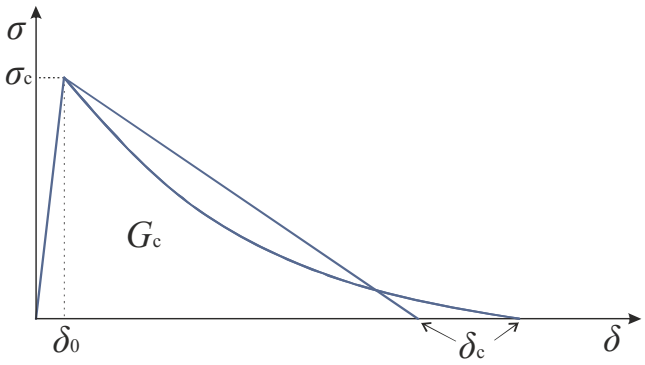

Figure 2.12: Typical traction-separation law (cohesive law).

On the other hand, the extrinsic approach relies on modeling of the softening (decreasing) part of the cohesive law only. The area under the curve also corresponds to the fracture toughness G_c of the cohesive zone. However, a steep ascend (very high stiffness) is included in the cohesive law for numerical purposes and prior to the softening part, without affecting the total area (G_c) under the law. The most common extrinsic model which is embedded in most commercial finite element software, is a linear one used extensively in a variety of fracture simulations. Developed extrinsic models over the years include triangular (Alfano and Crisfield, 2001), linear-parabolic (Allix and Corigliano, 1996), polynomial (Chen, 2002) and exponential (Chandra et. al, 2002).

Under the continuum assumption (see Figure 2.8), thin adhesive bonds to join structural members are a large field of application of CZM's (Campilho et al., 2008a), but the single row of cohesive elements used to model the bulk strip of adhesive makes it impossible to differentiate thickness-wise effects or concentrations of stresses towards the interface (Magalhães et al., 2005), providing an equivalent behaviour of the bond. Differences exist regarding the definition of the cohesive laws between the local approach modelling (the initial stiffness can use the penalty function method - extrinsic cohesive laws) and continuum CZM modelling (the initial stiffness must accurately reproduce the deformation behaviour of the thin material strip - intrinsic cohesive laws). In the local approach for bonded joints simulation, the adhesive is modeled as an elastoplastic continuum by solid FE elements and the "intrinsic fracture energy" is considered for the CZM laws instead of G_c relating to the required dissipation of energy to create a new surface, while the plastic dissipations of ductile materials take place at the solid elements representative of the adhesive bond. Thus, G_c is the sum of these two energy components, increasing by inclusion of the plastic dissipation of materials in the models. Under these assumptions, damage growth is ruled by the work of separation of the fracture surfaces instead of G_c, due to the dissipated energy by the continuum elements. The effects of external and internal constraints on the plastic dissipations of an adhesive bond are thus accountable for in the local

approach. On the other hand, compared to the continuum approach, to be described in the following, more parameters and computations are needed (Ji et al., 2010).

Among the CZM techniques, a methodology which relies on intrinsic cohesive laws and on the continuum approach (see Figure 2.8) for the numerical prediction of the loading and fracture behaviour of adhesive joints is based on the Embedded Process Zone (EPZ) approach, introduced by Thouless and his co-workers (Yang et al., 1999, 2000, 2001; Yang and Thouless, 2001). Kafkalidis and Thouless (2002) have developed the well known trapezoidal model for the description of the EPZ under the continuum approach, as shown in Figure 2.13. According to the EPZ, the adhesive layer works as the continuum which provides and transfers tractions between the adherents. From the numerical point of view, the adhesive material is totally represented by interface or cohesive elements that can model the kinematics incorporated in the EPZ. The constitutive relations are given in terms of opening and shear traction–separation laws under pure Mode I (Yang et al., 1999) and pure Mode II (Yang et al., 2001) loading and fracture, respectively. The EPZ approach has been also applied in finite element models to simulate mixed - mode loading and fracture (Campilho et al., 2008a; Campilho et al., 2009b; Campilho et al., 2009c). Yang and Thouless (2001) used the EPZ approach for the numerical prediction of geometries that undergo extensive plastic deformation under mixed - mode loading e.g. T-peel and single-lap specimens. The authors utilized a failure criterion together with the introduction of a phase angle to relate the pure Mode I and Mode II trapezoidal T-S laws and thus to develop a mixed-mode EPZ model. On the other hand, Campilho and his co-workers (Campilho et al., 2005, 2007, 2008a, 2008b, 2009a, 2009b, 2009c) developed a cohesive mixed-mode damage model to predict the behaviour of ductile adhesives with a trapezoidal shape T-S law representing loading and fracture of each fracture mode, within the framework of Elastic Plastic Fracture Mechanics. The trapezoidal model has been proven to be an effective T-S law that can adequately model the coupling between the behaviour of the adhesive/adherent interface and the behaviour of the adhesive itself, namely the adhesive failure and plasticity, respectively.

In the framework of CZM techniques and within the continuum approach, Paulino and his co-workers have made significant contributions by developing new traction-separation laws and by evaluating the effectiveness of the already existing ones in various types of loading and fracture conditions (Alfano et al., 2007; Alfano et al., 2009; Park et al., 2009). In particular, Alfano et al. (2007) and Alfano et al. (2009) have conducted a comparative numerical-experimental study, in order to show the influence of the shape of three intrinsic cohesive laws (triangular, trapezoidal and exponential) to the Mode I fracture of pre-cracked adhesively bonded Double Cantilever Beam specimens. One of the authors' major conclusion is that the triangular and trapezoidal laws yield promising results in the undamaged region of cracked adhesive joints since the pre-peak slope of the corresponding traction-separation laws can be controlled (intrinsic type).

Park et al. (2009) developed a potential-based constitutive model, shown in Figure 2.13 for the prediction of mixed-mode cohesive fracture. The derivation of the cohesive laws and the

mixed-mode model is based on the PRP potential (Park-Paulino-Roesler) also developed by the authors. In the PRP model, both normal and tangential interactions are described by polynomial potentials. The authors have introduced two parameters, one for each separate Mode (I or II), which control the softening behaviour of the corresponding cohesive law. In this way the PRP model is applicable to various material softening responses (brittle, quasi-brittle and ductile).

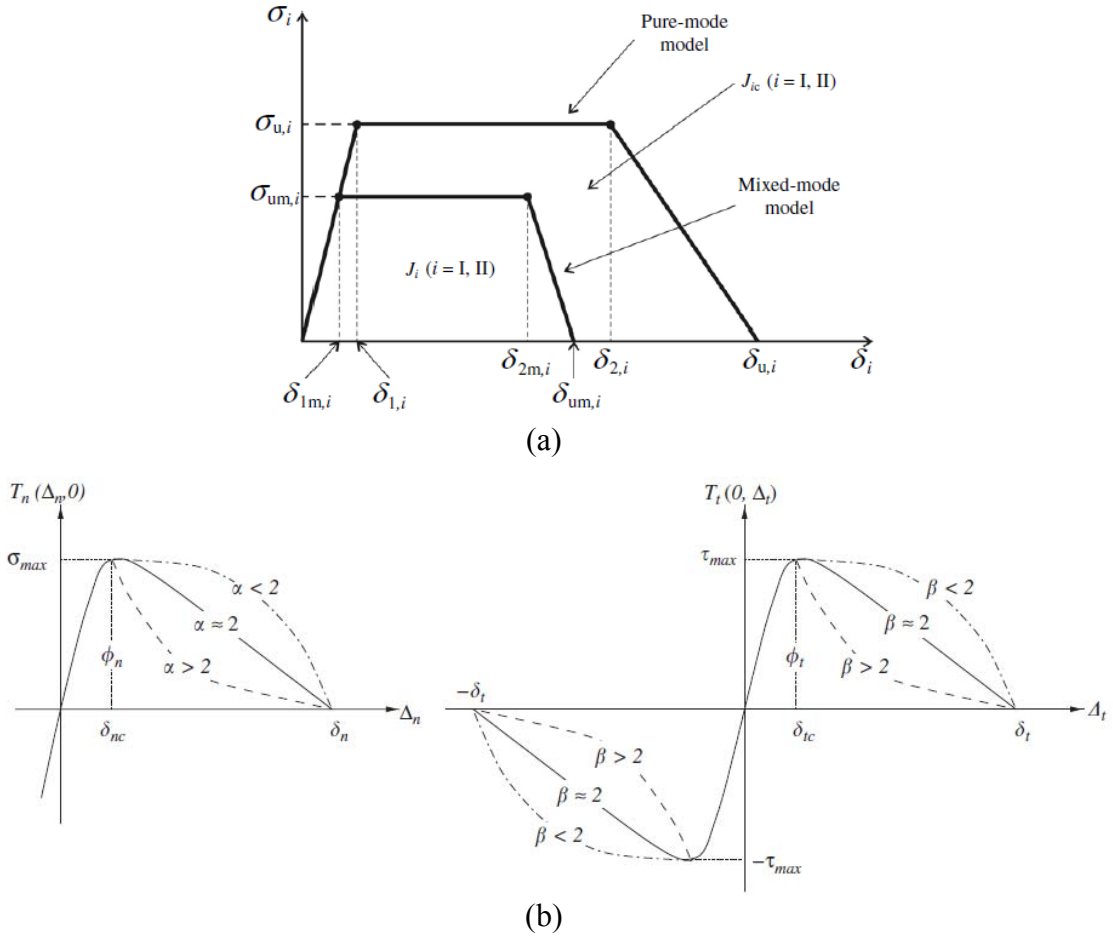

Figure 2.13: Trapezoidal laws (from Campilho et al. 2008) (a) and Park-Paulino-Roesler laws (from Park et al. 2009) (b).

2.3.3.2 Determination of cohesive parameters

Finite element analyses that include CZM techniques offer a powerful means to account for the largely nonlinear fracture behaviour of modern adhesively bonded joints, but the CZM parameters require careful calibrations by experimental data and respective validation in order to accurately simulate the failure process. Despite this fact, standardized methods for the definition of the critical stresses are not yet available. In recent years, many works were published regarding the definition of the CZM parameters (G_c or J_c if ductility is present and σ_c in Mode I and II, respectively) and a few data reduction techniques are currently available (e.g. the property determination technique, the direct method and the inverse method) that enclose varying degrees of complexity and expected accuracy of the results.

By the direct method, the complete CZM law and the respective shape for a given material strip or interface can be precisely estimated by the differentiation of the *J*-δ curves. The most commonly used experimental set-ups in order to measure Mode I and Mode II cohesive laws is the Double Cantilever Beam (DCB) and the End Notch Flexure (ENF) test, respectively, as shown in Figure 2.14. Ji et al. (2010) measured the Mode I cohesive laws of a bonded DCB joint, trying to provide data for the parameter calibrations in numerical models and also to investigate the relation between adhesive thickness and interface toughness. The same authors (Ji et al., 2011) have conducted experiments for measuring the Mode II cohesive laws by testing bonded ENF specimens. In both cases LOCTITE Hysol 9460 was utilized as the adhesive material system.

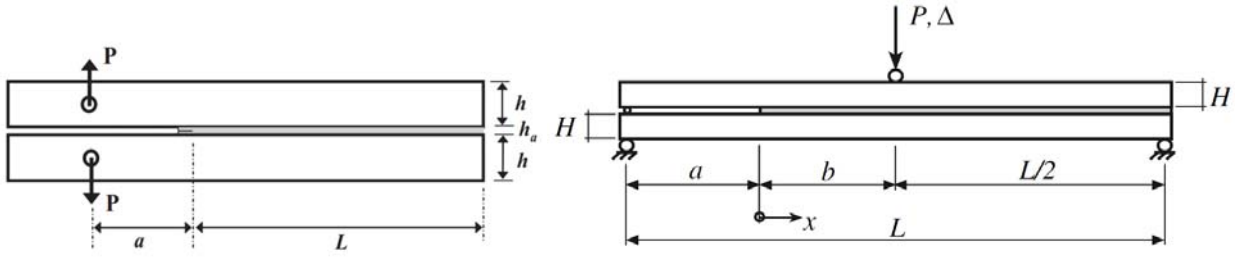

(a) (b)

Figure 2.14: Double Cantilever Beam (a) and End Notch Flexure (b) specimens for measurement of the pure Mode I and II cohesive laws.

Andersson and Stigh (2004) used a direct method to determine the continuum CZM parameters in Mode I of a ductile adhesive bond of Dow Betamate® XWI044-3 in a DCB test configuration, after approximation of the *J*-δ data to a series of exponential functions to reduce errors in the measured data. In the work of Carlberger and Stigh (2010), the continuum CZM laws of a thinbond of a ductile adhesive (Dow Betamate® XWlO44-3) were determined in tension and shear using the DCB and ENF test configurations, respectively. The values of J_{Ic} and J_{IIc} were derived by a *J*-integral formulation to accurately capture the large plastic straining effects present at the crack tip of the ductile adhesive (Yan et al., 2001a, b). Actually, the *J*-integral is a viable means to capture the adhesive nonlinearity for a monotonic loading process, i.e., if no unloading occurs. A typical J_{Ic} / δ_I and J_{IIc} / δ_{II} relation is shown in Figure 2.15a. To obtain the cohesive laws a differentiation was needed over the J_{Ic} / δ_I and J_{IIc} / δ_{II} data plots and typical results are presented in Figure 2.15b. It can be seen that the cohesive laws derived depended substantially on the adhesive layer thickness.

For the measurement of mixed mode cohesive laws, different experimental set-ups have been used. Efforts have been made to find a test set-up that will allow testing under the full range of mode-mixities, which means from pure Mode I to pure Mode II, with just one type of specimen geometry. One of the most used experiment set-ups is the Mixed Mode Bending (MMB), shown in Figure 2.16a, providing an easy variation of the mode ratio by just altering the lever length of the loading lever (de Moura et al., 2009). The MMB test can be considered as a

superposition of the DCB and the ENF tests mentioned before, used for the fracture characterization of pure Mode I and pure Mode II, respectively.

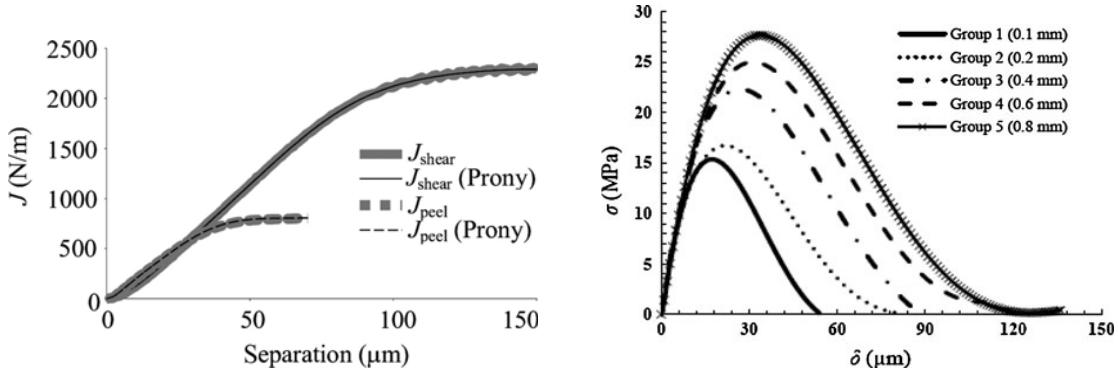

(a) (b)

Figure 2.15: Energy release rate versus separation (a) and measured cohesive laws (b).

Apart from the MMB specimen, other configurations have been also used. A promising one is presented in Choupani (2008), where the author used modified Arcan specimens. This test set-up is consisted of various combinations of adhesive, composite and metallic adherents with a special loading fixture, in which by altering the loading angle a full range mode mixity loading is achieved. Choupani (2008) was able to obtain Mode I, Mode II and mixed mode fracture data and perform numerical analyses of the experiments. His main goal was to measure the fracture toughness K_{Ic} and K_{IIc} and then derive formulas for the derivation of J_{Ic} and J_{IIc}. The experiment set-up and the geometry of the specimen used is shown in Figure 2.16b.

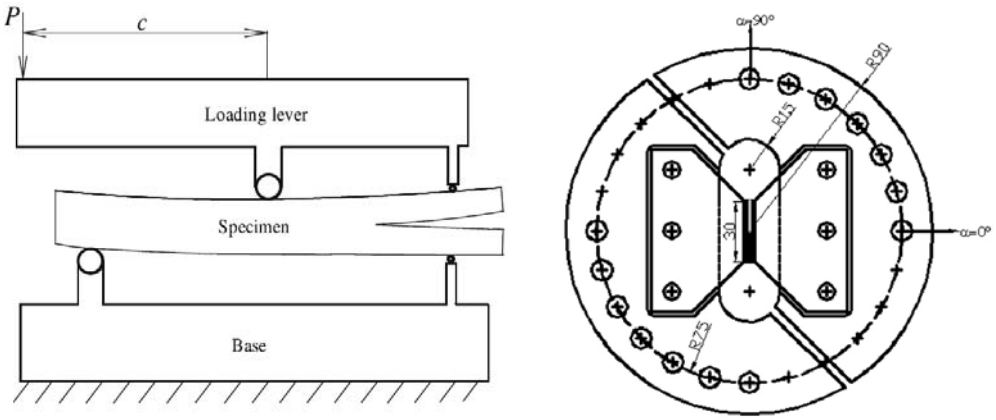

(a) (b)

Figure 2.16 Mixed Mode Bending Specimen (a) and the modified Arcan specimen (b).

A very promising experimental test for measuring pure and mixed mode cohesive laws is the Double Cantilever Beam with Uneven Bending Moments (DCB-UBM) proposed by Sørensen et al. (2006). In this study the specimen geometry used is called Double Cantilever Beam under Uneven Bending Moments (DCB-UBM). The principle of creating different bending moments in the two free beams of the DCB-UBM specimen is shown schematically in Figure 2.17. Forces of identical magnitude, P, are applied perpendicular to two transverse arms

connected to the end of the beams of the DCB specimen. The un-cracked end of the specimen is restricted from rotation but can move freely in the x_1-direction. Different moments are obtained if the length of the two moment arms, l_1 and l_2, of the transverse arms are uneven ($M_1 = P\ l_1$ and $M_2 = P\ l_2$). M_1 and M_2 are defined positive when they act in the counter clockwise direction, as shown in Figure 2.17. With one of the beam arm fixed, say $l_2 \geq 0$, the mode mixity can be changed simply by altering the other moment arm, l_1. The significant advantages of the DCB-UBM test are that the energy release rate can be calculated analytically with no need to measure the crack propagation. Moreover, since the specimen is loaded with pure moments, there are no transverse forces transmitted, reducing significantly this way any friction between the opening faces. The same specimen geometry can be used for all the range of mode mixities, so that there are no errors associated with differences in the process.

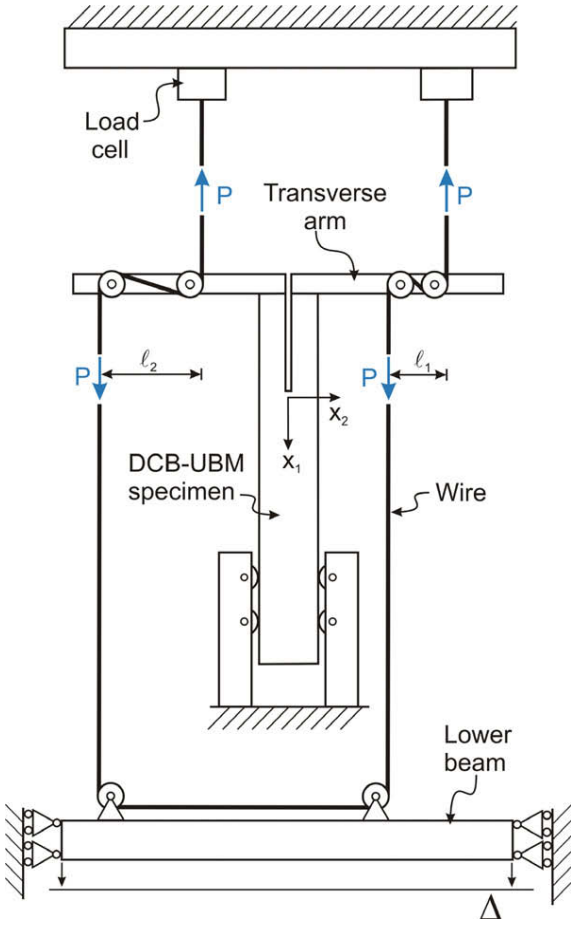

Figure 2.17: Schematic representation of the Double Cantilever Beam loaded with Uneven Bending Moments (DCB-UBM).

2.3.3.3 Applications of Cohesive Zone Models based on the Embedded Process Zone Approach

The majority of CZM studies relate to static applications. Concerning bonded joints, Yang et al. (1999) used a CZM, within the continuum framework, to simulate a pure tensile fracture in bonded DCB and T-peel joints, not specifying the adhesive used. A trapezoidal CZM law (see

Figure 2.13a) was employed to simulate the adhesive bond behaviour. The authors concluded that J_{Ic} and $\sigma_{u,I}$ are the dominant parameters in the FE analyses, while the two shape parameters $\delta_{1,I}/\delta_{u,I}$ and $\delta_{2,I}/\delta_{u,I}$ have a marginal influence on the results. As a result, the shape parameters were arbitrarily fixed at $\delta_{1,I}/\ \delta_{u,I}$ = 0.15 and $\delta_{2,I}/\ \delta_{u,I}$ = 0.5, while J_{Ic} and $\sigma_{u,I}$ were fitted by an inverse method between the experimental and FE data of the DCB specimens. By testing the proposed CZM law at varying conditions, the authors assumed that it could be used to predict the tensile fracture of different test geometries. The same authors considered an identical trapezoidal CZM law (Fig. 29) for elastic-plastic crack growth modelling in shear by the continuum approach of a t_a = 0.4 mm ductile adhesive bond of Ciba® XD4600, considering the ENF test (Yang et a1., 2001). The value of J_{IIc} was determined with a trial and error inverse procedure, by comparing the experimental and FE data for one particular set of dimensions. The two shape parameters, $\delta_{1,I}/\ \delta_{u,I}$ and $\delta_{2,I}/\ \delta_{u,I}$, were arbitrarily equaled to 0.15 and 0.5, respectively, because of numerical evidence that their effect on the fracture process was not significant. Stress $\sigma_{u,II}$ was estimated by the assumption that in the ENF tests performed, the local strains at the crack tip were approximately 40%. Using the shear stress-shear strain (τ - γ) experimental curve of the adhesive obtained by torsion tests of adhesively-bonded butt joints, the value of $\sigma_{u,II}$ = 35 MPa was found for γ = 40%, and thus it was used in the subsequent analyses. Comparison of the experimental and FE P-δ curves for one specimen is presented in Figure 2.18. Results from a FEM calculation using only the continuum properties of the adhesive bond with no failure criterion were superimposed in Figure 2.18, showing that the deformation behaviour of the specimen is only accurately captured until crack initiation, rendering the results invalid for crack propagation. The authors also emphasized the large difference of the CZM parameters for tension and shear loadings, justifying the use of mode dependent CZM relations to analyze the mixed mode fracture of bonded structures.

Yang and Thouless (2001) simulated the mixed mode fracture of plastically deforming asymmetric T-peel specimens and single lap joints using a mode dependent CZM to simulate the adhesive bond (Ciba® XD4600), equally by a continuum modelling approach. Tension and shear fracture parameters obtained from previous works were combined with mixed mode propagation criteria to provide quantitative predictions of the deformation and fracture load of bonded structures under a mixed mode loading. Tension and shear CZM laws, previously developed for this adhesive in the works of Yang et al. (1999), (2001), respectively, were used without modification with an energetic propagation criterion similar to that of Equation (2.1). Since experimentally both evaluated geometries undergo adhesive failures, the shear CZM parameters from the work of Yang et al. (2001) were used, since in this work adhesive failures also occurred in the ENF specimens tested.

Kafkalidis and Thouless (2002) performed a FE analysis of symmetric and asymmetric single lap joints using a continuum CZM approach that included the adhesive plasticity by means of trapezoidal CZM laws. The CZM laws, propagation criterion and analysis procedure were similar to those of Yang and Thouless (2001). Using CZM parameters determined for the

particular combination of materials used, the FE predictions for different bonded shapes (varying the overlap length*)* showed excellent agreement with the experimental observations. A few parametric studies on bonded joints or repairs are also available that use CZM's for optimization of the geometry (Campilho et al., 2009b), or evaluation of geometrical modifications to the adherents or adhesive bond to increase their load bearing capabilities (Campilho et al., 2008b).

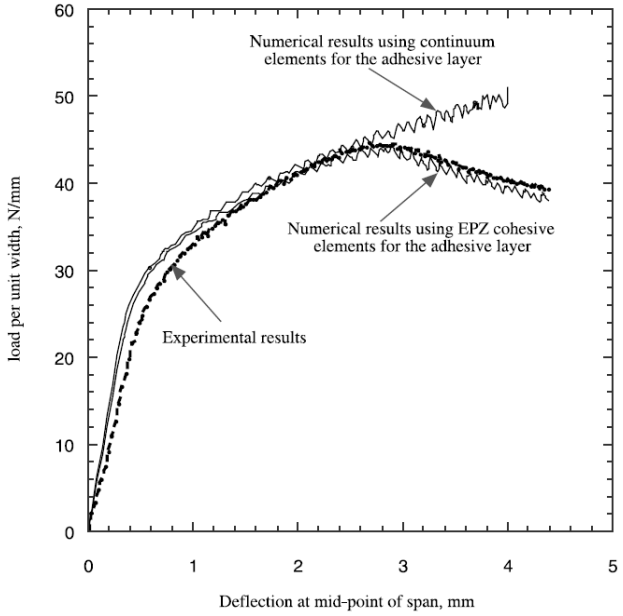

Figure 2.18: Experimental and numerical load-deflection plot for the ENF test (Yang et al., 2001).

Campilho et al. (2009a) experimentally tested carbon-epoxy scarf repairs in tension, using scarf angles between 2° and 45°, considering CZM's for the strength prediction. To account for the ductile behaviour of the adhesive (Huntsman Araldite® 2015), a trapezoidal CZM including the adhesive plasticity was used. The cohesive laws of the adhesive layer-continuum approach and composite interlaminar and composite intralaminar (in the transverse and fiber direction) local approach necessary to replicate numerically the experimental failure paths, were previously characterized with DCB and ENF tests for tension and shear, respectively, using an inverse methodology. Validation of the proposed model with experimental data was accomplished in terms of global stiffness, strength and corresponding value of *b,* and failure mode. The layout of cohesive elements in the models is depicted in Figure 2.19.

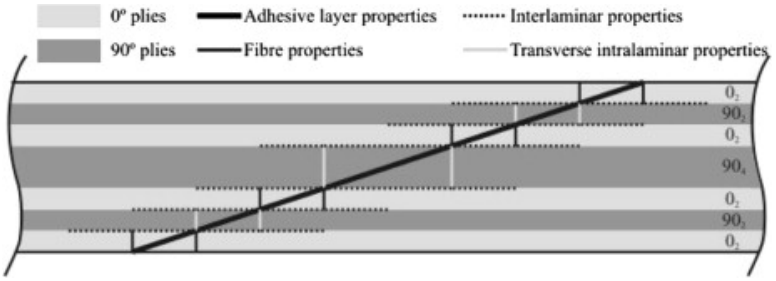

Figure 2.19: Layout of cohesive elements with different CZM laws in the scarf repair FE models (Campilho et al., 2009b).

The adhesive representative elements were inserted along the scarf replacing the adhesive bond, the interlaminar elements were positioned between different oriented plies, the transverse intralaminar elements were used vertically in the 90° plies to simulate intralaminar matrix cracking, and the fibre elements were placed vertically in the 0° plies to simulate fibre cracking. Two distinct failure modes were experimentally observed: types A and B failures. Type A failure was observed for the repairs with 15°, 25° and 45° scarf angles, consisting on a cohesive failure of the adhesive. Type B failure occurred for the scarf angles of 2°, 3°, 6° and 9°, representing a mixed cohesive and interlaminar/ intralaminar failure (Figure 2.20). A detailed discussion for this failure mode modification was provided, based on a stress analysis of the repairs. The CZM simulations accurately reproduced the experimental fracture modes, and the failure mode modification between types A and B, showing the effectiveness of CZM modelling for static applications.

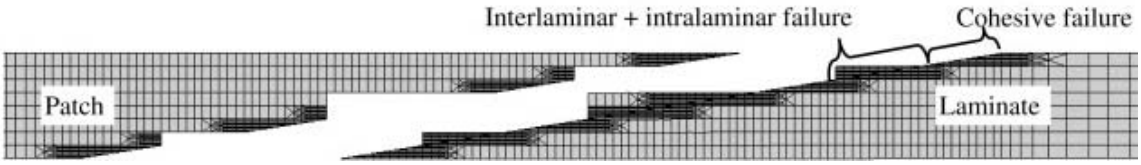

Figure 2.20: Type B failure for a 3° scarf angle repair: FE prediction (Campilho et al., 2009b).

The FE study of Campilho et al. (2009c) addressed the tensile strength optimization of carbon epoxy single and double strap bonded repairs by geometric modifications at the overlap. CZM's were considered for local modelling of the adhesive, i.e., to provide crack growth, whilst the ductile adhesive bond (Huntsman Araldite® 420) was modified by solid FE elements. Validation of the procedure was initially accomplished with experimental results from the literature.

2.4 Objectives and layout of PhD thesis

The main scope of this PhD thesis is the development of numerical tools for the computational analysis of engineering structures that involve adhesion problems, that is interface and interphase problems. The proposed numerical tools should be able to be implemented within

the framework of non-linear Finite Element Methods (FEM) and to be utilized by design engineers and researchers for the design and analysis of adhesively bonded joints and composite structures. For this purpose, particular focus has been initially given in the study of the failure mechanisms that evolve during the pure mode delamination propagation in fiber reinforced composite materials (interface problems) and later in the study of the mixed-mode loading and fracture of adhesively bonded joints (interphase problems). The proposed numerical tools involve novel constitutive relations that describe the aforementioned phenomena and are based on fracture and damage mechanics, in accordance to Cohesive Zone Modeling (CZM) techniques.

Initially, a continuum damage constitutive model is presented for the prediction of the in-plane failure modes of laminated composite materials, under the framework of progressive damage modeling. In the following, new cohesive laws are developed for the prediction of delamination initiation and propagation under Mode I and Mode II loading and fracture in fibrous laminated composite materials. Having developed numerical predictions of the failure response of composite materials, the next research activity is focused on providing constitutive relations for the predictions of structural adhesively bonded joints. The proposed constitutive relations are validated with tests conducted on steel-to-steel and composite-to-steel adhesive joint geometries that involve flat adherents. Next, a numerical parametric study, that involves axisymmetric adhesive joints (tubular cases), has been conducted, showing the potential of the proposed numerical tool.

In conclusion, the present PhD thesis provides separate advanced numerical tools that can be further integrated in one for the prediction of the failure response of structures that involve composite materials and adhesive joints. Thus, damages and failures occurring either within composite materials or within the adhesive layer of the joined members could be numerically captured and consequently the maximum allowable loading conditions of a structure can be accurately predicted.

In detail, the research activities performed within the framework of this PhD thesis are provided herein according to the following layout:

Progressive failure analysis of composite materials

Chapter 3 focuses on the numerical prediction of the post buckling progressive and final failure response of stiffened composite panels based on structural nonlinear finite element methods. For this purpose, a Progressive Failure Model (PFM), that accounts for all in-plane failure modes, is developed and applied to predict the behaviour of an experimentally tested blade-stiffened panel found in the literature. The developed PFM has been implemented in non-linear finite element analysis procedures under the framework of the commercial software Ansys. Failure initiation and failure propagation as well as the post buckling ultimate attained load have been numerically evaluated and compared to the corresponding experimental values.

Experimental and numerical investigation of the pure Mode I and II delamination growth

Chapter 4 involves an experimental and numerical investigation of the fiber bridging mechanisms incorporated in the Mode I and II fracture growth of laminated composite materials, within a combined framework of LEFM and damage mechanics. For this purpose, Glass Fiber Reinforced Polymer (GFRP) coupons have been manufactured and tested under a traditional DCB and ENF test configuration. The main focus of the experimental part is to investigate and compare the effectiveness of three different fiber bridging laws, calculated from three respective available in the literature data reduction schemes, describing the bridging zone, for the Mode I and II, respectively. The numerical investigation aims at validating the experimentally obtained bridging laws and proposing to the literature a novel effective numerical implementation (Traction-Separation law) of the experimentally obtained bridging laws. The proposed Traction-Separation laws aim at predicting the entire fracture process zone (fiber bridging and cohesive zone) developing during the delamination growth in pure Mode I and pure Mode II.

Development of a novel constitutive model for ductile adhesive joints

In Chapter 5 a new Traction–Separation law is developed that represents the constitutive relation of ductile adhesive materials. Two formulations are provided regarding the modelling space utilized for the finite element predictions, that is a 2D and a 3D space. Both proposed models (2D and 3D) are capable to predict the elastic, plastic and failure material response of a thin ductile adhesive layer constrained between two continuum media under mixed-mode loading and fracture conditions. The 2D model accounts for Mode I and Mode II fracture, whereas the 3D model additionally accounts for Mode III fracture. The proposed 2D and 3D models represent the constitutive response of user-developed 2D and 3D cohesive elements, respectively, that are utilized to model the mechanics and kinematics of the adhesive layer. Initially, the independent-mode proposed laws (loading and fracture in Mode I, II and III) are mathematically described and then introduced in a developed formulation that simulates the interdependency of the mixed-mode coupled laws.

Experimental and numerical investigation of metal-to-metal adhesive joints

For verification and validation purposes of the proposed 2D and 3D laws and mixed-mode model (Chapter 5), steel adherents have been adhesively bonded with a structural ductile adhesive material in order to fabricate a series of single lap and double strap adhesive joint configurations. The manufactured joints have been experimentally tested under uniaxial loading and their global response (force - displacement) has been recorded. Numerical predictions have been carried out of the tested specimens in a 2D and 3D space, respectively. Thus, corresponding numerical and experimental results have been compared for each joint case, respectively.

It has been concluded that uni-axial testing of the single lap and double strap joints, stresses the adhesive layer mostly in Mode I (peel stresses) and Mode II (in-plane shear stresses),

in a way that the contribution of Mode III (out-of-plane shear stresses) is of insignificant importance. For this purpose, a new to the literature experiment has been designed, which is based on a simple Single Lap Joint subjected to Eccentric Loading (SLJ-EL). The basic concept that lays behind this configuration is that the in-plane co-axial tensile loads, lead the adhesive layer to develop significant amounts of normal stresses, in-plane and out-of-plane shear stresses which correspond to Mode I, II and III loading and fracture. Thus, numerical predictions of the tested SLJ-EL specimens have shown the adequacy of the proposed 3D model to predict the mixed-mode response of adhesive joints, where all three fracture modes (Mode I, II and III) contribute to the failure of the adhesive layer. All the above work is described in Chapter 6.

Experimental and numerical investigation of composite-to-metal adhesive joints

Chapter 7 initially presents a combined experimental and numerical parametric study of adhesively bonded Single Lap Joint (SLJ) geometries between relatively thick dissimilar adherents. The primary objective of this study is to investigate the effect of various parameters, i.e. adherents' thicknesses (two different stiffness ratios, 0.175 and 0.35), adhesive thickness (0.5 and 0.8 mm) and overlap length (25 and 75 mm), on the failure load and failure mode of joints with dissimilar materials. The SLJ specimens were tested under a uniaxial tensile quasi-static displacement. The numerical part of this work focuses on predicting the experimental attained response, in terms of the force-displacement and force-strain curves, of the tested SLJ specimens with the use of the proposed 3D laws, described in Chapter 5.

Additionally, the experimental cohesive laws of a ductile adhesive layer obtained from DCB-UBM tests of composite-to-steel specimens have been utilized in numerical predictions according to the proposed 3D Traction-Separation laws (Chapter 5). All the above work is described in Chapter 7.

Numerical parametric analysis of tubular adhesive joints

Chapter 8 deals with the investigation of the effect of the geometrical configuration (including material selection and detail geometrical parameters) to the maximum strength of tubular joints subjected to internal pressure and axial loading, with the use of the proposed 3D laws. Two cases have been considered, that is tubular adhesive joints between composite tubes with equal thickness and a case where a tube is adhesively bonded to a steel flange. Thus, a Single Lap Joint (SLJ) and a Single Strap Joint (SSJ) geometrical configuration have been considered for the first case, whereas a SSJ configuration has been considered for the tube-to-flange joints. For the case of the SSJ configuration, two different strap thicknesses and two different materials have been considered together with 6 different overlap lengths, resulting to 24 study cases for the tube-to-tube and 24 study cases for the flange-to-tube adhesive joints, respectively.

3. Progressive failure analysis of composite materials

3.1 Introduction

This section deals with the development of a Progressive Failure Model (PFM) and its implementation to non-linear finite element analysis for the prediction of the failure process of a blade-stiffened composite panel under compressive loads.

The analysis and design of composite laminated materials has gained increasing interest in the field of marine structures. In fact, for more than 40 years, conventional fiberglass composites have dominated the recreational boating industry due to their advantages over different materials used for ship construction (Smith, 1990). The shipbuilding industry has already started to incorporate composite materials in new ship construction and to replace specific steel components with composite ones in existing ships (Mouring, 1999; Shenoi, 1993). The advantage of high strength to weight and high stiffness to weight ratio and the flexibility they offer to the designer for adjusting their strength so as to meet certain performance requirements, has turned them to be very attractive and promising, especially with the design of future structures.

Fiber reinforced plastic stiffened panels are commonly utilized as components for the construction of a composite marine structure. The introduction of stiffened skin panels manufactured from composite materials has increased the potential to produce even more efficient structures, (Shenoi, 1993a). The main beneficial advantage of the composite stiffened panels is that they offer significantly higher strength capacity than the skin panels without stiffeners, when loaded in compression.

Among the early works about buckling and postbuckling behaviour of composite structures is that by Stevens et al. (1995), with the major conclusion stating that during postbuckling, composite structures can carry loads higher than the critical buckling load. Several other researchers have studied the postbuckling behaviour of laminated composite stiffened panels. Postbuckling design is being used for steel structures in terms of weight savings. Orifici et al.

(2008a) state that the application of postbuckled design within the framework of composite structures has been limited, owing to concerns relating to the durability of composite materials, since the latter do not yield locally under the high local stress field developed in the postbuckling range.

In most cases, failure of stiffened panels has been experimentally measured to be far beyond their postbuckling range (Shenoi, 1993a, b; Orifici et al., 2008; Falzon, et al. 2000). There are several mechanisms involved in the failure of stiffened composite panels loaded in compression. Apart from fiber breakings, fiber buckling, matrix cracking, fiber-matrix shear and delamination, stiffener-skin separation is likely to occur and lead to catastrophic results, since the ribs carry most of the load (Raju et al., 1996). Classical non-linear analyses are unable to predict the behaviour of the stiffened panels afterwards the point of damage or failure initiation. However, Hinton et al. (2002) and Puck and Schurmann (1998) utilized various failure criteria to predict the onset of each different damage mechanisms that are separately involved in composite stiffened panels buckling failure. However, for panels that can withstand higher loads, beyond damage onset, the use of such analyses is not sufficient to predict ultimate failure.

Thus Lee (1982) pioneered an approach based on progressive failure analysis of composite structures with the use of the finite element method. Since then, numerous authors have developed numerical based algorithms to address the progressive failure and collapse of composite laminated structures (Naik et al., 2008; Laurin et al., 2007).

The implementation of progressive failure algorithms into a finite element analysis for the study of buckling and postbuckling behaviour of composite stiffened panels loaded in compression is a matter of increasing interest. Most previous studies have mainly focused on the progressive failure analysis of composite plates with cut-outs (Lopes et al., 2007; Labeas et al., 2008), since the stress concentrations developed at the edge of the cut-outs lead to guided failure paths, offering a well defined case for benchmarking and validation of the developed progressive failure models. To the authors' knowledge, progressive failure analysis of composite stiffened panels has not been sufficiently studied. Orifici et al. (2008b) has conducted a non-linear finite element analysis by introducing a stress-based adhesive degradation model in order to predict the failure mechanisms introduced by the debonding behaviour in blade-stiffened composite panels under compressive loads.

Falzon et al. (2000) experimentally investigated the postbuckling behaviour of blade-stiffened composite panels under compressive loads. According to the authors, two identical stiffened panels have been manufactured and tested under the same loading and boundary conditions, but failed under different mode. One of the panels failed explosively, whereas the other panel underwent a mode switch near its ultimate load capacity, according to experimental observations. In a latter work, Falzon and Hitchings (2003) achieved the numerical prediction of the mode-switch of the latter panel in its post-buckling range under the framework of a modified explicit dynamic analysis. However, to the authors' knowledge Falzon did not utilize any type of failure methodologies to numerically address failure process of either panel. Thus, in the present

work, experimental tests described by Falzon et al. (2000), have been numerically simulated with the implementation of a developed PFM into a non-linear finite element analysis.

3.2 Progressive failure model methodology

3.2.1 Overview

The basic concept that lies under the term progressive failure analysis is the progressive reduction of the material stiffness matrix of the plies that undergo damage or failure under specific failure modes. Failure initiation and propagation is detected with the use of failure criteria. By reducing certain material properties of the plies that satisfy a specific failure criterion in a rational manner, the ability of the composite structure to carry further load is decreased. This procedure carries on until the global stiffness matrix of the composite structure becomes "numerically unstable", a fact that, from a physical point of view, denotes total failure. The development of an efficient progressive failure model is based on the appropriate selection of two ingredients; the type of the failure criteria utilized and the implemented material degradation scheme.

The algorithm of the developed PFM in the present work is illustrated with the aid of the flowchart of Figure 3.1. The methodology followed requires that equilibrium must be obtained for both geometric and material nonlinearities (Lopes et al. 2007).

The geometric nonlinearity is required since buckling and postbuckling involve large rotations/strains and thus nonlinear strain measures and kinematics must be taken under consideration. The material nonlinearity is based on the degradation of the material properties of the laminas, to simulate damage mechanisms. The fracture behaviour of the modeled composite material system is assumed to be brittle. Hence, the composite material behaviour in terms of stress-strain relationship is considered to be linear until first failure detection, beyond which the material property degradation procedure is applied. The incremental/iterative solution of the nonlinear finite element equations has been addressed with the use of Newton – Raphson method. Simulations involving damage mechanics should be approached with a displacement control analysis, due to the form of the loading path of the structure (snap-through issues). In order to achieve convergence at certain sub-steps of the analysis where material nonlinearities cause sudden drop of the stiffness matrix, a line search algorithm is used to initially minimize the large residual force.

A progressive failure analysis of a structure that involves buckling and postbuckling, requires the following methodology to be considered (see Figure 3.1). Unless the structure has initial out-of-the-loading-plane deformations or lateral loading is applied, or both, the need for initial geometric imperfection is obligatory in order to trigger buckling in a finite element analysis. The critical buckling modeshape, which involves out-of-plane deformations, is usually scaled and imported as the initial stress free imperfect condition.

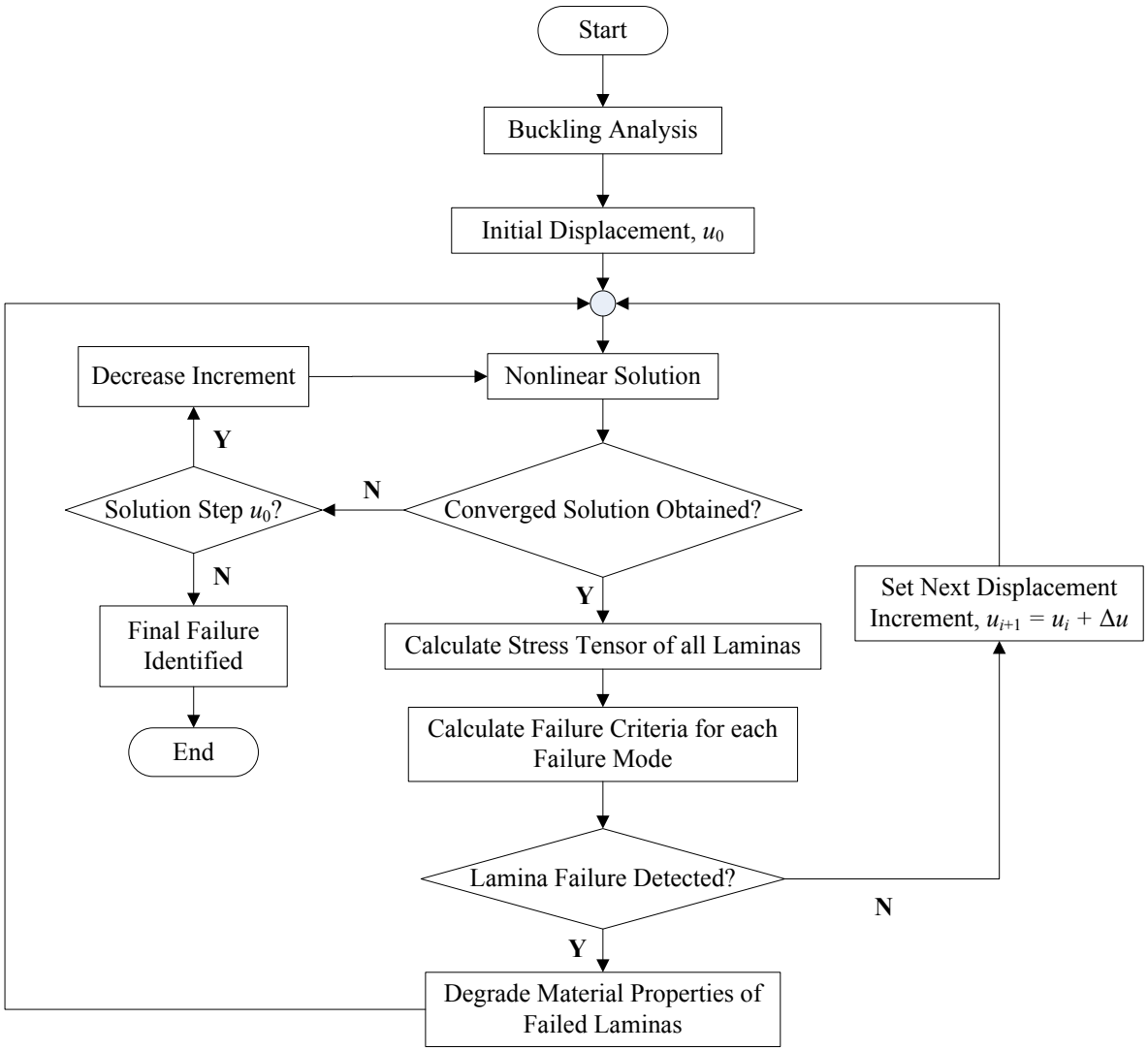

Figure 3.1: Flowchart of the developed PFM.

By considering a displacement controlled incremental solution, let u_i denoting the applied compressive in-plane displacement at the i^{th} step of the nonlinear analysis which varies from 0 to n. The variable u_0 (i=0) denotes the initially applied displacement, which is needed to establish the first finite element solution. After obtaining equilibrium at the i^{th} displacement step (including the initial step i=0), the stress tensor of all laminas and of all elements incorporated into the finite element mesh is calculated and stored. All these stresses are then introduced into specified failure criteria, which are then checked to determine whether any failures have occurred or not. If no failure has been detected, the displacement is incrementally increased by Δu to form $u_{i+1} = u_i + \Delta u$ and the analysis for the i+1 step is carried on. In the case where failure has been detected, specific changes in the material stiffness matrix are implemented based on the material degradation model utilized. This modification comprises for the nonlinearity associated with the material damage, as previously stated. Equilibrium is re-established by performing new nonlinear iterations at the i^{th} step until the point where no additional lamina/element failures are detected. The applied displacement is then increased in order to obtain equilibrium at the next

sub-step, which is based on the applied displacement u_{i+1}. This procedure is repeated until final failure is identified (complete loss of the ability of the modeled composite structure to carry further loads) in the framework of the main loop presented in Figure 3.1. Final failure takes place at the load level at which static equilibrium cannot be any further obtained. According to Lopes et al. (2007) at failure or close to, static equilibrium ceases to be achieved because fracture is in itself a dynamic process, with sudden dissipation of energy by means of conversion into kinetic energy of a great part of the accumulated strain energy. For this reason structural collapse may be simulated with the implementation of the progressive failure model in dynamic analyses (explicit or implicit) which take into account the inertia of the structure.

The above described PFM methodology has been implemented into the commercial finite element software ANSYS® v.11 and programmed in APDL language with the use of the software's feature namely "restart analysis". The following sections give in detail the failure criteria incorporated into the model and the respective material degradation rules utilized.

3.2.2 Failure criteria

In failure analyses of composite structures several approaches have been developed which can be utilized to characterize the onset and progression of failure. This involves monitoring a particular parameter that controls the damage development and growth. These damage approaches are in general based on theories of strength or fracture mechanics. In order to perform a more realistic failure analysis, the use of a distinct failure criterion is appropriate to describe each damage mechanism separately. Failure criteria can be separated into two classes regarding their ability to distinguish among the different failure modes incorporated in the failure of composite materials: independent and interactive. The former are easy to apply and give the mode of failure but neglect the effect of stress interactions in the failure mechanisms. The latter perform in the opposite way, as they consider stress interactions but do not give the failure mode.

The failure criteria incorporated in the present PFM are used to predict intralaminar failure modes involving fiber, matrix and fiber-matrix shear, individually. For the assessment of fiber and matrix failure modes, the independent failure criteria proposed by Hashin (1980) have been utilized. In order to identify fiber-matrix shear mode an expression described by Padhi et al. (1998) has been utilized. This expression actually refers to the interactive failure criteria proposed by Tsai in terms of a single tensor polynomial failure criterion by considering the failure index proposed by Tsai and Wu (1971). The failure criteria presented in Equations (3.1) – (3.6) are expressed in a reduced two dimensional form.

The calculated stresses at the i^{th} displacement step are transformed into the principal material properties coordinate system (1-2) of each lamina (considering the fiber orientation angle) and then introduced in the failure criteria for unidirectional composites (Hashin). The failure criteria are expressed in terms of limit stresses which are strength along fiber direction X, strength normal to fiber direction Y, shear strengths S and transverse shear strength R. The in-

plane stresses considered are σ_{11}, σ_{22} and σ_{12}. The subscript "1" denotes the along the fibers axis, whereas the subscript "2" denotes the transverse to fibers axis. The failure indices describing fiber and matrix failures which are based on the Hashin criteria are given by:
Fiber failure mode in tension: $\sigma_{11}> 0$

$$e_{\mathrm{f}}^2 = \left(\frac{\sigma_{11}}{X_{\mathrm{T}}}\right)^2 + \left(\frac{\sigma_{12}}{S_{12}}\right)^2 \tag{3.1}$$

Fiber failure mode in compression: $\sigma_{11}<0$

$$e_{\mathrm{f}}^2 = \left(\frac{\sigma_{11}}{X_{\mathrm{C}}}\right)^2 \tag{3.2}$$

Matrix failure mode in tension: $\sigma_{22}>0$

$$e_{\mathrm{m}}^2 = \left(\frac{\sigma_{22}}{Y_{\mathrm{T}}}\right)^2 + \left(\frac{\sigma_{12}}{S_{12}}\right)^2 \tag{3.3}$$

Matrix failure mode in compression: $\sigma_{22}<0$

$$e_{\mathrm{m}}^2 = \frac{1}{Y_{\mathrm{C}}}\left[\left(\frac{Y_{\mathrm{C}}}{2R}\right)^2 - 1\right]\sigma_{22} + \left(\frac{\sigma_{22}}{2R}\right)^2 + \left(\frac{\sigma_{12}}{S_{12}}\right)^2 \tag{3.4}$$

The subscripts "C" and "T" denote compression or tension, respectively. The expression that describes fiber-matrix shear failure mode is given by the polynomial failure criteria in the following form:

$$H_6 = F_{66}\sigma_{12}^2 \tag{3.5}$$

where F_{66} equals to $1/S^2$ according to the failure criteria of Tsai-Wu. Thus, the shear failure index is expressed by:

$$e_{\mathrm{s}}^2 = \left(\frac{\sigma_{12}}{S_{12}}\right)^2 \tag{3.6}$$

Failure occurs when one or more of the failure indices (e_{f}^2, e_{m}^2 and e_{s}^2) yields a value greater or equal to one. The determination of the dominating failure mode of a specific lamina at

the i^{th} displacement step is given from the maximum value of the respective failure index, which is considered afterwards for the application of the material property degradation scheme.

3.2.3 Failure methodology

Several material degradation methods can be found in the literature (Lopes et al., 2007; Labeas et al., 2008). Existing methods for damage modeling can be separated into two categories; methods that rely on ply discount techniques and methods that are based on continuum damage mechanics. Non-linear constitutive models defined in the framework of the mechanics of continuum media have been developed by Ladeveze et al., (2000) and others, as found in the literature. According to Lopes et al. (2007), the standard implementation of strain-softening constitutive models results in mesh-dependent results. The solution becomes non-objective and relies on the mesh refinement approach at a way that the computed energy dissipated decreases with the reduction of the element size. This obstacle can be partially overcome by scaling the material response, after the stress point that reflects to failure initiation, as a function of the size of the element so as to maintain the computed energy dissipation independent of the element size. This secures that the energy dissipation equals to the material fracture energy.

In order to avoid any kind of mesh dependencies, the damage model used in this work is based on ply discount techniques. If instant unloading instead of strain softening constitutive models of the damaged lamina is being utilized, then the material property degradation rules should be based on partial reduction schemes (percentage reduction of the corresponding material properties). Total reduction schemes (complete reduction of the corresponding material properties), often lead to ill-conditioned matrices that tend to cause inevitable convergence difficulties (Lopes et al., 2007). This phenomenon leads to conservative estimations of the final load attained, since failure identification is based on the loss of static equilibrium. For this purpose, the material property degradation rules proposed by Camanho and Matthews (1999) have been implemented into the proposed herein PFM for the failure analysis of the stiffened panels, which are based on partial reduction schemes. The adopted material property degradation rules are listed in Table 3.1.

Table 3.1: Material properties degradation scheme (Labeas et al. 2008).

Failure mode	Material property degradation rules
Fiber tensile failure	$E_{11} = 0.07\, E_{11}$
Fiber compressive failure	$E_{11} = 0.14\, E_{11}$
Matrix tensile failure	$E_{22} = 0.2E_{22}$, $G_{12} = 0.2G_{12}$, $G_{23} = 0.2G_{23}$
Matrix compressive failure	$E_{22} = 0.4E_{22}$, $G_{12} = 0.4G_{12}$, $G_{23} = 0.4G_{23}$
Fiber-matrix shear failure	$G_{12} = v_{12}$

According to Camanho and Matthews (1999), the stiffness reduction associated with failure due to compressive loads is different from the stiffness reduction associated with failure due to tensile loads. This effect leads to the assumption that the surfaces of the crack under tensile loading are traction free, whereas under compressive loading they can still carry load.

The degraded material properties S' are related to the original undamaged material properties S of each lamina through the damage operator. Thus the original and reduced material properties are arranged in the following vector form:

$$S = \{E_1 \quad E_2 \quad \nu_{12} \quad G_{12} \quad G_{23}\}^{\mathrm{T}} \tag{3.7}$$

$$S' = \{E_1' \quad E_2' \quad \nu_{12}' \quad G_{12}' \quad G_{23}'\}^{\mathrm{T}} \tag{3.8}$$

In order to optimize the performance of the developed algorithm in terms of decreasing the CPU cost, the material property degradation coefficients (presented in Table 3.1) are introduced into a 5x5 square matrix defined with the letter C. Each row of matrix C contains the coefficients representing the respective dominating failure mode and each column describes the sequence of the material properties to be degraded, in the same order as given by vector S or S':

$$C = \begin{bmatrix} 0.07 & 1 & 1 & 1 & 1 \\ 0.14 & 1 & 1 & 1 & 1 \\ 1 & 0.2 & 1 & 0.2 & 0.2 \\ 1 & 0.4 & 1 & 0.4 & 0.4 \\ 1 & 1 & \dfrac{G_{12}}{\nu_{12}} & \dfrac{\nu_{12}}{G_{12}} & 1 \end{bmatrix} \tag{3.9}$$

Thus, the material degradation procedure of each lamina can be expressed as follows:

$$S' = C^{\mathrm{T}} L S \tag{3.10}$$

where L defines a five component vector, where the dominating failure mode sets the value of unity to the respective component of vector L and the remaining components are set to zero. The component $C^{\mathrm{T}}L$ of Equation (3.10) defines the damage operator applied to the original undamaged material properties. The damage reduction scheme is applied only once, for each failure mode, in the element ply level.

3.3 Failure analysis of a stiffened panel

3.3.1 Geometry and materials

The stiffened panel which was experimentally studied under compressive loading by Falzon et al. (2000) has been considered in this work for the application of the developed PFM. The panel consists of four stiffeners not evenly spaced on the skin, as presented in Figure 3.2a. The spacing between the central two stiffeners is twice that of the outer stiffeners, as shown in Figure 3.2b.

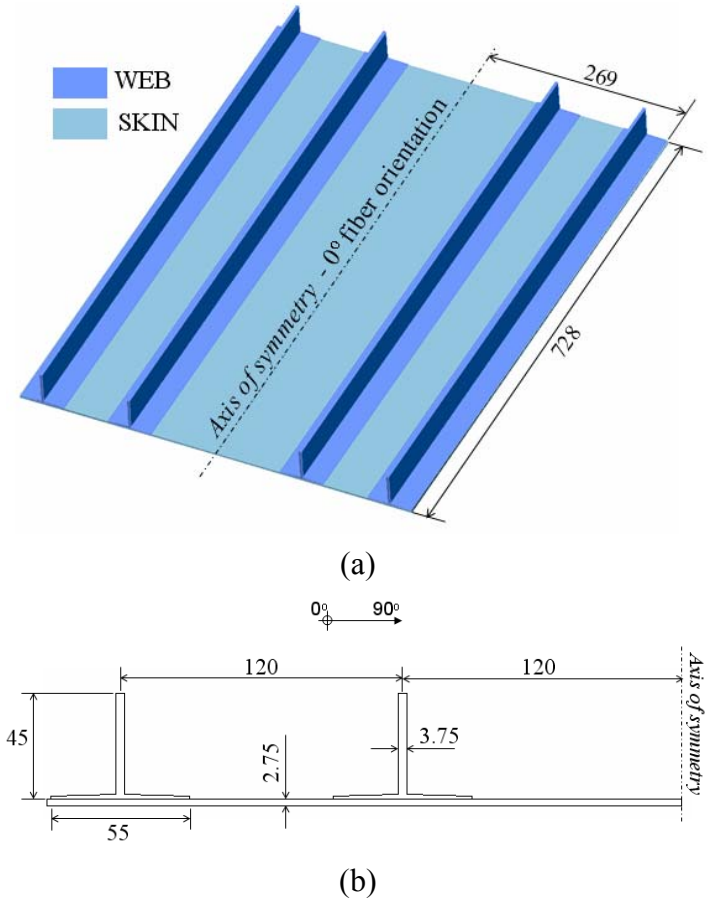

Figure 3.2: Geometry (a) and cross section (b) of the stiffened panel.

The panel and the skin have been manufactured from unidirectional prepreg T800/924C with material properties listed in Table 3.2. The ply thickness is 0.125mm and the stacking sequence of the skin is $\left[90/0_2/90/\pm45/0/90/\pm45/0\right]_S$. The stacking sequence of the stiffener is $\left[90/0/90/0/\pm45/90/0_2/90/\pm45/\pm45/90\right]_S$.

Table 3.2: Material properties used for T800/924C.

E_1	162 GPa
E_2	9.20 GPa
v_{12}	0.30
G_{12}	5.00 GPa
G_{23}	1.45 GPa
Intralaminar strength allowables in MPa	
X_T	2700
X_C	1650
Y_T	55
Y_C	255
S_{12}	100
R	20

3.3.2 Buckling analysis

The finite element mesh, loading and boundary conditions of the stiffened panel are shown in Figure 3.3.

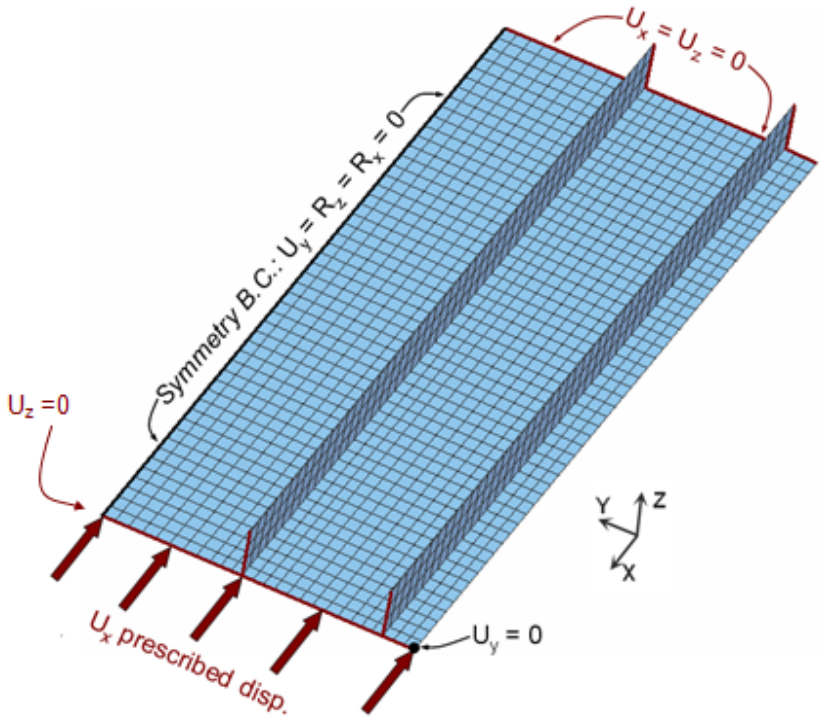

Figure 3.3: Finite element model of the simulated stiffened panel.

In order to simulate the laminated skin and stiffeners of the panel, "Shell281" continuum structural elements have been chosen from the ANSYS® v.11 element library. The layered element Shell281 has eight nodes with six degrees of freedom per node, it is transverse shear deformable and full integration is utilized for the computation of its stiffness. During the analysis three integration points through each lamina thickness were considered. The average element length used for the analyses is 2.75 mm. As described in section 3.2.1, an artificial geometrical imperfection is required to be introduced to the undeformed finite element mesh prior to the application of the compressive loading and the initiation of the non-linear analysis. This imperfection is in the shape of equilibrium state of the panel subjected to a loading acting perpendicular to one of the edges. Thus, such imperfection results from an eigenvalue analysis. The amplitudes of the critical buckling mode (1st buckling mode shape) are scaled according to calculated offsets and then added to the original nodal coordinates. An empirical rule commonly used for the geometrical perturbation values is that the maximum lateral perturbation is equal to 1% of the plate thickness, since when using a perturbation factor less than 1% no significant imperfection is introduced, leading to very high calculated initial buckling loads. Thus, in the present work a perturbation factor of 1% was used.

Figure 3.4 compares the first calculated buckling mode shape in terms of the out-of-plane displacement, between the eigenvalue analysis conducted herein and the respective one presented in Falzon et al. (2000). Note that the contour plot obtained from ANSYS buckling analysis is symmetry expanded, that is the other half of the model is reflected together with its corresponding output results. The results obtained from both analyses capture a four half wave-length mode shape with very good agreement. The initial buckling load calculated herein equals to 117.4 kN, a value which agrees very well with the respective value of 113.84 kN given by Falzon et al. (2000), (difference of 3%).

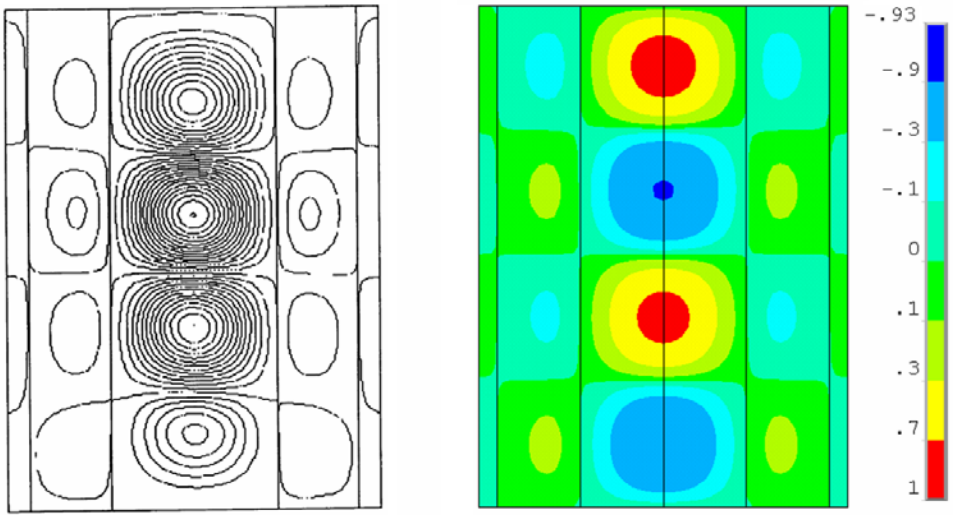

(a) (b)

Figure 3.4: First buckling modeshape: (a) Eigenvalue analysis by Falzon et al. (2000); (b) Current buckling analysis (Anyfantis and Tsouvalis, 2011a).

3.3.3 Failure analysis

In order to study the postbuckling behaviour and later the failure initiation and propagation occurring at the stiffened panel, prescribed displacement u_x (incremented by $u_{i+1} = u_i + \Delta u$) was applied to one edge of the plate. Comparisons of the results obtained from the experimental program carried by Falzon et al. (2000) with the respective results from finite element calculations are based on the measurement locations illustrated in Figure 3.5. In this figure, the measurement locations on the panel (M1, M2 and M3), where both experimental data and numerical results are compared, are depicted.

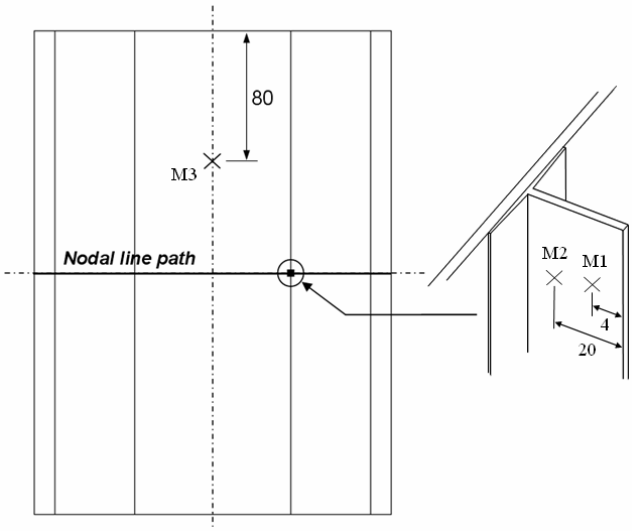

Figure 3.5: Measurement locations on the stiffened panel (dimensions in mm).

Figure 3.6 presents distributions of the lateral displacements (u_z) as obtained from finite element calculations (prior to failure initiation) and as experimentally registered in Falzon et al. (2000) with the aid of the Moire fringe pattern. The deformation pattern of the postbuckled panel (Figure 3.6b) denotes a rotation of the stiffeners due to their reduced torsional stiffness under increased compression with respect to Fig. 6a. Since, the distance between the central stiffeners is double of that between the edge stiffeners, buckling initiates earlier in the central zone and later in the side areas. The results from the numerical simulation (Figure 3.6b) are in very good agreement with the experimental Moire fringe pattern (Figure 3.6c). Both results indicate higher amplitudes of deformation in the central zone characterized by the increased number of the Moire fringes (Figure 3.6c) and by the red coloured areas (Figure 3.6b), in the experimental results and the finite element calculations, respectively. Figure 3.7 presents the variation of the out-of-plane displacement (u_z) along the centerline nodal path denoted in Figure 3.5. According to Figure 3.7, the lateral deformation of the centerline is consistent with the observed postbuckled behaviour. Initially, the central zone undergoes buckling deformation and any further increase in the compressive load causes the edge zones to develop as high lateral displacement as the central zone does. As a result, local buckling of the skin between the

stiffeners, global buckling along the panels length and stiffeners' stripping characterizes the buckling and postbuckling behaviour of the stiffened panel, respectively.

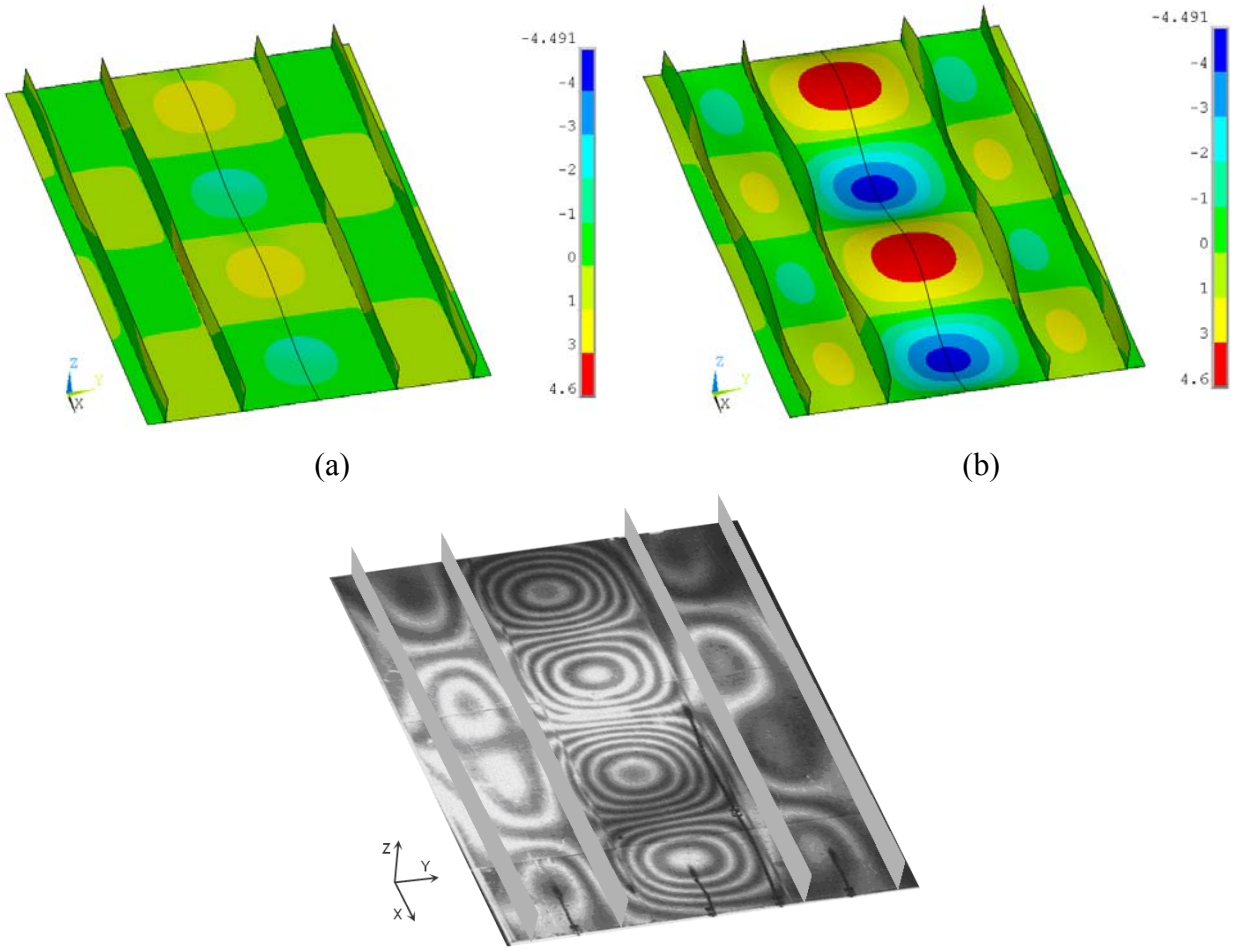

Figure 3.6: Buckling and postbuckling results: (a) Initial buckling deformation at 150 kN force; (b) Postbuckling deformation at 300kN force; (c) Moire fringe deformation at 300 kN force (figure graphically modified from Falzon et al., 2000).

According to Falzon et al. (2000) the first panel underwent a mode switch to five half-wavelengths prior to final failure at a load level of 601 kN whereas the failure of the second panel occurred at 573 kN and is characterized by sudden failure. The numerical analysis based on the developed PFM has shown that the maximum attained load of the stiffened panel is 532.4 kN, which yields a relative difference of 7% with respect to the second panel experimentally tested.

The axial reaction force as a function of the out-of-plane displacement is shown in Fig. 8. The lateral displacement was measured in the test from an LVDT placed at a buckle peak whereas in the finite element model this buckle peak was found to be 80 mm below the top edge of the panel, shown in Fig. 5 and denoted with the codename M3. The axial reaction force as a function of axial and shear strains evaluated at two locations on the central stiffeners are presented in Fig. 9 and Fig.10 respectively. The axial and shear strains history was measured in

the test from back-to-back strain gages bonded 4 mm and 20 mm from the top edge of the central stiffeners, shown in Fig. 5 and referred to as M1 and M2, respectively.

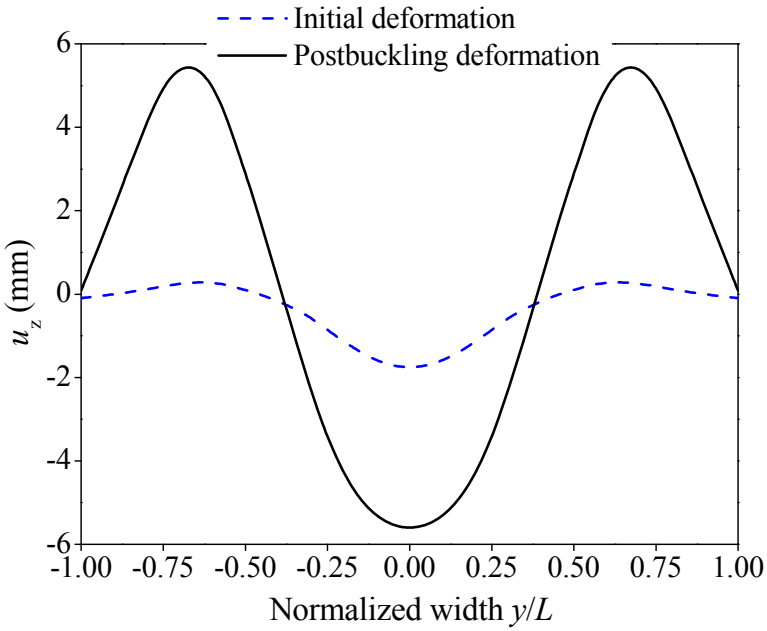

Figure 3.7: Buckled and postbuckled lateral deformation of the centerline nodal path.

Failure initiation determined by the first ply failure is predicted in the postbuckling region of the stiffened panel. The first failure is accumulated by matrix cracking occurring at 8.5 mm maximum out-of-plane displacement with the corresponding reaction force of 520 kN, as illustrated in Figure 3.8.

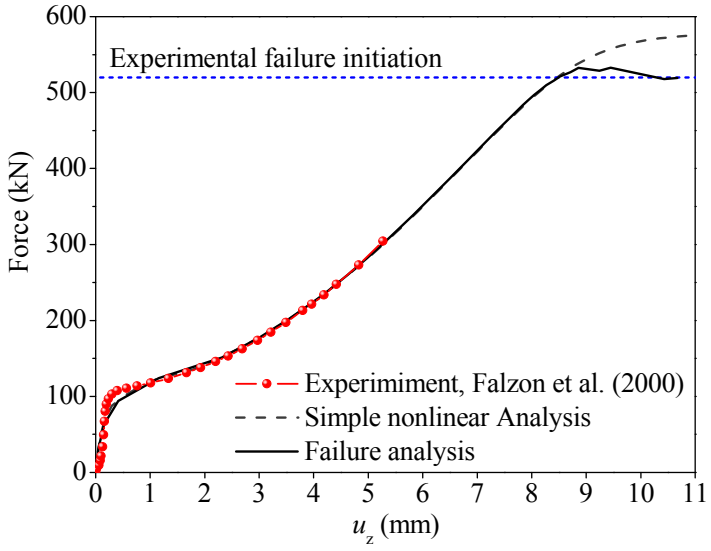

Figure 3.8: Force versus the out-of-plane displacement at M3 measurement location.

The combination of local longitudinal, transverse and shear stresses developed at the buckle peak measured at location M3 satisfied the respective failure criteria of the matrix cracking failure mode. The location of failure initiation was calculated at the outmost layers of

the skin elements at M3 location of the panel. The top and bottom layers of the skin having their fibers oriented at 90° from the loading axis are in fact more prone to damage initiation than the inner layers. This is expected since postbuckling is associated with bending of the plating. Thus, the developing bending strains and stresses are higher in the outer layers and they are either tensile or compressive on the outer and inner sides of the buckle peaks.

Furthermore, the absence of fibers along the loading direction at the outmost layers results in premature failure appearing in the form of matrix cracking. By slightly increasing the applied load, damage propagates rapidly in two different directions, normal to each other. As the load carrying ability of the initially damaged layers is reduced, the load is transferred to the adjacent layers which also fail under increased stress level. Damage propagates from the buckle peak to the edges of the panel in the zone below and above the nodal centerline as illustrated in Figure 3.5. This can be confirmed by the behaviour of the load versus out-of-plane deformation presented in Figure 3.8, where the slope of the curve decreases suddenly, after the point of failure initiation and forward. Once damage propagates to the central stiffeners, the outmost layers of the overlap part of the stiffener start to satisfy the matrix cracking failure criteria, they start to fail and the material properties are degraded respectively.

Apart from the buckling and postbuckling behaviour of the skin, the ribs are also deformed under buckling. This phenomenon leads to elevated bending stresses at the outmost layers of the web. The external layers of the web have their fibers oriented at 90° to the loading axis. Thus, failure in the form of matrix cracking of these layers results in immediate failure of the adjacent layers oriented at 0° and ±45° with fiber failure and matrix failure, respectively. This fact is observed through Figure 3.9 and Figure 3.10, where axial and shear strains versus load are presented, respectively. In these figures the experimentally evaluated results of Falzon et al. (2000), the predicted results from the simple nonlinear finite element analysis and the numerical results with the introduction of the developed PFM are compared.

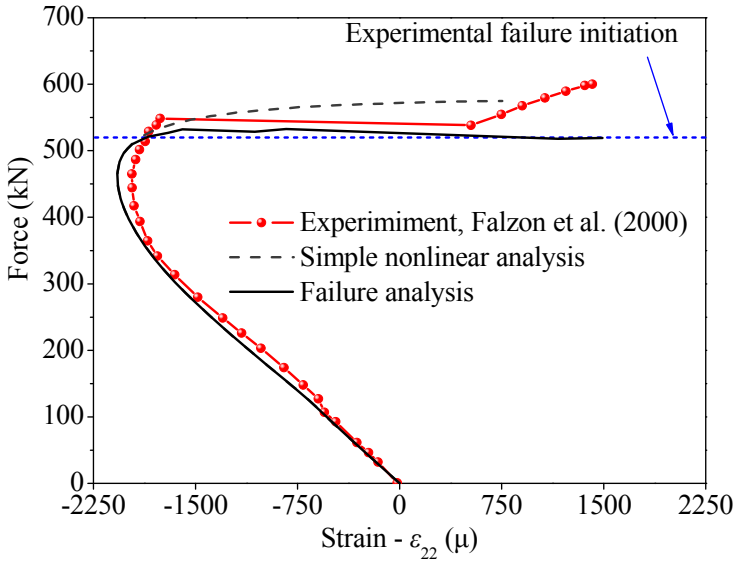

Figure 3.9: Force versus axial strains at M1 measurement location.

The strain results obtained from the non-linear analyses are in great agreement with the respective experimental ones, until the failure initiation load. The introduction of the developed PFM results in a sudden decrease of the slope of the curves, which is in accordance with the experimental curves. The load capacity loss of the panel coming from the properties degradation of the layers at the buckle peaks, affects the behaviour of the central ribs after failure initiation. Under approximately constant load level, strains tend rapidly to decrease in amplitude and even change their sign, as illustrated in Figure 3.9. This implies that bending moments change their sign, since the layer at the measurement location M3 tends to develop tensile stresses instead of compressive stresses being developed until failure initiation. The reaction force-axial strains curve calculated with the PFM is in good agreement with the experimentally evaluated respective results in the plateau region.

The behaviour of the shear strains presented in Figure 3.10 is analogous to the behaviour of the axial strains previously described. The numerically calculated curve is again characterized by a sudden drop in the slope, followed by a plateau region after the failure initiation load.

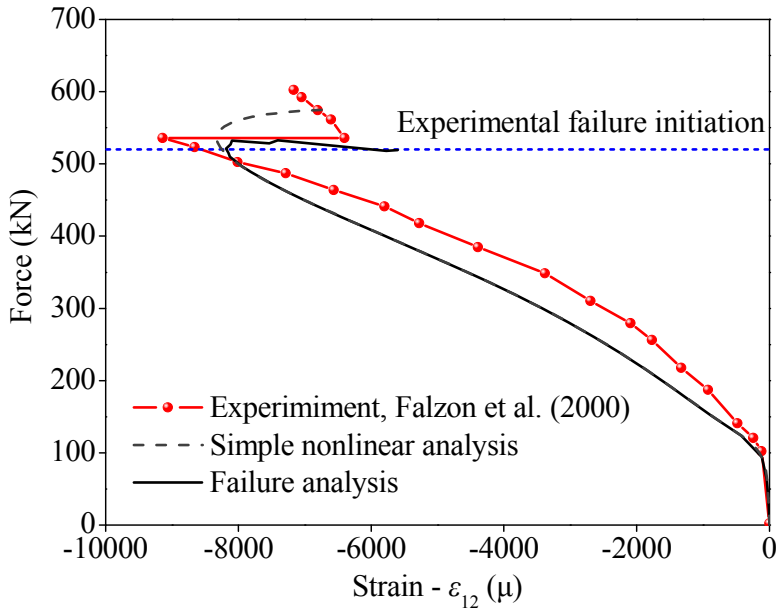

Figure 3.10: Force versus shear strains at M2 measurement location.

Figure 3.11 compares the effect of the introduction of the developed PFM to the simple nonlinear analysis in terms of the out-of-plane deformation field of the panel under the maximum applied displacement, which is common in both cases.

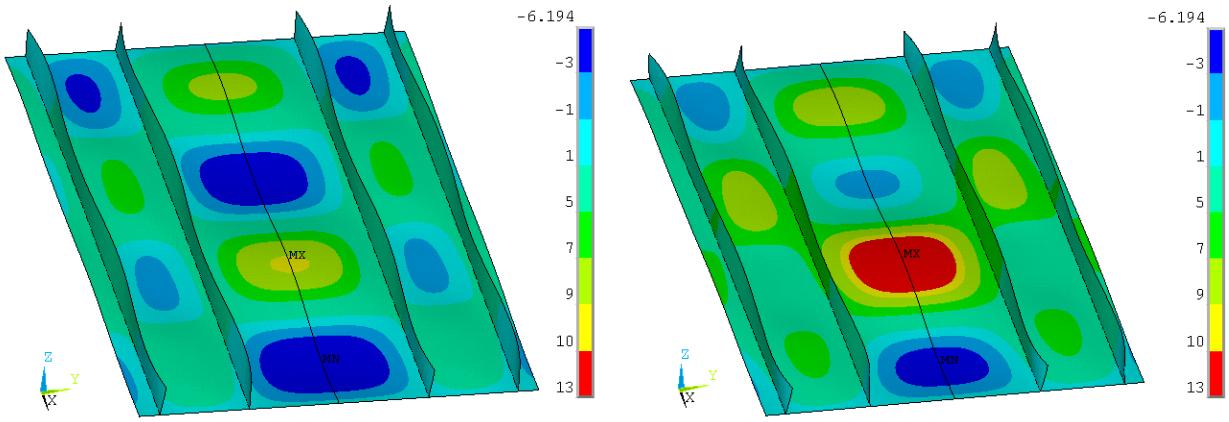

(a) (b)

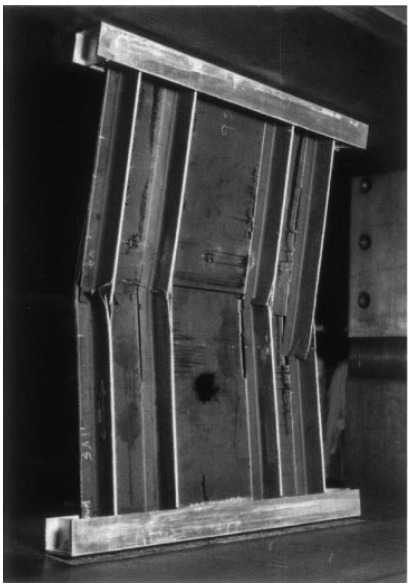

(c)

Figure 3.11: Contour plot of u_z at complete failure from the simple nonlinear analysis results (a), with PFM (Anyfantis and Tsouvalis, 2011a) (b) and experimental failure of the panel Falzon et al. (2000) (c).

The deformation predicted in the framework of the failure analysis is based on the postbuckling shape of the panel and shows that maximum amplitudes are concentrated at the buckle peak near the centerline of the panel. The material properties degradation reduced the stiffness of several layers in the area of the buckle peak. This fact elevated the compliance and turned the central zone of the stiffened panel to develop high out-of-plane deformations. This behaviour is illustrated in Figure 3.12, where the lateral displacement along the central nodal line is compared with results obtained from the simple nonlinear and from the failure analysis.

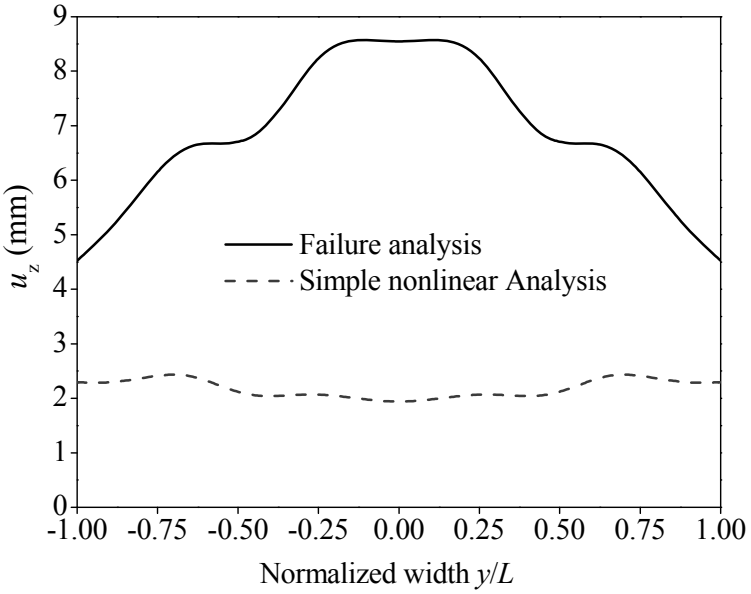

Figure 3.12: Lateral deformation of the central nodal line at the maximum attained applied displacement (prior to complete failure).

3.4 Conclusions

In this Chapter, a Progressive Failure Model (PFM) has been developed and utilized as the constitutive relation of continuum shell elements for the prediction of the behaviour of an experimentally tested composite blade-stiffened panel found in the literature, within its buckling and postbuckling range. The basic concept that lays behind the PFM is the progressive degradation of the material properties of the composite layers that undergo damage, according to specific failure criteria and under an iterative numerical scheme. A combined framework of Hashin and Tsai-Wu failure criteria together with the employment of a material property degradation scheme are being utilized in this study and give relatively accurate predictions with respect to the experimental results. Failure initiation and propagation is calculated, owing to the accumulation of the intralaminar failure modes induced in fibre reinforced composite materials. Hashin failure criteria have been employed in order to address the fiber and matrix failure modes in compression and tension. On the other hand, the Tsai – Wu failure criterion has been utilized for addressing shear failure. Failure detection is followed by the introduction of corresponding material degradation rules depending on the individual failure mechanisms. Failure initiation and failure propagation as well as the post buckling ultimate attained load have been numerically evaluated. Final failure behaviour of the simulated stiffened panel is due to sudden global failure, as concluded from comparisons between numerical and experimental results being in good agreement.

The failure analysis of the panel has shown that failure initiation is associated with matrix cracking at the buckle peaks. Failure propagation has an intensive effect on the stiffness of the panel due to the rapid progression of failure and the subsequent stiffness degradation. The initial local buckling of the skin between the stiffeners turns into global buckling of the panel. After

failure initiation and up to the final failure, no further increase in the load capacity of the panels has been evaluated. The simulation results denote that the panel fails abruptly, a fact that is consistent with the failure mode of one of the panels experimentally studied. The other panel undergoes a mode switch prior to failure. In order to address this phenomenon, inertia effects should be considered in the framework of a nonlinear dynamic analysis, not considered in this study. The developed PFM is an efficient analysis and design tool in addressing the failure mechanisms that are involved in the buckling and postbuckling behaviour of composite structures loaded in compression.

This page has been intentionally left blank

4. Experimental and numerical investigation of pure Mode I and II delamination growth

4.1 Description of the problem

Among their outstanding mechanical properties, the high strength-to-weight ratio is one of the most challenging properties of composites that have turned them to be candidate structural materials in almost all industrial applications. However, laminated fibrous composites have low through-thickness mechanical properties, poor impact damage tolerance, and low interlaminar fracture toughness. As a result, they are susceptible to delamination damage, which is defined as a crack between two adjacent layers, either in service conditions or during their fabrication.

Determination of the mechanisms incorporated in the interlaminar fracture of composite materials is focused on characterizing either the opening mode I (Mode I) or the shear mode II (Mode II), mostly within the framework of Linear Elastic Fracture Mechanics (LEFM), as shown in section 2.3.2. The most commonly employed approach to characterize interlaminar fracture resistance of composites is by determining the Strain Energy Release Rate (ERR - G). If crack growth resistance is independent of the crack length α, then the SERR magnitude is a material constant that equals to the fracture toughness denoted by $G_{I,0}$ or $G_{II,0}$ in the case of Mode I or Mode II, respectively (Broek, 1986).

For the determination of $G_{I,0}$ under pure Mode I loading, the Double Cantilever Beam (DCB) test has been accepted as a standard method (ASTM D5528-01, 2007; ISO 15024:2001, 2001) for the determination of $G_{I,0}$ under pure Mode I loading. Several authors have utilized the DCB test in order to address the process of delamination initiation and propagation (Sorensen et al., 2007; Sorensen et al., 2008; Szekrényes and Uj, 2005).

For the measurement of $G_{II,0}$ a standard does not exist but many efficient experimental procedures can be found in the literature. The End Notched Flexure (ENF), End Loaded Split (ELS) and Four Point ENF (4ENF) tests are the most popular tests adopted in the literature. The ENF test (Barret and Foschi, 1997) is most widely used due to its simple fixture based on a conventional three-point bending set-up, and has been adopted by the Japan Industrial Standards Group (JIS) as a standard test. On the other hand the ELS (Blackman et al., 2006) and 4ENF

(Martin and Davidson, 1999) tests require a more complicated test set-up than that of the ENF test and present some problems related to large friction effects (Schuecker and Davidson, 2000). Particularly the 4ENF test requires a four-point bending device that allows free rotation of the two loading points, in order to ensure that the desired equal loading can be achieved (Martin and Davidson, 1999). The ELS specimen is more prone to large displacements (Wang et al., 1995) as it is treated as a cantilever beam and thus experimental results are affected by the variability in the clamping boundary conditions (Hashemi et al., 1990). On the other hand, in recent years the DCB-UBM test (Double Cantilever Beam - DCB specimen loaded by Uneven Bending Moments) has been used often for the characterization of pure and mixed mode fracture of composite structures (Sørensen and Jacobsen, 2003; Sørensen and Jacobsen, 2009). However, the complexity of the DCB-UBM experimental set-up (see section 2.3.3.2) makes it difficult to be applied. Therefore, in this work the DCB and ENF test configurations are adopted, for the Mode I and II loading and fracture characterization, respectively.

Delamination growth in fibrous composites is followed, most of the times, by fiber bridging mechanisms e.g. fibers crossing over from one crack face to its opposite, due to fiber debonding and pull-out, and applying closure stresses to the crack faces, as illustrated in Figure 4.1a. Fiber bridgings influence the magnitude of fracture toughness as crack propagates. This phenomenon is well described by the R-curve (fracture resistance curve) where, after crack initiation ($G_{I,0}$ or $G_{II,0}$) and during crack growth, the ERR magnitude increases until it reaches a plateau, namely steady state fracture toughness ($G_{I,SS}$ or $G_{II,SS}$), Suo et al. (1992). According to Suo et al. (1992) the R-curve must not be taken as a material property because it depends on the geometrical characteristics of the specimens used in the experimental programme. Instead, a bridging law which can be easily derived from an R-curve, e.g. through its differentiation with respect to the local opening or sliding, can be considered as an interfacial material property of the composite system considered (Sørensen and Jacobsen, 2009). A bridging law in fact describes the bridging zone in terms of the closure stress (σ_i), due to the existence and development of fiber bridgings, versus the pre-crack tip opening displacement (δ^*), as crack propagates (see Figure 4.1b). After crack initiation, which occurs at a characteristic stress value called critical bridging stress $\sigma_{c,i}$ (i = Mode I or II), the fiber bridging zone is described by a linear or non-linear softening law until a maximum value of δ_i^* (i = Mode I or II) is reached, namely $\delta_{c,i}^*$ (region A in Figure 4.1). Beyond $\delta_{c,i}^*$ the bridging fibers lose their load carrying capability and fail, by leaving behind part of the crack faces traction-free (region B in Figure 4.1).

Taking advantage of the fact that the R-curve describes fiber bridging mechanisms, several authors have utilized the J-integral approach to describe the fiber bridging behaviour in terms of a traction-separation law in Mode I and II (see section 2.3.2). The most significant advantage of a bridging law is that it overcomes the theoretical stress singularity of the crack tip by assigning a definite stress value $\sigma_{c,i}$ which quantifies the initiation of the bridging zone. For this reason, a bridging law can be implemented into numerical procedures for predictions of the

delamination process. A traction-separation law is actually a numerical representation of a bridging law, properly modified for implementation into finite element methods.

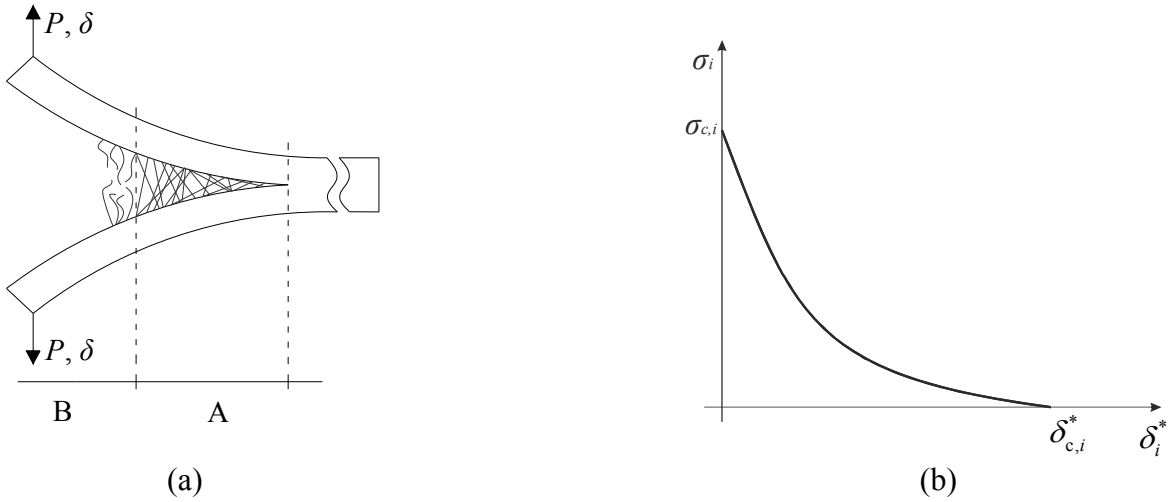

Figure 4.1: The bridging zone as formed during Mode I fracture (a) and as described by a fiber bridging law (i = Mode I or II) (b).

The present work involves an experimental and numerical investigation of the fiber bridging mechanisms incorporated in the Mode I and II fracture growth of laminated composite materials, within a combined framework of LEFM and damage mechanics. For this purpose, Glass Fiber Reinforced Polymer (GFRP) coupons have been manufactured and tested under traditional DCB and ENF test configurations. The main focus of the experimental part is to investigate and compare the effectiveness of three different fiber bridging laws, calculated from three respective available in the literature data reduction schemes, describing the bridging zone, for the Mode I and II, respectively. The numerical investigation aims at validating the experimentally obtained bridging laws and at proposing to the literature a new effective numerical implementation of the experimentally obtained ridging laws. Thus, the derived bridging laws have been converted to Traction-Separation (T-S) laws according to three different models for the simulation of the DCB (Mode I) case and two different models for the simulation of the ENF (Mode II) case. The obtained bridging laws and further T-S models from each data reduction scheme were implemented into interface finite elements for the numerical simulation of the DCB and ENF tests. The corresponding finite element results were compared with the respective experimentally measured magnitudes.

4.2 Materials, geometry and test parameters

Six layers of 600 gr/m^2 unidirectional glass fabric (UD) have been stacked together with epoxy resin (D.E.R. 353 Liquid Epoxy Resin and Epamine PC13 hardener) to manufacture a composite laminated plate. During manufacturing, a 58 μm thick PTFE film was inserted in the mid-plane and along one of the edges of the laminate for the creation of an artificial initial

delamination. This PTFE film is thicker that the usual corresponding films used in the literature, in order to comply with the increased layer thickness of the quite heavy UD glass reinforcement used in the present study. Moreover, this relatively thick PTFE artificial crack film simulates better the physical defects that can be found in normal composite marine structures. The UD fabrics were initially impregnated with the epoxy/hardener matrix system by the hand lay-up method and afterwards the plate was cured at 25 ^{o}C for 48 hours under constant 0.6 bar pressure with the aid of vacuum bagging. After the curing process, four DCB and five ENF specimens were cut out from the plate with the use of waterjet. The composite system had a fibre weight fraction of 50% with orthotropic elastic properties listed in Table 4.1.

Table 4.1: Glass/Epoxy elastic material properties.

E_1 (MPa)	E_2 (MPa)	E_3 (MPa)	ν_{12}	ν_{13}	ν_{23}	G_{12} (MPa)	G_{13} (MPa)	G_{23} (MPa)
18000	2200	2200	0.29	0.29	0.38	1800	1800	1600

The geometry and dimensions of the DCB and ENF specimens are given in Figure 4.2 and Figure 4.3, respectively. The actual thickness of the DCB and ENF specimens is $2h$ = 4.55±0.1 mm and their width b is equal to 20 mm. The hatched areas depicted in these figures represent the pre-crack α_0 (initial delamination length), chosen to be equal to 50 mm in accordance with ASTM D5528-01, 2007. As far as the ENF tests are concerned, in order to achieve crack growth stability, the initial crack length, α_0, was chosen to be equal to 70% of the half length of the specimen Carlsson et al., (1986), resulting in a value of α_0 equal to 35 mm.

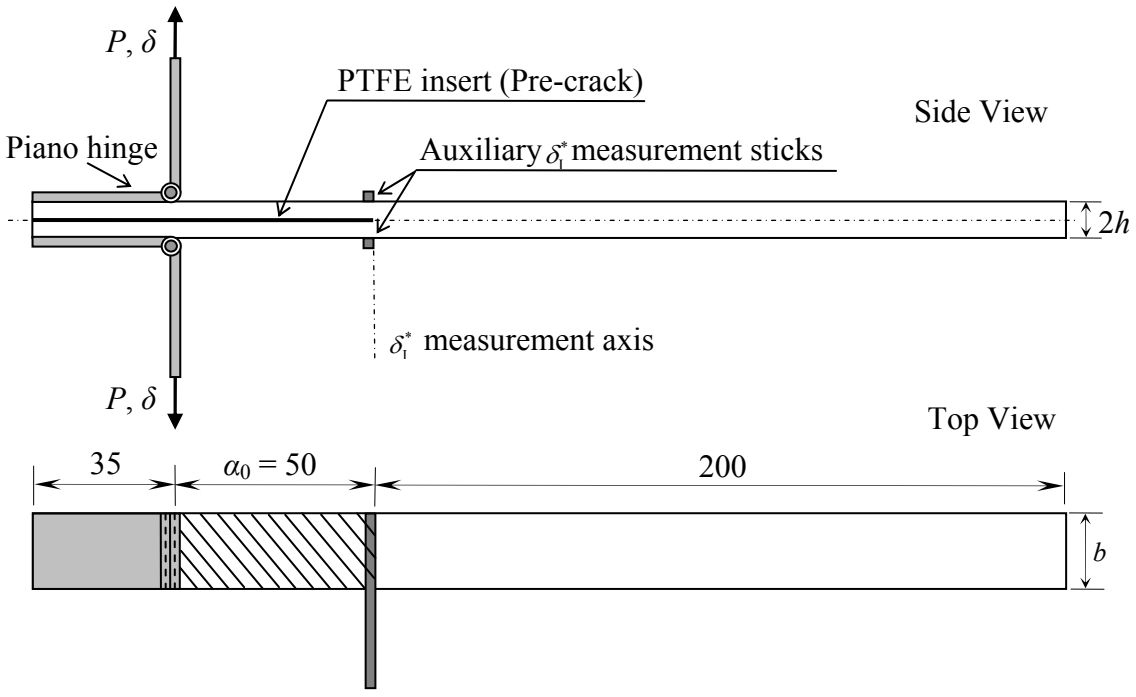

Figure 4.2: Schematic side and top view of the tested DCB specimens (dimensions in mm).

Two 1.5 mm thick piano hinges aligned with the specimen axis and loading line were adhesively bonded to the pre-cracked edge of the DCB specimens with the use of two-part toughened epoxy adhesive. During the curing of the adhesive, the piano hinges were under constant pressure with the aid of clamps and provisions were taken so as to ensure a constant adhesive thickness. The specimens were left 48 hours after the completion of the curing process of the adhesive before the experimental testing.

As regards the DCB specimens, crack length, α, is defined as the distance from the loading line to the crack tip. Crack propagation was monitored by visual inspection of the crack length through the use of a high resolution (1920x1080), 60 frames per second video camera equipped with 16x optical zoom lens, recording the marked side of the specimens. Additionally, two plastic auxiliary measurement sticks (see Figure 4.2) were bonded at the pre-crack tip of the DCB specimens, and were placed in-between a high-speed laser scan micrometer (Keyence LS5041) for monitoring the pre-crack opening displacement δ^* magnitude during the tests.

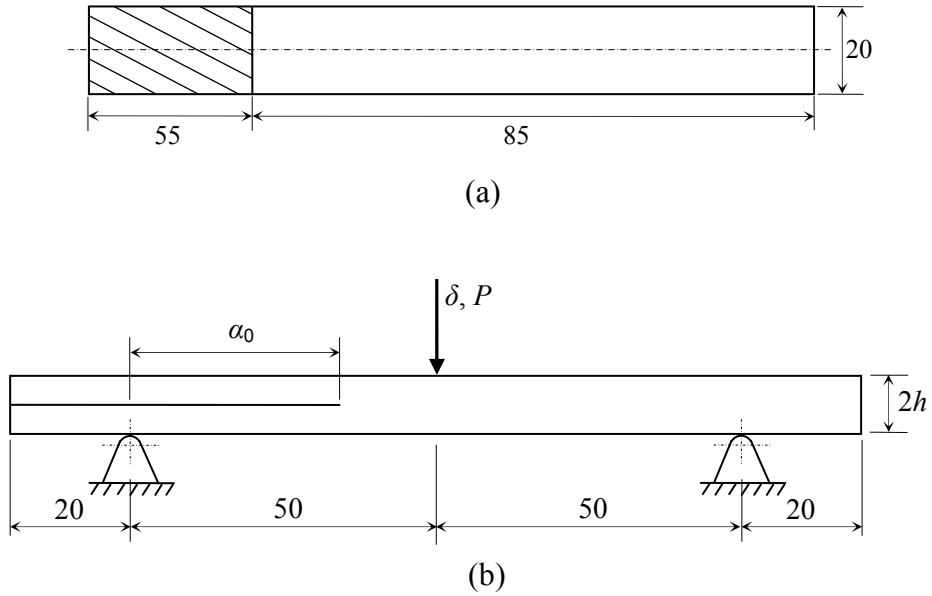

Figure 4.3: Geometry (a) and experimental set-up of the ENF specimens (dimensions in mm).

In aiding crack length measurements, thin vertical lines have been marked on the lateral sides of the specimens with a spacing of 5 mm ($\Delta\alpha$) for the DCB specimens and 2mm ($\Delta\alpha$) for the ENF specimens. Prior to the creation of these marks, a thin layer of a water-soluble white correction fluid was applied to enhance visualization of crack growth. Monitoring of the crack length in Mode II fracture propagation ENF tests is considered to be a rather difficult task, since crack grows without a clear opening Blackman et al. (2006). Besides the obvious reason that there is no physical crack opening, local plasticity and microcracks formed in front of the crack tip at crack initiation and at the early stages of crack propagation foster this difficulty.

The DCB specimens were loaded in displacement controlled tension δ at a 2 mm/min speed. During each DCB test the load-applied displacement curve (P-δ) and the relative pre-crack tip opening displacement (δ*) were recorded as a function of time. On the other hand, the

ENF specimens were loaded in 3-point bending by a static displacement, applied with a speed of 0.5 mm/min. The load-bending displacement curve (P–δ) was recorded during each test. Crack propagation was monitored by visual inspection of the crack length with the aid of a high resolution video camera (1920x1080) equipped with 16x optical zoom lens, which was recording the marked side of the specimens with a rate of 60 frames per second. All tests were conducted by an MTS hydraulic testing machine (858 Mini Bionix II) equipped with a 15 kN load cell.

4.3 Data reduction schemes - Overview

The term data reduction scheme refers to the method utilized for the calculation of the energy release rate (ERR) magnitude. The reduction scheme is applied on the data of the opening (Mode I) or the sliding (Mode II) displacement, in order to apply in the sequence the J-integral approach and derive a bridging law. For the calculation of the ERR in Mode I, three different data reduction schemes have been considered:

- Corrected Beam Theory - CBT
- Experimental Compliance Method - ECM
- Modified Compliance Calibration - MCC

The CBT, ECM and MCC methods are the ones proposed in ASTM D5528-01.

For the calculation of the ERR in Mode II, i.e. ENF fracture tests, three reliable data reduction schemes have been considered:

- Compliance Calibration Method - CCM
- Corrected Beam Theory - CBT
- Compliance-Based Beam Method – CBBM

Since a standard is not yet available for the calculation of the ERR in Mode II, the selected methods are taken from the literature.

4.3.1 Data reduction schemes for the DCB tests

The Corrected Beam Theory (CBT) data reduction scheme is one of the most frequently used methods for calculating the ERR magnitude, expressed in terms of the crack length α. CBT was introduced by Williams (1989) and is given by the following formula:

$$G_{\mathrm{I}} = \frac{3P\delta}{2b(\alpha + |\Delta|)} \tag{4.1}$$

where $|\Delta|$ is a correction factor for the crack tip rotation, determined experimentally by generating a linear regression of the cubic root of the compliance ($C^{1/3}$) versus the delamination

length (see Figure 4.4a). The compliance C is defined as the ratio of the point load displacement to the applied load (δ/P).

The Experimental Compliance Method (ECM) has been a classical data reduction scheme for addressing G_I, since its introduction to the composite community by Berry (1983). This method utilizes the Irwin – Kies equation for the calculation of G_I:

$$G_I = \frac{P^2}{2b}\frac{dC}{d\alpha} \tag{4.2}$$

According to ECM, a power function is fitted with the use of the least-square method over the compliance versus the crack length plot, so as to obtain the R coefficient and the n power exponent (see Figure 4.4b) needed for the following expression, Berry 1983:

$$C = R\alpha^n \tag{4.3}$$

Thus, by differentiating Equation (4.3) and substituting it to Equation (4.2) the Irwin – Kies equation takes the form:

$$G_I = \frac{P^2 nR\alpha^{n-1}}{2b} \tag{4.4}$$

The Modified Compliance Calibration (MCC) method utilizes the following expression for the determination of the ERR values as a function of the crack length:

$$G_I = \frac{3P^2 C(\alpha)^{2/3}}{2A_1 bh} \tag{4.5}$$

where A_1 is a compliance calibration term, taken as the slope of a straight line generated by the least-square fit of the delamination length normalized by the specimen thickness (α/h) versus the cubic root of the compliance (see Figure 4.4c).

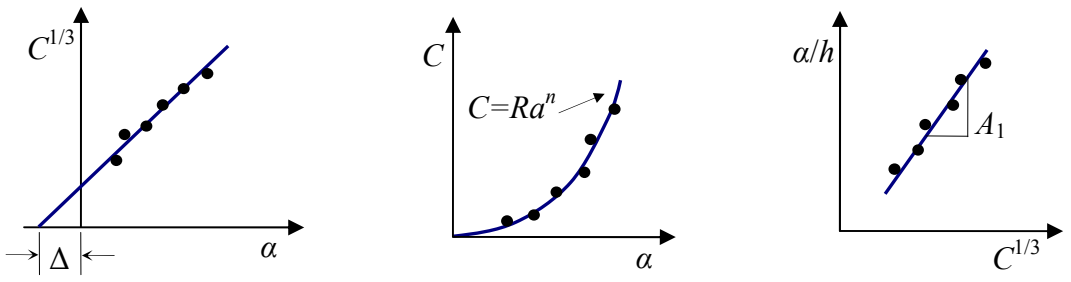

(a) (b) (c)

Figure 4.4: Least-square fits to obtain the parameters needed for the CBT (a), ECM (b) and MCC (c) data reduction schemes.

4.3.2 Data reduction schemes for the ENF tests

The CCM has been a classical data reduction scheme for addressing G_{II}, since its introduction to the composite community by Russell and Street (1985). This method utilizes the Irwin – Kies equation (Irwin and Kies, 1954) for the calculation of G_{II}:

$$G_{II} = \frac{P^2}{2b}\frac{dC}{d\alpha} \tag{4.6}$$

where C is the compliance of the specimen (bending displacement per unit load, $C = \delta/P$). The compliance C is expressed in terms of a constant term C_0 and a term proportional to the cubic power of the crack length α according to the following equation:

$$C = C_0 + ma^3 \tag{4.7}$$

where constant term C_0 equals to the initial compliance at crack initiation (α_0). Coefficient m can be determined from the slope of the experimental curve of the compliance versus the cubic power of crack length. By differentiating Equation (4.7) with respect to the crack length and substituting in Equation (4.6), the G_{II} values are given for each discrete measured crack length α_i ($i = 0,...,n$, where 0 corresponds to crack initiation and n to the maximum number of crack tip measurements) by Equation (4.8).

$$G_{II} = \frac{3m\alpha^2 P^2}{2b} \tag{4.8}$$

CBT method has been proposed for ENF tests by Wang and Williams (1992). This approach is based on a beam elastic foundation model and takes into account corrections of the measured crack length α. The calculation of G_{II} is given by:

$$G_{II} = \frac{9\left(\alpha + 0.42\Delta_1\right)^2 P^2}{16b^2h^3E_1} \tag{4.9}$$

where E_1 is the modulus along the specimens' longitudinal direction and Δ_1 is a crack length correction, accounting for the developed shear deformation when the specimen is loaded, which is given in the following form by de Moura and de Morais (2008):

$$\Delta_1 = h\sqrt{\frac{E_1}{11G_{13}}\left[3 - 2\left(\frac{\Gamma}{1+\Gamma}\right)^2\right]} \tag{4.10}$$

and Γ is given by

$$\Gamma = 1.18\frac{\sqrt{E_1 E_3}}{G_{13}} \tag{4.11}$$

where E_3 and G_{13} are the transverse and shear moduli, respectively.

The CCM and CBT data reduction schemes require accurate crack length measurements, which present difficulties in obtaining with the crack monitoring technique used in this study. Thus, de Moura et al. (2009) proposed a novel, beam theory based calculation method, incorporating the crack equivalent concept and applied this method to composite bonded ENF tests. According to the authors, CBBM depends only on specimen's compliance during the tests and considers several effects neglected by the classical methods that affect the behaviour of the specimen and consequently the P–δ curve. The most important advantage of this method is its ability to obtain an R-curve explicitly through the P–δ curve, since monitoring of the crack propagation length hides difficulties. The calculation of G_{II} is obtained by modifying the Irwin – Kies equation, as follows:

$$G_{II} = \frac{9\alpha_e^2 P^2}{16 b^2 E_f h^3} \tag{4.12}$$

where α_e is the equivalent crack length expressing a correction to the real crack length in order to account for the bridging zone influence and given by Equation (4.13):

$$\alpha_e = \left[\frac{C_c}{C_{0c}}\alpha_0^3 + \left(\frac{C_c}{C_{0c}} - 1\right)\frac{2L^3}{3}\right]^{1/3} \tag{4.13}$$

The flexural modulus of the specimen E_f has an important influence on the slope and behaviour of the global P–δ curve. Thus, it is calculated through the relation of the initial compliance C_0 with α_0.

$$E_f = \frac{3\alpha_0^3 + 2L^3}{8bh^3 C_{0c}} \tag{4.14}$$

where

$$C_{0c} = C_0 - \frac{3L}{10 G_{13} bh} \tag{4.15}$$

The corrected compliance C_c is given by Equation (4.16):

$$C_c = C - \frac{3L}{10G_{13}bh} \tag{4.16}$$

where C is the compliance of the ENF specimens during the test and its calculation is based on the beam theory.

$$C = \frac{3\alpha^3 + 2L^3}{8bh^3E_1} + \frac{3L}{10G_{13}bh} \tag{4.17}$$

4.4 *J*-integral approach

In order to characterize the R-curve effect (fracture toughness' increase as delamination grows), the *J*-integral approach is considered for the derivation of the bridging law. By calculating the *J*-integral around the crack tip and along the crack faces and by considering the existence of a bridging zone, the following expression of the energy release rate is obtained for Mode I and II (Suo et al. 1992):

$$G_{I,ss} = G_{I,0} + G_{I,b} \tag{4.18a}$$

$$G_{II,ss} = G_{II,0} + G_{II,b} \tag{4.18b}$$

where

$$G_{I,b} = \int_0^{\delta_I^*} \sigma(\delta_I)\,\mathrm{d}\delta_I \tag{4.19a}$$

$$G_{II,b} = \int_0^{\delta_{II}^*} \sigma(\delta_{II})\,\mathrm{d}\delta_{II} \tag{4.19b}$$

where δ_I and δ_{II} are the local relative opening and sliding magnitudes of the crack faces for the Mode I and II loading and fracture, respectively. $G_{I,0}$ and $G_{II,0}$ are the initial fracture toughness (at crack initiation) components, which involves matrix cracking and is assumed to be constant. The bridging increase fracture toughness components $G_{I,b}$ and $G_{II,b}$ are calculated by the integration of the bridging stresses σ_I and σ_{II} with respect to δ_I and δ_{II}, respectively. Hence, after the integration in Equation (4.19), the $G_{I,b}$ and $G_{II,b}$ magnitudes are expressed in terms of the pre-crack tip opening displacement δ_I^* and δ_{II}^*, respectively. In fact $G_{I,b}$, $G_{II,b}$ involve the contribution of the fibre bridging to the steady state fracture toughness, namely $G_{I,SS}$ and $G_{II,SS}$. According to Equation (4.19) the bridging stresses σ depend on the local opening and not on the crack

trajectory. Thus, by differentiating Equations (4.18) with respect to δ_{I}^{*} and δ_{II}^{*}, separately for the Mode I and Mode II case, the following expression of the bridging law is generated:

$$\sigma_{\mathrm{I}}(\delta_{\mathrm{I}}^{*}) = \frac{\partial G_{\mathrm{I}}}{\partial \delta_{\mathrm{I}}^{*}} \tag{4.20a}$$

$$\sigma_{\mathrm{II}}(\delta_{\mathrm{II}}^{*}) = \frac{\partial G_{\mathrm{II}}}{\partial \delta_{\mathrm{II}}^{*}} \tag{4.20b}$$

where $\sigma_{\mathrm{I}}(\delta_{\mathrm{I}}^{*})$ and $\sigma_{\mathrm{II}}(\delta_{\mathrm{II}}^{*})$ are the experimentally obtained bridging stress developed between the crack faces and expressed in terms of the opening and sliding of the pre-crack tip, for the Mode I and II respectively. As it can be seen from Equations (4.20), the components $G_{\mathrm{I},0}$ and $G_{\mathrm{II},0}$ have been vanished, since they are constant terms.

4.5 Experimental results

Processing of the experimental results obtained from the DCB and ENF tests aims at calculating two magnitudes; the critical fracture energy or initial fracture toughness in Mode I ($G_{\mathrm{I},0}$) and Mode II ($G_{\mathrm{II},0}$) from the crack initiation monitoring and the R-curve in Mode I (G_{I} - δ_{I}^{*}) and II (G_{II} - δ_{II}^{*}) from the crack propagation monitoring. Thus, the three data reduction schemes described in section 4.3.1 for the DCB tests (CBT, ECM and MCC) and section 4.3.2 for the ENF tests (CCM, CBT and CBBM), are adopted for the construction of the corresponding R-curves in Mode I and Mode II, respectively. Then, the discrete G_{I} - δ_{I}^{*} and G_{II} - δ_{II}^{*} data sets are fitted with the use of analytical functions. This step is important for acquiring continuous description of either G_{I} - δ_{I}^{*} or G_{II} - δ_{II}^{*} relation, in order to apply the *J*-integral approach (Equation (4.20)) analytically, without the need of using numerical differentiation schemes.

4.5.1 Post-processing of the DCB test results

The global response of the tested DCB specimens in terms of the registered load (P) versus the applied displacement (δ) data is presented in Figure 4.5. All four experimental curves exhibit an initial linear response, followed by increasing non-linearities as the crack begins to propagate. After the maximum load is attained, the slope of the load-displacement curves begins to soften together with delamination progression. The softening behaviour of the tested specimens with codenames 1 and 2 is in great agreement, whereas the respective behaviour of specimens 3 and 4 seems to vary. Such deviations are attributed to the existence of transverse fiber yarns and/or fiber knits in the vicinity of the pre-crack tip.

A typical P-δ-α plot is additionally presented in Figure 4.5 for specimen 1. The circles on the graph indicate the crack length in mm, as measured from the high resolution video camera by

image processing techniques. The same procedure was followed for the derivation of the *P*-*δ*-*α* data sets for specimens 2, 3 and 4.

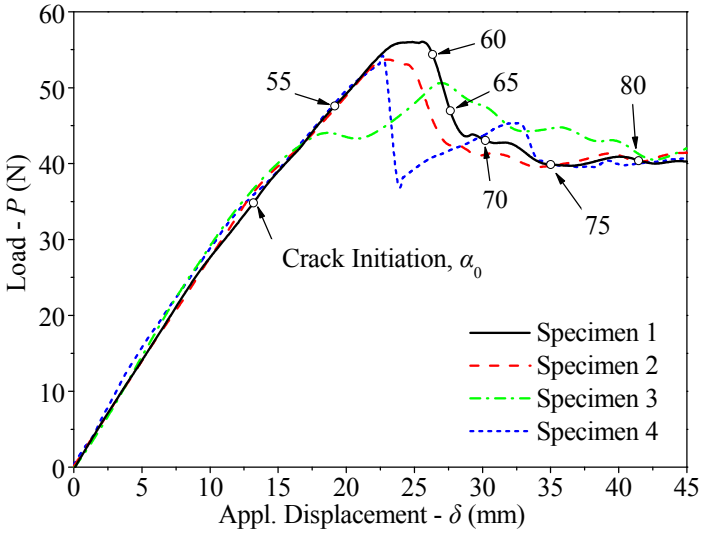

Figure 4.5: Load – displacement results from all DCB tests.

It should be pointed out that crack initiated directly from the PTFE insert film and in each case propagated along the mid-plane of the specimens. The crack propagated in a stable manner during the tests, as denoted by Figure 4.6. A closer study of the results of Figure 4.5 and Figure 4.6 reveals that, for every specimen, the rate of increase of the crack propagation was slightly slowed down at the point where the maximum load was obtained.

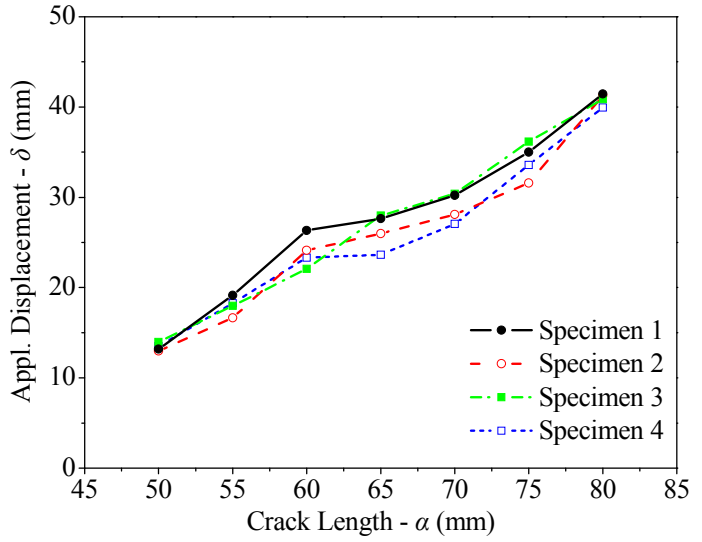

Figure 4.6: Displacement versus crack length obtained from the tested DCB specimens.

The compliance was calculated from the expression $C_i = \delta_i / P_i$ for each value of α_i and Equation (4.3) was utilized for fitting the experimental compliances for each specimen, in accordance with the ECM data reduction scheme. The corresponding results are shown in Figure Figure 4.7 and the coefficients *R,* together with their respective exponents *n*, are listed in Table

4.2. The crack length measurements vary from 50 mm (crack initiation) to 80 mm with an increment $\Delta\alpha$ equal to 5 mm.

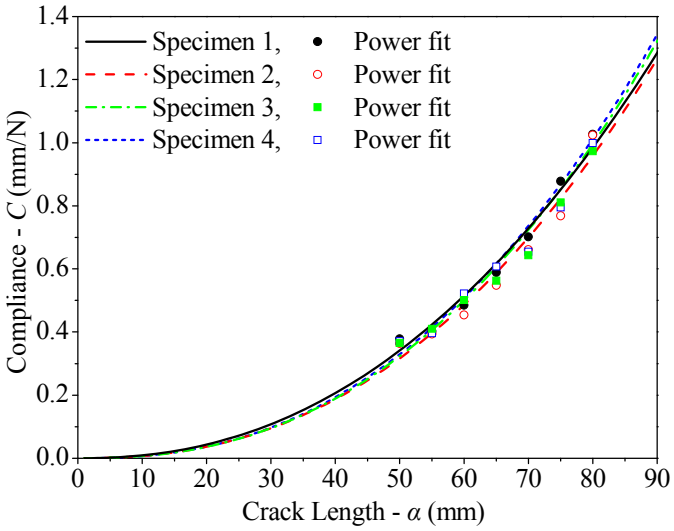

Figure 4.7: Compliance ($C = \delta / P$) versus crack length.

The ERR values for each crack length α_i were calculated according to the CBT, ECM and MCC data reduction schemes by utilizing Equations (4.1), (4.4) and (4.5), respectively. Parameters $|\Delta|$ and A_1 which are defined in the CBT and MCC schemes and are necessary magnitudes for the calculation of G_I, are listed in Table 4.2. $G_{I,0}$ values are quite close between each other, not only among the tested specimens but also among the methods adopted for their calculation, since the obtained mean values from the CBT, ECM and MCC methods equal to 0.58, 0.51 and 0.57 N/mm, respectively.

Figure 4.8 presents the R-curves obtained with the CBT, ECM and MCC data reduction schemes. The G_I magnitude increases as the delamination propagates, thus denoting the existence of fiber bridging mechanisms. After a certain crack length, G_I seems to converge to an average plateau level, the steady state fracture toughness $G_{I,SS}$. Figure 4.9 presents a magnified view of a DCB test, where the fiber bridging phenomenon dominates at the specimens' mid-plane during delamination growth.

Table 4.2: Experimental parameters calculated with the CBT, ECM and MCC data reduction schemes.

Specimen	CBT	ECM		MCC
	$\|\Delta\|$	R	n	A_1
1	23.29	5.05E-5	2.25	19.50
2	17.59	3.14E-5	2.36	20.59
3	15.93	2.87E-5	2.39	18.90
4	16.49	2.78E-5	2.39	19.01

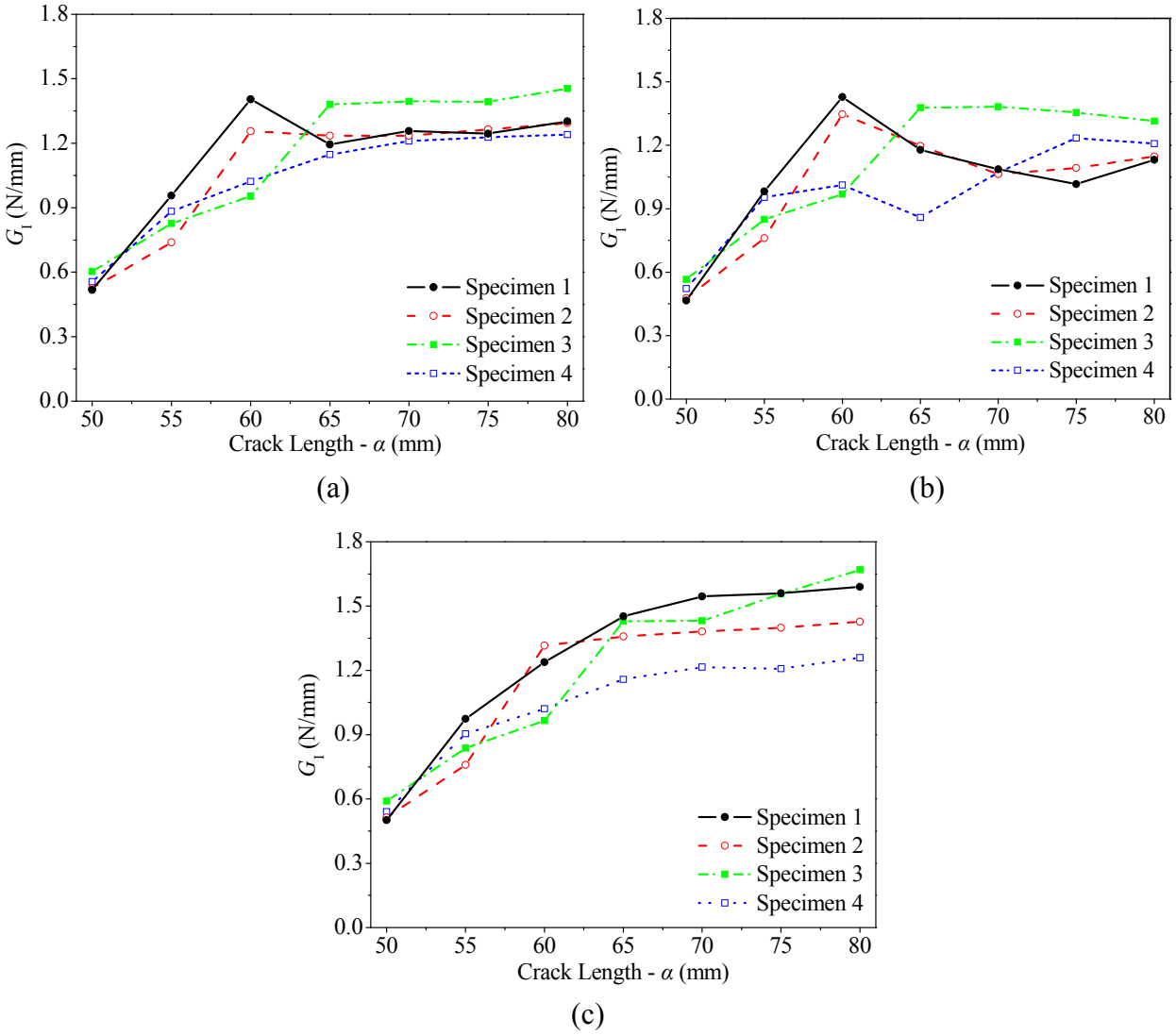

Figure 4.8: R-curves of the tested DCB specimens calculated with the CBT (a), ECM (b) and MCC (c) data reduction scheme.

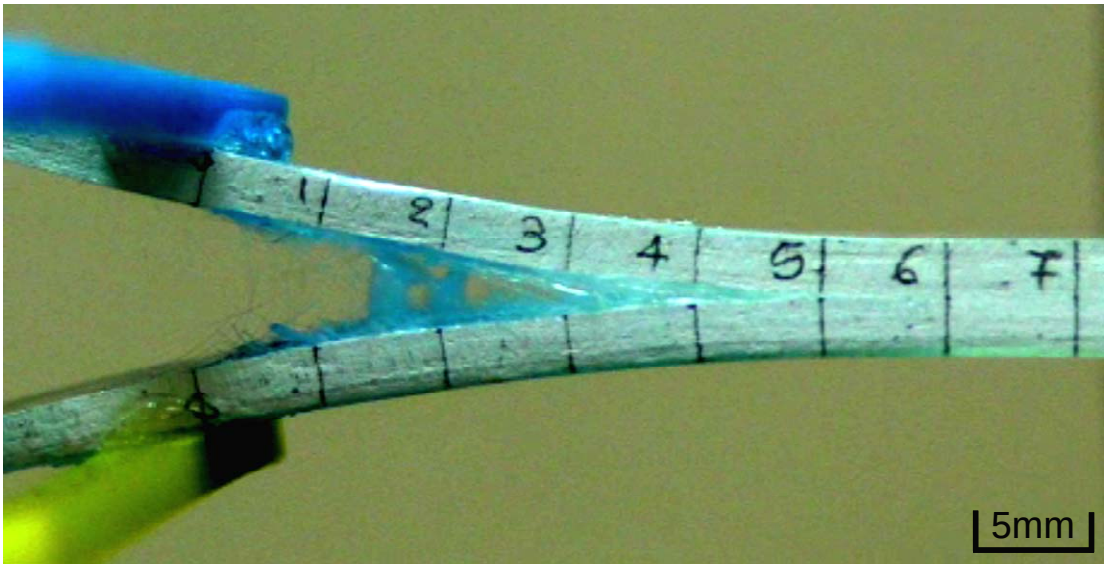

Figure 4.9: Fiber bridgings developed during the DCB tests.

The pre-crack tip opening displacement (δ_I^*) was monitored as a function of time with the use of the high-speed laser scan micrometer. These registered data were related to the corresponding applied displacement data δ directly through the time parameter. Thus, the δ_I^*-α discrete data sets can be easily obtained by combining the P-δ-α data sets (see Figure 4.5) with the corresponding δ_I^* magnitude measured from each DCB test.

Since the main scope of this work is to derive a law that will characterize the bridging zone and that can be used as a material property of the composite material system, an analytical function (fitting function) that describes the trend of all specimens data sets must be determined. This procedure is required in order to apply the J-integral approach (use of Equation (4.20)) to the G_I - δ_I^* relation and hence produce an analytical form of the resulting bridging law. A different technique could pertain to the numerical differentiation of the discrete experimental G_I - δ_I^* data sets according to Equation (4.20), so as to derive the bridging laws. This technique would yield a bridging law characterized by discontinuities and lack of smoothness and hence it could not be directly implemented in a numerical procedure (e.g. finite element method).

Several efforts have been made towards finding a fitting function that would yield a value of the adjusted coefficient of determination (R^2) as close to unity as possible, according to the least square method. All three G_I - δ_I^* data sets are best described with the use of an exponential fitting function yielding values of R^2 that equal to 0.75, 0.71 and 0.83 for the CBT, ECM and MCC methods, respectively, as shown in Figure 4.10. The form of the exponential fitted function is given by the following equation:

$$G_I\left(\delta_I^*\right) = C_1 \exp(\delta_I^* / C_2) + C_3 \tag{4.21}$$

where C_1, C_2 and C_3 are the fitted coefficients listed in Table 4.3 for the three cases of Figure 4.10. The value of the average steady state fracture toughness $G_{I,SS}$ is taken equal to the asymptote of each separate exponential function. The respective results are also listed in Table 4.3.

Table 4.3: Calculated coefficients of the exponential function used for fitting the $G_I - \delta^*$ data sets and energetic characteristic parameters.

	C_1	C_2	C_3	$G_{I,0}$ (N/mm)	$G_{I,SS}$ (N/mm)	$G_{I,b}$ (N/mm)	$I_{exp,I}$ (N/mm)
CBT	-0.705	-1.054	1.286	0.58	1.28	0.70	0.695
ECM	-0.651	-0.444	1.163	0.51	1.16	0.65	0.654
MCC	-0.834	-1.384	1.408	0.57	1.40	0.83	0.825

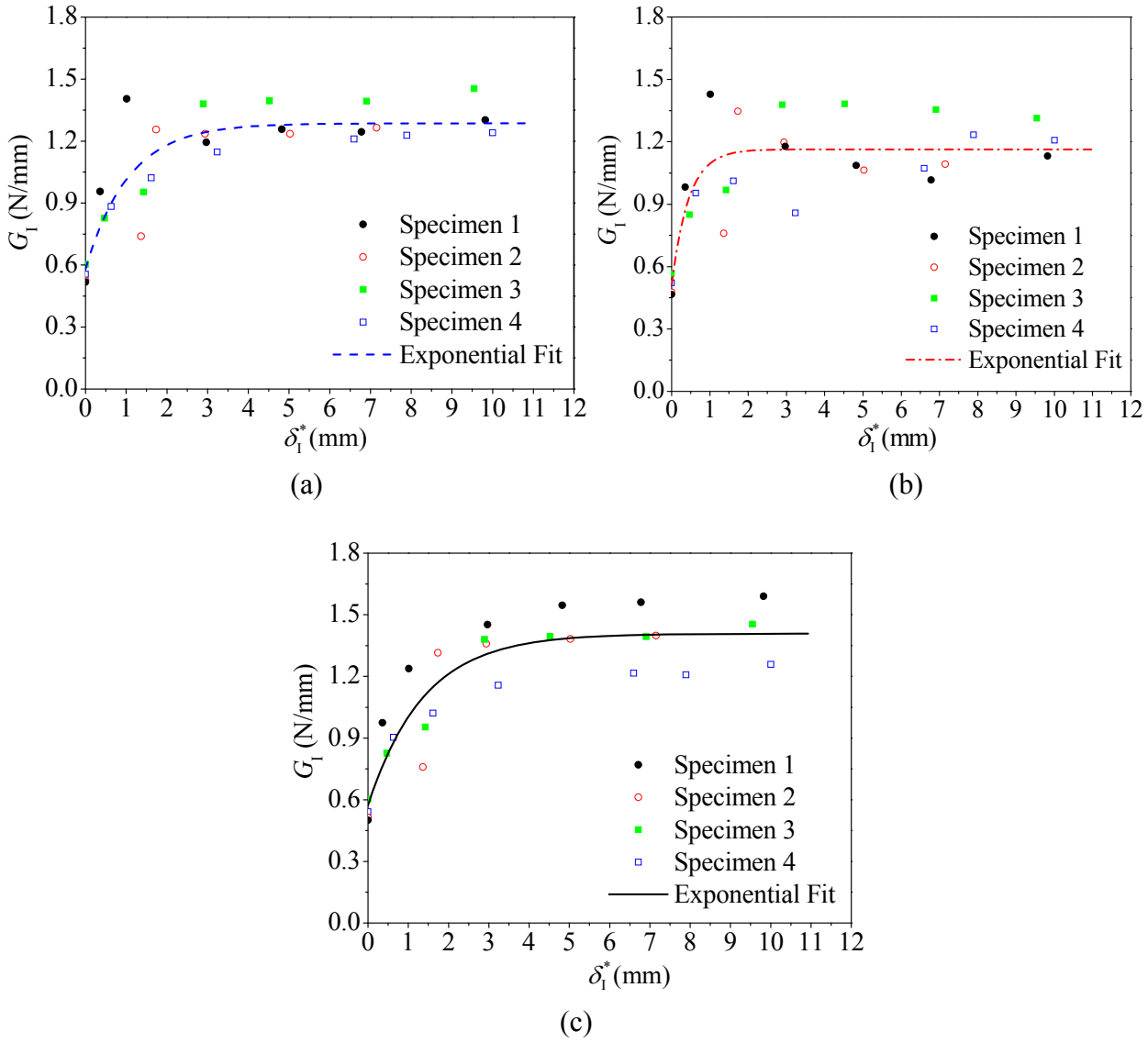

Figure 4.10: G_I - δ_I^* data sets calculated with the CBT (a), ECM (b) and MCC (c) data reduction scheme.

By applying Equation (4.20) to the continuous G_I - δ_I^* curves plotted together in Figure 4.11a for reasons of comparison, the resulting bridging laws are shown in Figure 4.11b. In these two figures a moderate disagreement between the results obtained from the ECM and the other two methods is observed. The accuracy of the ECM is based on the number of the discrete points used to fit the $C - \alpha$ relationship (see Figure 4.7) and probably this is the reason for the above mentioned disagreement. However, all three calculated bridging laws have the same exponential softening behaviour. On the contrary, the critical bridging stress $\sigma_{c,I}$ and the critical crack opening displacement $\delta_{c,I}^*$ (stress release bound) of the obtained bridging laws vary. The magnitude of the critical bridging stress relies on the magnitude of the initial slope of its respective G_I - δ_I^* curve, since it is calculated through the differentiation of the latter (Equation (4.20)). Thus, stiffer initial slopes yield higher values of the critical bridging stress and the opposite. This can be seen when comparing Figure 4.11a with Figure 4.11b. The obtained $\sigma_{c,I}$ and

$\delta_{c,I}^{*}$ values of the experimentally obtained bridging laws from the CBT, ECM and MCC methods are listed in Table 4.4.

A very interesting issue is the comparison of the energy uptake (I_{exp}) at the completion of the FPZ, which equals to the magnitude of the definite integral of the experimentally obtained bridging laws shown in Figure 4.11b. As shown from Table 4.3, the I_{exp} values are in great agreement with the fiber bridging increase fracture toughness $G_{I,b}$, calculated from the subtraction of $G_{I,0}$ from $G_{I,SS}$. This fact is in accordance with the J-integral approach and denotes that the obtained bridging laws describe only the FPZ of the composites' interface without taking into account the initial ERR needed for crack initiation ($G_{I,0}$).

Table 4.4: Parameters of the experimentally obtained bridging laws.

	$\sigma_{c,I}$ (MPa)	$\delta_{c,I}^{*}$ (mm)
CBT	0.66	5.97
ECM	1.47	2.98
MCC	0.6	6.34

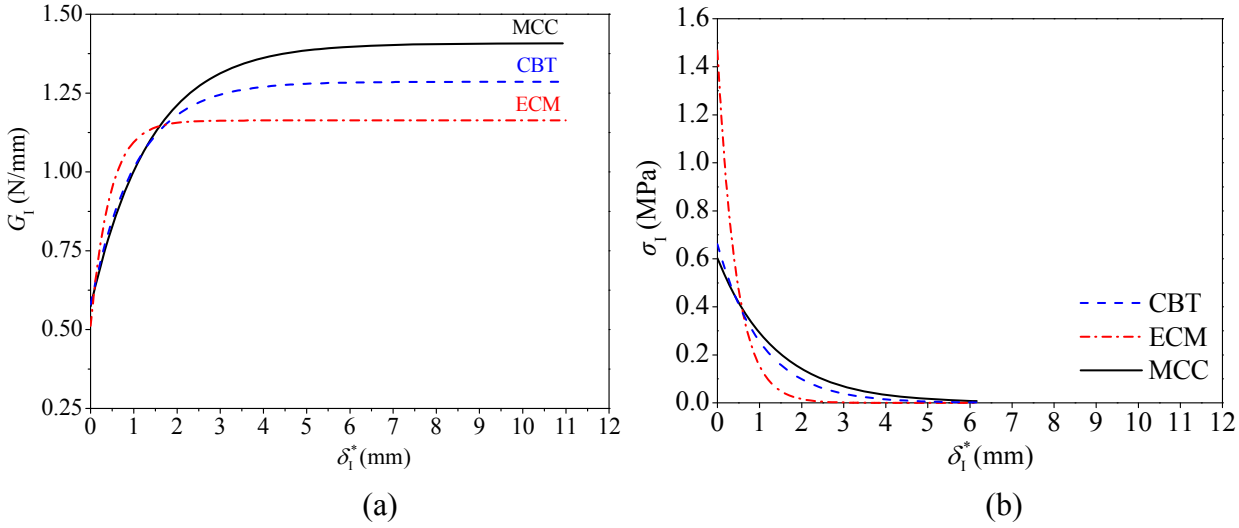

Figure 4.11: Analytical fit of the experimentally obtained $G_{I,0}$ - δ^{*} data sets (a) and their corresponding calculated bridging laws.

4.5.2 Post-processing of the ENF test results

The same processing procedure is followed for the derivation of the Mode II bridging laws from the ENF test results as described in the previous section (4.5.1). The global response of the tested ENF specimens in terms of load-bending displacement curves is depicted in Figure 4.12. All five experimental curves of this figure denote a good repeatability of the results and exhibit an initially linear response, followed by increasing non-linearities, as the crack begins to propagate.

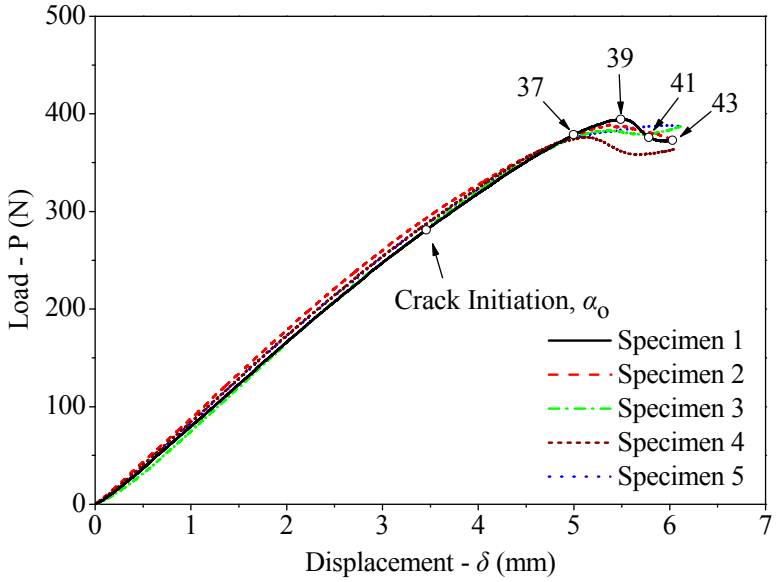

Figure 4.12: Load – displacement results from all ENF tests.

According to Figure 4.12, four of the specimens clearly exhibit a maximum load level, after which the slope of the load-displacement curves begins to slightly soften together with delamination progression, thus indicating entrance into a steady-state condition. The fifth specimen does not exhibit any drop of the load after a certain maximum load level, but even this seems to enter into a steady-state condition. The crack propagated in a stable manner during the displacement control fracture testing of all specimens.

A typical *P*-*δ*-*α* curve is additionally presented in Figure 4.12. The circles on the graph indicate the crack length in mm, measured from the left support of each specimen (see Figure 4.3b), as extracted from the high resolution video by image processing techniques. Figure 4.13 shows the crack as it propagates in Mode II during the test. It is noteworthy that the crack initiated directly from the insert film and for all tests propagated along the mid-plane of the specimens.

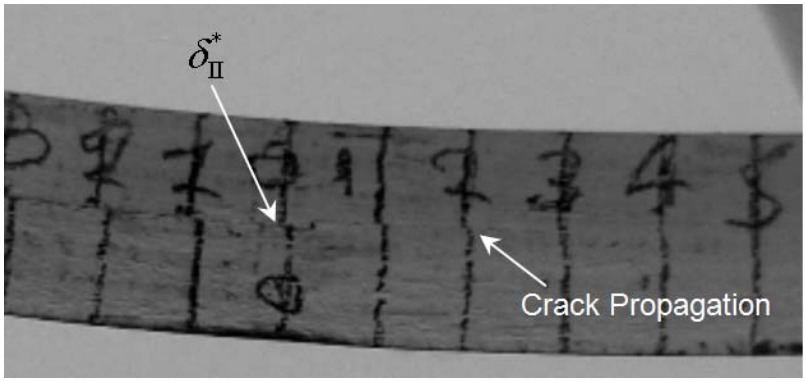

Figure 4.13: Crack propagation in Mode II.

For the calculation of the ERR values with CCM, the compliance C must be calculated. Thus the ratio $C_i = \delta_i/P_i$ has been used directly for the calculation of the compliance for each value of α_i. The compliances of the ENF tests are presented in Figure 4.14 as a function of the cubic power of the crack length, for all crack length values where measurements were taken (α_i = 35, 37, 39, 41 and 43 mm). It is observed that the compliance of all tested specimens increases together with the cubic power of the crack length, without important changes in the slope. This is in accordance with the CCM method and specifically with Equation (4.7). The derivation of coefficient m is necessary for the calculation of the G_{II} values (see Equation (4.8)). Hence, a linear regression based on the least square method was performed over the discrete $C - \alpha^3$ data sets from each ENF test (see Figure 4.14). The obtained slope from each linear fitting function was utilized as coefficient m. The linear fittings simulate very accurately the experimental measurements, exhibiting values of the coefficient of determination that vary within the range of 0.95 – 0.99. The ERR values calculated from Equation (4.8) for all specimens are listed in Table 4.5.

Table 4.5: Fracture toughness values, G_{II}, as calculated from CCM (in N/mm).

	crack length (in mm)				
	$\alpha_0 = 35$	$\alpha_1 = 37$	$\alpha_2 = 39$	$\alpha_3 = 41$	$\alpha_4 = 43$
Specimen 1	0.66	1.24	1.60	1.83	2.02
Specimen 2	0.65	1.34	1.58	1.71	1.92
Specimen 3	0.79	1.41	1.63	1.65	1.86
Specimen 4	0.75	1.61	1.97	2.15	2.24
Specimen 5	0.79	1.60	1.92	1.93	2.09
Mean value	*0.73*	*1.44*	*1.74*	*1.85*	*2.03*
COV (%)	*9.4*	*11.3*	*10.86*	*10.66*	*7.4*

COV: Coefficient of variance

Table 4.6: Fracture toughness values, G_{II}, as calculated from CBT (in N/mm).

	crack length (in mm)				
	$\alpha_0 = 35$	$\alpha_1 = 37$	$\alpha_2 = 39$	$\alpha_3 = 41$	$\alpha_4 = 43$
Specimen 1	0.63	1.18	1.52	1.74	1.74
Specimen 2	0.64	1.31	1.54	1.67	1.77
Specimen 3	0.60	1.29	1.58	1.71	1.73
Specimen 4	0.67	1.36	1.63	1.68	1.68
Specimen 5	0.72	1.27	1.48	1.65	1.70
Mean value	0.65	1.28	1.55	1.69	1.72
COV (%)	7.0	5.2	3.8	2.0	2.1

COV: Coefficient of variance

Table 4.7: Fracture toughness values, G_{II}, as calculated from CBBM (in N/mm).

	crack length (in mm)				
	$\alpha_0 = 35$	$\alpha_1 = 37$	$\alpha_2 = 39$	$\alpha_3 = 41$	$\alpha_4 = 43$
Specimen 1	0.64	1.17	1.53	1.75	1.97
Specimen 2	0.65	1.28	1.59	1.74	1.97
Specimen 3	0.58	1.01	1.41	1.71	1.82
Specimen 4	0.70	1.34	1.70	1.79	1.85
Specimen 5	0.73	1.26	1.51	1.72	1.68
Mean value	0.66	1.21	1.55	1.74	1.85
COV (%)	8.6	10.8	7.0	1.7	6.4

COV: Coefficient of variance

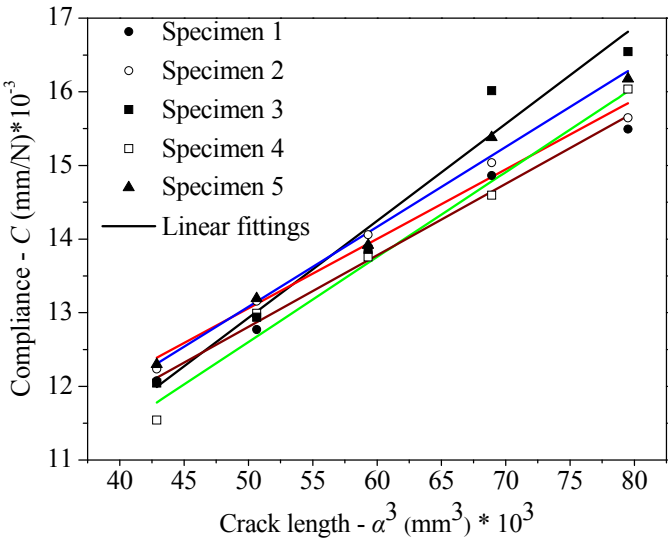

Figure 4.14: Experimentally measured compliance vs. cubic crack length for the ENF specimens.

For the calculation of the G_{II} magnitude with the CBT and CBBM data reduction schemes, Equation (4.9) to (4.11) and (4.12) to (4.17) have been utilized, respectively. The corresponding G_{II} calculated values are listed in Table 4.6 and Table 4.7. The ERR values have been derived in terms of the equivalent crack length, α_e, in the case of CBBM, which is calculated by Equation (4.13). This calculation yields as many values as the recorded P–δ data during each test. Thus, for reasons of comparison, G_{II} values obtained by the CBBM method are listed in 4.17 with respect to the real crack length as experimentally measured, without any loss of generality. It must be mentioned that G_{II} values obtained using CBT and CBBM methods exhibit very good repeatability since their coefficient of variance (COV) for each crack length attains low values. In the case of the G_{II} values calculated with the CCM method, coefficients of variance is slightly higher.

Figure 4.15 presents the R-curves obtained from the mean values of fracture toughness from all five specimens, as a function of the crack length, as calculated by CCM, CBT and CBBM. The CBBM data reduction scheme has yielded a continuous R-curve in comparison to

the respective curves obtained from CCM and CBT which appear to be discrete. As Figure 4.15 shows and Table 4.5 to Table 4.7 indicate, fracture toughness increases together with crack propagation. The R-curve obtained from the CBT scheme reaches a plateau region (steady state fracture toughness, $G_{II,SS}$), where it is assumed that the ERR remains stable for any further increase of the crack length. In the case of the CCM and CBBM schemes results, Figure 4.15 indicates that this steady state conditions is marginally achieved. As it is shown from Table 4.5 to Table 4.7, fracture toughness at crack initiation, $G_{II,0}$, and steady state fracture toughness, $G_{II,SS}$, indicate very good repeatability with a coefficient variation approximately equal to 6%. The R-curves obtained by CBT and CBBM are in quite good agreement between each other, whereas the R-curve obtained by CCM exhibits slightly higher values.

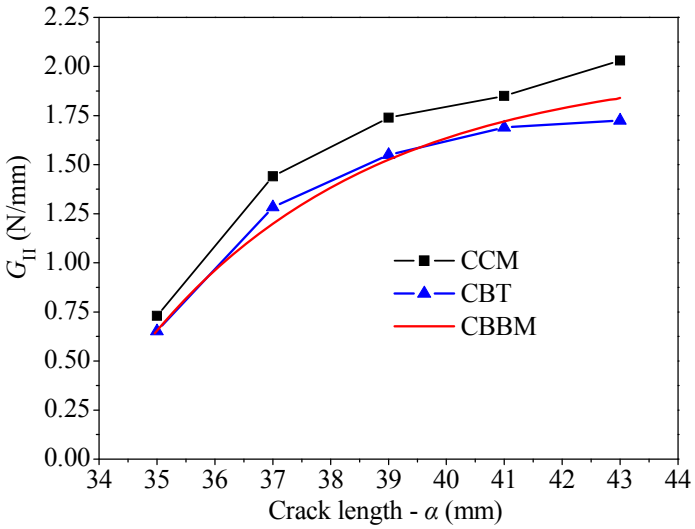

Figure 4.15: Experimentally measured R-curves from all specimens.

For obtaining the bridging law described by Equation (4.20), definition of function G_{II}–δ_{II}^* is required. In fact function G_{II}–δ_{II}^* can be implicitly defined by combining the relationships G_{II}–α shown in Figure 4.15 and function δ_{II}^*–α. Using the recordings of the high definition camera, function δ_{II}^*–α was defined with image processing techniques and is shown in Figure 4.16. This function was then used to calculate the final experimentally derived function G_{II}–δ_{II}^*. In the sequence, three G_{II}–δ_{II}^* discrete data sets were plotted corresponding to the three data reduction schemes, and analytical functions were fitted to the results for each case separately. This procedure is necessary for deriving a smooth differential relationship from Equation (4.20b), appropriate for implementation into a numerical procedure (e.g. finite element method). If numerical differentiation was performed on the discrete experimental G_{II} - δ_{II}^* data sets, we would result in a bridging law characterized by discontinuities and lack of smoothness and hence not directly implemented in a numerical procedure. Figure 4.17 presents the respective G_{II}–δ_{II}^* data sets, together with their corresponding fitting functions.

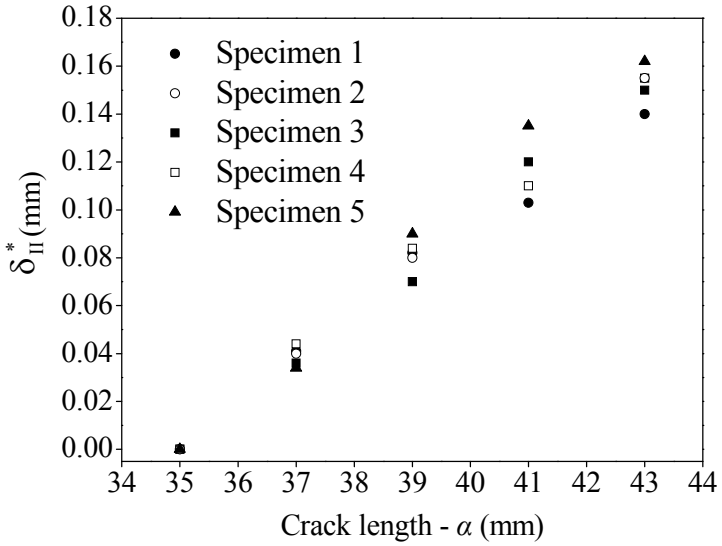

Figure 4.16: Sliding displacement at the pre-crack tip in terms of the crack length.

Several efforts have been made towards finding the best fitting functions, corresponding to a value of the coefficient of determination, R^2, as close to unity as possible. For this reason, two candidate analytical functions were utilized for fitting the data sets, i.e. a second order polynomial with the following analytical expression:

$$G_{II}(\delta_{II}^{*}) = C_1 \delta_{II}^{*2} + C_2 \delta_{II}^{*} + C_3 \tag{4.22}$$

and a power law with the following analytical expression:

$$G_{II}(\delta_{II}^{*}) = C_1 \left(\delta_{II}^{*} + C_2\right)^{C_3} \tag{4.23}$$

The $G_{II} - \delta_{II}^{*}$ data set produced using CCM exhibits significant variations. Nevertheless, results from each test exhibit the same behaviour in terms of their corresponding change in slope, as depicted in Figure 4.17a. A second order polynomial (parabola) fitting function was utilized for the regression of the $G_{II} - \delta_{II}^{*}$ data set reduced with CCM, which yields a value of R^2 equal to 0.87, since the other candidate function (power law) did not adequately describe the increasing behaviour of the G_{II} values (see Table 4.8). It should be pointed out that the parabola function captures in a very satisfactory manner the behaviour of the data sets up to a δ_{II}^{*} value of 0.14 mm. Beyond that point the function begins to decay. This unphysical behaviour was not considered for further calculations and thus the part of the $G_{II} - \delta_{II}^{*}$ parabola fitting curve for values of δ_{II}^{*} higher than 0.14 mm was omitted, as shown in Figure 4.17a.

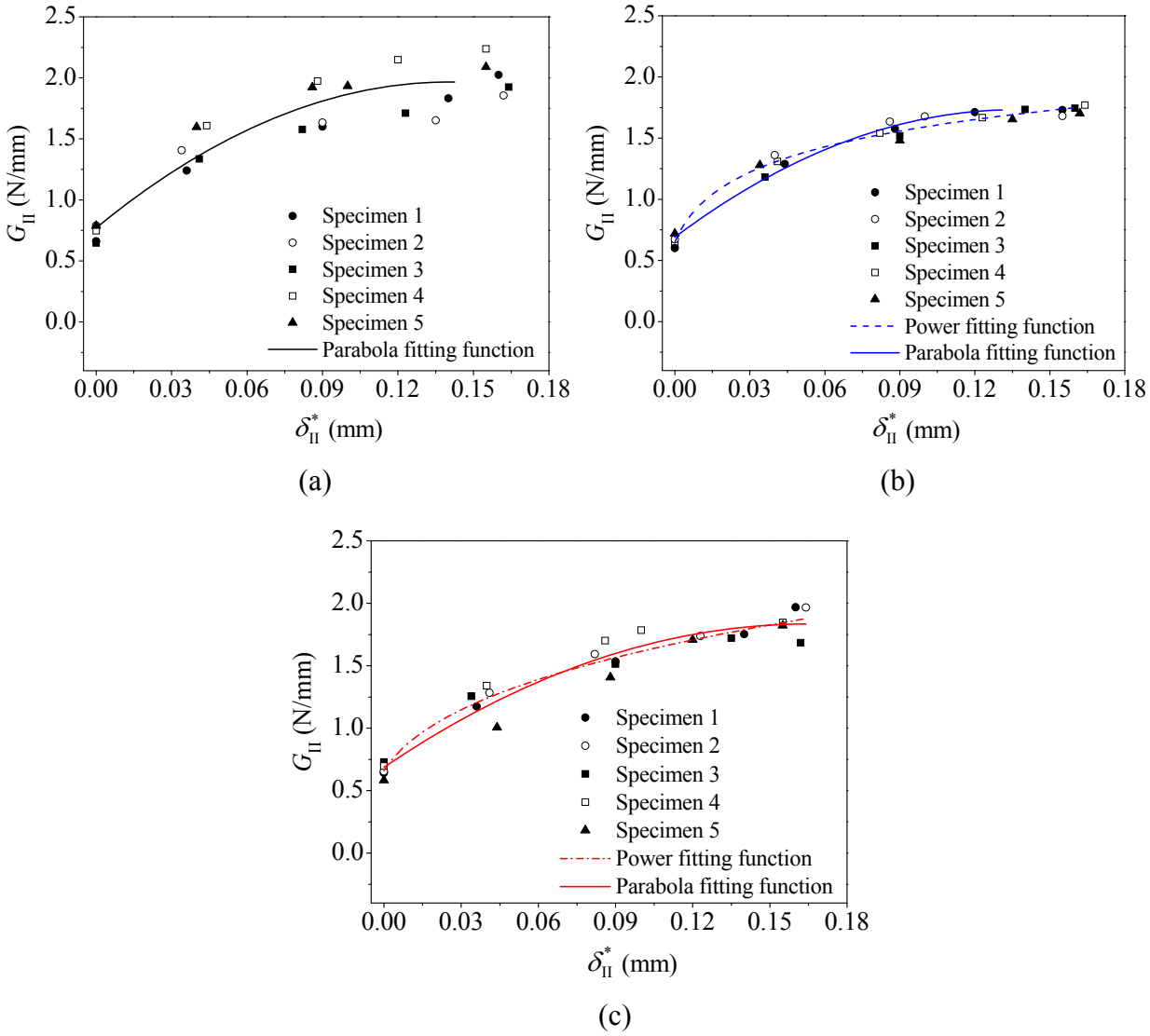

Figure 4.17: G_{II} - δ_{II}^* data sets calculated with the CCM (a), CBT (b) and CBBM (c) data reduction scheme.

In contrast to the above case, $G_{II}-\delta_{II}^*$ data sets reduced with CBT and CBBM have a very lower dispersion, as shown in Figure 4.17b and Figure 4.17c, respectively. The results obtained with CBT exhibit a low increase rate of the fracture toughness, without clearly reaching a steady state value. This behaviour is well described with the use of a power law and a second order polynomial (parabola), as shown in Figure 4.17b. The corresponding values of the coefficients are listed in Table 4.8. Additionally, the R^2 coefficients for the CBT data set regression are 0.89 and 0.82 for the power law and the parabola fittings, respectively. For the same reasons as in the case of Figure 4.17a, the part of the $G_{II}-\delta_{II}^*$ parabola fitting curve for values of δ_{II}^* higher than 0.13 mm was omitted.

In the case of the CBBM results, steady state fracture toughness was reached near the final experimentally measured values of G_{II} and δ_{II}^*. Thus, again a power law ($R^2 = 0.87$) and a

parabola function ($R^2 = 0.94$) were utilized for fitting the corresponding CBBM $G_{II} - \delta_{II}^*$ dataset, as presented in Figure 4.17c. The corresponding values of the coefficients are listed in Table 4.8.

With the $G_{II} - \delta_{II}^*$ functions known for the three cases considered in this study, the bridging laws $\sigma_{II} - \delta_{II}^*$ can be then obtained from Equation (4.20b). The differentiation with respect to δ_{II}^* of the second order polynomial fitting functions leads to linear bridging laws and of the power fitting functions to non-linear bridging laws. Figure 4.18 compares all bridging laws inferred by CCM, CBT and CBBM data reduction schemes. For reasons of clarity the linear bridging laws are plotted together in Figure 4.18a whereas the non-linear bridging laws (power laws) are compared in Figure 4.18b. At crack initiation the shear traction attains a peak, followed by a decay to zero, which depends on the specific $G_{II} - \delta_{II}^*$ function adopted for each case. Finally, after a certain value of δ_{II}^*, namely $\delta_{c,II}^*$, shear traction becomes zero denoting the completion of the FPZ under further crack growth. The mean value of $\delta_{c,II}^*$ for all cases can be seen in Table 4.8.

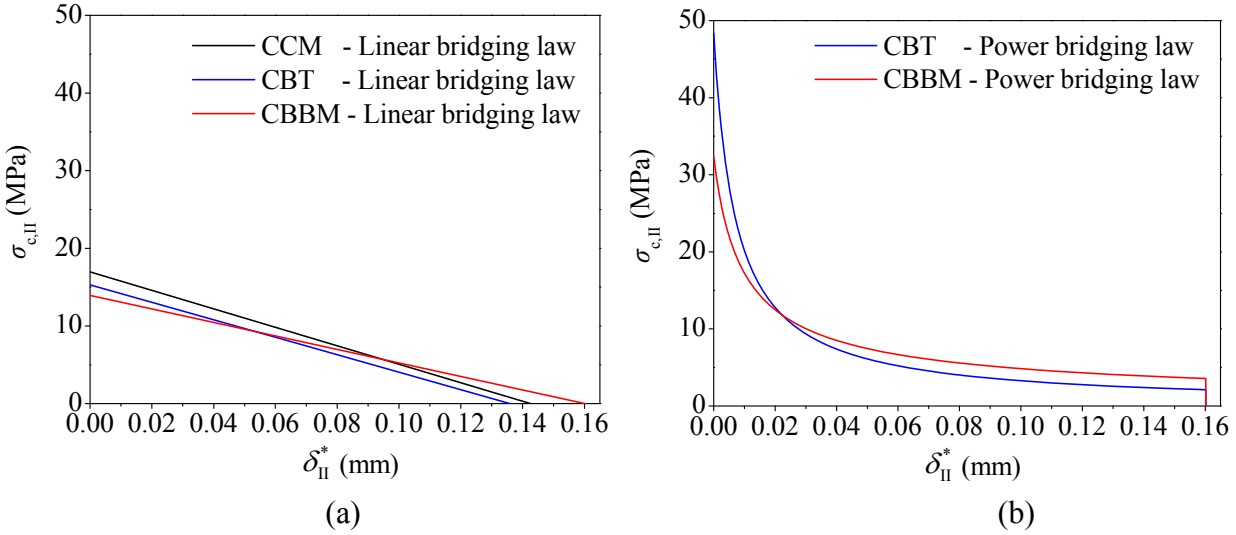

Figure 4.18: Linear (a) and power (b) experimental bridging law as derived from the J-integral approach.

Table 4.8 compares the values of the area integrals ($I_{exp,II}$) calculated from each bridging law, with the mean values of the $G_{II,b}$ magnitude (from Equation (4.27)) for the three data reduction schemes. The area integrals are in very good agreement with the corresponding $G_{II,b}$ values for the three cases (CCM, CBT and CBBM), denoting the validity of the fitting functions used to describe the data sets produced from each different case.

The area under each $\sigma_{II} - \delta_{II}^*$ curve, $I_{exp,II}$, is a characteristic property of the obtained bridging law which expresses the energy uptake at the completion of the bridging zone and in a theoretical basis its value must agree with the fibre bridging fracture toughness increase, $G_{II,b}$. The $G_{II,b}$ magnitude is calculated explicitly by $G_{II,SS} = G_{II,0} + G_{II,b}$.

Table 4.8: Parameters of the proposed traction-separation law.

	Bridging Law	C_1	C_2	C_3	$I_{exp,II}$ (N/mm)	$G_{II,b}$ (N/mm)	$G_{II,0}$ (N/mm)
CCM	Linear	-60.14	16.97	0.77	1.21	1.3	0.73
CBT	Power	2.65	0.00015	0.224	1.10	1.07	0.65
	Linear	-56.2	15.3	0.69	1.04		
CBBM	Power	3.30	0.0065	0.32	1.20	1.19	0.66
	Linear	-42.4	13.9	0.667	1.15		

The calculated softening behaviour of the bridging laws is based on the functions used to fit the $G_{II}-\delta_{II}^{*}$ data sets. The bridging stress at the initiation of the crack propagation (critical bridging stress, $\sigma_{c,II}$) calculated with the CCM, CBT and CBBM methods are given in Table 4.9 together with the critical Mode II sliding of each law, respectively.

Table 4.9: Parameters of the experimentally obtained Mode II bridging laws.

	Bridging Law	$\sigma_{c,II}$ (MPa)	$\delta_{c,II}^{*}$ (mm)
CCM	Linear	16.97	0.14
CBT	Power	48.40	0.16
	Linear	15.30	0.14
CBBM	Power	32.40	0.16
	Linear	13.90	0.16

4.6 Fracture Process Zone (FPZ) characterization

Loading and fracture of DCB and ENF composite specimens lead to the Mode I and II delamination growth, respectively. During this process a Fracture Process Zone (FPZ) is formed in the plane were delamination propagates, which consists of a fibre bridging zone and a cohesive zone, as schematically presented in Figure 4.19. The latter includes local plasticity of the matrix material together with the creation of microcracks. The fibre bridging zone is quantified by a bridging law, whereas the cohesive zone is quantified by a cohesive model. The cohesive zone is geometrically located ahead of the physical crack tip, whereas the bridging zone is formed behind the crack tip (Sorensen et al. 2008). In the previous sections, the experimental bridging laws have been obtained in pure Mode I and II delamination growth. The corresponding experimental cohesive laws cannot be calculated, since the obtained $G_I-\delta_I^{*}$ and $G_{II}-\delta_{II}^{*}$ data sets presented in Figure 4.10 and Figure 4.17, respectively, provide information only for the bridging zone (lack of data below $G_{I,0}$ and $G_{II,0}$). The only available information for the cohesive zone is

the initial fracture toughness $G_{I,0}$ and $G_{II,0}$, which from a physical point of view quantify the energy needed for the formation of the cohesive zone. However, during the application of the *J*-integral to the analytical fitting functions of Figure 4.10 and Figure 4.17, the $G_{I,0}$ and $G_{II,0}$ magnitudes vanish, since these are constant terms (see section 4.4). The constitutive response of either bridging or cohesive zone is described by a Traction – Separation model (T-S) σ_i - δ_i (i = I or II for Mode I or II, respectively).

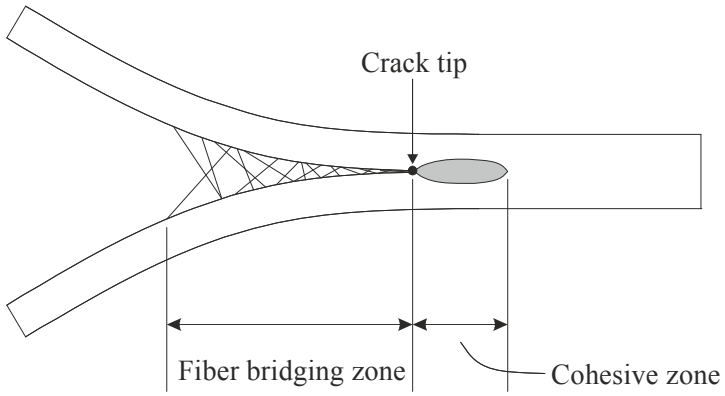

Figure 4.19: Formation of the Fracture Process Zone during delamination growth.

The following two sections aim at proposing a procedure on how the experimental bridging laws can be effectively implemented into numerical simulations. Regardless of the data reduction scheme utilized for the derivation of the bridging laws (CBT, ECM and MCC for the DCB tests and CCM, CBT and CBBM for the ENF tests), these laws are subjected to specific amendments and enhancements, in order to describe the FPZ resulting from the subsequent formation of the bridging and cohesive zone. Thus, a new T-S model is proposed that yields very promising results in the numerical prediction of the Mode I and Mode II delamination propagation, as it will be shown in the following sections. For reasons of comparison, in both test cases (DCB and ENF) a T-S model has been developed that does not include the cohesive zone, i.e. $G_{I,0}$ or $G_{II,0}$. In addition, a T-S model available in the literature is included, which will be used latter for the DCB simulations only.

4.6.1 Mode I fiber bridging and cohesive models

The derived bridging laws shown in Figure 4.11b must be subjected to several modifications in order to be treated as Traction-Separation (T-S) laws.

The first approach aims at utilizing the bridging laws shown in Figure 4.11b without taking into account the initial fracture toughness $G_{I,0}$. The corresponding T-S law type is presented in Figure 4.20a. The right hand side decreasing part of this curve is exactly the experimental bridging laws, as obtained from the *J*-integral approach. The curve includes also the incorporation of an initial linear response until the point with co-ordinates $\sigma_{c,I}$ - $\delta_{0,I}$. This amendment is necessary in order to overcome the stress singularity point at $\delta_1^* = 0$ (see Figure

4.11b). Hence, an initial linear stiffness K_I is introduced and its magnitude is chosen to be very high (10^5 MPa/ mm) in order to allow the stresses to be transferred through the mid-plane interface invariantly and without leading to numerical instabilities of the non-linear solution. The first linear part of the traction-separation law of Figure 4.20a is given by the following expression:

$$\sigma_I\left(\delta_I\right) = K_I\delta_I \qquad \text{for} \qquad 0 \le \delta_I \le \delta_{I,0} \tag{4.24}$$

The preceding equation is utilized to describe loading prior to the initiation of the stress-release softening function, which occurs at $\sigma_{c,I}$. From that point and forward the experimental bridging law is utilized. By differentiating Equation (4.21) according to Equation (4.20a), the $\sigma_I = f(\delta_I)$ relation is given by:

$$\sigma_I\left(\delta_I\right) = C_1/C_2 \exp\left(\frac{\delta_I}{C_2}\right) \qquad \text{for} \qquad \delta_{I,0} < \delta_I \le \delta_{I,c} \tag{4.25}$$

The total area under the traction-separation law ($0 \le \delta_I \le \delta_{I,c}$) of Figure 4.20a equals to I_{exp}, which in turn equals to the fiber bridging increase fracture toughness $G_{I,b}$ as previously described (see Table 4.3) and is given by the following equation:

$$G_{I,b} = \frac{1}{2}\sigma_{c,I}\delta_{I,0} + C_1\left[\exp\left(\delta_{I,c}/C_2\right) - \exp\left(\delta_{I,0}/C_2\right)\right] \tag{4.26}$$

Having defined the initial linear stiffness K_I, the $\delta_{0,I}$ magnitude can be easily obtained from Equation (4.24). For this type of traction-separation law, $\delta_{c,I}$ is equal to the experimentally evaluated $\delta^*_{c,I}$, since $\delta_{0,I}$ is relatively very small when compared to $\delta_{c,I}$. Thus the contribution of the first term of the right hand side of Equation (4.26) is negligible and the $G_{I,b}$ magnitude equals to I_{exp}.

In the current interface formulation, it is assumed that normal compressive stresses do not induce damage, but their existence indicates contact conditions, which must be taken under consideration. For this purpose, when normal stresses σ_I are compressive and hence the δ_I magnitude is negative denoting contact between the adjacent surfaces of the interface, a penalty contact algorithm is used to describe the traction-separation relationship:

$$\sigma_I\left(\delta_I\right) = K_p\delta_I \qquad \text{for} \qquad \delta_I < 0 \tag{4.27}$$

where K_p is the penalty stiffness, chosen to be equal to 10^5 MPa/mm.

The initial fracture toughness $G_{I,0}$ must be taken into account into the traction-separation laws, since a constant term is assumed, which vanishes during the differentiation of Equation

(4.18a) to derive Equation (4.20a). This modification is necessary in order to attain the total energy uptake ($G_{I,SS}$) accumulated during crack initiation and the formation of the FPZ. In fact, the $G_{I,0}$ magnitude corresponds to the energy uptake for crack initiation.

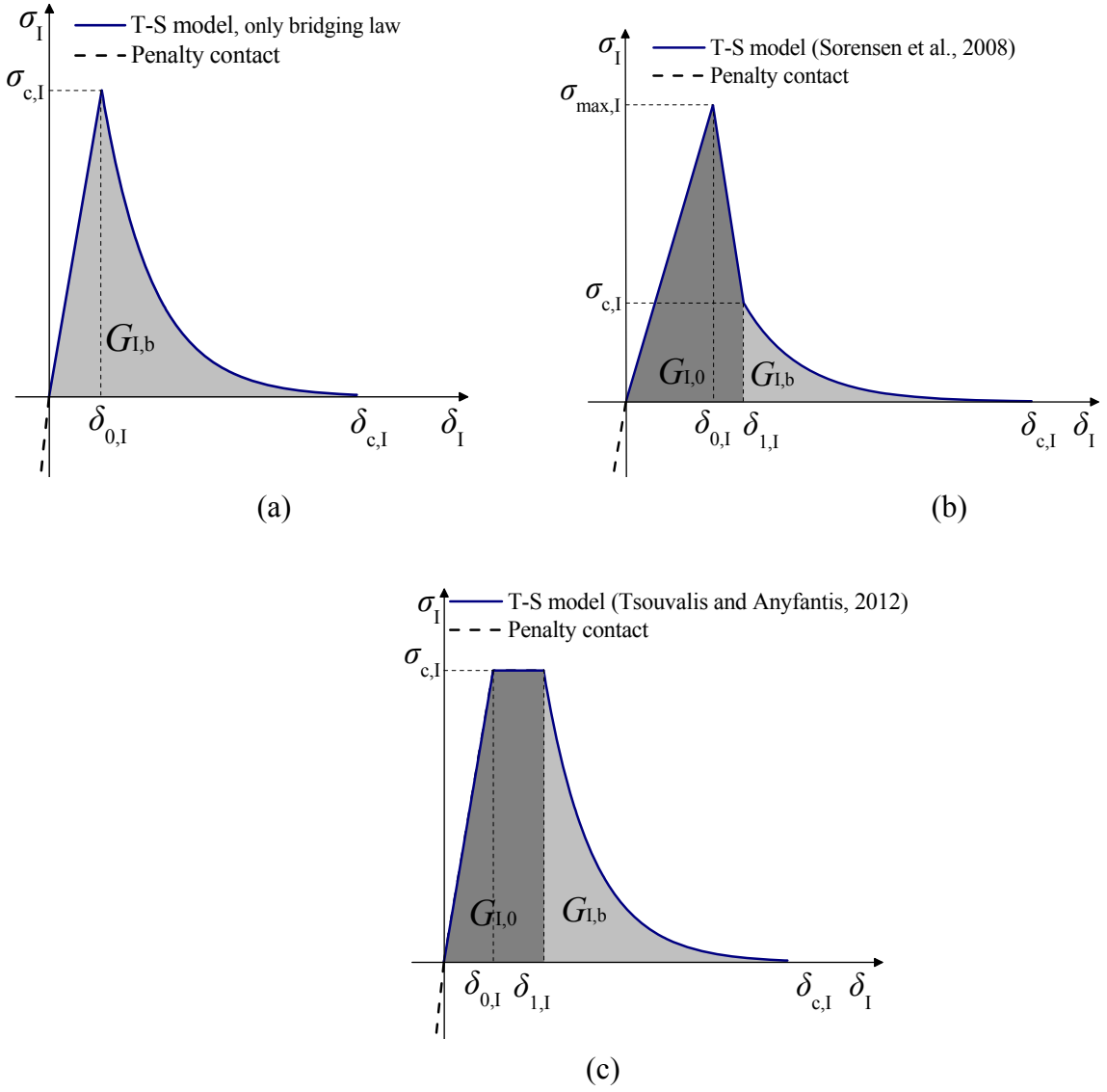

Figure 4.20: Traction-Separation (T-S) model without $G_{I,0}$ (a), three-parameters T-S model of the Fracture Process Zone (cohesive and bridging zone (with $G_{II,0}$),Sorensen et al. (2007) (b) and proposed T-S model of the Fracture Process Zone (cohesive and bridging zone (with $G_{II,0}$), Tsouvalis and Anyfantis (2012) (c).

A promising traction-separation law, namely the three-parameters model, that incorporates $G_{I,0}$ into the experimentally evaluated bridging laws, was initially proposed by Tamuzs et al. (2001) and recently utilized in a modified version, as presented in Figure 4.20b, and described by Sorensen et al. (2008). According to Sorensen et al. (2008) and Figure 4.20b, there are two key stress magnitudes, namely $\sigma_{c,I}$ and $\sigma_{max,I}$. The $\sigma_{c,I}$ magnitude, as previously, corresponds to the critical bridging stress experimentally obtained. On the other hand, magnitude

$\sigma_{max,I}$ is chosen to be equal to 40% of the matrix material strength (S_u). For the epoxy resin used herein as the matrix material, S_u equals to 44.7MPa (Dow Chemical Company, 2012). In this model, the initial slope K_I equals to the through-thickness Young modulus (E_3) divided by the constitutive interface element thickness, which in our case equals to one. Having defined K_I and $\sigma_{max,I}$ magnitudes, the equation describing the first linear part of the three-parameters model is given by Equation (4.24). Thus, one can easily obtain from this equation the separation parameter $\delta_{0,I}$, which is equal to 0.0081 mm for all cases.

The $\delta_{1,I}$ magnitude is determined directly from the expression used to calculate the area under the traction-separation curve until that point, which equals to the experimentally determined value of $G_{I,0}$ (denoted as the dark grey area in Figure 4.20b), Sorensen et al. (2008). Thus, the corresponding calculated values of $\delta_{1,I}$ for the traction-separation laws calculated from the CBT, ECM and MCC methods are 0.0626, 0.0527 and 0.0617 mm respectively.

The remaining part of the curve from $\delta_{1,I}$ to $\delta_{c,I}$ is based again on the experimentally obtained bridging laws as described by Equation (4.25). Hence, magnitude $\delta_{c,I}$ is calculated by summing the determined $\delta_{1,I}$ values with the experimentally evaluated $\delta_{c,I}^{*}$ values for each case.

In most cases, $\sigma_{max,I}$ is much higher than $\sigma_{c,I}$. This fact leads to numerical instabilities and convergence of the non-linear solution is difficult to be achieved unless the chosen time step is extremely small and artificial damping is utilized in the element formulation. Thus, in general, the three-parameters model depicted in Figure 4.20b is based on $G_{I,0}$ and not on the exact value of $\sigma_{max,I}$, Sorensen et al. (2008).

An effective traction-separation law is proposed in this work (Tsouvalis and Anyfantis, 2012), that addresses the issue of embedding $G_{I,0}$ to the experimentally evaluated bridging law, as depicted in Figure 4.20c. The main advantage of this procedure is that no extra parameters need to be assumed or/and adjusted for achieving numerical convergence. The initial linear part is described by Equation (4.24) and the same values of K_I and $\delta_{0,I}$ are utilized, as given for the traction-separation law of Figure 4.20a.

Regarding the next part of the curve, the critical stress is maintained constant until $\delta_{1,I}$ is reached and is described by:

$$\sigma_I(\delta_I) = \sigma_{c,I} \qquad \text{for} \qquad \delta_{0,I} < \delta_I \le \delta_{1,I} \tag{4.28}$$

The area under the curve shown in Figure 4.20c between $\delta_I = 0$ and $\delta_I = \delta_{1,I}$ expresses the $G_{I,0}$ magnitude, which is given by the following expression:

$$G_{I,0} = \frac{1}{2}\sigma_{c,I}\delta_{I,0} + \sigma_{c,I}\left(\delta_{I,1} - \delta_{I,0}\right) \tag{4.29}$$

Having $G_{I,0}$ and $\delta_{0,I}$ magnitudes known, $\delta_{1,I}$ can be easily calculated from Equation (4.32). After the completion of the crack initiation process at $\delta_{1,I}$, the normal stresses σ_I are being

released according to the exponential softening behaviour given by the experimentally evaluated bridging laws. Thus, with any further increase in the separation δ_I beyond the value of $\delta_{1,I}$ the stresses are described by the following relation:

$$\sigma_I(\delta_I) = \sigma_{c,I} \exp\left(-(\delta_I - \delta_{1,I})\sigma_{c,I} / G_{I,0}\right) \qquad \text{for} \qquad \delta_{1,I} < \delta_I \le \delta_{c,I} \tag{4.30}$$

where

$$\delta_{c,I} = \delta_{1,I} + \delta^*_{c,I} \tag{4.31}$$

Beyond $\delta_{c,I}$ the bridging fibers lose their load carrying capacity and fail. Thus the stresses are totally released:

$$\sigma_I(\delta_I) = 0 \qquad \text{for} \qquad \delta_I > \delta_{c,I} \tag{4.32}$$

Having incorporated the $G_{I,0}$ magnitude into the proposed traction-separation law, the total energy uptake at the completion of the FPZ is the desired ERR magnitude that equals to the steady-state fracture toughness $G_{I,SS}$ and is defined by the total area under the curve σ_I - δ_I of Figure 4.20c, which is given by:

$$G_{I,SS} = G_{I,0} + G_{I,b} \tag{4.33}$$

$$G_{I,SS} = \tfrac{1}{2}\sigma_{c,I}\delta_{0,I} + \sigma_{c,I}\left(\delta_{1,I} - \delta_{0,I}\right) + G_{I,0}\left[\exp\left(-\delta_{1,I}\sigma_{c,I} / G_{I,0}\right) - \exp\left(-\delta_{c,I}\sigma_{c,I} / G_{I,0}\right)\right] \tag{4.34}$$

The parameters of the proposed traction-separation laws utilized for the simulation of the present DCB tests are listed in Table 4.10.

Table 4.10: Parameters used for the DCB simulation with the proposed traction-separation law.

	$\sigma_{c,I}$ (MPa)	$\delta_{0,I}$ (mm)	$\delta_{1,I}$ (mm)	$\delta_{c,I}$ (mm)
CBT	0.66	10^{-5}	0.88	6.85
ECM	1.47	10^{-5}	0.35	3.33
MCC	0.6	10^{-5}	0.96	7.30

4.6.2 Mode II fiber bridging and cohesive models

As in the previous section, an initial stiffness K_{II} is introduced to describe the σ_{II} (δ_{II}) relation, in order to overcome the theoretical stress singularity point at $\delta_{II}^{*} = 0$ (see Figure 4.18), as:

$$\sigma_{II}\left(\delta_{II}\right) = K_{II}\delta_{II} \qquad \text{for} \qquad 0 \le \delta_{II} \le \delta_{0,II} \tag{4.35}$$

The slope K_{II} of the preceded equation is chosen to be high enough so as to allow the stresses to transfer through the mid-plane interface invariantly. Thus, the optimum interface stiffness is the highest value that does not lead to numerical instabilities (de Moura et al. 2008). Maintaining the critical bridging stress value $\sigma_{c,II}$ calculated by Equation (4.20b) unchangeable, a very small value of $\delta_{0,II}$ is generated. The initial fracture toughness $G_{II,0}$ must be embedded to the traction-separation laws, since it disappears during the differentiation of Equation (4.18b) to derive Equation (4.20b).

The first traction-separation model aimed at utilizing the experimentally obtained bridging laws without embedding the initial fracture toughness $G_{II,0}$ (as in Figure 4.20a), for reasons of comparison. Thus, only the fibre bridging zone is modelled. The corresponding T-S model is presented in Figure 4.21. Equation (4.35) is utilized to describe loading prior to the initiation of the stress-release softening function, which occurs at $\sigma_{c,I}$. From that point and forward the experimental bridging law is utilized. By differentiating Equation (4.22) and Equation (4.23) according to Equation (4.20b), the $\sigma_{II} = f\ (\delta_{II})$ relation of the linear bridging laws (parabola regression of the $G_{II} - \delta_{II}^{*}$ data sets) is given by:

$$\sigma_{II}(\delta_{II}) = 2C_1\,\delta_{II} + C_2 \qquad \text{for} \qquad \delta_{0,II} < \delta_{II} \le \delta_{c,II} \tag{4.36}$$

and the $\sigma_{II} = f\ (\delta_{II})$ relation of the power bridging laws (power regression of the $G_{II} - \delta_{II}^{*}$ data sets) is given by:

$$\sigma_{II}(\delta_{II}) = C_1 C_3 (\delta_{II} + C_2)^{C_3 - 1} \qquad \text{for} \qquad \delta_{0,II} < \delta_{II} \le \delta_{c,II} \tag{4.37}$$

The total area under the curve shown in Figure 4.21a and Figure 4.21b equals to the fibre bridging fracture toughness increase $G_{II,b}$. The corresponding analytic formula of the $G_{II,b}$ magnitude for the T-S model of Figure 4.21a is,

$$G_{II,b} = \frac{1}{2}\sigma_{c,II}\delta_{c,II} \tag{4.38}$$

whereas the analytic formula of the $G_{II,b}$ magnitude for the T-S model of Figure 4.21b is

$$G_{\mathrm{II,b}} = \frac{1}{2}\sigma_{\mathrm{c,II}}\delta_{0,\mathrm{II}} + C_1\left[(C_2 - \delta_{\mathrm{c,II}})^{C_3} - (C_2 - \delta_{0,\mathrm{II}})^{C_3}\right] \tag{4.39}$$

Since $\delta_{0,\mathrm{II}}$ is several orders of magnitude smaller than $\delta^*_{\mathrm{c,II}}$, the magnitude of $\delta_{\mathrm{c,II}}$ remains equal to $\delta^*_{\mathrm{c,II}}$ for all obtained bridging laws.

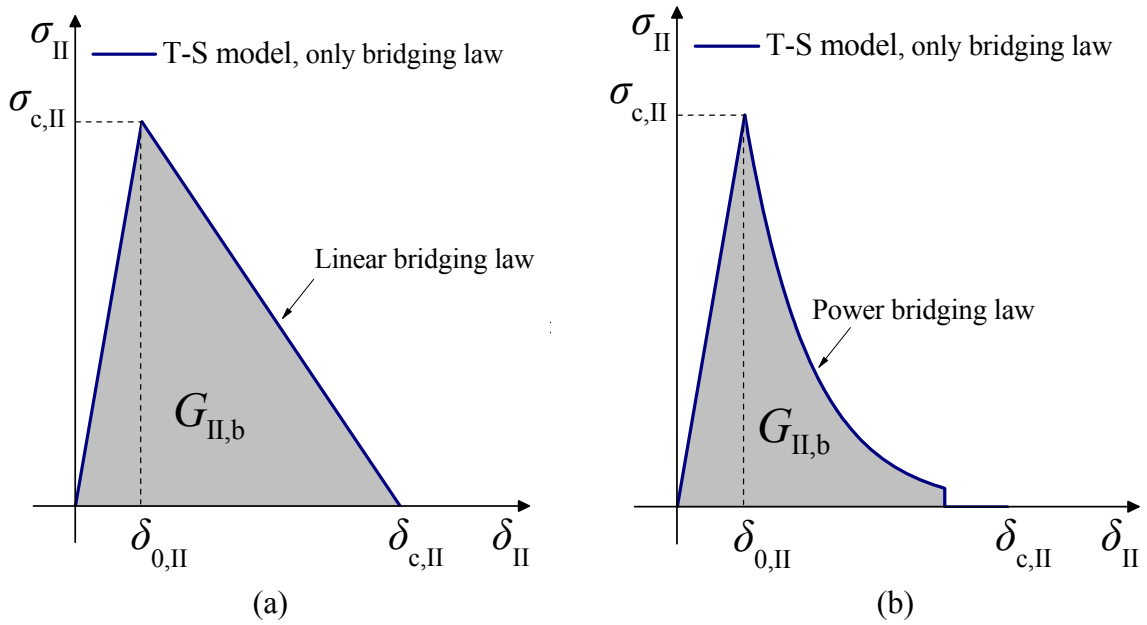

Figure 4.21: Linear (a) and power (b) Traction-Separation (T-S) model of the bridging zone (without $G_{\mathrm{II,0}}$).

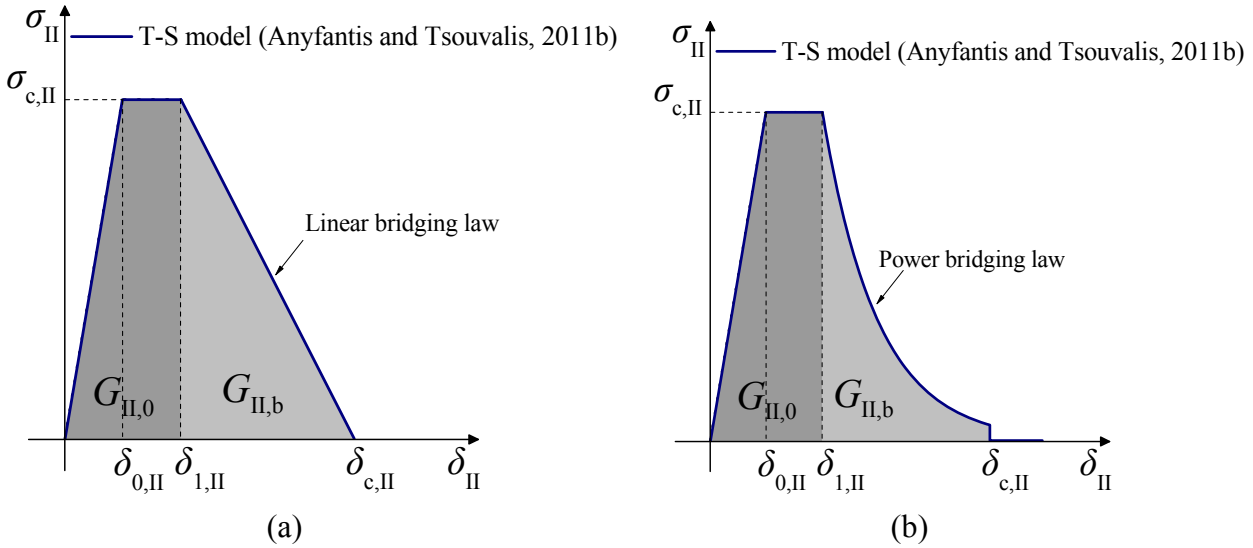

Figure 4.22: Linear (a) and power (b) proposed Traction-Separation (T-S) model of the Fracture Process Zone (cohesive and bridging zone (with $G_{\mathrm{II,0}}$), (Anyfantis and Tsouvalis, 2011b).

A new effective traction-separation model is proposed and presented in Figure 4.22, which involves both bridging and cohesive zone, i.e. Fracture Process Zone (FPZ). This model is actually is the same one proposed for addressing the FPZ in Mode I (see Figure 4.20c) and

addresses the issue of embedding $G_{II,0}$ to the experimentally evaluated bridging law and hence incorporating the cohesive zone into the traction-separation model. According to this model, the stresses that develop during the formation of the cohesive zone are assumed to remain constant. The main advantage of this procedure is that no extra parameters need to be assumed or/and adequately adjusted for achieving numerical convergence. The initial slope K_{II} and the relative displacement $\delta_{0,II}$ are calculated by the aforementioned procedure and the initial behaviour of σ_{II} (δ_{II}) relation is given by Equation (4.35). Afterwards, the critical stress is maintained constant until displacement $\delta_{1,II}$ is reached, as described by:

$$\sigma_{II}(\delta_{II}) = \sigma_{c,II} \quad \text{for} \quad \delta_{0,II} < \delta_{II} \le \delta_{1,II} \tag{4.40}$$

The areas under the curves of both plots shown in Figure 4.22 between $\delta_{II} = 0$ and $\delta_{II} = \delta_{1,II}$ express magnitude $G_{II,0}$ and are given by the following expressions

$$G_{II,0} = \frac{1}{2}\sigma_{c,II}\delta_{II,0} + \sigma_{c,II}\left(\delta_{II,1} - \delta_{II,0}\right) \tag{4.41}$$

Having $G_{II,0}$, $\sigma_{c,II}$ and $\delta_{0,II}$ magnitudes known, $\delta_{1,II}$ can be easily calculated from Equation (4.41). In fact the first term of the right hand side of Equation (4.41) is negligibly small compared to the remaining term and thus it does not practically contribute to the $G_{II,0}$ magnitude. After the completion of the cohesive zone at $\delta_{1,II}$, the shear tractions σ_{II} are being released according to the softening behaviour described by the experimentally evaluated bridging laws. Thus, with any further increase in the relative displacement beyond the value of $\delta_{1,II}$, the tractions are given by the experimentally obtained bridging laws. Therefore, Equation (4.36) and Equation (4.37) can be rewritten within the range of ($\delta_{1,II}$ - $\delta_{c,II}$), as following:

$$\sigma_{II}(\delta_{II}) = 2C_1\left(\delta_{II} - \delta_{1,II}\right)\delta_{II} + C_2 \quad \text{for} \quad \delta_{1,II} < \delta_{II} \le \delta_{c,II} \tag{4.42}$$

$$\sigma_{II}(\delta_{II}) = C_1C_3(\delta_{II} - \delta_{1,II} + C_2)^{C_3-1} \quad \text{for} \quad \delta_{II,0} < \delta_{II} \le \delta_{II,c} \tag{4.43}$$

The critical relative displacement is expressed by:

$$\delta_{c,II} = \delta_{1,II} + \delta^*_{c,II} \tag{4.44}$$

Beyond $\delta_{c,II}$, the bridging fibres lose their load carrying capacity and fail. Thus the closure tractions are totally released:

$$\sigma_{II}\left(\delta_{II}\right) = 0 \quad \text{for} \quad \delta_{II} > \delta_{c,II} \tag{4.45}$$

The total energy uptake at the completion of the FPZ is defined by the total area under the curve σ_{II} - δ_{II} . Thus, the calculated steady state fracture toughness $G_{II,SS}$ is given by Equation (4.38) and Equation (4.39) for the linear and power T-S model, respectively.

$$G_{II,SS} = G_{II,0} + G_{II,b} \tag{4.46}$$

$$G_{II,SS} = \frac{1}{2}\sigma_{c,II}(\delta_{c,II} + \delta_{0,II}) + \sigma_{c,II}\left(\delta_{1,II} - \delta_{0,II}\right) \tag{4.47}$$

$$G_{II,SS} = \frac{1}{2}\sigma_{c,II}\delta_{0,II} + \sigma_{c,II}\left(\delta_{1,II} - \delta_{0,II}\right) + C_1\left[(C_2 - \delta_{c,II})^{C_3} - (C_2 - \delta_{0,II})^{C_3}\right] \tag{4.48}$$

4.7 Numerical modeling of the experiments

4.7.1 Mesh, loading and boundary conditions

The finite element mesh of the tested DCB and ENF specimens is presented in Figure 4.23 and Figure 4.24, respectively, together with its corresponding loading and boundary conditions. The nodes located at the right edge of the DCB model were considered to have all their degrees of freedom constrained (see Figure 4.23). Two vertical prescribed displacement conditions with opposite sign have been applied at the corner nodes of the other edge of the DCB model, in order to simulate the experimental loading condition (see Figure 4.2). The pre-crack has been modeled by introducing pairs of nodes at the adjacent to the midline element edges, with no coupling or merging between them. In this way, each lever arm in the pre-crack area is independent to the other.

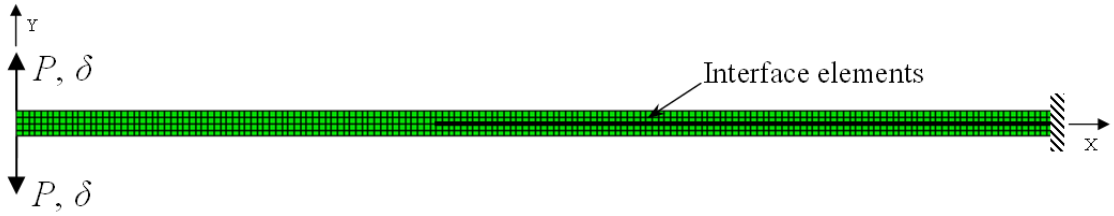

Figure 4.23: Finite element mesh of the tested DCB specimens.

The two supports and the load application device, utilized for the three-point bending of the ENF specimens, were modelled as semi-circles with rigid elements and had their real dimensions (diameter = 4 mm). Frictionless contact surfaces were considered between these three items and the corresponding areas of the specimen. The finite element mesh was refined at the regions of the supports and at the region where the crack would propagate (Figure 4.24b). The penalty contact algorithm has been applied for the simulation of the contact mechanics incorporated in the adjacent to the pre-crack region element faces (see Figure 4.24b). The magnitude of the friction coefficient in the pre-crack region was selected to be equal to zero,

since the global response finite element results of the ENF model do not exhibit significant sensitivity to the variation of this magnitude.

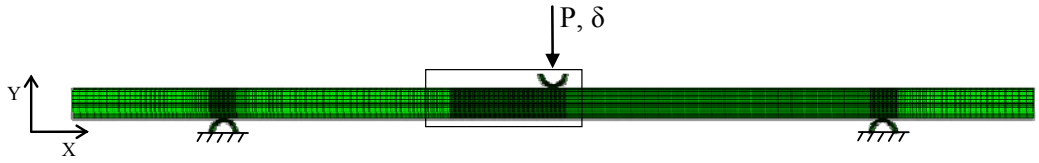

(a)

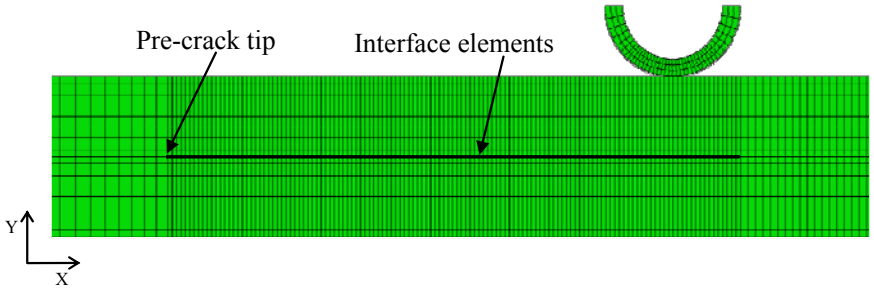

(b)

Figure 4.24: Finite element model of the tested ENF specimens (a) and magnified area presenting the crack propagation region of the ENF model (b).

The composite material has been modelled with CPS8 continuum 2D elements available in the element library of ABAQUS® 6.8. A more dense mesh has been utilized in the ENF model and particularly in the crack propagation area compared to the DCB model, as shown in Figure 4.24 and Figure 4.23, respectively. This is necessary since the crack faces come into contact as crack propagates during the three-point bending of the ENF model. These contact boundary conditions are highly non-linear and thus a dense mesh facilitates the convergence of the solution of the non-linear equations and boundary conditions that arise. The material properties of the composite system listed in Table 4.1 have been considered for the analyses. In order to account for geometrical and material nonlinearities, the Newton-Raphson method has been utilized together with a line search algorithm. A displacement controlled approach is utilized for aiding the convergence of the non-linear solution and avoiding numerical instability issues involved in crack growth analyses, where softening behaviour is apparent. In the mid-plane of the specimens and just after the pre-crack, user developed interface elements (see Appendix A2) have been embedded for modeling the delamination propagation process. The Mode I and Mode II Traction- Separation laws presented in section 4.6.1 and 4.6.2 are utilized as constitutive relations of the user developed interface elements.

Appendix A includes the formulation of the plane interface elements utilized in 3-dimensional analyses (Appendix A1), where volumetric elements are used, and additionally includes the formulation of the line interface elements utilized in 2-dimensional analyses (Appendix A2), where plane elements are used. In fact the 2D formulation of the line interface

elements is based on the 3D plane interface element formulation but is reduced to a 2-dimensional space.

For the creation of the finite element mesh (plane and interface elements), ANSYS® v.11 has been utilized and then the nodal coordinates and the element connectivity were accordingly transferred to ABAQUS® CAE modeling environment, where the properties, loading and boundary conditions were applied and the solution took place. This process is necessary, since the quadratic developed 2D and 3D interface elements (Appendix A) are not available at the ABAQUS® element library and thus cannot be embedded explicitly. This modeling procedure is followed for the creation of all models within this PhD thesis.

4.8 Numerical results

4.8.1 Finite element predictions of the DCB tests

A typical variation of the through-thickness stress σ_y over the domain of a DCB coupon, based on the finite element model of Figure 4.23 is presented in Figure 4.25. These stresses close to the interface in fact balance the implied σ_I tractions in the delamination growth plane, which result from the constitutive response of the interface elements according to the utilized T-S model and the corresponding data reduction scheme used for the calculation of the bridging law. The red-to-yellow contours represent the tensile stresses σ_y that signify the tendency of the two delamination faces to close, owing to the Fracture Process Zone (FPZ). The two components of the FPZ, that is the bridging and the cohesive zone depicted in Figure 4.25, have been fully developed and propagate in a stable manner during the delamination propagation in the DCB specimen. The blue-to-light green contours represent contact compressive stresses, as developed during crack propagation and modeled with the penalty method.

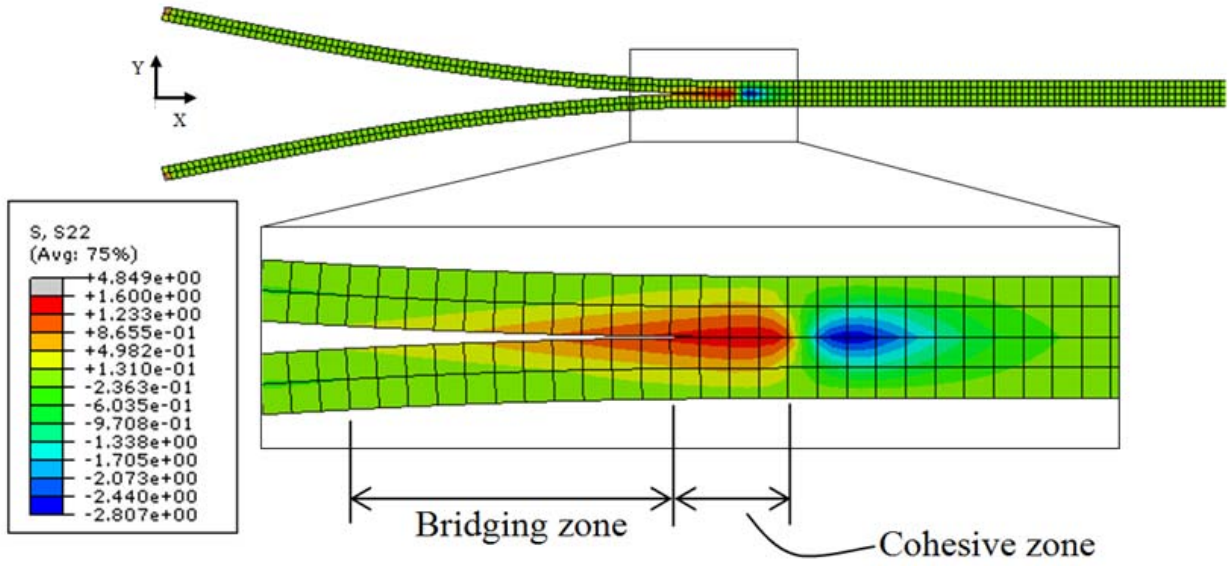

Figure 4.25: Typical σ_y stress distribution during crack propagation of a DCB test simulation.

As far as the DCB numerical predictions is concerned, the experimentally obtained bridging laws from the CBT, ECM and MCC methods were appropriately modified according to the two T-S models shown in Figure 4.20a and Figure 4.20b and the respective proposed model of Figure 4.20c. The numerical *P*-*δ* curves obtained from the three constitutive relations for each data reduction scheme are compared with the respective experimental curves in Figure 4.26. Experimental curves from all specimens are plotted in these figures, since the traction-separation laws utilized for the simulations constitute a material property describing the interface behaviour of the specific composite system.

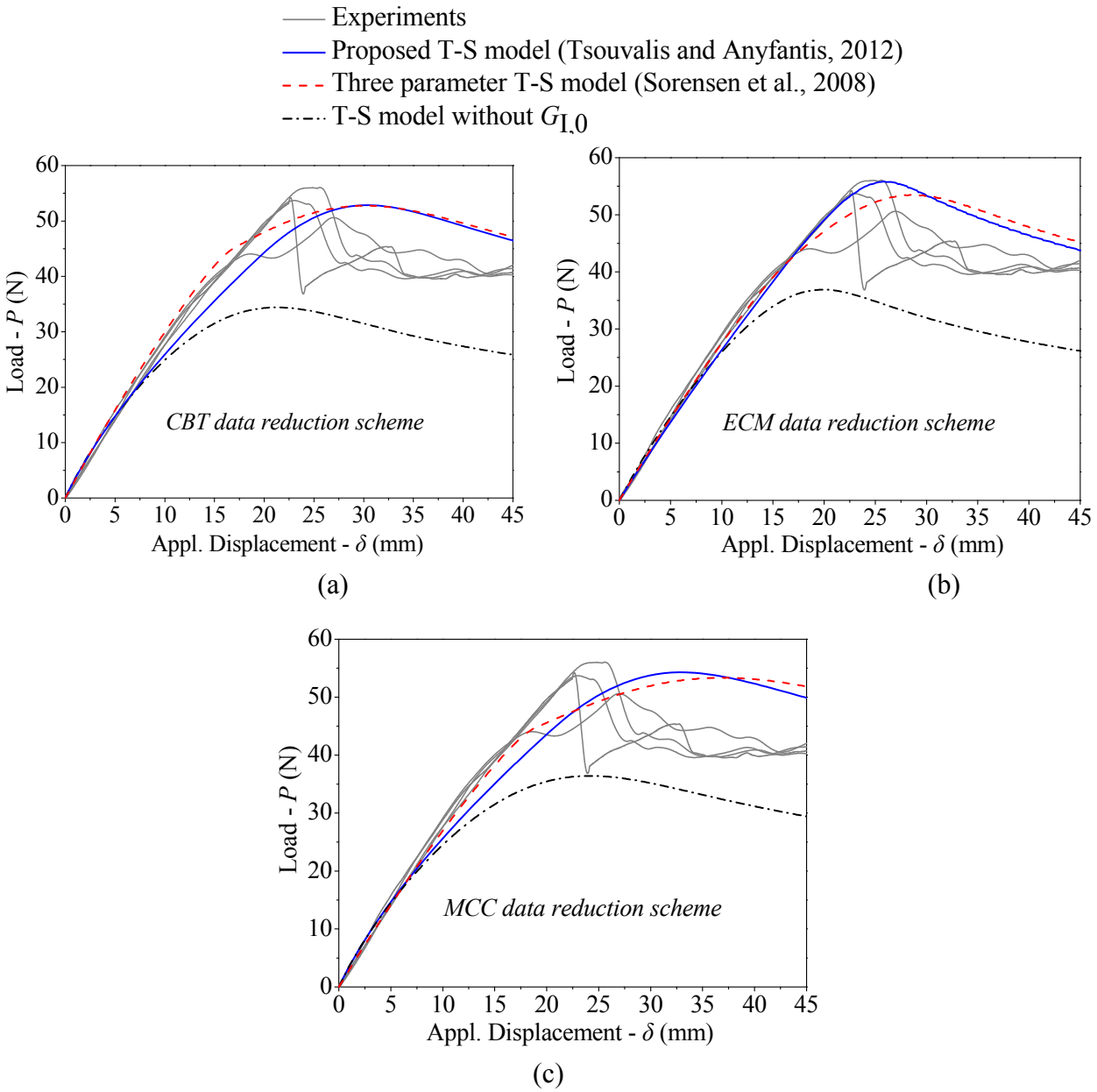

Figure 4.26: Numerical *P*-*δ* curves of the DCB simulations obtained from the three Traction-Separation (T-S) models for the CBT (a), ECM (b) and MCC(c) data reduction schemes.

All numerically calculated curves exhibit an initial linear response based on the bending stiffness of the DCB specimen lever arms. The point where the slope of all *P*-*δ* numerical curves

begins to diverge from linearity coincides with crack initiation and the following increasing nonlinearities describe delamination propagation. The comparison between the numerical and the experimental results will be made on the basis of the load at which divergence from linearity occurs, of the maximum load attained and of the applied displacement corresponding to this maximum load.

The T-S model which neglects the initial fracture toughness $G_{I,0}$ (Figure 4.20a), fails to adequately reproduce the experimental results for all three data reduction schemes. According to this model, crack initiates at the maximum bridging stress $\sigma_{c,I}$ and beyond this magnitude the delamination propagates. In terms of the P-δ plot, numerical results indicate that crack initiates at approximately 20 N for the CBT and MCC methods and at 26.5 N for the ECM method, instead of the experimentally measured value of approximately 35 N. These deviations between the numerically calculated values are reasonable, since $\sigma_{c,I}$ is equal to 0.66 and 0.6 MPa for the CBT and MCC methods and 1.47 MPa for the ECM method, as shown in Table 4.4. The maximum calculated load for this traction-separation law is equal to 34, 37 and 36.5 N for the CBT, ECM and MCC data reduction schemes, respectively, quite lower than the experimentally measured value of approximately 55 N. This law actually underestimates the required load for crack initiation and crack propagation, denoting the need for incorporating the $G_{I,0}$ magnitude into it. Regarding the displacement value corresponding to the maximum load, CBT and ECM schemes predict a significantly lower value, whereas MCC scheme predicts it with relative accuracy.

The three parameters T-S model which incorporates $G_{I,0}$ (Figure 4.20b), yields more accurate results from the previous modeling that neglects it. The delamination initiates between 35 and 40 N for all data reduction schemes, thus being close to the measured average load level at crack initiation, which is approximately equal to 35 N. The maximum numerical load is approximately equal to 53 N, compared also well to the experimental average value of 55 N. However, the numerical displacement values corresponding to this maximum load are far greater than the average experimental one, especially for the case of the MCC scheme.

The proposed T-S model, which also incorporates $G_{I,0}$, presents the more accurate prediction with respect to the maximum attained load. Moreover, in combination with the ECM data reduction scheme, exhibits also an almost perfect match with the experimental measurements up to the maximum load, predicting quite accurately the delamination initiation, the maximum load and the displacement corresponding to it. In combination with the other two reduction schemes, delamination initiation is not accurately predicted.

The softening behaviour beyond the maximum attained load that is predicted by the P-δ numerical curves is in all cases smooth, thus not being similar to the experimental measurements which indicate an initial abrupt load reduction, which is followed by a smoother softening. A possible reason for this difference may be that the composite lever arms start to locally fail after a certain load, a fact which has not been taken into account in the FE models. An additional reason may be the fact that the behaviour after the delamination initiation may not be sufficiently modeled by a single function, but separate functions are needed for modeling the behaviour

before and after the maximum load, as the change of the delamination growth rate in Figure 4.6 indicates.

4.8.2 Finite element predictions of the ENF tests

The deformed configuration of the ENF finite element model of Figure 4.24 is presented in Figure 4.27. The relative sliding between the upper and the lower half of the specimen denotes the crack propagation process. Figure 4.27 also presents a typical variation of the in-plane shear stress σ_{xy} over the domain of a ENF coupon. As in the DCB case, these stresses balance the implied σ_{II} tractions in the delamination growth plane, which result from the constitutive response of the interface elements according to the utilized T-S model and the corresponding data reduction scheme used for the calculation of the bridging law. The red-to-green contours represent the shear stresses σ_{xy} that signify the tendency of the two delamination faces to close, owing to the Fracture Process Zone (FPZ). The two components of the FPZ, that is the bridging and the cohesive zone depicted in Figure 4.27, have been fully developed and propagate in a stable manner during the delamination propagation of the ENF specimen.

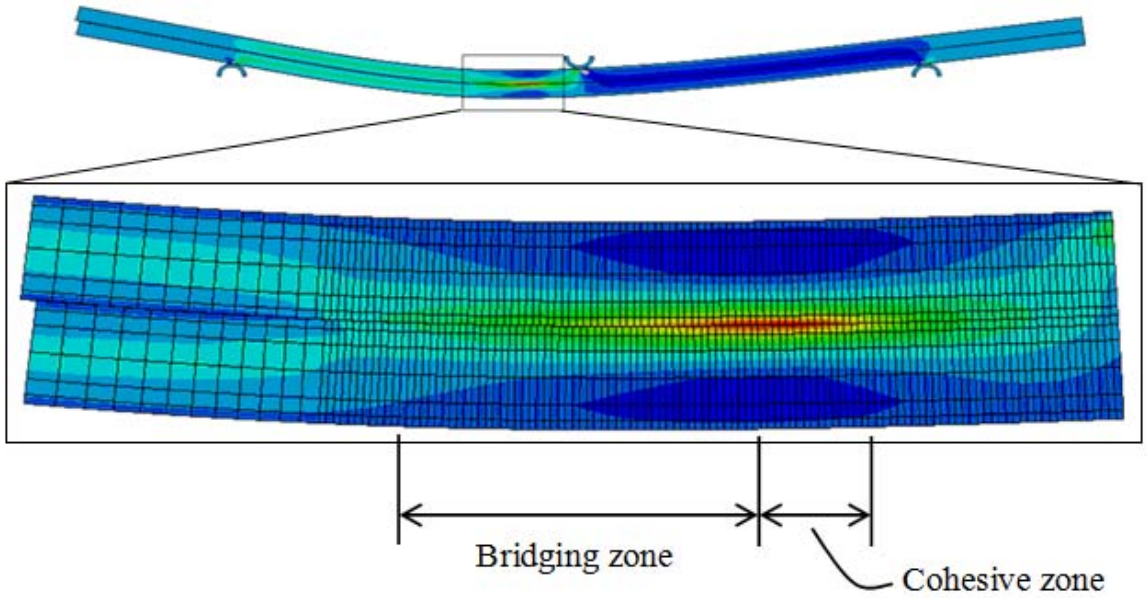

Figure 4.27: Typical shear stress σ_{xy} distribution during crack propagation of a ENF test simulation.

The experimentally obtained bridging laws from the CCM, CBT and CBBM methods were appropriately modified according to both the T-S model that does not account for the cohesive zone ($G_{II,0}$ magnitude, see Figure 4.21) and that taking into account the cohesive zone (see Figure 4.22), as described in the previous section. The numerical P–δ curves calculated using the available T-S models for each one of the three data reduction schemes are compared with the experimental curves in Figure 4.28.

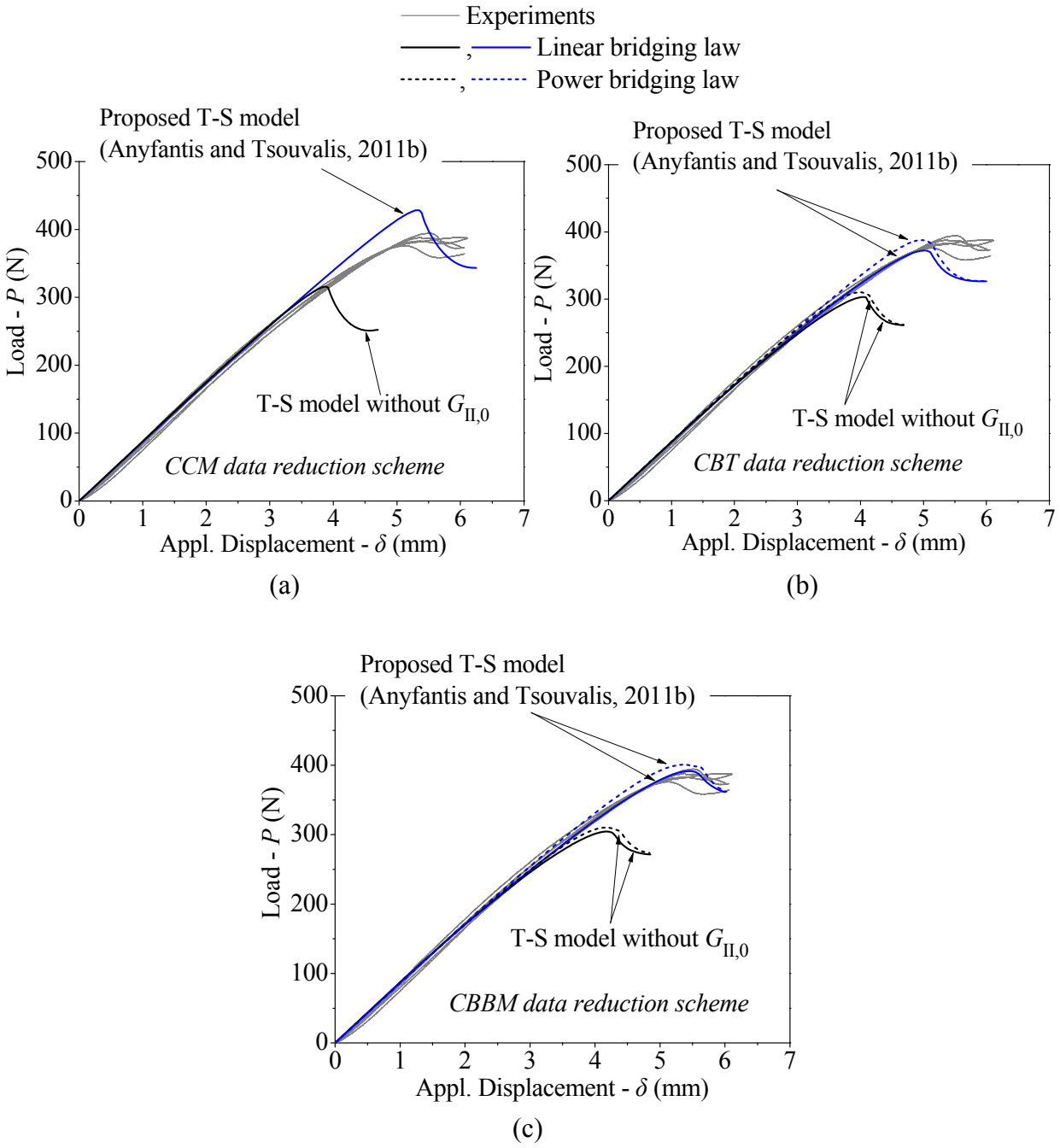

Figure 4.28: Numerical P-δ curves of the ENF simulations obtained from the three Traction-Separation (T-S) models for the CCM (a), CBT (b) and CBBM (c) data reduction schemes.

All numerical curves exhibit an initial linear response based on the bending stiffness of the ENF specimen, followed by increasing non-linearities, caused by the softening behaviour of the bridging laws. As it can be seen from Figure 4.28, the T-S model which neglects the initial fracture toughness $G_{II,0}$ and thus the existence of the cohesive zone provides only a qualitatively correct prediction of the response of the specimen for all bridging laws; however it fails to predict the experimental failure load and the corresponding bending displacement in all cases.

The results obtained when utilizing the proposed new T-S model of Figure 4.22 are very promising for the simulation of the ENF test. The numerical $P–\delta$ curves calculated with this model predict quite accurately the failure load for all bridging law schemes used, although there are small deviations in the corresponding bending displacement for the CCM and CBT data reduction schemes. The numerical results obtained with the linear and power traction separation laws for the CBT and CBBM methods, do not show important differences. However, the power laws seem to yield more stiff results when compared to the corresponding results from the utilization of the linear traction-separation laws, which fit better to the experimental measurements. The numerical $P–\delta$ curves produced when using the power and linear laws derived from the CBBM data reduction scheme exhibit the best agreement with the corresponding $P–\delta$ experimental curves.

Thus, the linear traction separation model predicts very accurately both the failure load and the corresponding bending displacement value, its numerical results coinciding almost perfectly with the experimentally measured response. This model, in contrast to the other one (power function) for the CBT and CBBM schemes, predicts accurately the non-linearities which start to appear at approximately 300 N, when the crack starts to propagate.

4.9 Conclusions

In this Chapter new constitutive relations of cohesive elements have been developed for simulating interlaminar fracture in fibrous composite laminates. Thus, in this study fracture tests of unidirectional glass fiber /epoxy Double Cantilever Beam (DCB) and End Notch Flexure (ENF) coupons have been conducted, in order to address the fiber bridging mechanisms that are involved in the well-known Fracture Process Zone under Mode I and Mode II delamination growth, respectively. Processing of the experimental measurements include construction of the R-curves (ERR versus crack length), reconstruction of these curves in terms of the pre-crack tip opening or sliding displacement and calculation of the corresponding bridging laws through the *J*-integral approach. For the calculation of the ERR in Mode I fracture, three different data reduction schemes have been utilized (Corrected Beam Theory - CBT, Experimental Compliance Method - ECM and Modified Compliance Calibration - MCC). For the calculation of the ERR in Mode II fracture, three corresponding data reduction schemes have been utilized (Compliance Calibration Method - CCM, Corrected Beam Theory - CBT and Compliance-Based Beam Method - CBBM). Thus, different bridging laws have been obtained according to the data reduction scheme utilized either in the DCB case or in the ENF case.

In order to investigate the effectiveness of the obtained bridging laws, the fracture tests were simulated with the finite element method. The experimentally evaluated bridging laws were converted into Traction-Separation models applicable to user defined interface/cohesive finite elements and simulation of the fracture tests has been carried out. A new to the literature Traction-Separation model is proposed that addresses both the developed cohesive and fiber bridging zone during Mode I or II delamination propagation and eliminates the need for any

estimation of the magnitudes and parameters which are necessary to fit the numerical results over the respective experimental ones.

The conclusions drawn are as follows:

- In a direction transverse to the delamination path (weft direction), fiber yarns seem to affect the ERR magnitude as crack propagates, as concluded from the force – applied displacement (P - δ) experimental measurements for the case of the DCB tests.
- The energy uptake defined by the area under the experimentally evaluated bridging laws (Mode I or II) equals to the fiber bridging fracture toughness and does not include the initial fracture toughness (quantification of the cohesive zone) calculated at crack initiation.
- The initial slope of either $G_{\mathrm{I}} - \delta_{\mathrm{I}}^{*}$ or $G_{\mathrm{II}} - \delta_{\mathrm{II}}^{*}$ curve influences the magnitude of the critical bridging stress obtained from the J-integral approach.
- In order to utilize the obtained bridging law as a material property of the interface to be modelled (e.g. as a constitutive relation of interface elements), the initial fracture toughness magnitude must be taken into account.
- In the case of the composite material system adopted herein and for Mode I delamination growth, the bridging law calculated from the ECM data reduction scheme and modified according to the proposed Traction - Separation model gives quite accurate results regarding the characterization of the Fracture Process Zone.
- For the ENF tests the proposed Traction-Separation model with the linear softening function as produced from the CBBM scheme is very promising in numerical simulations for Mode II fracture growth.
- The properties of the proposed Traction - Separation model are derived through a straightforward experimental procedure that involves fracture propagation tests (DCB or ENF tests for Mode I or II fracture, respectively).

The Traction - Separation model provides a simple and easy-to-program tool for the simulation of the delamination initiation and propagation process in fibrous composite materials. Additionally, in comparison with the existing models in Mode I, it is smoother, hence, convergence of the non-linear numerical solution is easier to be achieved.

5. Development of a novel constitutive model for ductile adhesive joints

5.1 Introduction

In the framework of the numerical analysis of adhesive joints with finite element methods, Cohesive Zone Modeling (CZM) techniques have been mostly utilized by many researchers and design engineers. Relative information is given in detail regarding the theoretical background and state-of-the-art in section 2.3. However, a brief description is provided in this section for aiding the reader to cope with CZM methodologies.

In CZM techniques, interface elements are incorporated in the lines (of a 2D model) or in the surfaces (of a 3D model) where damage initiation and propagation is supposed to take place. The latter are controlled through the constitutive relation of the utilized interface elements, given by a CZM law which is described through a Traction-Separation (T-S) law.

Thus, CZM laws are established between paired nodes of interface elements and they can be used to connect superimposed nodes of elements representing different materials or different plies in composites, to simulate a zero thickness interface (local approach; Pardoen et al., 2005), or they can be applied directly between two non-contacting materials to simulate a thin strip of finite thickness between them, e.g. to simulate an adhesive bond (continuum approach; Xie and Waas, 2006).

A very promising CZM methodology, based on the continuum approach, for the numerical prediction of the loading and fracture behaviour of adhesive joints is based on the Embedded Process Zone (EPZ), introduced by Thouless and his coworkers, (Yang et al., 1999; Li et al., 2005; Yang et al., 2001; Yang and Thouless, 2001). The general concept that lays behind the term EPZ is that the adhesive layer is responsible for providing tractions σ between the involved substrates (Yang and Thouless, 2001). From the numerical point of view, the adhesive material is totally represented by interface elements that can model the kinematics incorporated in the EPZ.

The development of a mixed-mode EPZ model is divided into two main phases. The first phase involves the development of a model in pure Mode I, pure Mode II and pure Mode III loading and fracture, in terms of a T-S law, $\sigma(\delta)$. Magnitude δ is the local separation (opening in Mode I or sliding in Mode II and Mode III) of the adjacent substrates, calculated at their interface. Such a law consists first of an increasing behaviour of the tractions developed in the EPZ up to a peak value, followed by a traction softening function to zero level. The traction increasing part involves the linear elastic and upcoming plasticity behaviour of the adhesive layer utilized, whereas the second part involves damage initiation and propagation owing to the creation of microcracks, nucleation of voids and the extensive plasticity (fibrous deformations). The second phase involves the incorporation of damage and fracture criteria in order to couple the pure mode laws under the framework of a mixed-mode model.

In this work a new T-S law, which describes the embedded process zone of a ductile adhesive material constrained between substrates that form a structural adhesive joint, is developed and formulated under the combined framework of fracture and damage mechanics. The new T-S law will be referred as proposed EPZ law.

The proposed EPZ law has been formulated to describe the mixed-mode response of an adhesive layer subjected to Mode I and II loading and fracture (Anyfantis and Tsouvalis, 2012a) and of an adhesive layer subjected to Mode I, II and III loading and fracture (Anyfantis and Tsouvalis, 2012b), respectively. Thus, section 5.2 provides the mathematical description and the numerical implementation of the proposed EPZ law which addresses the loading and fracture behaviour of a ductile adhesive material in either pure Mode I, II and III. On the other hand, sections 5.3 and 5.4 provide a developed formulation that simulates the interdependency of the pure mode EPZ laws coupled under Mode I and II mixity (2D proposed mixed-mode EPZ model) or under Mode I, II and III mixity (3D proposed mixed-mode EPZ model), respectively. The proposed 2D and 3D EPZ laws and mixed-mode models have been implemented in Equation (A1.20) and Equation (A2.28) for the description of the constitutive relation of the 2D and 3D interface elements given in Appendix A1 and Appendix A2, respectively.

5.2 Proposed pure mode EPZ laws

The proposed pure mode EPZ laws are presented in Figure 5.1 and are formulated so as to be utilized either in 2-dimensional or in 3-dimensinal finite element modeling of adhesive joints. Within the following formulation a subscript, namely i, has been utilized to distinguish the parameters and magnitudes involved in each separate law. This subscript equals to I, II or III when referring to Mode I, Mode II or Mode III, respectively. Thus, for the 2D proposed EPZ laws i equals to I or II only, whereas for the 3D proposed EPZ laws i equals to I, II or III (Mode III is included in the 3D formulation only).

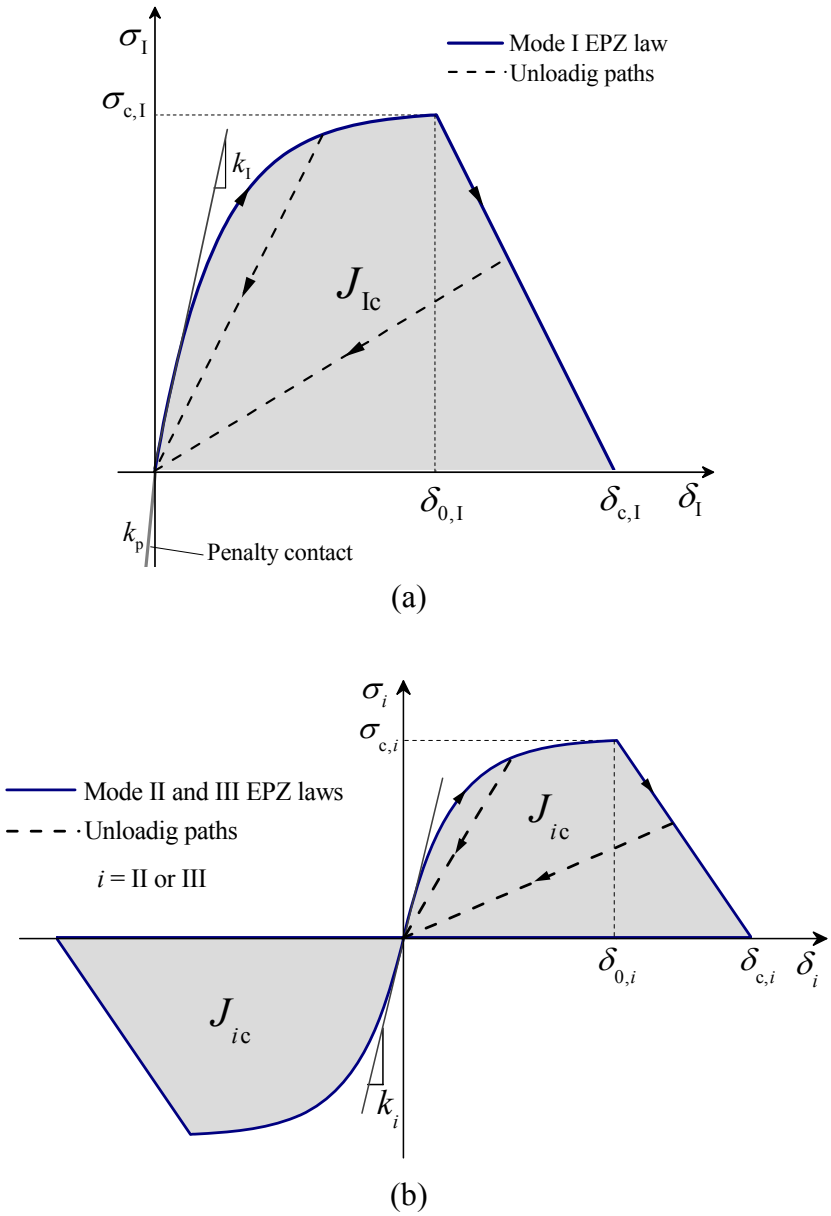

Figure 5.1: Proposed EPZ laws for the prediction of Mode I (a) and Mode II or III (b) loading and fracture (Anyfantis and Tsouvalis, 2012a; 2012b).

The σ_I tractions that are used to describe loading and fracture in the Mode I EPZ law, express the normal to the adhesive bondline stresses, known as peel or cleavage stresses, whereas σ_{II} and σ_{III} tractions describe the in-plane and out-of-plane shear stresses, respectively. The traction strengthening part of the proposed laws is defined by an exponential function, which aims at describing the elastoplastic behaviour of a ductile adhesive layer. This part differentiates the proposed EPZ law from the trapezoidal law which describes this region with an elastic – perfectly plastic approach, i.e. tractions are maintained constant after the initial linear elastic region (first inflexion point) until they enter the softening part (second inflexion point). For the description of the traction softening part (damage propagation) a linear function is utilized, as also given in the trapezoidal law.

The reversibility of the laws (unloading paths) has been included in the following formulation, as shown in Figure 5.1 by the linear unloading paths, for both traction strengthening and softening parts (dash lines).

The analytical function utilized for the description of the elastoplastic behaviour of a ductile adhesive material including its reversibility, is given by the following equation:

$$\sigma_i\left(\delta_i\right)=\frac{\sigma_{\mathrm{c},i}}{\delta_{i,\max}}\left[1-\exp\left(-\frac{\delta_{i,\max}k_i}{\sigma_{\mathrm{c},i}}\right)\right]\delta_i \qquad \text{for} \qquad 0\le\delta_i<\delta_{0,i} \tag{5.1}$$

where subscript i equals to I, II or III. The magnitude $\sigma_{\mathrm{c},i}$ represents the critical stress and the magnitude $\delta_{0,i}$ is its corresponding separation at damage initiation under pure mode loading and fracture conditions. Magnitude $\delta_{i,\max}$ is equal to the maximum separation calculated at a converged time step of the non-linear analysis procedure. Thus, during loading, both δ_i and $\delta_{i,\max}$ magnitudes are equal and together increasing and tractions follow the exponential function. However, if at given time step the calculated δ_i is less than $\delta_{i,\max}$, unloading is detected and hence $\delta_{i,\max}$ remains constant and equal to the last value of δ_i. As aforementioned, during unloading, tractions follow the linear paths to conclude to the origin (see Figure 5.1).

In order to avoid interpenetration between the, adjacent to the cohesive elements, continuum elements, a penalty contact algorithm has been included only in the formulation of Mode I EPZ law (see Figure 5.1). The contact algorithm is activated when δ_i becomes less than zero and hence tractions are described by:

$$\sigma_{\mathrm{I}}\left(\delta_{\mathrm{I}}\right)=k_{\mathrm{p}}\delta_{\mathrm{I}} \qquad \text{for} \qquad \delta_{\mathrm{I}}<0 \tag{5.2}$$

where k_{p} is the penalty magnitude ($\approx 10^5 \div 10^6$ MPa/mm, Tsouvalis and Anyfantis 2011a). It is assumed that negative stresses do not induce damage but treated only as contact conditions. The initial slope of Equation (5.1) is equal only to magnitude k_i, which is called initial stiffness, as seen from the following equation.

$$\left.\frac{\partial\sigma_i}{\partial\delta_i}\right|_{\delta_i=0}=k_i \tag{5.3}$$

This characteristic of the current exponential form is advantageous with regards to the development of the mixed-mode loading and fracture model, which will be described in the following. The initial stiffness k_i is directly defined for each mode by dividing the corresponding elastic constant of the adhesive material with the adhesive thickness (Campilho et al., 2005; Campilho et al., 2007; Campilho et al., 2008a), $k_{\mathrm{I}} = E_{\mathrm{a}} / t_{\mathrm{a}}$, $k_{\mathrm{II}} = G_{\mathrm{a}} / t_{\mathrm{a}}$ and $k_{\mathrm{III}} = k_{\mathrm{II}}$, where E_{a} and G_{a} is the Young and shear modulus of the adhesive, respectively, and t_{a} the adhesive thickness.

Magnitude $\delta_{0,i}$ can be directly defined or implicitly calculated, considering that the exponential form of Equation (5.1), on a theoretical basis, tends asymptotically to the horizontal asymptote $\sigma_{c,i}$. Thus, the corresponding ordinate is selected equal to (1-e)$\sigma_{c,i}$, where (1-e) is the tolerance and e is the numerical error between the asymptote $\sigma_{c,i}$ and the corresponding value utilized in the numerical analysis, as depicted in Figure 5.2.

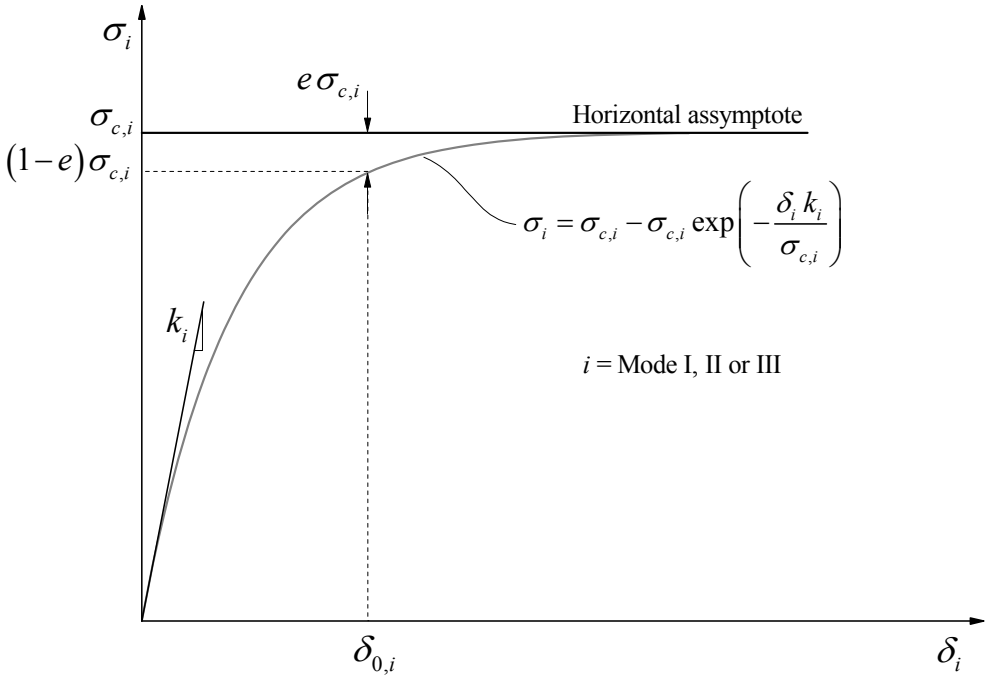

Figure 5.2: Exponential form utilized for the traction strengthening part of the proposed EPZ law.

Substituting the left hand side of Equation (5.1) with the term (1-e)$\sigma_{c,i}$ and solving with respect to $\delta_{0,i}$, the following relation is obtained:

$$\delta_{0,i} = -\frac{\ln(e)\ \sigma_{c,i}}{k_i} \tag{5.4}$$

As aforementioned, damage initiation and propagation is described by a linear traction softening function in the proposed EPZ laws. The term damage includes every type of degradation occurring within the adhesive layer, i.e. creation of microcracks, nucleation of voids and the extensive plasticity (fibrous deformations) etc. The linear softening function utilized in the formulation laws, from the critical traction point to the traction–free regime is given by Equation (5.5).

$$\sigma_i\left(\delta_i\right) = -\frac{(1-e)\sigma_{c,i}}{\delta_{c,i}-\delta_{0,i}}\delta_i + \frac{(1-e)\sigma_{c,i}\delta_{c,i}}{\delta_{c,i}-\delta_{0,i}} \qquad \text{for} \quad \delta_{0,i} \le \delta_i < \delta_{c,i} \tag{5.5}$$

where $\delta_{c,i}$ is the critical separation. In order to include reversibility (unloading) in the softening part, a control parameter of the damage extension D has been introduced which varies within the range [0,1].

$$D = 1 - \frac{\delta_{0,i}\left(\delta_{c,i} - \delta_{i,\max}\right)}{\delta_{i,\max}\left(\delta_{c,i} - \delta_{0,i}\right)} \tag{5.6}$$

At this point Equation (5.5) can be rewritten in the following form, which includes both loading and loading:

$$\sigma_i\left(\delta_i\right) = (1-D)(1-e)\sigma_{c,i}\frac{\delta_i}{\delta_{0,i}} \quad \text{for} \quad \delta_{0,i} \le \delta_i < \delta_{c,i} \tag{5.7}$$

Beyond the critical separation, the corresponding tractions are set to zero, hence leaving behind new traction–free surfaces (physical cracking).

$$\sigma_i\left(\delta_i\right) = 0 \quad \text{for} \quad \delta_i \ge \delta_{c,i} \tag{5.8}$$

The total energy consumed at the end of the proposed EPZ law is given by the definite integral (area) of its curve.

$$J_{ic} = \int_0^{\delta_{c,i}} \sigma_i d\delta_i = \frac{\sigma_{c,i}}{k_i}\left[k_i\delta_{0,i} - \sigma_{c,i} + \sigma_{c,i}\exp\left(-\frac{\delta_{0,i}k_i}{\sigma_{c,i}}\right)\right] + \frac{1}{2}\sigma_{c,i}\left(\delta_{c,i} - \delta_{0,i}\right) \tag{5.9}$$

The selection of the proposed particular shape of the EPZ law has been made on the basis of the fact that this shape is a very good analytic fit of experimental T-S laws measured from steel-to-steel adhesive joints, as found in the literature for pure Mode I (Ji et al., 2010) and pure Mode II (Leffler et al., 2007), respectively. To the author knowledge, measurements of experimental T-S laws are rare in the literature.

Figure 5.3 presents the analytical fitting of a typical experimental T-S law, obtained from DCB (Ji et al., 2010) and ENF tests (Leffler et al., 2007), with the proposed EPZ laws (Equation (5.1) and Equation (5.5)), for both pure Mode I and pure Mode II, respectively. Despite the fact that the experimental T-S laws have been obtained for different adhesive systems (LOCTITE Hysol 9460 for the DCB tests and DOW Betamate XW1044-3 for the ENF tests) the mechanical behaviour of both adhesive materials is characterized as ductile.

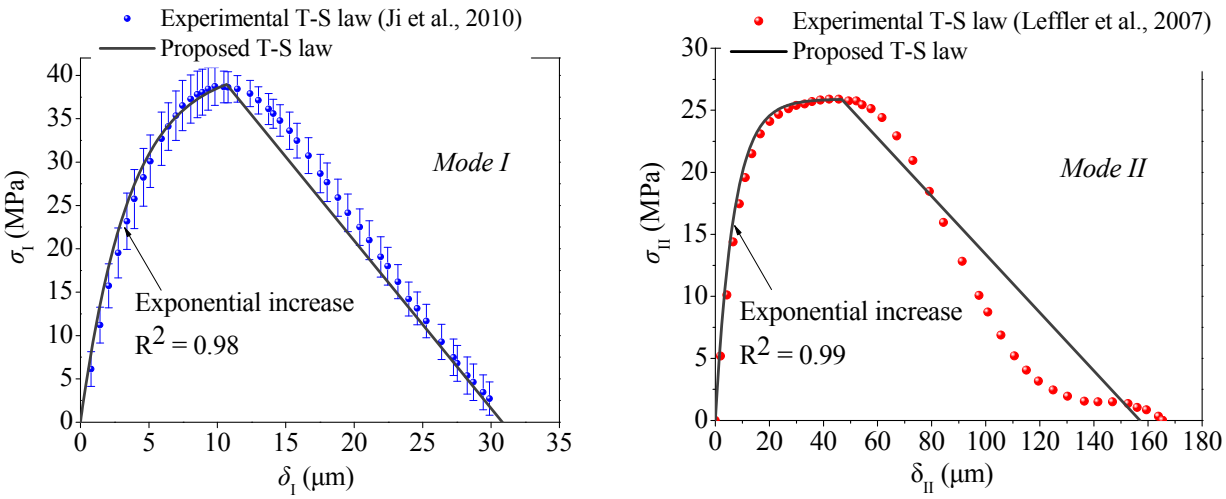

Figure 5.3: Analytical fitting with Equation (5.1) and Equation (5.5) of a typical experimental T-S law obtained from Ji et al. (2010) and Leffler et al. (2007) through Mode I - DCB tests (a) and Mode II – ENF tests (b), respectively.

According to Figure 5.3, the traction increasing part has been fitted with great accuracy by Equation (5.1), yielding a coefficient of determination (R^2) equal to 0.98 and 0.99 for the Mode I and Mode II case, respectively. On the other hand, the experimentally measured traction softening part (damage propagation region) in Mode I has a linear trend with a local non-linearity at the beginning of the descend, whereas in Mode II a highly non-linear behaviour is attained. However, it is impossible to formulate the coupling (interdependency) between a linear and a highly non-linear softening response within a numerical scheme, in order to yield a mixed-mode constitutive model. Additionally, Campilho et al. (2005), Campilho et al. (2007), Yang et al. (1999), Li et al. (2005), Yang et al. (2001) and Yang and Thouless (2001) state that a linear softening is adequate for modelling the physical phenomena occurring during damage propagation in the EPZ. For this purpose, within the present PhD thesis, no efforts were made to utilize a non-linear softening function and thus a linear description (Equation (5.5)) has been adopted.

5.3 Proposed 2D mixed-mode EPZ model

Having defined the pure mode EPZ laws in Mode I and Mode II, the next phase is focused on the formulation of the 2D mixed-mode EPZ model (see Figure 5.4). The present model accounts for the dependency between Mode I and Mode II loading and fracture and thus it can be used in plane stress/strain finite element modeling of adhesive joints.

Two are the guiding magnitudes through this formulation; the mode mixity ratio β, which is given by:

$$\beta = \frac{\delta_{\mathrm{II}}}{\delta_{\mathrm{I}}} \tag{5.10}$$

and the coupling of deformations, that is the equivalent deformation δ_{m}

$$\delta_{\mathrm{m}} = \sqrt{\delta_{\mathrm{I}}^2 + \delta_{\mathrm{II}}^2} \tag{5.11}$$

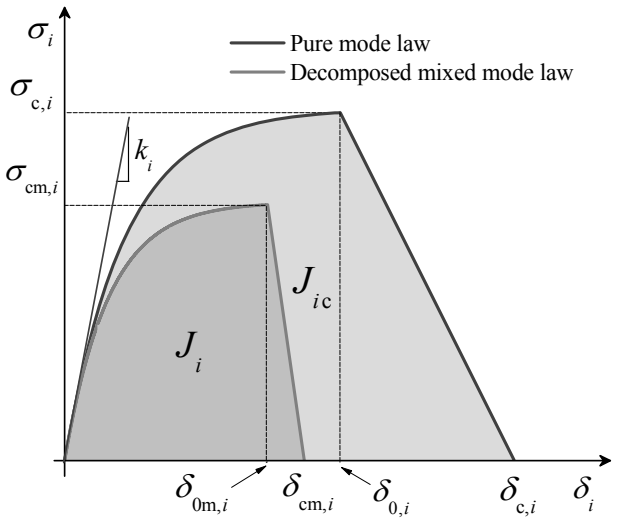

Figure 5.4: Proposed 2D mixed-mode EPZ model (i = I or II).

The mixed-mode formulation utilizes Equation (5.10) and Equation (5.11) for the composition of the mixed-mode EPZ law from the two pure mode EPZ laws and under a certain mode mixity ratio. The same fundamental equations combined with damage and fracture criteria will be used for the determination of the parameters characterizing the decomposed laws from the calculated mixed-mode EPZ law, under a particular mode mixity ratio. For the prediction of damage initiation under mixed mode loading, the quadratic stress criterion is utilized, (Campilho et al., 2008):

$$\left(\frac{\left\langle \sigma_{\mathrm{cm,I}} \right\rangle}{\sigma_{\mathrm{c,I}}} \right)^2 + \left(\frac{\sigma_{\mathrm{cm,II}}}{\sigma_{\mathrm{c,II}}} \right)^2 = 1 \tag{5.12}$$

where $\sigma_{\mathrm{cm,I}}$ and $\sigma_{\mathrm{cm,II}}$ are the decomposed critical tractions in Mode I and Mode II mixed-mode law (see Figure 5.4). The Macaulay brackets $\langle\ \rangle$ are used to show that negative normal tractions do not induce damage and in that case $\sigma_{\mathrm{cm,I}}$ equals to zero and thus only tangential tractions (shear stresses) are involved within the EPZ. By solving Equation (5.4) with respect to $\sigma_{\mathrm{c},i}$ and

$\sigma_{\mathrm{cm},i}$ (for i = I, II) separately and substituting into Equation (5.12), the quadratic stress criterion can be rewritten in terms of the deformation field as:

$$\left(\frac{\left\langle \delta_{\mathrm{0m,I}} \right\rangle}{\delta_{\mathrm{0,I}}}\right)^2 + \left(\frac{\delta_{\mathrm{0m,II}}}{\delta_{\mathrm{0,II}}}\right)^2 = 1 \tag{5.13}$$

where $\delta_{\mathrm{0m,I}}$ and $\delta_{\mathrm{0m,II}}$ are the mixed mode decomposed relative displacements where damage initiates. By substituting Equation (5.10) and Equation (5.11) into Equation (5.13), the mixed mode total relative displacement δ_{0m} can be obtained as follows:

$$\delta_{\mathrm{0m}} = \delta_{\mathrm{0,I}}\delta_{\mathrm{0,II}}\sqrt{\frac{1+\beta^2}{\delta_{\mathrm{0,II}}^2 + \beta^2\delta_{\mathrm{0,I}}^2}} \tag{5.14}$$

Again, by substituting Equation (5.10) and Equation (5.11) into Equation (5.14), the decomposed relative displacement in Mode I is obtained by

$$\delta_{\mathrm{0m,I}} = \frac{\delta_{\mathrm{0,I}}\delta_{\mathrm{0,II}}}{\sqrt{\delta_{\mathrm{0,II}}^2 + \beta^2\delta_{\mathrm{0,I}}^2}} \tag{5.15}$$

and in Mode II by

$$\delta_{\mathrm{0m,II}} = \beta\frac{\delta_{\mathrm{0,I}}\delta_{\mathrm{0,II}}}{\sqrt{\delta_{\mathrm{0,II}}^2 + \beta^2\delta_{\mathrm{0,I}}^2}} \tag{5.16}$$

Having calculated $\delta_{\mathrm{0m,I}}$ and $\delta_{\mathrm{0m,II}}$, the mixed-mode decomposed critical stress at each Mode i, $\sigma_{\mathrm{cm},i}$ can be calculated by utilizing Equation (5.4).

$$\sigma_{\mathrm{cm},i} = -\frac{k_i\delta_{\mathrm{0m},i}}{\ln(e)} \tag{5.17}$$

The decomposed mixed-mode EPZ laws in Mode I and Mode II retain the initial slope k_i (and thus the initial linear elastic response) of their respective pure mode EPZ law, as shown in Figure 5.4. This proofs the advantageous characteristic of Equation (5.1), according to which the linear elastic properties of the adhesive material are maintained under any mode mixity conditions.

For the prediction of damage propagation in the adhesive layer, the linear energetic fracture criterion (Equation (5.18)), that couples the fracture energies in Mode I (J_{I}) and Mode II (J_{II}), has been considered, (Campilho et al., 2008).

$$\frac{J_{\mathrm{I}}}{J_{\mathrm{Ic}}}+\frac{J_{\mathrm{II}}}{J_{\mathrm{IIc}}}=1 \tag{5.18}$$

From a physical point of view, the satisfaction of the preceding criterion implies that the tractions in the EPZ are eliminated and thus new traction free crack faces are generated. The fracture energies J_i are given in the same way as in Equation (5.9), by calculating the definite integral of the decomposed mixed mode EPZ laws:

$$J_i=\int_0^{\delta_{\mathrm{cm},i}}\sigma_i\,d\delta_i=\frac{\sigma_{\mathrm{cm},i}}{k_i}\left[k_i\delta_{0\mathrm{m},i}-\sigma_{\mathrm{cm},i}+\sigma_{\mathrm{cm},i}\exp\left(-\frac{\delta_{0\mathrm{m},i}k_i}{\sigma_{\mathrm{cm},i}}\right)\right]+\frac{1}{2}\sigma_{\mathrm{cm},i}\left(\delta_{\mathrm{cm},i}-\delta_{0\mathrm{m},i}\right) \tag{5.19}$$

The substitution of Equation (5.15) to Equation (5.17) into Equation (5.19) yields a direct calculation of the decomposed relative displacements $\delta_{\mathrm{cm,I}}$ and $\delta_{\mathrm{cm,II}}$ in Mode I and Mode II, respectively

$$\delta_{\mathrm{cm,I}}=\frac{2J_{\mathrm{Ic}}J_{\mathrm{IIc}}-2C_{\mathrm{I}}J_{\mathrm{IIc}}-2C_{\mathrm{II}}J_{\mathrm{Ic}}+\delta_{0\mathrm{m,I}}J_{\mathrm{IIc}}\sigma_{\mathrm{cm,I}}+\delta_{0\mathrm{m,II}}J_{\mathrm{Ic}}\sigma_{\mathrm{cm,II}}}{J_{\mathrm{IIc}}\sigma_{\mathrm{cm,I}}+\beta J_{\mathrm{Ic}}\sigma_{\mathrm{cm,II}}} \tag{5.20}$$

$$\delta_{\mathrm{cm,II}}=\beta\frac{2J_{\mathrm{Ic}}J_{\mathrm{IIc}}-2C_{\mathrm{I}}J_{\mathrm{IIc}}-2C_{\mathrm{II}}J_{\mathrm{Ic}}+\delta_{0\mathrm{m,I}}J_{\mathrm{IIc}}\sigma_{\mathrm{cm,I}}+\delta_{0\mathrm{m,II}}J_{\mathrm{Ic}}\sigma_{\mathrm{cm,II}}}{J_{\mathrm{IIc}}\sigma_{\mathrm{cm,I}}+\beta J_{\mathrm{Ic}}\sigma_{\mathrm{cm,II}}} \tag{5.21}$$

where C_i (i = I, II) is the definite integral of the decomposed exponential part of each mixed-mode T-S law.

$$C_i=\left(\frac{\sigma_{\mathrm{cm},i}}{k_i}\right)\left[\left(\delta_{0\mathrm{m},i}k_i\right)+\sigma_{\mathrm{cm},i}\exp\left(-\frac{\delta_{0\mathrm{m},i}k_i}{\sigma_{\mathrm{cm},i}}\right)-\sigma_{\mathrm{cm},i}\right] \tag{5.22}$$

Magnitude δ_{cm} can thus be obtained from Equation (5.11). The geometric representation of the deformation parameters involved in the preceding formulation is shown in Figure 5.5.

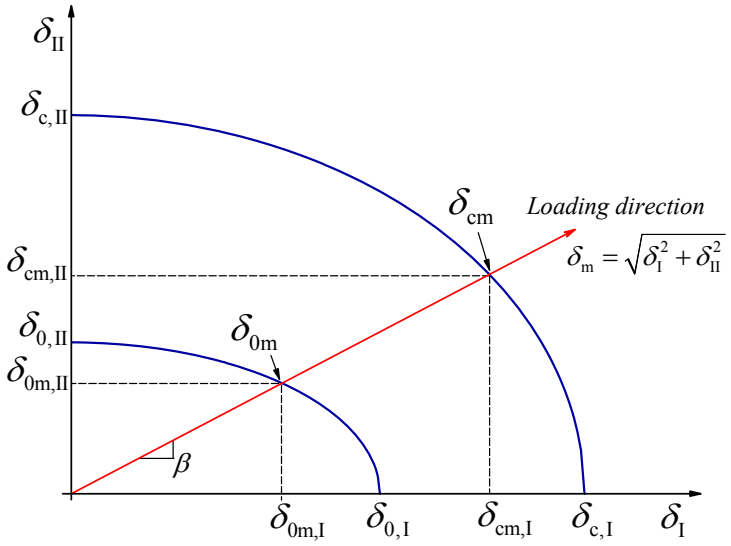

Figure 5.5: Geometric representation of the deformation parameters under constant mode mixity β.

Having calculated all necessary parameters involved in the mixed-mode EPZ laws, their computational implementation is provided. Loading and unloading is also considered in the mixed-mode laws. The traction increasing part is given from the following equation, which is similar to Equation (5.1):

$$\sigma_{m,i}\left(\delta_i\right) = \frac{\sigma_{cm,i}}{\delta_{i,max}}\left[1-\exp\left(-\frac{\delta_{i,max}k_i}{\sigma_{cm,i}}\right)\right]\delta_i \quad \text{for} \quad 0 \le \delta_i < \delta_{0m,i} \tag{5.23}$$

The damage parameter at this point is formulated according to the mixed-mode separation δ_m as follows:

$$D = 1-\frac{\delta_{0m}\left(\delta_{cm}-\delta_m\right)}{\delta_m\left(\delta_{cm}-\delta_{0m}\right)} \tag{5.24}$$

The linear softening part for both loading and unloading is described from the following equation which takes under consideration the preceding damage parameter D:

$$\sigma_{m,i}\left(\delta_i\right) = (1-D)(1-e)\,\sigma_{cm,i}\frac{\delta_i}{\delta_{0m,i}} \quad \text{for} \quad \delta_{0m} \le \delta_m < \delta_{cm} \tag{5.25}$$

Finally, the traction free region beyond the critical separation is given by the following equation:

$$\sigma_{m,i}\left(\delta_i\right) = 0 \quad \text{for} \quad \delta_m \ge \delta_{cm} \tag{5.26}$$

5.4 Proposed 3D mixed-mode EPZ model

In this section, the proposed pure mode EPZ laws (Mode I, II and III), are formulated under a 3D mixed-mode model that accounts for their coupling and interdependency. The proposed mixed-mode model is presented in Figure 5.6 and is the same one that accounts for the 2D mixed-mode model (Figure 5.4). Two cases are considered according to the sign of the normal tractions σ_{I}, since positive tractions contribute to the loading and fracture and negative tractions denote contact in the adhesive bondline. Thus, one case considers the Mode I, II and III mixity (positive σ_{I}) and the remaining one considers only Mode II and III mixity (negative σ_{I}).

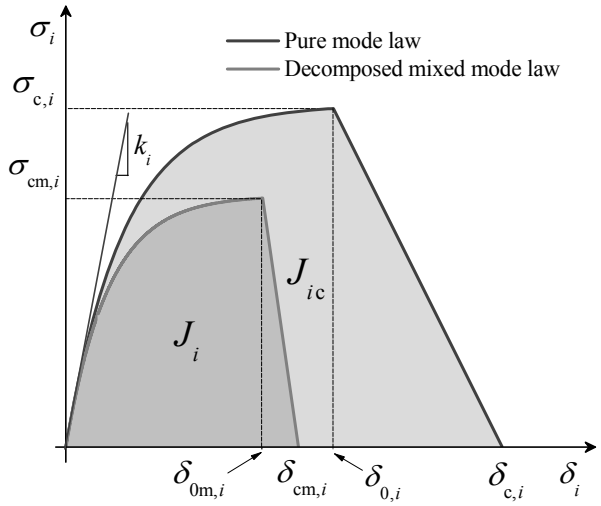

Figure 5.6: Proposed 3D mixed-mode EPZ model (i = I, II or III).

5.4.1 Mode I, II and III mixed-mode model

The guiding parameters for the formulation of the 3D mixed-mode model are the mode mixity ratios:

$$\beta_{\mathrm{II}} = \frac{\delta_{\mathrm{II}}}{\delta_{\mathrm{I}}} \quad \text{and} \quad \beta_{\mathrm{III}} = \frac{\delta_{\mathrm{III}}}{\delta_{\mathrm{I}}} \tag{5.26}$$

and the resultant total separation δ_{m}

$$\delta_{\mathrm{m}} = \sqrt{\delta_{\mathrm{I}}^2 + \delta_{\mathrm{II}}^2 + \delta_{\mathrm{III}}^2} \tag{5.27}$$

The current formulation is based on Equation (5.26) and Equation (5.27) for the composition of the 3D mixed-mode EPZ laws for given pure mode EPZ laws, under constant mode mixity ratios. The same basic equations combined with damage initiation and propagation criteria are utilized for the definition of the parameters that characterize the three decomposed mixed-mode EPZ laws calculated from the mixed-mode model.

Damage initiation under mixed-mode loading is predicted with the use of the quadratic stress criterion (Campilho et al., 2008):

$$\left(\frac{\sigma_{\mathrm{cm,I}}}{\sigma_{\mathrm{c,I}}}\right)^2+\left(\frac{\sigma_{\mathrm{cm,II}}}{\sigma_{\mathrm{c,II}}}\right)^2+\left(\frac{\sigma_{\mathrm{cm,III}}}{\sigma_{\mathrm{c,III}}}\right)^2=1 \tag{5.28}$$

where $\sigma_{\mathrm{cm,I}}$, $\sigma_{\mathrm{cm,II}}$ and $\sigma_{\mathrm{cm,III}}$ are the critical stresses of the decomposed mixed-mode EPZ laws (see Figure 5.6). Solving Equation (5.4) with respect to $\sigma_{\mathrm{c},i}$ and $\sigma_{\mathrm{cm},i}$ (for i = I, II και III) separately and substituting to Equation (5.28), the stress criterion is written as:

$$\left(\frac{\delta_{\mathrm{0m,I}}}{\delta_{\mathrm{0,I}}}\right)^2+\left(\frac{\delta_{\mathrm{0m,II}}}{\delta_{\mathrm{0,II}}}\right)^2+\left(\frac{\delta_{\mathrm{0m,III}}}{\delta_{\mathrm{0,III}}}\right)^2=1 \tag{5.29}$$

where $\delta_{\mathrm{0m,I}}$, $\delta_{\mathrm{0m,II}}$ and $\delta_{\mathrm{0m,III}}$ are the obtained mixed-mode separations denoting the actual damage initiation point. Substituting Equation (5.26) and Equation (5.27) into Equation (5.29), the resultant total separation δ_{0m} is obtained:

$$\delta_{\mathrm{0m}}=\sqrt{\frac{1+\beta_{\mathrm{II}}^2+\beta_{\mathrm{III}}^2}{\frac{1}{\delta_{\mathrm{0,I}}^2}+\frac{\beta_{\mathrm{II}}^2}{\delta_{\mathrm{0,II}}^2}+\frac{\beta_{\mathrm{III}}^2}{\delta_{\mathrm{0,III}}^2}}} \tag{5.30}$$

Substituting Equation (5.26) and (5.27) into Equation (5.30) the decomposed separation in Mode I loading and fracture is obtained:

$$\delta_{\mathrm{0m,I}}=\frac{\delta_{\mathrm{0,m}}}{\sqrt{1+\beta_{\mathrm{II}}^2+\beta_{\mathrm{III}}^2}} \tag{5.31}$$

and in Mode II and III loading and fracture:

$$\delta_{\mathrm{0m,II}}=\beta_{\mathrm{II}}\delta_{\mathrm{0m,I}} \quad \text{and} \quad \delta_{\mathrm{0m,II}}=\beta_{\mathrm{III}}\delta_{\mathrm{0m,I}} \tag{5.32}$$

Having calculated $\delta_{\mathrm{0m,I}}$, $\delta_{\mathrm{0m,II}}$ and $\delta_{\mathrm{0m,III}}$ the decomposed critical stresses $\sigma_{\mathrm{cm},i}$ may be calculated for each Mode i, by utilizing Equation (5.4).

$$\sigma_{\mathrm{cm},i}=-\frac{k_i\delta_{\mathrm{0m},i}}{\ln(e)} \tag{5.33}$$

The decomposed EPZ laws maintain their initial slope k_i (and thus their initial linear elastic stiffness) from the respective pure mode loading and fracture laws, as shown in Figure 5.6. This fact proofs the advantage of the selected exponential form (Equation (5.3)), according to which the linear elastic response is modeled regardless the mode-mixity ratios.

The linear energetic fracture criterion has been selected for the prediction of damage propagation within the adhesive layer, which provides the needed coupling between the fracture energies in Mode I (J_{I}), Mode II (J_{II}) and Mode III (J_{III}), Campilho et al. (2008).

$$\frac{J_{\mathrm{I}}}{J_{\mathrm{Ic}}}+\frac{J_{\mathrm{II}}}{J_{\mathrm{IIc}}}+\frac{J_{\mathrm{III}}}{J_{\mathrm{IIIc}}}=1 \tag{5.34}$$

From the physical point of view, the satisfaction of the preceding criterion denotes the elimination of the tractions within the embedded process zone and thus new traction–free surfaces are being generated. Fracture energies J_i are being calculated, as in Equation (5.9), through the definite integral of the decomposed mixed-mode EPZ laws:

$$J_i=\int_0^{\delta_{\mathrm{cm},i}}\sigma_i\,d\delta_i=\frac{\sigma_{\mathrm{cm},i}}{k_i}\left[k_i\delta_{0\mathrm{m},i}-\sigma_{\mathrm{cm},i}+\sigma_{\mathrm{cm},i}\exp\left(-\frac{\delta_{0\mathrm{m},i}k_i}{\sigma_{\mathrm{cm},i}}\right)\right]+\frac{1}{2}\sigma_{\mathrm{cm},i}\left(\delta_{\mathrm{cm},i}-\delta_{0\mathrm{m},i}\right) \tag{5.35}$$

Substituting Equation (5.26) and Equation (5.35) into Equation (5.34), an exact calculation of the decomposed critical separations $\delta_{\mathrm{cm,I}}$, $\delta_{\mathrm{cm,II}}$ and $\delta_{\mathrm{cm,III}}$ is obtained, respectively:

$$\delta_{\mathrm{cm,I}}=\frac{2J_{\mathrm{Ic}}J_{\mathrm{IIc}}J_{\mathrm{IIIc}}-2C_{\mathrm{I}}J_{\mathrm{IIc}}J_{\mathrm{IIIc}}-2C_{\mathrm{II}}J_{\mathrm{Ic}}J_{\mathrm{IIIc}}-2C_{\mathrm{III}}J_{\mathrm{Ic}}J_{\mathrm{IIc}}+\delta_{0\mathrm{m,I}}J_{\mathrm{IIIc}}J_{\mathrm{IIc}}\sigma_{\mathrm{cm,I}}+\delta_{0\mathrm{m,II}}J_{\mathrm{Ic}}J_{\mathrm{IIIc}}\sigma_{\mathrm{cm,II}}+\delta_{0\mathrm{m,III}}J_{\mathrm{Ic}}J_{\mathrm{IIc}}\sigma_{\mathrm{cm,III}}}{J_{\mathrm{IIc}}J_{\mathrm{IIIc}}\sigma_{\mathrm{cm,I}}+\beta_{\mathrm{II}}J_{\mathrm{Ic}}J_{\mathrm{IIIc}}\sigma_{\mathrm{cm,II}}+\beta_{\mathrm{III}}J_{\mathrm{Ic}}J_{\mathrm{IIc}}\sigma_{\mathrm{cm,III}}} \tag{5.36a}$$

$$\delta_{\mathrm{cm,II}}=\beta_{\mathrm{II}}\delta_{\mathrm{cm,I}} \tag{5.36b}$$

$$\delta_{\mathrm{cm,III}}=\beta_{\mathrm{III}}\delta_{\mathrm{cm,I}} \tag{5.36c}$$

where C_i (i = I, II και III) is the area under the decomposed EPZ laws that is given from the exponential function.

$$C_i=\left(\frac{\sigma_{\mathrm{cm},i}}{k_i}\right)\left[\left(\delta_{0\mathrm{m},i}\,k_i\right)+\sigma_{\mathrm{cm},i}\exp\left(-\frac{\delta_{0\mathrm{m},i}\,k_i}{\sigma_{\mathrm{cm},i}}\right)-\sigma_{\mathrm{cm},i}\right] \tag{5.37}$$

Magnitude δ_{cm} is calculated through Equation (5.27).

$$\delta_{\mathrm{cm}} = \sqrt{\delta_{\mathrm{cm,I}}^2 + \delta_{\mathrm{cm,II}}^2 + \delta_{\mathrm{cm,III}}^2} \tag{5.38}$$

Having calculated all necessary parameters involved in the mixed-mode EPZ laws, their computational implementation is provided. Loading and unloading is also considered in the mixed-mode laws. The traction increasing part is given from the following equation, which is similar to Equation (5.1):

$$\sigma_{\mathrm{m},i}\left(\delta_i\right) = \frac{\sigma_{\mathrm{cm},i}}{\delta_{i,\max}}\left[1-\exp\left(-\frac{\delta_{i,\max}k_i}{\sigma_{\mathrm{cm},i}}\right)\right]\delta_i \quad \text{for} \quad 0 \le \delta_i < \delta_{0\mathrm{m},i} \tag{5.39}$$

A damage parameter is also used that controls the extension of failure D within range [0,1]:

$$D = 1 - \frac{\delta_{0\mathrm{m}}\left(\delta_{\mathrm{cm}} - \delta_{\mathrm{m}}\right)}{\delta_{\mathrm{m}}\left(\delta_{\mathrm{cm}} - \delta_{0\mathrm{m}}\right)} \tag{5.40}$$

The softening part is given by the following function:

$$\sigma_{\mathrm{m},i}\left(\delta_i\right) = (1-D)(1-e)\,\sigma_{\mathrm{cm},i}\,\frac{\delta_i}{\delta_{0\mathrm{m},i}} \quad \text{for} \quad \delta_{0\mathrm{m}} \le \delta_{\mathrm{m}} < \delta_{\mathrm{cm}} \tag{5.41}$$

Lastly, tractions after the critical separations are being totally released:

$$\sigma_{\mathrm{m},i}\left(\delta_i\right) = 0 \quad \text{for} \quad \delta_{\mathrm{m}} \ge \delta_{\mathrm{cm}} \tag{5.42}$$

5.4.2 Mode II and III mixed-mode model

In the case where tractions σ_{I} are negative and assuming that these negative tractions do not induce any damage but act only as contact stresses, coupling between only Mode II and III loading and fracture is present. The coupling of the two modes is given by one mode mixity ratio:

$$\beta_{\mathrm{c}} = \frac{\delta_{\mathrm{II}}}{\delta_{\mathrm{III}}} \tag{5.43}$$

and, consequently, the resultant total separation δ_{m} is given by:

$$\delta_{\mathrm{m}} = \sqrt{\delta_{\mathrm{II}}^2 + \delta_{\mathrm{III}}^2} \tag{5.44}$$

For the prediction of damage initiation, the quadratic stress criterion is being utilized:

$$\left(\frac{\sigma_{\mathrm{cm,II}}}{\sigma_{\mathrm{c,II}}}\right)^2+\left(\frac{\sigma_{\mathrm{cm,III}}}{\sigma_{\mathrm{c,III}}}\right)^2=1 \tag{5.45}$$

Solving Equation (5.4) with respect to $\sigma_{\mathrm{c},i}$ and $\sigma_{\mathrm{cm},i}$ (for i = II και III) separately and substituting to Equation (5.45), the stress criterion is written as:

$$\left(\frac{\delta_{\mathrm{0m,II}}}{\delta_{\mathrm{0,II}}}\right)^2+\left(\frac{\delta_{\mathrm{0m,III}}}{\delta_{\mathrm{0,III}}}\right)^2=1 \tag{5.46}$$

Substituting Equation (5.43) and Equation (5.44) into Equation (5.46) the resultant total separation δ_{0m} is obtained:

$$\delta_{\mathrm{0m}}=\sqrt{\frac{1+\beta_{\mathrm{c}}^2}{\frac{\beta_{\mathrm{c}}^2}{\delta_{\mathrm{0,II}}^2}+\frac{1}{\delta_{\mathrm{0,III}}^2}}} \tag{5.47}$$

Separations $\delta_{\mathrm{0m,II}}$ and $\delta_{\mathrm{0m,III}}$ are calculated through Equation (5.43), Equation (5.44) and Equation (5.47):

$$\delta_{\mathrm{0m,II}}=\beta_{\mathrm{c}}\delta_{\mathrm{0m,III}} \quad \text{and} \quad \delta_{\mathrm{0m,III}}=\frac{\delta_{\mathrm{0,m}}}{\sqrt{1+\beta_{\mathrm{c}}^2}} \tag{5.48}$$

The decomposed critical stresses are calculated with the use of Equation (5.33) for i = II or III. Damage propagation is predicted again with the use of the linear energetic criterion:

$$\frac{J_{\mathrm{II}}}{J_{\mathrm{IIc}}}+\frac{J_{\mathrm{III}}}{J_{\mathrm{IIIc}}}=1 \tag{5.49}$$

By substituting Equation (5.43) and Equation (5.35) into Equation (5.49), an exact expression is derived for $\delta_{\mathrm{cm,II}}$ and $\delta_{\mathrm{cm,III}}$, respectively:

$$\delta_{\mathrm{cm,III}}=\frac{2J_{\mathrm{IIc}}J_{\mathrm{IIIc}}-2C_{\mathrm{II}}J_{\mathrm{IIIc}}-2C_{\mathrm{III}}J_{\mathrm{IIc}}+\delta_{\mathrm{0m,II}}J_{\mathrm{IIIc}}\sigma_{\mathrm{cm,II}}+\delta_{\mathrm{0m,III}}J_{\mathrm{IIc}}\sigma_{\mathrm{cm,III}}}{J_{\mathrm{IIc}}\sigma_{\mathrm{cm,III}}+\beta_{\mathrm{c}}J_{\mathrm{IIIc}}\sigma_{\mathrm{cm,II}}} \tag{5.50a}$$

$$\delta_{\mathrm{cm,II}}=\beta_{\mathrm{c}}\delta_{\mathrm{cm,III}} \tag{5.50b}$$

where C_i (i = II και III) is given by Equation 5.37.

5.5 Conclusions

In this chapter a new to the literature Traction-Separation (T-S) law is developed for modelling the elastic, plastic and damage material response of a ductile adhesive layer, under the framework of the Embedded Process Zone approach. The shape of the proposed T-S law is characterized by two regions, i.e. a traction increasing part and a traction decreasing part. The initial increasing part is mathematically described by an exponential function, the selection of which is based on analytical fittings of experimentally measured cohesive laws. The selected exponential function provides a very useful advantage, according to which the initial slope is maintained constant regardless the selection of the remaining parameters. Within the exponential traction increasing part, the elastic and plastic behaviour of the adhesive layer is described whereas within the linear traction decrease part, damage initiation and propagation is described.

Initially the pure mode laws where formulated for modeling the pure Mode I, Mode II and Mode III loading and fracture. Then, these laws were incorporated in a developed mixed-mode model which accounts for the mixed-mode loading and fracture response of the adhesive material. The developed model is formulated so as to be utilized in 2-dimensional (Mode I and Mode II) and 3-dimensional (Mode I, Mode II and Mode III) finite element procedures. Within these models, the interdependency and coupling of the pure mode laws has been done on the basis of introducing dependent relations of the separation field (δ_I, δ_{II} and δ_{III}), i.e. mode mixities and equivalent separations. These two guiding parameters through the formulation meet the nominal quadratic stress criterion and the linear energetic criterion which correspond to the damage initiation and propagation point, respectively.

From the numerical point of view the great advantage of the proposed T-S law shape is that convergence of the non-linear solution becomes much easier, since the traction gradients vary smoothly within the laws. Additionally, three physical parameters must be defined for each pure mode law and one numerical parameter for the mixed-mode model. In the following chapters (6, 7 and 8) the proposed mixed-mode model is utilized for the numerical prediction of steel-to-steel and composite-to-steel adhesive joints involving either flat or tubular adherents.

This page has been intentionally left blank

6. Experimental and numerical investigation of metal-to-metal adhesive joints

6.1 Description of work

This chapter focuses on the verification and validation of the proposed constitutive model described in chapter 5, with metal-to-metal adhesive joints. Thus, for the validation of the proposed 2D and 3D mixed-mode EPZ models, two simple yet common joint configurations have been adopted, that is a Single Lap Joint (SLJ) and a Double Strap Joint (DSJ). These types of joints are good candidates for validating numerical models, since the involved adhesive material in both cases is loaded under mixed-mode conditions (Tsouvalis and Anyfantis, 2010).

The experimental program involves the fabrication and testing of SLJ and DSJ specimens, which consist of relatively thick metal substrates and a structural ductile adhesive material. All specimens were loaded by a uniaxial static tensile displacement and during the experiments the global response (force-displacement) of each joint was monitored. Additionally, a study of the effect of the surface preparation on the strength of the joints is considered only for the DSJ geometrical configuration. This is done by testing two sets of DSJ bonded specimens, which differ in the technique utilized for the surface preparation of the bond areas of the metal substrates, namely grit blasting (GB) and the use of simple sandpaper (SP), in order to produce different surface roughness. According to the experimental results, the GB technique has yield higher values of surface roughness, compared to the SP technique, which in turn has led to higher strength limits of the corresponding tested DSJ coupons (Anyfantis and Tsouvalis, 2009). For this reason, the bond surfaces of the metal substrates of the SLJ specimens have been grit blasted prior to the application of the adhesive material in order to fabricate the adhesive joints. A simple analytical model is also developed in Anyfantis and Tsouvalis (2009) by modifying a corresponding model provided by Xiao et al. (2004) and its validity against the produced experimental DSJ results is investigated.

The response of the coupons was numerically predicted with the use of the proposed 2D and 3D laws and mixed-mode EPZ model within the framework of finite element analysis procedures and comparisons with corresponding experimental measurements are provided.

Initially, the proposed pure mode EPZ laws have been utilized as is, in a plane strain analysis (2D space – 2D EPZ laws), without considering their coupling or interdependency through the entire loading history. This, analysis will show the adequacy and effectiveness of the selected shape of the proposed EPZ laws, that is an exponential traction increase part followed by a linear traction decrease part. Then, the proposed EPZ laws were utilized in the developed 2D and 3D mixed-mode EPZ model for the prediction of the mixed-mode loading and fracture behaviour of the adhesive layer. The developed stress fields (peel, in-plane and out-of-plane shear) are presented as they evolve during the loading of both joint cases. Comparisons are also given from the FEA results of both joint configurations with the use of 2D continuum elements and with the use of the 2D mixed-mode EPZ model in interface elements, within the linear elastic region of the adhesive material utilized. Moreover, the numerical results obtained from the utilization of the proposed EPZ laws are compared with the corresponding results obtained from the trapezoidal T-S laws and the 2-Dimensional PRP cohesive model (see section 2.3.3.1).

6.2 Single Lap and Double Strap adhesive joints

6.2.1 Experimental programme

The geometry and dimensions of the fabricated and tested SLJ and DSJ specimens are presented in Figure 6.1. Normal marine grade steel has been used for the manufacturing of all metal substrates. Araldite 2015 has been utilized for the fabrication of the adhesive joints, which is a relatively stiff two-component epoxy adhesive manufactured by Huntsman Container Corporation Ltd. The actual width of the SLJ and DSJ specimens is 28.5 mm and 23.5 mm, respectively.

One of the scopes of the experimental program was to study the influence of the surface preparation method on the strength of DSJs. Hence, two texturing techniques were used for the bonding surface preparation of the substrates in order to generate different levels of surface roughness, namely grit blasting (GB) and use of simple sandpaper (SP). All adherents were first degreased with acetone before the application of the specific surface preparation procedure. SP treatment was performed using first a coarse sandpaper (100), followed by a finer one (200). With regard to the GB specimens, the common in the shipbuilding industry Sa2½ near-white grit blast cleaning was applied (approx. 2.5 mm grit size), according to the Swedish standards. At the end of both surface preparation procedures, the specimens were cleaned with solvent and then let to dry.

After the above treatment, the average surface roughness, Ra, of the bonding surfaces of the adherents was measured using a portable roughness measurement instrument with a 1 mm diameter stylus tip. The sampling length was 8 mm and the cutoff limit was 0.8 mm for each measurement. The measured average Ra values were equal to 4.15 μm (CoV = 2%) and 2.28 μm (CoV = 4.6%) for the GB and SP areas, respectively. These values indicate, besides a very good

repeatability of measurements (very low Coefficient of Variation - CoV), that the average roughness attained by using the GB procedure was clearly larger than that attained by the SP method (approximately double). As it will be shown latter on, the grit blasted DSJ specimens attained higher loads than the ones treated with sandpaper. Thus the GB procedure was applied over the bond areas of the SLJ specimens, which yielded average Ra values equal to 4.68 μm (CoV = 1.6%).

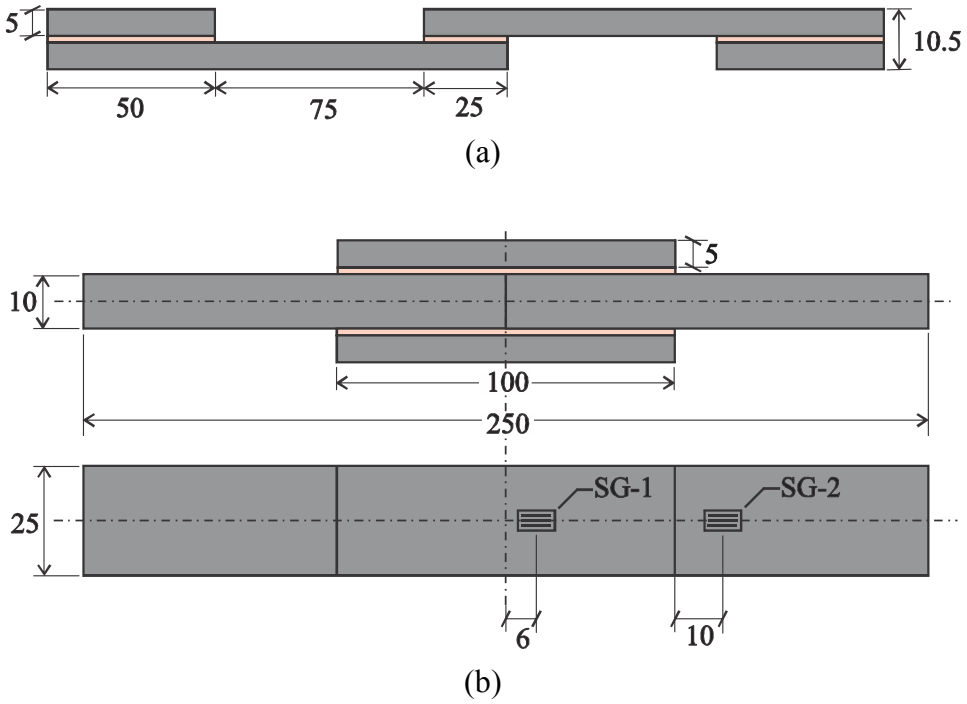

Figure 6.1: Dimensions (in mm) and geometrical configuration of the SLJ (a) and the DSJ (b) specimens.

During the bonding procedure of the both SLJ and DSJ specimens, some very small 0.5 mm diameter Cu particles were spread onto the bonding surfaces. These particles functioned as spacers for the bond and kept the adhesive layer thickness as close to the value of 0.5 mm as possible, ensuring at the same time a constant and uniform adhesive layer thickness among all specimens. Thus, as subsequent corresponding measurements indicated, the thickness of the cured adhesive layer was 0.5±0.01 mm. Before bonding the straps the adherents were placed in contact and a thin PTFE film was inserted in-between them, avoiding thus the creation of a butt type adhesive joint. After the assembly, the specimens were cured in an oven under a uniform pressure loading. According to the adhesive material manufacturer, curing procedure consisted of heating the specimens in 60°C for 4 hours, followed by a slow cooling to ambient temperature. The specimens were left in ambient temperature for 48 hours before performing the tests.

The specimens were loaded by a uniaxial static tensile displacement, applied with a speed of 0.1 mm/min by an MTS hydraulic testing machine. Two strain gage sensors (SG-1 and SG-2) were placed on each DSJ specimen, the first on the free surface of one of the straps and the second on the free surface of the inner adherent, at the positions shown in Figure 6.1b. They both had a gage length of 10 mm. Their aim was to monitor strains at these two parts for reasons of

comparison with the respective numerical results. During the tests the applied displacement together with the reaction forces were monitored. Nine in total specimens were tested, six DSJ specimens (three treated with GB and three treated with SP) and three SLJ specimens. Figure 6.2 shows one specimen of each case under experimental conditions.

(a) (b)

Figure 6.2: Experimental test of (a) a SLJ and (b) a DSJ specimen.

6.2.2 Analytical calculation of the stiffness prediction of DSJ

The analytical model presented by Xiao et al. (2004) is focused on the stiffness prediction of a double lap shear joint (DLS). In the present study, Xiao's assumptions are adopted, aiming at modifying his model to account for DSJs. Figure 6.1 is a schematic view of a DSJ in its undeformed (a) and deformed (b) state. Half of the joint is shown in this figure, to the right of its axis of symmetry y. In addition, the thickness of the adhesive layer is shown exaggerated. The joint is loaded by a tensile axial load F in x-direction. The part of the inner adherent outside the strap joint is denoted as segment 1, whereas segment 2 signifies half of the length of each strap, from its axis of symmetry to its edge. L_1 and L_2 are the lengths of segments 1 and 2, respectively, whereas u_1 and u_2 are their corresponding axial deformations and u_3 is the axial deformation of the adhesive layer.

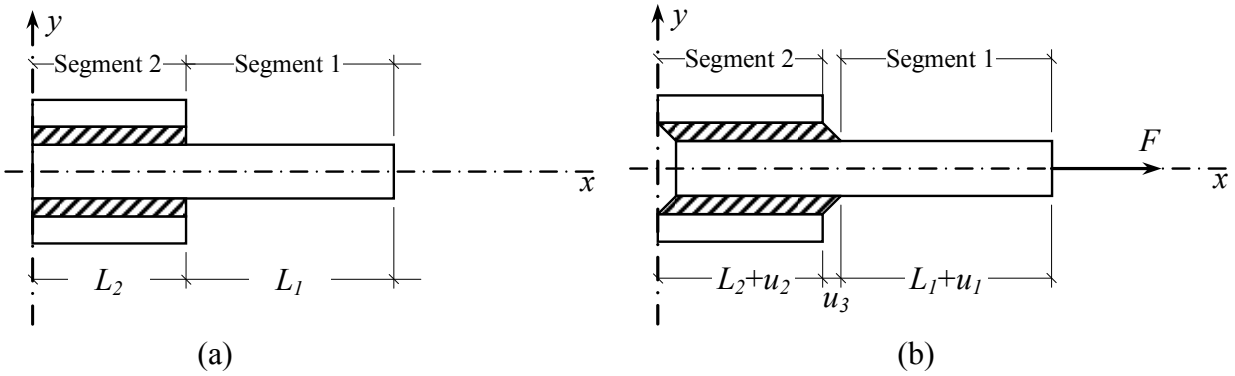

Figure 6.3: Schematic view of a DSJ in its undeformed (a) and deformed (b) state (half the joint is shown).

The realistic assumption that load F applied to the joint is uniform over the length of segment 1, results in the development of a constant tensile stress σ_1 over the length L_1, which is given by the following simple equation:

$$\sigma_1 = \frac{F}{b t_1} \tag{6.1}$$

where b is the width of the joint and t_1 the thickness of the inner adherent. Furthermore, Equation (6.2) and Equation (6.3) below describe the well known linear elastic stress-strain and strain-displacement relations, respectively, in segment 1,

$$\sigma_1 = \varepsilon_1 E_s \tag{6.2}$$

$$\varepsilon_1 = \frac{u_1}{L_1} \tag{6.3}$$

where ε denotes strain and E_S is the modulus of elasticity of the inner adherent (equal to that of steel in the present case). Substitution of Equation (6.2) and Equation (6.3) into Equation (6.1) yields the following expression for the total axial deformation u_{1T} of both segments 1 (the one shown in Figure 6.3 and its symmetric), as a function of the applied load F.

$$u_{1T} = 2u_1 = \frac{2L_1 F}{b t_1 E_s} \tag{6.4}$$

Generating a free body diagram of segment 2, shear traction forces develop at the interface of the strap and the adhesive layer. Applying symmetry conditions to segment 2 at y-axis, the eccentricity of these shear traction forces introduces a bending effect on the straps. This effect is very small since the lever arm (half of the strap thickness) is very small. The above fact has been verified from finite element analyses of the current problem, where it was shown that y-displacement of the free edge of the strap was negligible compared to the other displacements.

Moreover, strap bending affects more the peel stresses in the adhesive and not the overall axial stiffness of the joint which is the objective of the present analytical approach. Thus, by neglecting bending of the straps, it can be considered that segment 2 is deforming only in the axial (x) direction. Following the same procedure as that followed for segment 1 and taking into account that each strap transfers a load $F/2$, the following expression is derived for the total axial deformation of each strap:

$$u_{2\mathrm{T}} = 2u_2 = \frac{L_2 F}{b t_2 E_\mathrm{s}} \tag{6.5}$$

where t_2 is the thickness of each strap and E_s is the strap modulus of elasticity (equal again to that of steel in the present case). With regard to the behaviour of the adhesive, it is assumed that it deforms under a uniform shear stress state and shear forces are uniformly distributed over its interfaces with either the strap or the inner adherent. Thus the constant shear stress developed in the adhesive, τ_{av}, is given by:

$$\tau_{\mathrm{av.}} = \frac{F}{2bL_2} \tag{6.6}$$

whereas the axial deformation of the adhesive is

$$u_3 = t_\mathrm{a} \cdot \gamma \tag{6.7}$$

where, t_α is the thickness of each adhesive layer and γ the assumed uniform shear strain of the adhesive. Moreover, the shear stress of the adhesive can be expressed as

$$\tau_{\mathrm{av.}} = G\gamma \tag{6.8}$$

where G is the shear modulus of the adhesive material. Substituting Equation (6.7) and Equation (6.8) into Equation (6.6), the total axial deformation of the adhesive layers of the joint is given by the following expression:

$$u_{3\mathrm{T}} = 2u_3 = \frac{F t_\mathrm{a}}{b L_2 G} \tag{6.9}$$

According to the initially made assumption for a linear response of the DSJ, its load-axial deformation behaviour is described by the following simple formula:

$$u_\mathrm{T} = KF \tag{6.10}$$

where u_T is the total axial deformation of the DSJ and K its axial stiffness. Thus, taking into account that

$$u_T = u_{1T} + u_{2T} + u_{3T} \tag{6.11}$$

and substituting Equation (6.4), Equation (6.5) and Equation (6.9) into Equation (6.11) and the result into Equation (6.10), the following analytical expression for the axial stiffness K of the DSJ as a function of the material properties of its constituents and its geometric characteristics is obtained:

$$K = \frac{1}{b}\left[\frac{2 \cdot L_1}{t_1 \cdot E_S} + \frac{t_a}{L_2 \cdot G} + \frac{L_2}{t_2 \cdot E_S}\right] \tag{6.12}$$

This definition of the axial stiffness will be compared to the corresponding experimental results in section 6.24.

6.2.3 Numerical modelling of the SLJ and DSJ geometries

6.2.3.1 2D Plane stress finite element models

Two modeling procedures have been adopted for the numerical simulation of the SLJ and DSJ configurations in a 2dimensional space. Both procedures share common boundary/loading conditions and the element type used for all substrates, but differentiate on the finite element approach followed for modeling the adhesive layer, as presented in Figure 6.4 and Figure 6.5. Only one quarter of the DSJ has been modelled (Figure 6.5), due to the symmetry it presents and the corresponding boundary/symmetry conditions that have been applied.

The first procedure is based on modeling the adhesive layer with continuum elements, whereas the second is based on embedding the interface elements, described in Appendix A2, at the adhesive bondline (see Figure 6.4 and Figure 6.5). The first modeling procedure aims at providing only the deformation and stress field of the adhesive joint within the linear elastic region of the adhesive material, for reasons of comparison and validation with the respective results given by the second modeling procedure. The latter modeling approach utilizes the proposed EPZ laws or mixed-mode model to predict the linear elastic, non-linear elastic and plastic behaviour as well as damage initiation and propagation, all developing in the EPZ of the adhesive bondline.

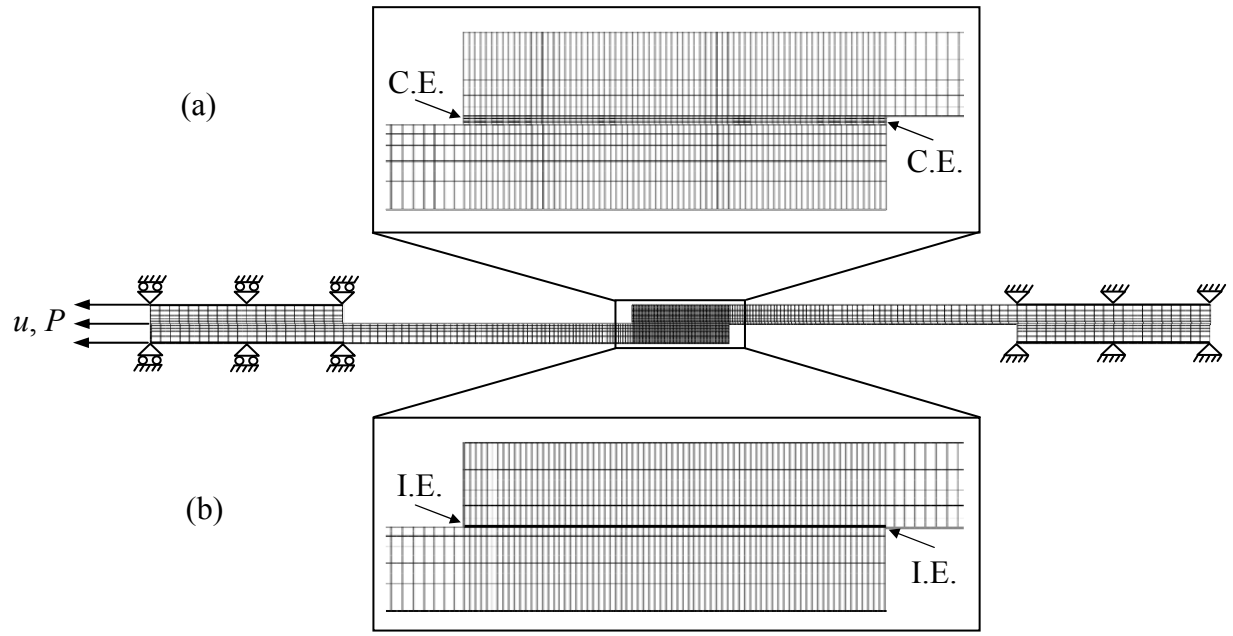

Figure 6.4: 2D plane stress finite element model of the adhesive layer of SLJ specimens: (a) with continuum elements - C.E. and (b) with interface elements - I.E..

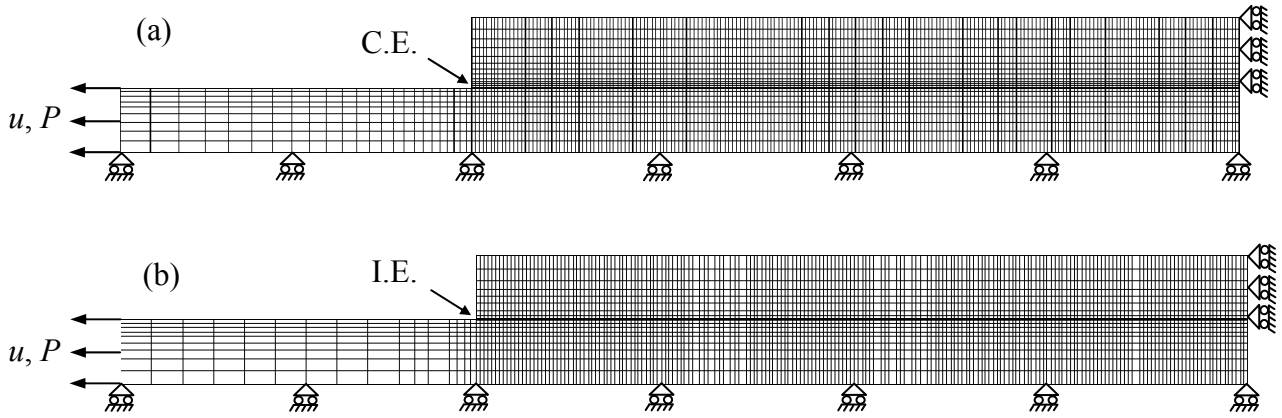

Figure 6.5: 2D plane stress finite element model of the adhesive layer of DSJ specimens: (a) with continuum elements - C.E. and (b) with interface elements - I.E..

The continuum 2D elements CPS8 available in the element library of ABAQUS® 6.10 have been used to model the substrates of the joints in both modelling procedures and the adhesive layer in the first modelling procedure. A comparative study between the FE results obtained with plane stress elements (CPS8) and plane strain elements (CPE8) has shown very small differences. Plane strain elements yield slightly increased force values (≈ 1.8%) for given applied displacements compared to the corresponding results from the plane stress elements. On the other hand, plane stress element results show better agreement with the respective experimental results for both cases considered (SLJ and DSJ), which is in agreement with Yang et al. (2001) for similar geometry tests. Since plane strain elements overestimate the stiffness of the models, plane stress elements have been utilized. Four layers of elements have been placed

through the adhesive thickness in the first modelling procedure, whereas the element length in the overlap area was 0.25 mm in all finite element models.

In order to account for geometrical and material nonlinearities, the Newton-Raphson method has been utilized together with a line search algorithm. A displacement controlled approach is utilized for aiding the convergence of the non-linear solution and for avoiding numerical instability issues involved in crack growth analyses, where softening behaviour is apparent.

6.2.3.2 3D Volumetric finite element models

Figure 6.6 and Figure 6.7 present the 3D finite element models constructed for the simulation of the SLJ and DSJ joints, respectively. For the case of the SLJ geometry, loading and boundary conditions have been applied on the areas of the tabs that are constrained in the grips of the testing machine, as shown in Figure 6.6. As far as the DSJ case is concerned, the 1/4 part has been modeled due to its geometrical, loading and boundary conditions symmetry and the corresponding constrains have been applied to its boundary domain, as depicted in Figure 6.7. Quadratic 20-node brick elements (C3D20) available in the ABAQUS® element library have been utilized for the metal substrates in both cases.

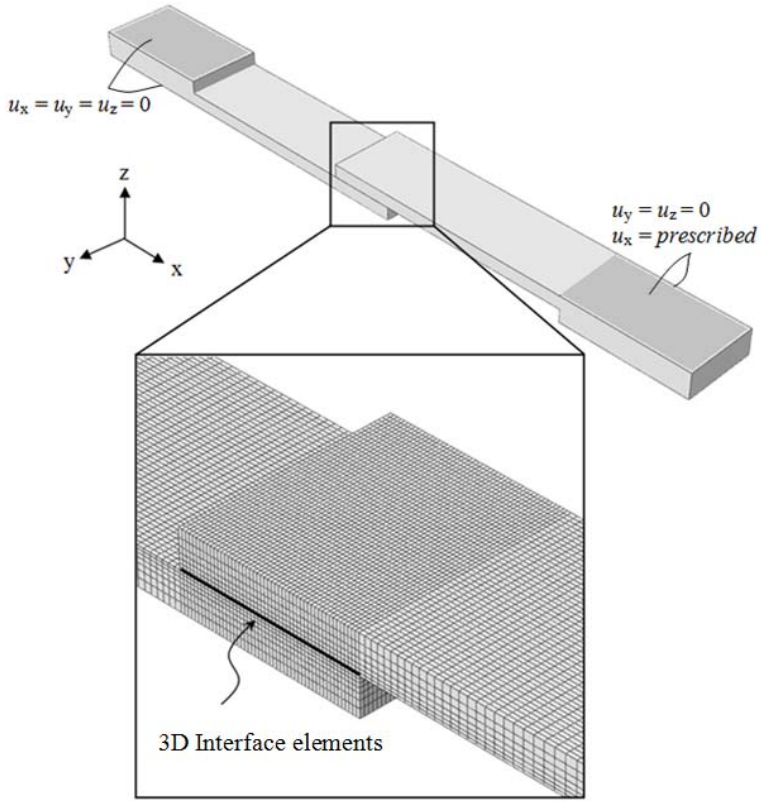

Figure 6.6: 3D finite element model of the SLJ – boundary conditions and detail of the overlap area.

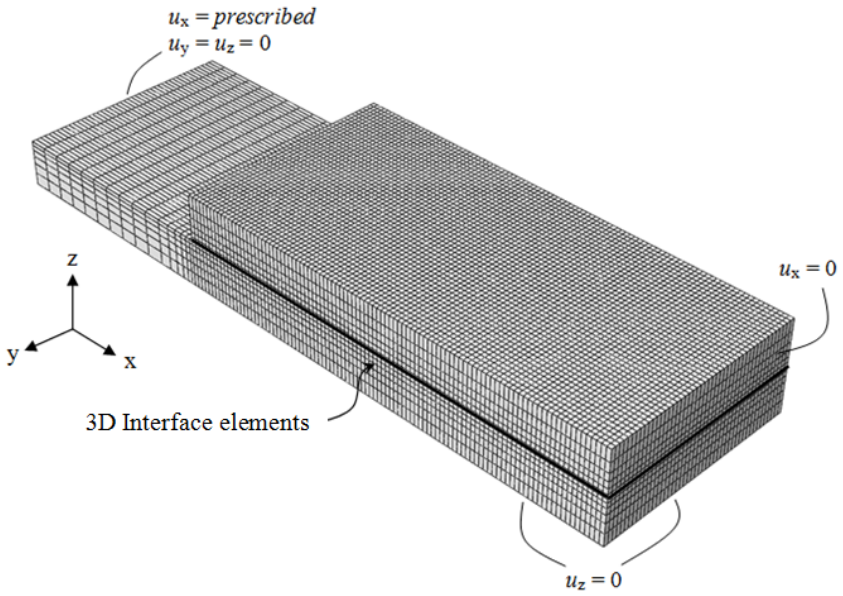

Figure 6.7: 3D finite element model of the DSJ.

The whole adhesive layer is represented by plane interface elements, described in Appendix A1, (placed between adjacent continuum elements in the overlap areas) and the proposed EPZ laws or mixed-mode model have been utilized for the description of their constitutive relation. The cohesive elements utilized have constant dimensions (0.5 x 0.5) mm^2 in the entire overlap areas. For the numerical integration of the stiffness matrix and the internal force vector, a 3 x 3 Gaussian quadrature rule has been used. The Newton-Raphson method has been utilized for the solution of the displacement control non-linear problem augmented by the line search algorithm.

6.2.3.3 Parameters of the proposed EPZ mixed-mode models

The implementation of the proposed mixed-mode EPZ model (2D or 3D), within the framework of the interface finite element formulation, requires the definition of the pure Mode I, pure Mode II and pure Mode III (for the 3D model) EPZ law parameters that describe the structural ductile adhesive adopted herein (HUNTSMAN Araldite 2015). In order to provide accurate measures of the required parameters of the Mode I, Mode II and Mode III loading and fracture, DCB and ENF specimens should be fabricated and tested, respectively, by utilizing the same materials and fabrication procedure as involved in the fabrication of the SLJ and DSJ specimens. Since, within the framework of the current work such experiments were not available, the corresponding parameters were taken from the literature. Thus, the parameters for the proposed pure EPZ laws in Mode, Mode II and Mode III are listed in Table 6.1. The parameters used for the Mode II law are also used for the Mode III law, since both refer to shear loading and fracture.

For the calculation of the initial elastic stiffness k_{I}, k_{II} and k_{III} in Mode I, II and III loading (see section 5.2), E_a was taken equal to 1850 MPa, G_a equal to 711.5 Mpa (magnitudes taken from the adhesive's manufacturer property datasheet – Araldite 2015, Huntsman Co.) and t_a equal to 0.5 mm. The critical tractions $\sigma_{c,I}$ and $\sigma_{c,II}$ and the fracture energy J_{Ic} were taken from the manufacturers' data sheet, which were measured from steel-to-steel adhesive joints. Parameters $\sigma_{c,I}$ and $\sigma_{c,II}$ have been taken equal to the strength of the adhesive material and the lap shear strength (measured from steel-to-steel lap shear specimens), respectively. The fracture toughness J_{IIc} was taken from de Moura et al. 2009. Additionally, parameters $\delta_{0,I}$, $\delta_{0,II}$ and $\delta_{0,III}$ ($\delta_{0,II} = \delta_{0,III}$) are needed for the complete definition of the proposed EPZ laws. Since, experimental information about these specific values is not provided, Equation (5.4) has been utilized for their derivation. In fact, the error e is a numerical utilized parameter without a physical interpretation, thus its selection is described in the following sections where the numerical results are presented together with the corresponding experimental ones. A value of the error e equal to 0.1% has been finally utilized for both joint geometries.

Table 6.1: Physical parameters of the proposed pure mode EPZ laws.

Mode i	k_i (N/mm^3)	$\sigma_{c,i}$ (MPa)	J_{ic} (N/mm)
I	3700	30.0	4.0
II	1423	18.5	4.7
III	1423	18.5	4.7

6.2.4 Experimental and Numerical results of the SLJ and DSJ geometries

6.2.4.1 Effect of the surface preparation technique

The global response of the tested DSJ specimens in terms of force-applied displacement curves is depicted in Figure 6.8. All six experimental curves of this figure denote an initially linear response, followed by increasing non-linearities, as the adhesive layer enters plasticity deformed and the joint begins to progressively debond. Moreover, it seems that the sandpaper treated specimens exhibit larger non-linearities, since their failure is more progressive than that of their corresponding GB specimens and two out of the three fail at larger axial displacements. On the contrary, grit blasted specimens exhibit a slightly greater stiffness than that of the sandpaper treated ones, leading also to slightly higher failure load values. The experimental measurements of Figure 6.8 exhibit a very good repeatability, apart from the response of one of the SP treated specimens, which will be explained later.

The results from applying the analytical Equation (6.10) in the present problem are also presented in Figure 6.8 (dotted line). It is evident that the analytical model predicts very well the initial part of the force-displacement response, being bounded by its own basic assumptions of linear elastic behaviour.

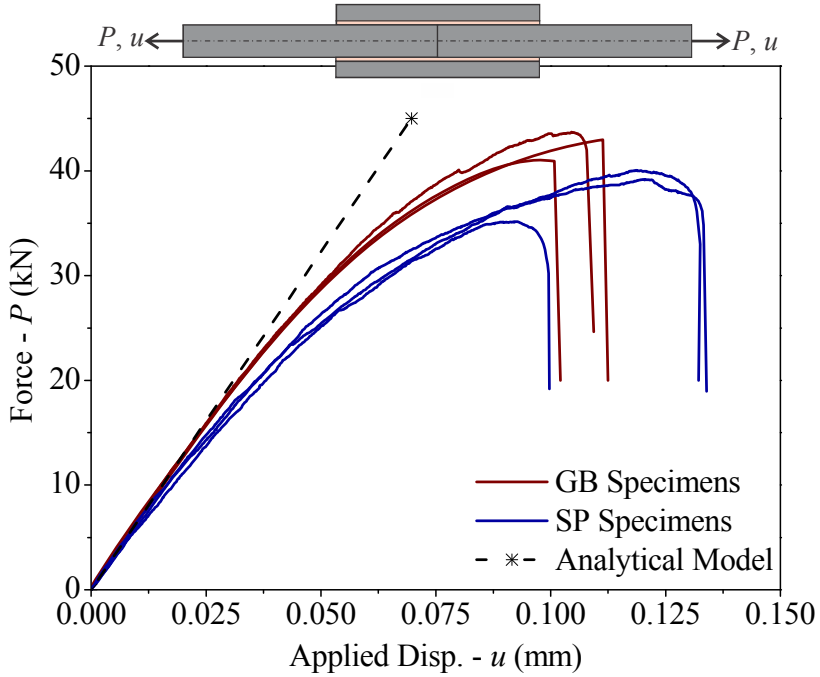

Figure 6.8: Force vs. applied displacement for the tested DSJ specimens.

Figure 6.9 presents the variation of strains measured by SG-1 on the strap and SG-2 on the inner adherent, respectively, as a function of the applied loading. Once more, strain measurements exhibit a good repeatability, except the same one case which will be discussed later. The behaviour of strains from both sensors is linear, as expected, reaching maximum values just before the failure of the joint. These maximum values are well below the yield point of steel (<< 2000 με). This behaviour is justified by the fact that the steel adherents are quite stiff and, therefore, the weak point of the joint is the adhesive layer which fails first. Thus the adherents are not heavily loaded, resulting in low maximum strains.

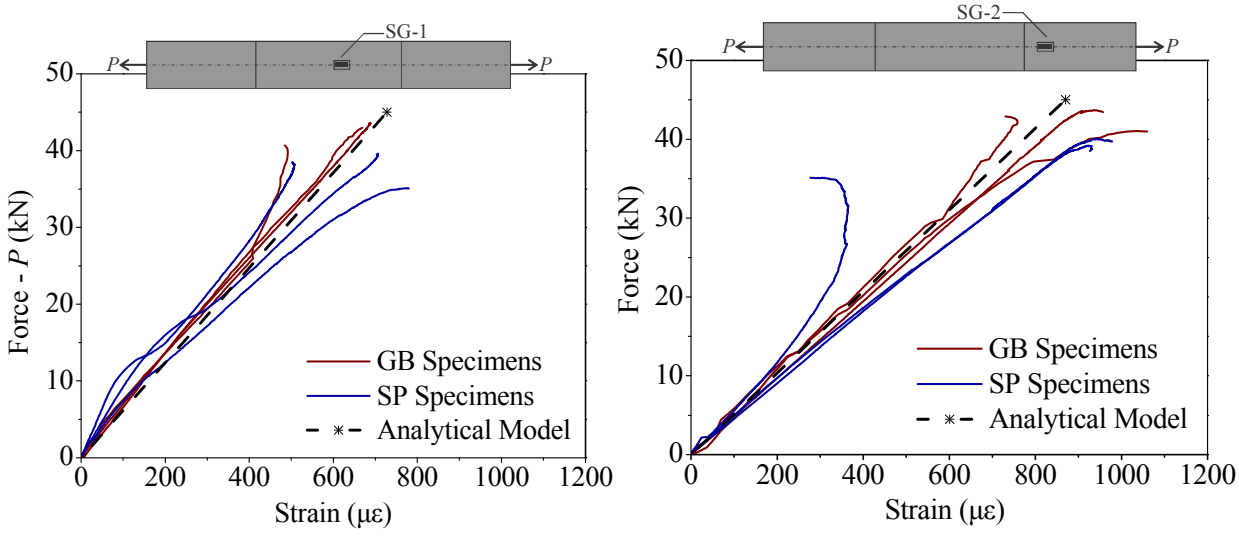

Figure 6.9: Variation of strains from SG-1 on the strap (a) and SG-2 on the inner adherend.

An exception to the above normal strains behaviour is that exhibited by the strain measured at location SG-2 of specimen SP-1 (blue curve that diverges from linearity in Figure 6.9b). Such a behaviour, where, after a certain load level, strain gradually stops to increase and begins to decrease, denotes a bending behaviour of the DSJ, with the compressive side being that of the strain gage (the upper one in Figure 6.1b). Taking into account the perfectly symmetric geometry of the joint with respect to *x*-axis (see Figure 6.1b), the only cause that can result in such a bending behaviour is the unsymmetric way of gradual failure of the adhesive layers, below and above the inner adherent. Thus, it seems that in specimen SP-1, the lower adhesive layers started to fail before and more rapidly than the upper ones, thus forcing the specimen to bend upwards, creating a compressive strain component on its upper surface, which, when superimposed to the global tensile strain, is responsible for the particular shape of the corresponding curve in Figure 6.9b. This bending behaviour had a negative effect on specimen SP-1, resulting in a decreased failure load compared to that of the other specimens which, more or less, exhibited a pure tensile behaviour up to their failure. As Figure 6.8 shows, this decrease is significant, being approximately equal to 12%. Therefore, the above example makes clear that the aim should always be a completely symmetric DSJ with identical and uniform adhesive layers on both sides of the inner adherent.

The analytical model of section 6.2.2 was also applied to calculate the strains in the strap (segment 2) and the inner adherent (segment 1) and the results are also plotted in Figure 6.9 (dotted lines). The very good prediction of the analytical model is evident, since, as discussed before, strains at these two locations behave almost linearly up to the joint failure.

6.2.4.2 Effect of the shape of the proposed laws – Uncoupled approach

This section aims at investigating the effectiveness of the selected shape of proposed EPZ laws, that is an exponential traction increase part followed by a linear traction decrease part (see section 5.2), through a plane strain analysis (2D space – 2D EPZ laws) of the SLJ and DSJ geometries, without considering their coupling and interdependency during the entire loading history. This task is important prior to the incorporation of the proposed EPZ laws in the developed mixed-mode model, which is necessary for the accurate prediction of the mixed-mode loading and fracture response of the adhesive layer.

For this purpose, the 2D finite element models of the SLJ and DSJ geometries, presented in Figure 6.4b and Figure 6.5b, have been adopted for finite element predictions. For the implementation of the proposed EPZ laws into the interface elements that describe the behaviour of an adhesive layer, four sets of characteristic constitutive parameters must be defined, separately for Mode I and II. The first set involves the initial elastic response of the adhesive and is described by the ratio between the Young's or shear modulus and the adhesive thickness $k_I = E_a / t_a$ and $k_{II} = G_a/t_a$, for Mode I and Mode II respectively, given in Table 6.1 .The rest three sets of cohesive parameters involve the critical stresses ($\sigma_{c,I}$ and $\sigma_{c,II}$) together with their respective

relative displacement values ($\delta_{0,I}$ and $\delta_{II,0}$) and the critical separations after which tractions vanish ($\delta_{c,I}$ and $\delta_{c,II}$). The latter have been defined implicitly through the J_{Ic} and J_{IIc} integrals, by solving Equation (6.9) with respect to $\delta_{c,I}$ and $\delta_{c,II}$ magnitudes. Since in this part the mixed-mode model is not included within the constitutive formulation of the interface elements, the material properties (EPZ parameters) listed in Table 6.1 do not yield accurate results and thus cannot be utilized as is.

In the independent and uncoupled formulation utilized herein, these parameters evolve together as a natural result of the interaction between the deformation of the substrates and the behaviour of the two separate cohesive laws. This means that the initially defined pure mode EPZ laws (together with their parameters), remain constant through the analysis procedure. By taking as granted the initial stiffnesses k_I and k_{II}, Mode I critical stress $\sigma_{c,I}$ (see Table 6.1) and $\delta_{0,I}$ and $\delta_{II,0}$ from de Moura et al. (2009), the remaining magnitudes were obtained by an inverse method, i.e. by fitting the numerically calculated load-displacement response of the SLJ and DSJ configuration over the respective experimentally measured data. Only one experimental case has been adopted from each joint case, both treated with grit blasting (GB) surface preparation technique.

Figure 6.11 illustrates a comparison between the load/displacement curves obtained from the SLJ and DSJ tests and the FEA results based on the proposed EPZ laws shown in Figure 6.10. It is not surprising that two separate EPZ law sets have been obtained (one for the SLJ and one for the DSJ model), since regardless the mixed mode response of the adhesive layer, the formulation of the EPZ laws remains uncoupled.

Both experimental curves obtained from SLJ and DSJ tests denote an initially linear response, followed by increasing non-linearities as the adhesive layer begins to substantially deform plastically.

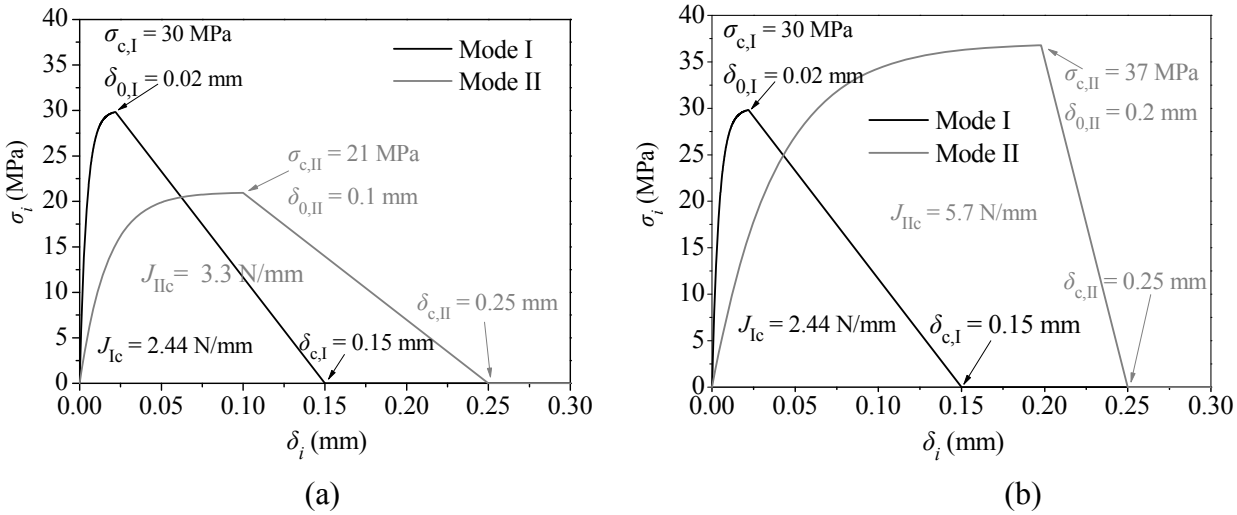

Figure 6.10: Proposed EPZ laws together with their corresponding parameters as obtained through a best fit analysis between numerical and experimental results of a SLJ (a) and DSJ (b) specimen.

Figure 6.11 shows that, although the numerical results were fitted to the experimental data by selecting appropriate values for some of the EPZ law parameters, the proposed exponential character of the proposed EPZ law proved adequate for modelling the elastoplastic behaviour of the ductile adhesive up to the maximum attained stress in the opening Mode I and the sliding Mode II responses. The DSJ attained much higher loads than the SLJ. This is reasonable, since the bonding surface of the DSJ is four times larger than that of the SLJ. Additionally, due to the symmetry of the DSJ configuration, the adhesive layer is stressed mostly in shear whereas the geometrical eccentricity of the SLJ leads to the development of cleavage stresses at the adhesive edge. Cleavage stresses are the most critical stresses that jeopardize the integrity of the joint by leading to premature failure. According to experimental observations and numerical predictions, in both cases and after the maximum attained load, the joints debonded in a sudden manner until complete failure. This debonding procedure is represented by the softening behaviour of the load/displacement curves after the maximum load. The sudden debonding behaviour was simulated with the use of a linear softening function which was incorporated separately in each of the EPZ laws describing pure mode failure. The FEA of the DSJ additionally captured the softening behaviour, as depicted in Figure 6.11b. The SLJ experimental curve exhibits a softening response characterized by a slower rate in comparison to the rate of the respective DSJ softening behaviour. In this case, the linear softening part of the EPZ law used for the simulation of the EPZ of the SLJ (see Figure 6.10a) in combination with the uncoupled approach, did not capture the softening behaviour of the experimentally obtained response curve, as shown in Figure 6.11a. Nevertheless it is essential to state that, instead of the shear stresses, the cleavage ones being developed at the adhesive edge are responsible for crack initiation, as cleavage stresses peak at 0.02 mm with a value of 30 MPa, whereas shear stresses peak at 0.1 mm having a value of 21 MPa. After crack initiation, total failure of the adhesive depends on the developed shear cohesive law.

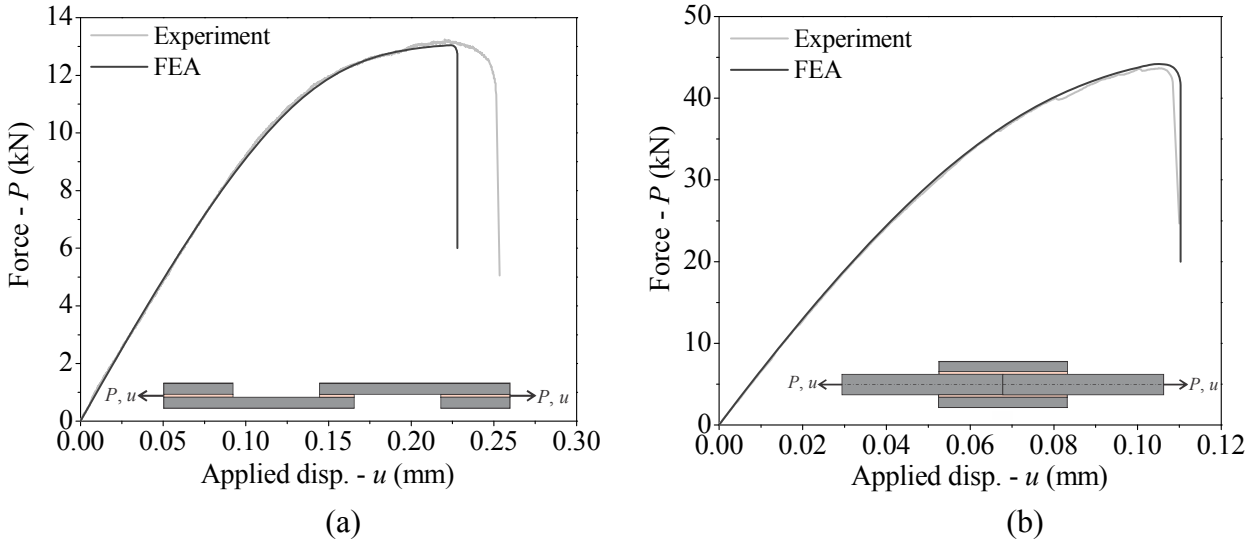

Figure 6.11: Experimental and numerical global response of a SLJ (a) and a DSJ (b) specimen.

On the other hand, although the DSJ configuration is a shear lap type of joint in which the adhesive is loaded mostly in pure shear, the Mode I failure process must be additionally incorporated into the mixed mode cohesive law in order to numerically capture failure initiation. Finally, the cohesive law in Mode II contributes mostly to the total energy release rate during the mixed mode fracture process of the DSJ, since J_{IIc} is almost twice as J_{Ic}.

6.2.4.3 Validation of the 2D and 3D proposed mixed-mode model – Coupled Approach

6.2.4.3.1 Global response of the SLJ and DSJ geometries

In contrast to the uncoupled approach of the EPZ laws followed in the previous section, in this section the proposed EPZ laws are utilized in a coupled form, according to the proposed 2D and 3D mixed-mode models described in sections 5.3 and 5.4, respectively, for the prediction of the SLJ and DSJ experimental results.

Initially the 2D mixed-mode model is considered for validation. For this purpose, the 2D finite element models of the SLJ and DSJ geometries, presented in Figure 6.4b and Figure 6.5b have been adopted for finite element predictions. The parameters that define the pure mode EPZ laws are the ones listed in Table 6.1, only for Mode I and Mode II. The obtained Finite Element Analysis (FEA) results are compared with the corresponding experimentally measured data for the SLJ and DSJ configurations in Figure 6.12.

The experimental measurements from all three tested specimens (all treated with grit blasting surface preparation technique) from each case respectively are plotted in this figure. It is noteworthy that the pure mode parameters given in Table 6.1 have been utilized for the FEA of both joint configurations. Additionally, parameters $\delta_{0,I}$ and $\delta_{0,II}$ are needed for the complete definition of the proposed EPZ laws. Since, experimental information about these specific values is not provided, Equation (6.4) has been utilized for their derivation. As described in section 5.2, these parameters are defined through the error e, which is a numerical parameter without a physical interpretation. Thus, their values are calculated through a best fit analysis between the corresponding numerical and experimental results, which has led to a common value for e equal to 0.1% utilized for the prediction of both joint geometries. It is noteworthy to mention that the experimental cohesive laws that describe Mode I (Ji et al. 2010) and Mode II (Leffler et al. 2007) loading and failure, even though obtained from different ductile adhesive systems (LOCTITE Hysol 9460 for the DCB tests and DOW Betamate XW1044-3 for the ENF tests) than the one utilized in this work (Huntsman Ltd. Araldite 2015), yield an error e equal to 0.08% and 0.1%, respectively, as derived through a best fit analysis. Despite the fact of the different adhesive systems used, the value of e obtained from the best fit analysis of both SLJ and DSJ models is equal to the corresponding one calculated from the best fit analysis of the Mode II experimental law (0.1%) and close enough to the one obtained from the Mode I law (0.08%). This is good evidence that the error value obtained from the best fit analysis of the SLJ and DSJ models is not

arbitrary. A sensitivity analysis regarding the effect of the error e value to the finite element predictions is given later on this work.

Figure 6.12 also compares the FEA results obtained by utilizing the trapezoidal EPZ laws within the framework of the mixed-mode model described in Campilho et al. (2008) and presented in Figure 2.13a in section 2.3.3.1. The corresponding parameters utilized are the same as those for the proposed EPZ laws (see Table 6.1). Parameters $\delta_{2,I}$ and $\delta_{2,II}$ corresponding to the second inflexion point of the trapezoidal EPZ laws have been taken equal to the respective $\delta_{0,I}$ and $\delta_{0,II}$ parameters calculated from the best fit analysis (through the error e). Thus, $\delta_{2,I}$ and $\delta_{2,II}$ have been taken equal to 0.0691 mm and 0.898 mm, respectively for both joint models.

Additionally, for reasons of completeness, the results obtained from the PRP (Park-Paulino-Roesler) cohesive model (see Figure 2.13b, Park et al. (2009)) have been also compared with the aforementioned numerical and experimental results in Figure 6.12. The PRP intrinsic cohesive model consists of potential-based polynomial laws that are formulated for predicting mixed-mode cohesive loading and fracture. The comparison of the PRP model with the proposed EPZ mixed-mode model aims at validating the effectiveness of the proposed formulation, since in the PRP model the separate fracture modes are coupled directly within the PRP potential without the use of damage or fracture criteria, as utilized in the proposed formulation (Equation (5.12) and Equation (5.18)). The physical parameters of the PRP cohesive model that must be defined are the normal and tangential cohesive strengths ($\sigma_{c,I}$ and $\sigma_{c,II}$ or σ_{max} and τ_{max} in Figure 2.13b, respectively) and the Mode I and II fracture energies (J_{Ic} and J_{IIc}), taken equal to those for the proposed EPZ laws (see Table 6.1). The initial elastic slope of the intrinsic PRP normal (Mode I) and tangential (Mode II) laws is calculated implicitly through the initial slope indicators $\lambda_n = \delta_{nc} / \delta_n$ and $\lambda_t = \delta_{tc} / \delta_t$, defined as the ratio of the critical crack opening to the final crack opening, as depicted in Figure 2.13b. In order to include the physical initial slopes k_I and k_{II} (see Table 6.1) in the PRP laws, the respective values of the λ_n and λ_t have been calculated, given the $\sigma_{c,i}$ and J_{ic} parameters. The corresponding values, utilized in the numerical analyses, are listed in Table 6.2.

Table 6.2: Parameters used for the PRP cohesive model.

$\alpha = \beta = 2$ (quasi-brittle)		$\alpha = \beta = 1.1$ (ductile)	
λ_n	λ_t	λ_n	λ_t
0.2084	0.1879	0.5771	0.5453

Moreover, two shape parameters (α and β) that control the material softening responses (brittle, quasi-brittle and ductile) must be defined, according to the PRP model. In the current work, two cases have been taken into account regarding the behaviour of the EPZ. The first case considers a brittle behaviour ($\alpha = \beta = 2$) and the remaining one considers a ductile behaviour ($\alpha = \beta = 1.1$). The values selected for the α and β shape parameters that represent the ductile

behaviour are the smallest possible, since the PRP cohesive laws cannot mathematically be defined for lower values.

According to Figure 6.12, apart from the relatively small numerical differences between the experimental registered curves from each specimen set, all three respective experimental curves share a common behaviour, which can be divided into three regions. The first region is described by a linear behaviour, followed by increasing non-linearities up to the load carrying capacity level of each joint, which bounds the second region of the curves. The third region is described by a softening behaviour, which denotes the inability of each joint to carry further load. In this region failure mechanisms are developing in the adhesive/substrate system, i.e. plasticity of the ductile adhesive, void nucleation in the adhesive, debonding at the adhesive/adherent interface, micro-cracking, etc.

As far as the FEA results obtained with the proposed EPZ laws are concerned, the initial linear and the following non-linear region depend thoroughly on the adhesive material elastoplastic response, described by the exponential behaviour of the EPZ laws, which yields very promising results (see Figure 6.12). On the other hand, the corresponding FEA results obtained with the trapezoidal laws capture the initial linear region but fail to capture the experimental non-linear region, in each case. As regards the PRP model FEA results, a very good agreement with the experimental results is observed. This agreement is better when utilizing shape parameters that represent brittle behaviour ($\alpha = \beta = 2$) rather than when utilizing shape parameters that represent ductile behaviour ($\alpha = \beta = 1.1$), particularly for the DSJ model (Figure 6.12b). A very good agreement is also observed in the response predicted from the proposed and PRP model up to the maximum experimental load, in both test cases considered. The behaviour of the response obtained from the PRP model after the maximum load is un-realistic, since, according to the experimental results, damage progression is characterized as rapid and not gradual as depicted in Figure 6.12. This behaviour is accurately predicted by the proposed EPZ model. The PRP model overestimates the maximum applied displacement (elongation at break), a magnitude of great significance when designing ductile adhesive joints.

Nevertheless, both EPZ models (proposed and trapezoidal) and the PRP model predict the experimental maximum attained load with very good accuracy for both joint configurations, as listed in Table 6.3. This conclusion validates the effectiveness of the proposed mixed-mode EPZ model in predicting the maximum attained load of a joint.

Table 6.3: Experimental and numerical strength of joints (kN).

	Experiments	Proposed laws		Trapezoidal laws		PRP model ($\alpha = \beta = 2$)		PRP model ($\alpha = \beta = 1.1$)	
		Value	% diff.	Value	% diff.	Value	% diff.	Value	% diff.
SLJ	13.4	13.0	2.1	12.9	2.5	12.86	4.0	12.79	4.6
DSJ	42.5	42.6	0.2	43.5	1.6	43.46	1.6	43.36	1.6

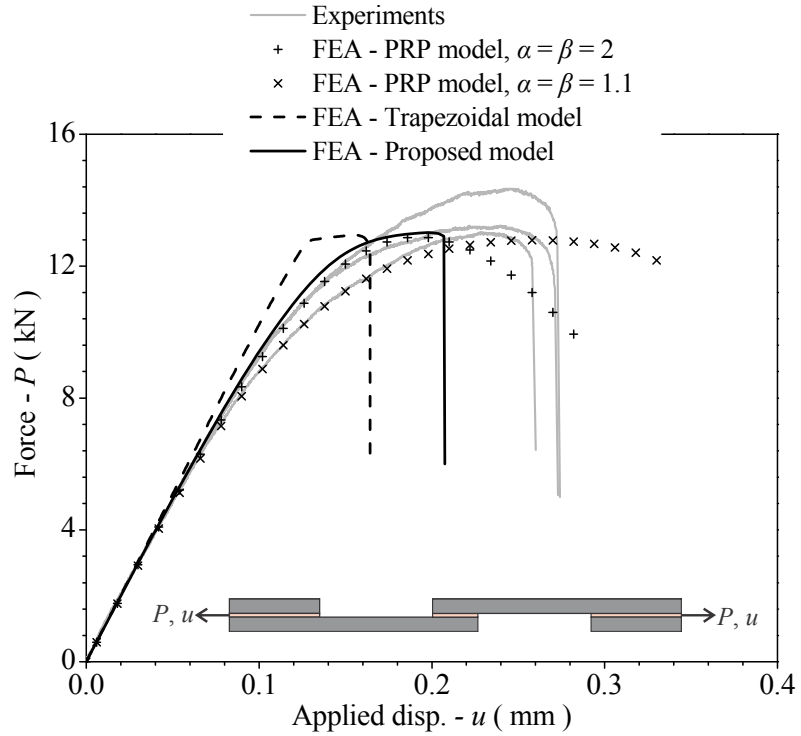

(a)

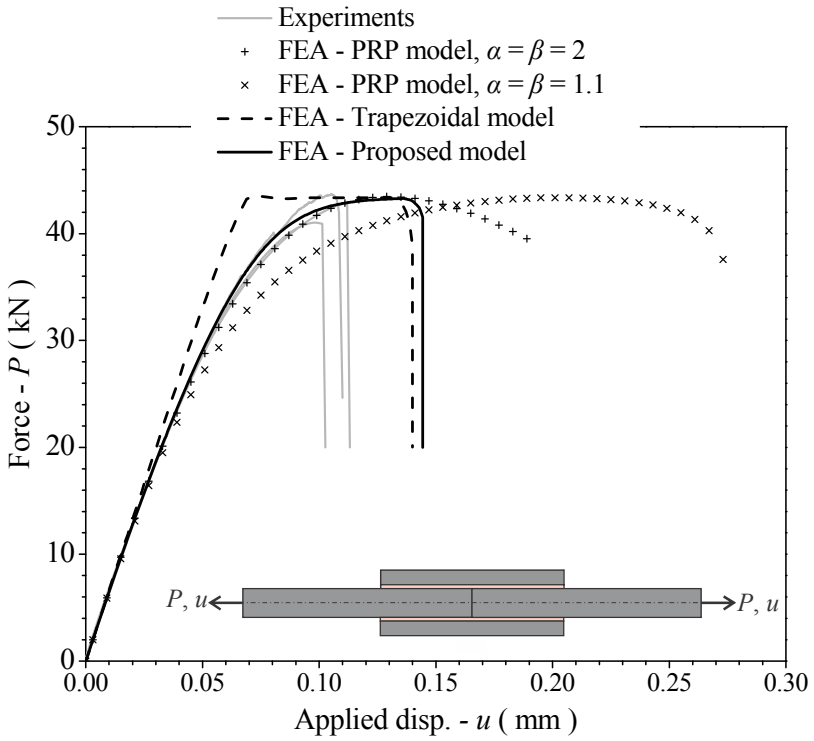

(b)

Figure 6.12: Global response of (a) SLJ and (b) DSJ, in terms of the applied displacement - u and reaction force - P, as experimentally registered and numerically calculated with the 2D proposed, trapezoidal EPZ mixed-mode model and PRP model.

During the tests, only elastic stresses were developed at the metal substrates of both joint types. The experimentally measured and numerically predicted strains, at the two locations of the DSJ specimens as depicted in Figure 6.1b (SG-1 on the strap and SG-2 on the inner adherent), are presented in Figure 6.13. Strain measurements exhibit a good repeatability, except one case of SG-1 strains shown in Figure 6.13a. The behaviour of strains from both sensors is linear, as expected, reaching maximum values just before the failure of the joint. These maximum values are well below the yield point of steel (<< 2000 με). This behaviour is justified by the fact that the steel adherents are quite stiff and, therefore, the weak point of the joint is the adhesive layer which fails first. Thus the adherents are not heavily loaded, resulting in low maximum strains. This elastic behaviour was accurately predicted by the FEA with the mixed-mode EPZ model.

The selection of a linear softening function for the description of the traction-separation relationship in Mode I and Mode II found to be very promising for the prediction of the failure process of the SLJ and DSJ, as shown in both Figure 6.12 and Figure 6.13. The FEA results obtained with the incorporation of the pure mode EPZ laws into the mixed-mode EPZ model are in very good agreement with the corresponding experimental ones.

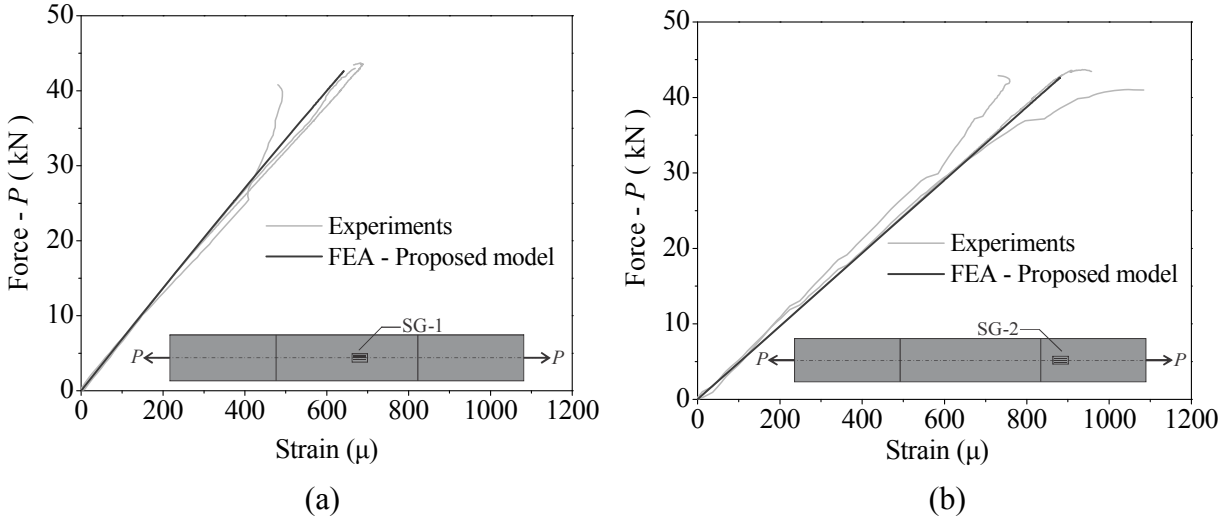

Figure 6.13:Reaction force vs. strains of the DSJ as experimentally registered and numerically calculated (a) on the strap-SG1 and (b) on the inner adherent-SG2.

In an effort to initially validate the proposed 3D mixed-mode model described in section 6.3, the SLJ and DSJ geometries have been considered for FEA in a 3-dimensional space. For this purpose, the 3D finite element models of the SLJ and DSJ geometries, presented in Figure 6.6 and Figure 6.7 have been adopted for finite element predictions. The parameters that define the pure mode EPZ laws are the ones listed in Table 6.1, for Mode I, Mode II and Mode III. The error *e* equal to 0.1% utilized in the previous 2D FEA has been also used for the proposed 3D mixed-mode model. The obtained FEA results from the 3D mixed-mode model are compared with the corresponding ones obtained from the 2D mixed-mode model (see Figure 6.12) and the experimentally measured data for the SLJ and DSJ configurations in Figure 6.14.

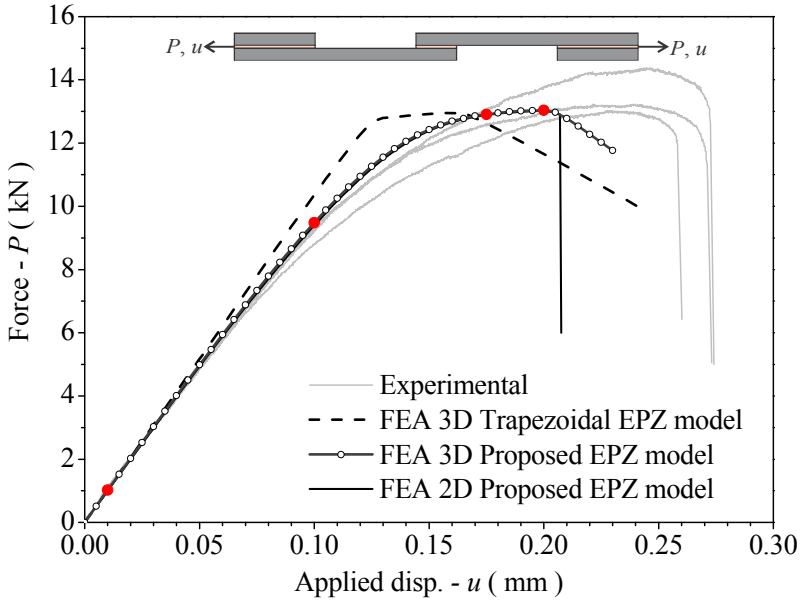

(a)

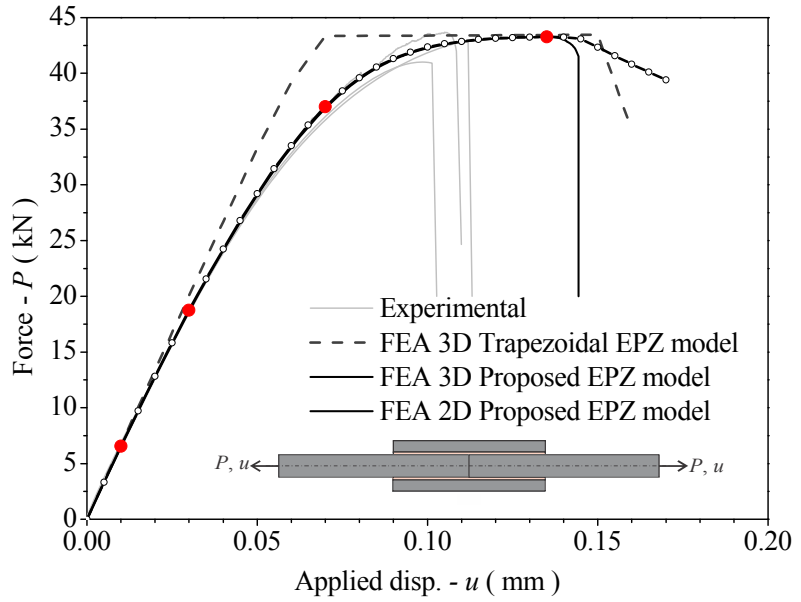

(b)

Figure 6.14: Global response of (a) SLJ and (b) DSJ, in terms of the applied displacement - u and reaction force - P, as experimentally registered and numerically calculated with the 2D, 3D proposed and 3D trapezoidal EPZ mixed-mode mode.

In this figure numerical predictions obtained from the 3D trapezoidal mixed-mode model given by Campilho et al. (2009a) are also presented. The parameters utilized for its definition are the ones listed in Table 6.1 and additionally $\delta_{2,I}$ and $\delta_{2,II}$ ($\delta_{2,III} = \delta_{2,II}$) have been taken equal to 0.0691 mm and 0.898 mm, respectively for both joint models, as for the 2D trapezoidal model.

According to Figure 6.14 in both joint cases considered, there is an identical match of the numerical global response obtained from the 2D and 3D proposed mixed-mode model, up to the maximum attained force. This is expected since the cases analyzed are in fact plane stress (in-plane loading) and thus the contribution of the Mode III loading and fracture to the mixed-mode

response of the adhesive layer is insignificant. This statement will be proven later on, where the variation of stresses on the adhesive layer is presented. The predicted softening behaviour (region after the joints' strength) by both the 3D proposed and the trapezoidal mixed-mode models is not accurate compared to the corresponding experimental behaviour and the one predicted with the 2D proposed model, for both joint geometries. The experimental softening is characterized as sudden and dynamic. However, the 2D proposed model captures this sudden drop in the force. It can be assumed that the Mode III stresses, that is out-of-plane shear stresses, introduced with the implementation of the 3D proposed or trapezoidal models in these plane stress problems are responsible for the smooth drop of the force after the attainment of its peak value.

6.2.4.3.2 Sensitivity of the error parameter

As aforementioned, the physical parameters of the pure mode proposed EPZ laws utilized for the FEA of the SLJ and DSJ configurations are listed in Table 6.1. In these particular cases, magnitudes $\delta_{0,i}$ (i = I, II and III) are unknown parameters, since an experimentally measured T-S law is not available for pure Mode I and II loading and fracture of the bi-material system. Thus, Equation (6.4), which relates $\delta_{0,i}$ to the corresponding $\sigma_{0,i}$ magnitude through the error e, has been utilized. A parametric analysis of the SLJ and DSJ FEA results has been carried out investigating the sensitivity of the error value e, based on the 2D proposed EPZ mixed-mode model. The corresponding results are presented in terms of the global response of the joints in Figure 6.15. The pure mode EPZ law parameters utilized are the ones listed in Table 6.1, whereas three values of the error e have been taken into account in the parametric analysis, e.g. 1%, 0.1% and 0.01%. It must be noted that in all three cases the same fracture toughness value J_{ci} (i = I, II) has been utilized.

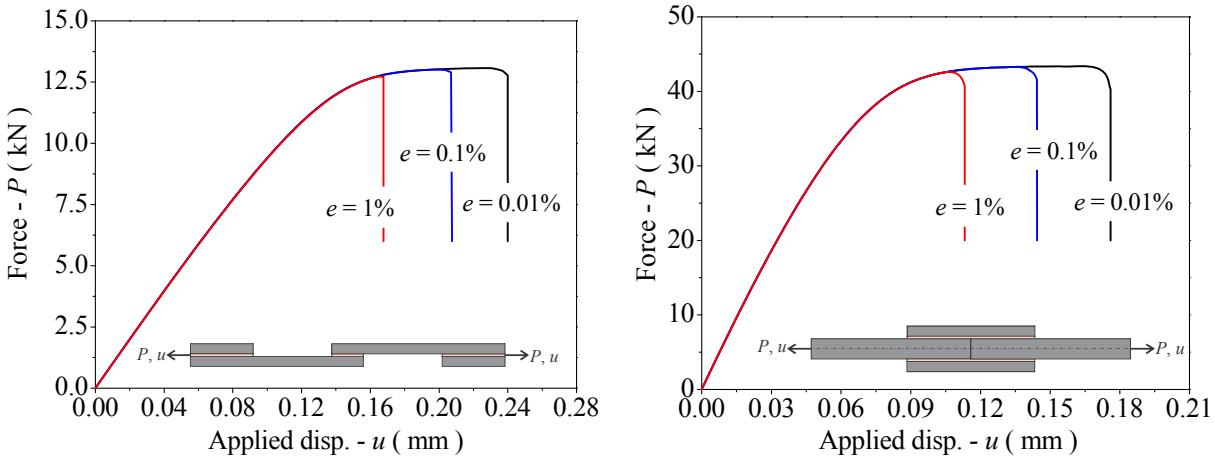

Figure 6.15: Sensitivity analysis results of the error value e utilized in the FEA of the SLJ (a) and the DSJ (b).

As concluded from the FEA results (see Figure 6.15) the value of the selected error *e* has a small effect on the maximum attained force, whereas it has a higher effect on its corresponding displacement of each joint configuration. From the results obtained in the framework of the sensitivity study and from the comparisons between the experimental and FEA results, it can be concluded that an error *e* value equal to 1% results in an accurate prediction of the joint strength (in terms of the maximum load carrying capacity) and in a conservative prediction of the corresponding displacement at failure. When designing an adhesive joint with respect to its attained load (e.g. strength), the proposed EPZ model yields very promising results, since an error *e* value ranging from 0.01 to 1% does not affect the linear and the non-linear load path (see Figure 6.15) up to the strength limit. This is significant during the analysis and design of a ductile adhesive joint, because the yield initiation (point where the non-linear region initiates in the *P-u* plots) is usually taken as the load allowable limit.

6.2.4.3.3 Continuum and EPZ linear elastic stresses

In order to yield more confident conclusions regarding the capabilities of the proposed mixed-mode EPZ model, some further insight has been given in the developed stress field within the bondline area. The stresses in the adhesive bonded joints are being transferred from one substrate to the other through the adhesive layer. For this purpose, comparisons between the FEA results obtained from the two modeling procedures provided in section 6.2.3.1 are presented. In fact, the FEA results of the models of the SLJ and DSJ configurations presented in Figure 6.4 and Figure 6.5 are given within the linear elastic region of the adhesive material. Thus, for the models with continuum elements of the adhesive layer (see Figure 6.4a and Figure 6.5a) only the adhesives' elastic properties were utilized during the analyses.

Figure 6.16 and Figure 6.17 compare the von Mises stress variation in the vicinity of the overlap area of the SLJ and DSJ models, respectively, as calculated with the utilization of continuum and interface elements for the adhesive layer. The same stress contour range has been used in each corresponding case, in order to provide qualitative comparisons.

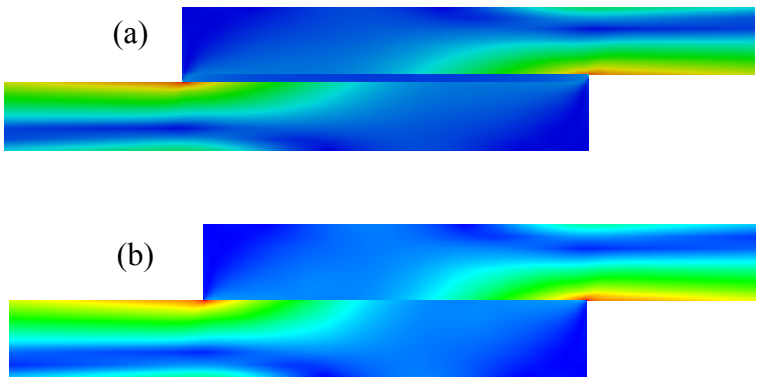

Figure 6.16: Von Mises stress distribution developed in the linear elastic region of the SLJ configuration, modeled with (a) 2D continuum elements and (b) interface elements.

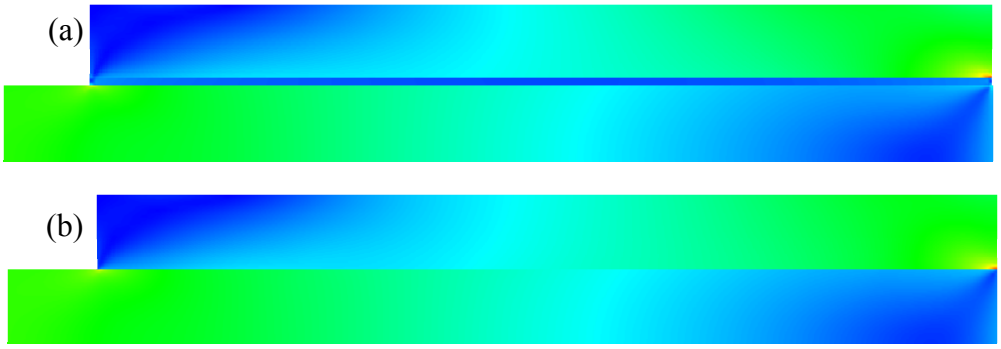

Figure 6.17: Von Mises stress distribution developed in the linear elastic region of the DSJ configuration, modeled with (a) continuum elements and (b) interface elements.

The continuum elements model, by its nature, provides the variation of stresses both through the thickness and along the length of the adhesive layer, whereas the interface elements model provides stress variations only along the bondline. Within the latter model, stresses are transferred between the substrates by means of tractions that obey the proposed EPZ laws and apply on the interface. A study of Figure 6.16 and Figure 6.17 reveals that the stress distributions are almost identical between each other in each case. This conclusion verifies the accuracy of the proposed FEA model in the linear elastic region.

Apart from the contour plots presented, which in fact provide a qualitative representation of the developed stress field, an effort to compare the peel and shear stress magnitudes as they vary in the bond area, is made. For this purpose, the peel and shear stress distribution along the bondline as a function of the non-dimensional overlap length (x/L) is plotted for the case of the SLJ and DSJ in Figure 6.18 and Figure 6.19, respectively. These results are calculated at the load levels of 1 kN and 2 kN for the SLJ and DSJ, respectively. Normal σ_I and tangential σ_{II} tractions obtained from the interface elements model are denoted as σ_y and τ_{xy}, respectively, in Figure 6.18 and Figure 6.19, according to the planes stress models.

The stress distributions resulting from the FEA of the models which utilize continuum elements for the adhesive layer are taken from a path lying at the midline of the thickness of the adhesive layer. The start point of the path ($x = 0$) is at the left hand side of the adhesive layers' edge, whereas the end point is at the adhesive layers' opposite edge ($x = L$) for both joints, as presented in Figure 6.18 and Figure 6.19. The magnitude L denotes the overlap length, where for the SLJ this magnitude equals to 25 mm and for the DSJ equals to 50 mm. In the formulation presented in section 5.2, it is assumed that negative peel stresses do not induce damage and are treated as contact stresses described by Equation (5.2). Thus, compressive peel stresses (contact stresses) calculated from the interface elements are not presented in Figure 6.18a and Figure 6.19a, since they do not represent the true stress state of the adhesive material, in contrast with the results calculated from the continuum elements used for the adhesive.

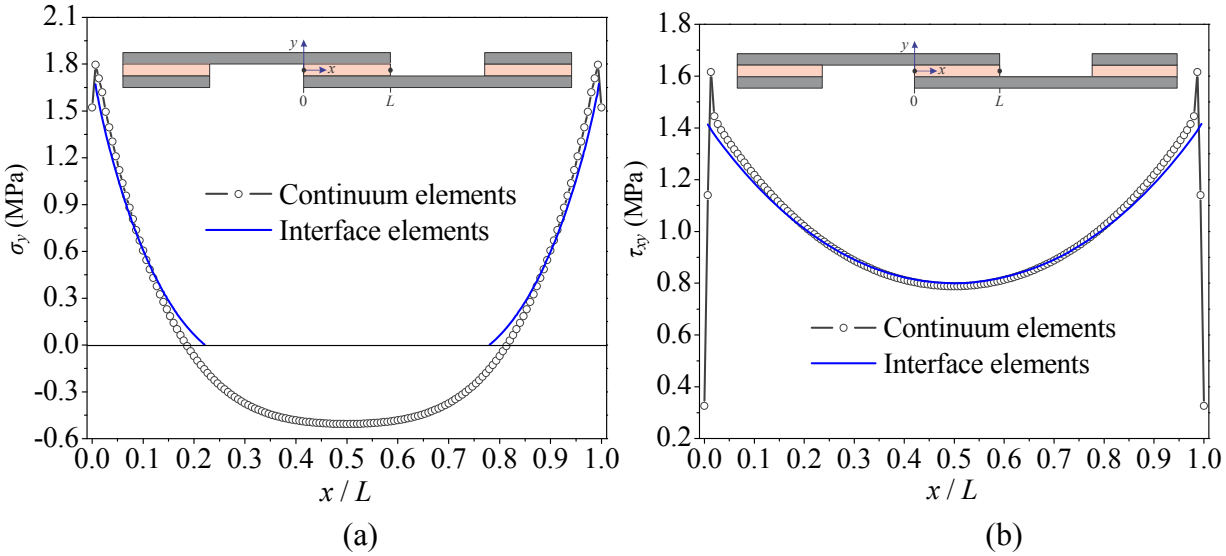

Figure 6.18: Variation of (a) peel σ_y and (b) shear τ_{xy} stresses along the bondline of the SLJ.

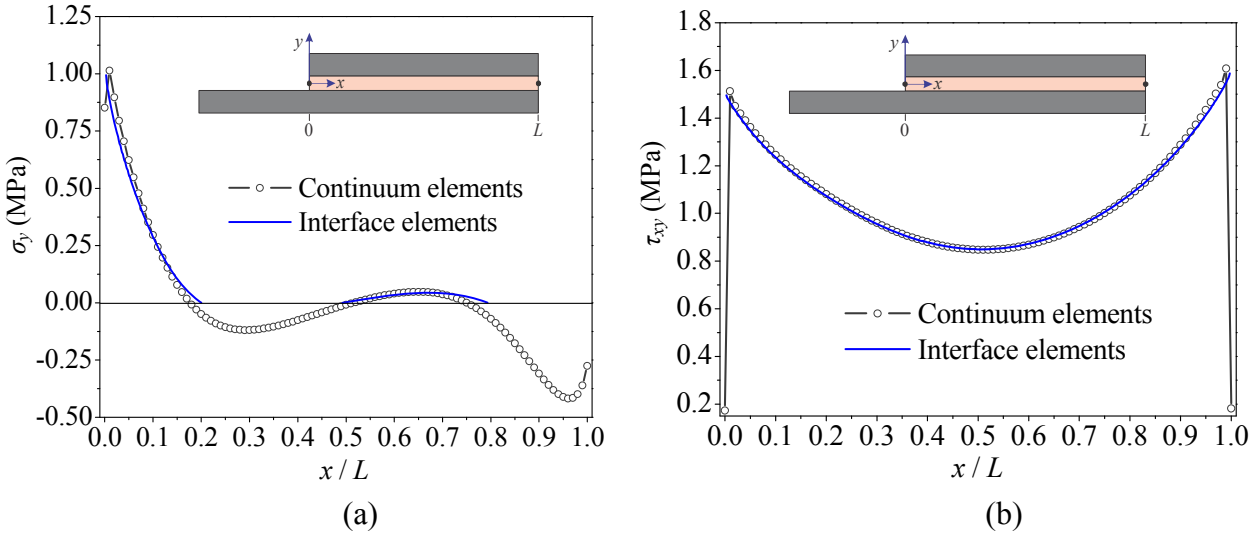

Figure 6.19: Variation of (a) peel σ_y and (b) shear τ_{xy} stresses along the bondline of the DSJ.

The FEA results obtained with the implementation of the mixed-mode EPZ model show good agreement with the respective results obtained with continuum elements for the adhesive layer, in term of both shape and magnitude along the overlap length, particularly near the adhesive edges where cracks initiate. The peel and shear stress free boundary conditions at the edges of the adhesive are captured when using continuum elements for the adhesive material. On the contrary, interface elements fail to capture this behaviour. This is expected, since the tractions being developed in the embedded process zone, depend on the corresponding separations, which are based on the deformation of two adjacent continuum elements. Thus, in the linear elastic region, only zero separations would yield zero tractions. In the case of the SLJ, both peel and shear stresses (see Figure 6.18) are symmetric about the middle of the overlap length (at x = 12.5 mm) and attain their maximum values at the free edges of the adhesive layer,

that is at x = 0 and 25 mm. The maximum percentage difference of the shear stresses calculated with the two different modeling procedures does not exceed 7.5%. On the other hand, shear stresses peak at the middle of the DSJ model (right edge) at $x = L$. The distribution of the shear stresses along the overlap length is in excellent agreement between both FEA models of the DSJ (Figure 6.19b). Nevertheless, the peak peel stresses obtained from interface elements are accurately predicted at the adhesive edges for the SLJ (Figure 6.19a) and at the left edge of the DSJ (Fig. 16a). The differences in these graphs regarding the points where stresses change sign are attributed to the effect of compressive stresses to the through the thickness stress variation, which is not included in the interface element formulation.

6.2.4.3.4 EPZ stress distributions on the bond area

This section aims at providing the calculated stress fields on the adhesive area domains of the SLJ and DSL models, as calculated with the 3D proposed EPZ mixed-mode model. Within the linear elastic region, where the developed tractions are analogous to the separations through the k_I, k_{II} and k_{III} stiffness constants, the resulting von Mises equivalent stresses developed at the steel adherents of the SLJ and DSJ configurations are presented in Figure 6.20.

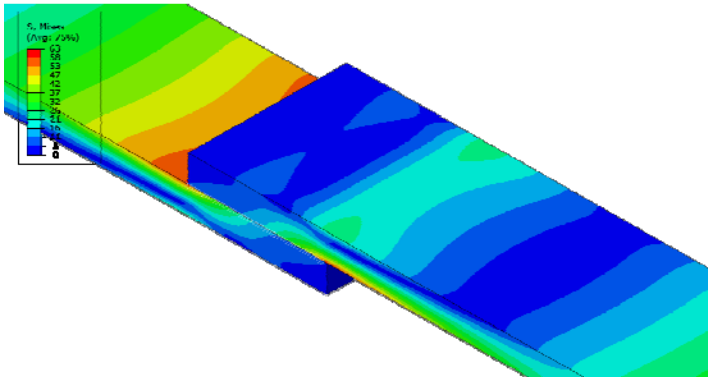

(a)

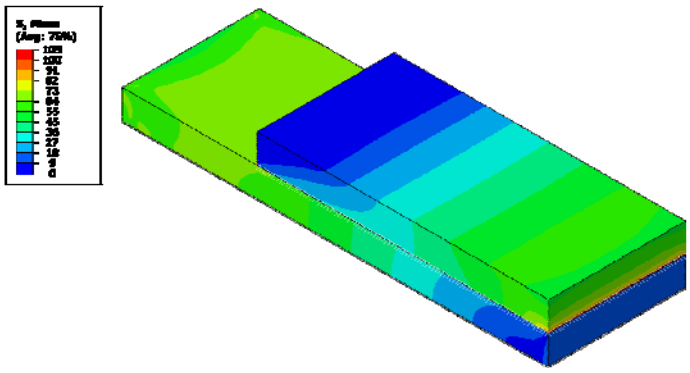

(b)

Figure 6.20: 3D Von Mises stress distributions calculated within the linear elastic range of the adhesive material of the SLJ (a) and DSJ (b) model.

For the presentation of the calculated stress fields, 2-dimensional contour graphs have been utilized with normalized axes, as schematically shown in Figure 6.21 for the SLJ and the DSJ configurations. Peel stress σ_z, in-plane shear τ_{xz} and out-of-plane shear τ_{yz} stresses correspond to the Mode I, II and III loading and failure modes, respectively. It is reminded that, since 1/4 of the DSJ configuration has been modeled, corresponding results are presented on half of the DSJ bond area.

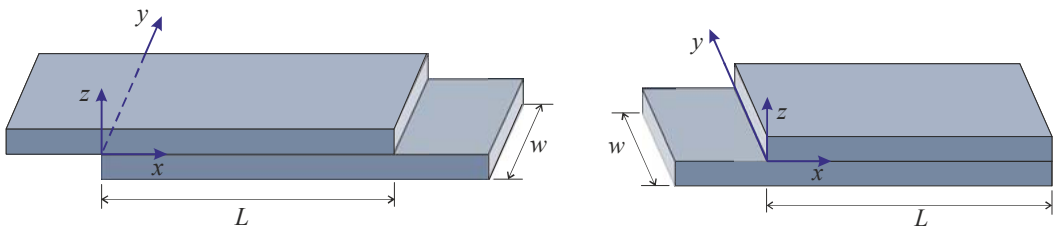

(a) (b)

Figure 6.21: Dimensions and coordinate system of the overlap area of the SLJ (a) and the DSJ (b) configurations.

Figure 6.22 and Figure 6.23 present the σ_z and τ_{xz} stress variations at three levels throughout the non-linear loading history of the SLJ model; at 0.01 mm (very early, linear phase), at 0.1 mm (when response starts to deviate from linearity) and at 0.2 mm (near the maximum load). Figure 6.24 presents the out-of-plane shear stress τ_{yz} variation only for the last level, since these stress values are very small.

At a first glance, the peel and in-plane shear stresses are symmetrical both with respect to x direction (at $y/w = 0.5$) and with respect to y direction (at $x/L = 0.5$). On the other hand, out-of-plane shear stresses are anti-symmetrical, a behaviour which is reasonable since the SLJ geometry is anti-symmetric by nature. The linear elastic σ_z and τ_{xz} stress variations (Figure 6.22a and Figure 6.23a) present a peak at the middle of the two opposite x-edges (x/L = 0 and 1), reducing in a non-linear manner as x/L tends to 0.5. More specifically, in this early stage peel stresses are negative in most of the adhesive area, a fact that denotes contact conditions, whereas in-plane shear stresses are very small. At the next evaluation point (u = 0.1 mm, Figure 6.22b and Figure 6.23b), negative peel stresses cover a slightly smaller area than before, whereas in-plane shear stresses have redistributed and peak at the four corners of the adhesive area. At the maximum joint strength point (u = 0.2 mm, Figure 6.22c and Figure 6.23c), lower value peel stresses are generally obtained, with the negative stresses denoting contact developing in a quite smaller area than before. The corresponding in-plane shear stresses attain their maximum values (18.5 MPa) in most of the adhesive area, becoming lower near the edges in x-direction (x/L = 0 and 1). This maximum value is equal to the shear strength of the adhesive $\sigma_{c,II}$ (see Table 6.1), a fact that shows that the SLJ configuration is shear dominated. The out-of-plane shear stresses τ_{yz}, presented in Figure 6.24, remain at very low levels (0.75 MPa) and thus can be characterized as elastic during the whole SLJ's loading history. In fact τ_{yz} stresses do not contribute to the loading and failure of the adhesive layer.

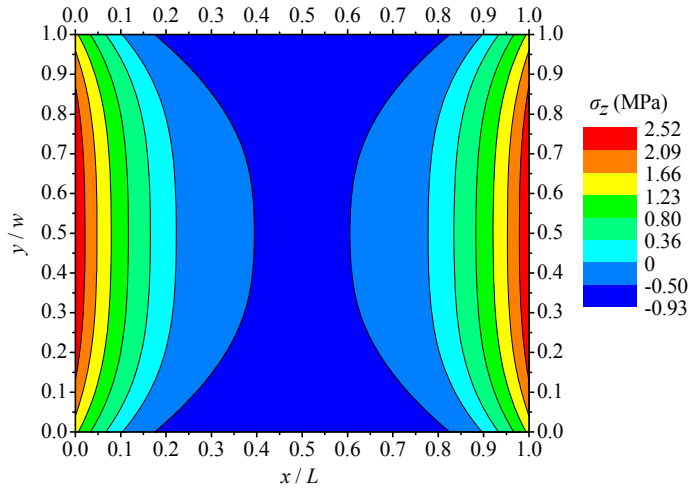

(a)

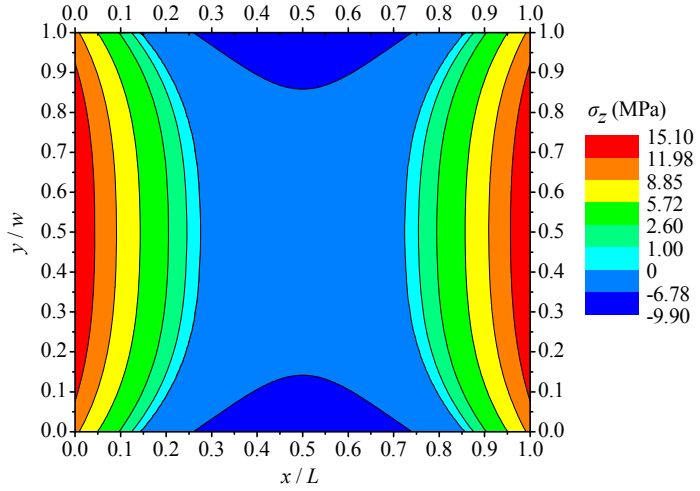

(b)

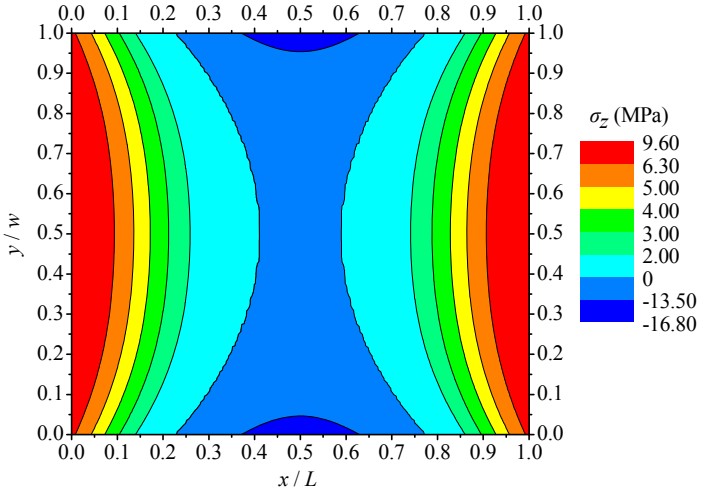

(c)

Figure 6.22: Peel stresses σ_z distributions over the adhesive area of the 3D SLJ model for applied displacement u equal to 0.01 mm (a), 0.1 mm (b) and 0.2 mm (c).

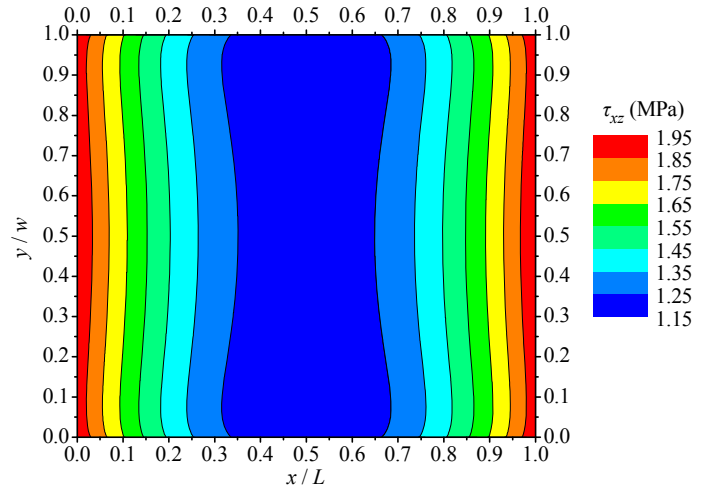

(a)

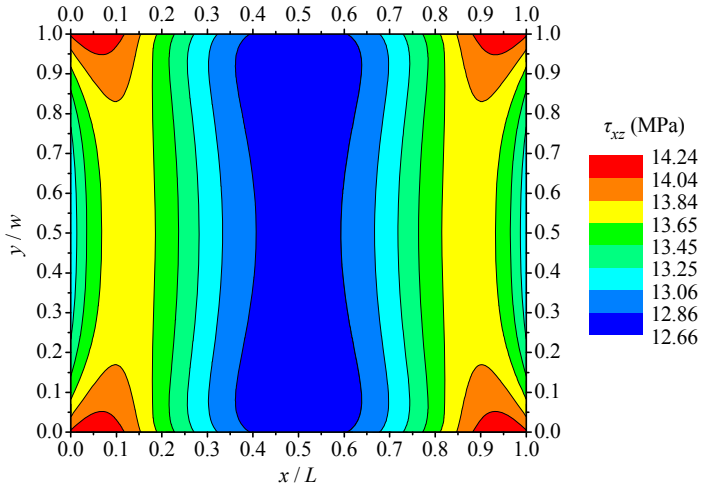

(b)

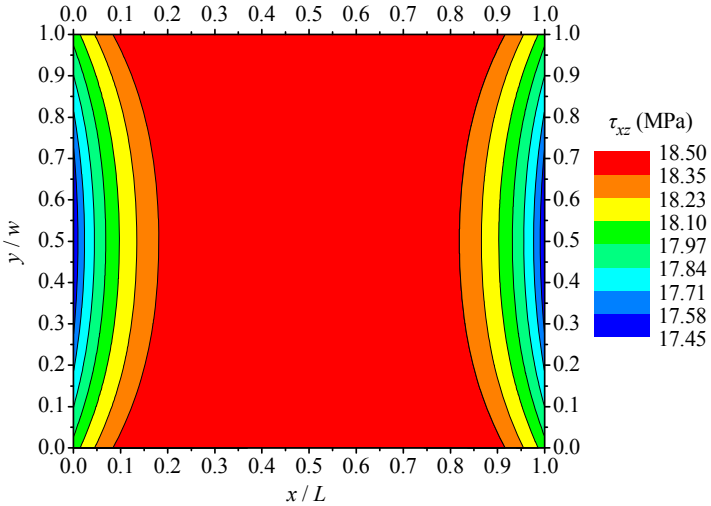

(c)

Figure 6.23: In-plane shear stresses τ_{xz} distributions over the adhesive area of the 3D SLJ model for applied displacement u equal to 0.01 mm (a), 0.1 mm (b) and 0.2 mm (c).

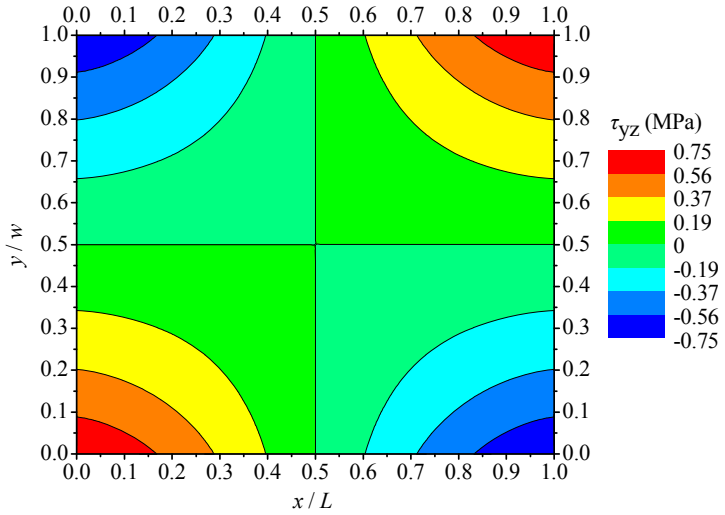

Figure 6.24: Out-of-plane shear stresses τ_{yz} distributions over the adhesive area of the 3D SLJ model for applied displacement u equal to 0.2 mm.

Same as before, Figure 6.25 and Figure 6.26 present the peel, σ_z, and the in-plane shear, τ_{xz}, stress variations at three levels throughout the non-linear loading history of the DSJ model; at 0.01 mm (very early, linear phase), at 0.07 mm (when response starts to deviate from linearity) and at 0.11 mm (near the maximum load). Figure 6.27 presents the out-of-plane shear, τ_{yz} , stress variation only for the last level, since these stress values are very small. As a general observation, the peel and in-plane shear stresses are symmetrical both with respect to x direction (at $y/w = 1$) and with respect to y direction (at $x/L = 0.5$), reminding that only half of the bond area is shown in these figures. The out-of-plane shear stresses however, are symmetrical with respect to x direction (at $y/w = 1$) and anti-symmetrical with respect to y direction (at $x/L = 0.5$). The linear elastic σ_z stresses (Figure 6.25a) peak at the middle of the adhesive's free edge ($x/L = 0$, $y/w = 0.5$) and are being reduced in a non-linear manner as x/L tends to 0.2. These stresses are negative in most of the adhesive area, a fact that denotes contact conditions. Within the area between $x/L = 0.51$ and $x/L = 0.76$, positive peel stresses develop, that remain in low levels compared to the maximum ones. The in-plane elastic shear stresses τ_{xz} (Figure 6.26a) develop in the entire bond area and peak at the middle of the joint (at $x/L = 1$).

At the second evaluation point ($u = 0.07$ mm), positive peel stresses (Figure 6.25b) develop in a larger area near the adhesive edge (from $x/L = 0$ to 0.33) when compared to the corresponding stress field in Figure 6.25a. Also, the positive peel stress area between $x/L = 0.51$ and $x/L = 0.76$ vanishes. The peak values of the in-plane shear stresses at that point (Figure 6.26b) are again constrained at the middle of the joint (at $x/L = 1$) and are being reduced towards position $x/L = 0.5$.

At the maximum joint strength point ($u = 0.11$ mm, Figure 6.25c and Figure 6.26c) peel stresses maintain their peak values at $x/L = 0$ and develop in an extended area up to $x/L = 0.4$. The peak stresses at $x/L = 0$ are equal to 8.6 MPa, small compared to the tensile strength of the adhesive $\sigma_{c,I}$, which is equal to 30 MPa (see Table 1). The in-plane shear stresses τ_{xz} redistribute in a way that are reduced in the vicinity of $x/L = 0$ and $x/L = 1$ and maximize in the internal bond

area (from x/L = 0.15 and x/L = 0.91). The maximum τ_{xz} values are equal to 18.31 MPa, a value close enough to the shear strength of the adhesive $\sigma_{c,II}$ (18.5 MPa). According to this last note, DSJ geometry can be characterized as a shear dominated joint type. The out-of-plane shear stresses τ_{yz}, presented in Figure 6.27, remain at very low levels (0.99 MPa) and thus can be characterized as elastic during the whole DSJ's loading history. As was the case for the SLJ configuration too, stresses τ_{yz} do not significantly contribute to the loading and failure of the adhesive layer.

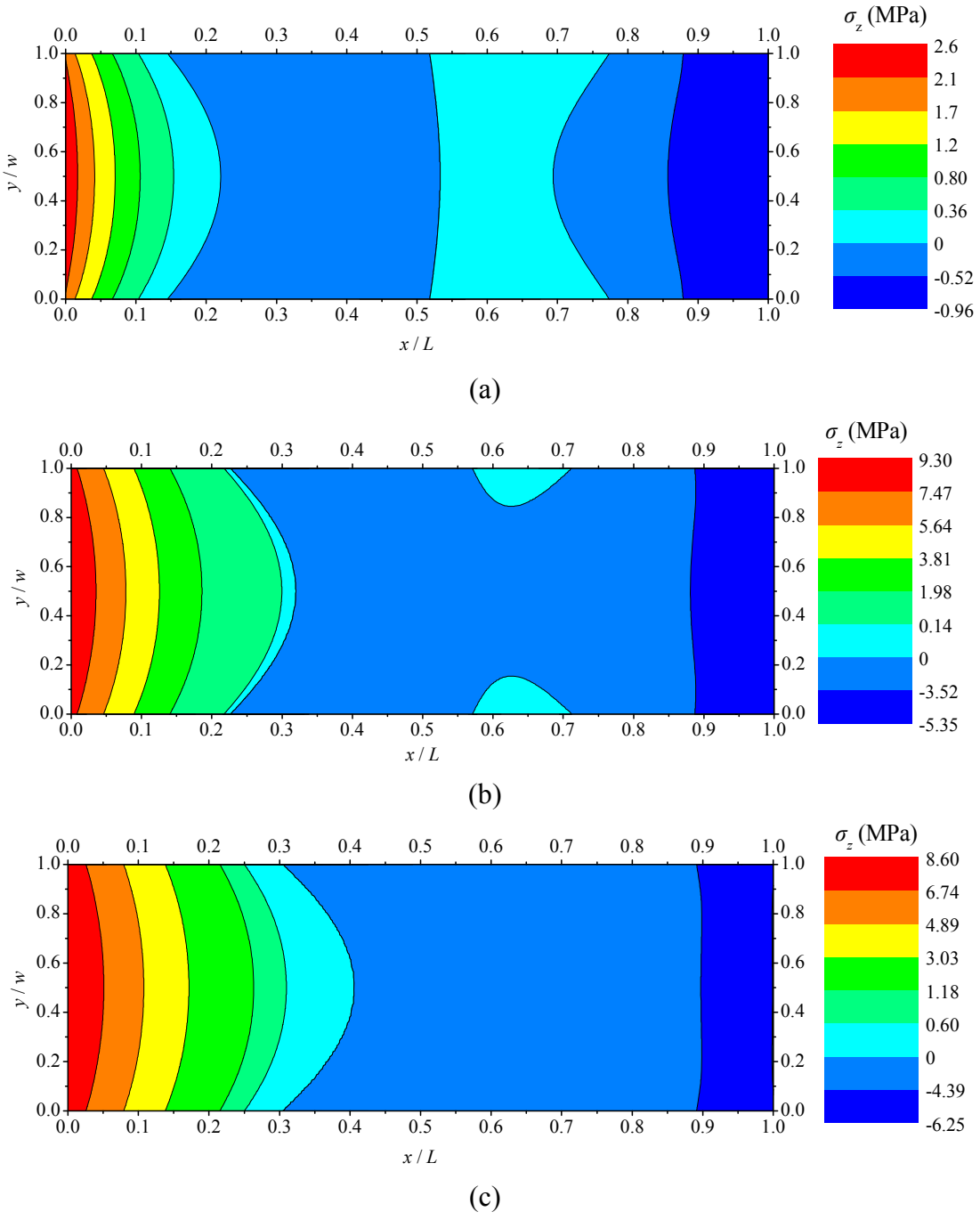

Figure 6.25: Peel stresses σ_z distributions over the adhesive area of the 3D DSJ model for applied displacement u equal to 0.01 mm (a), 0.07 mm (b) and 0.11 mm (c).

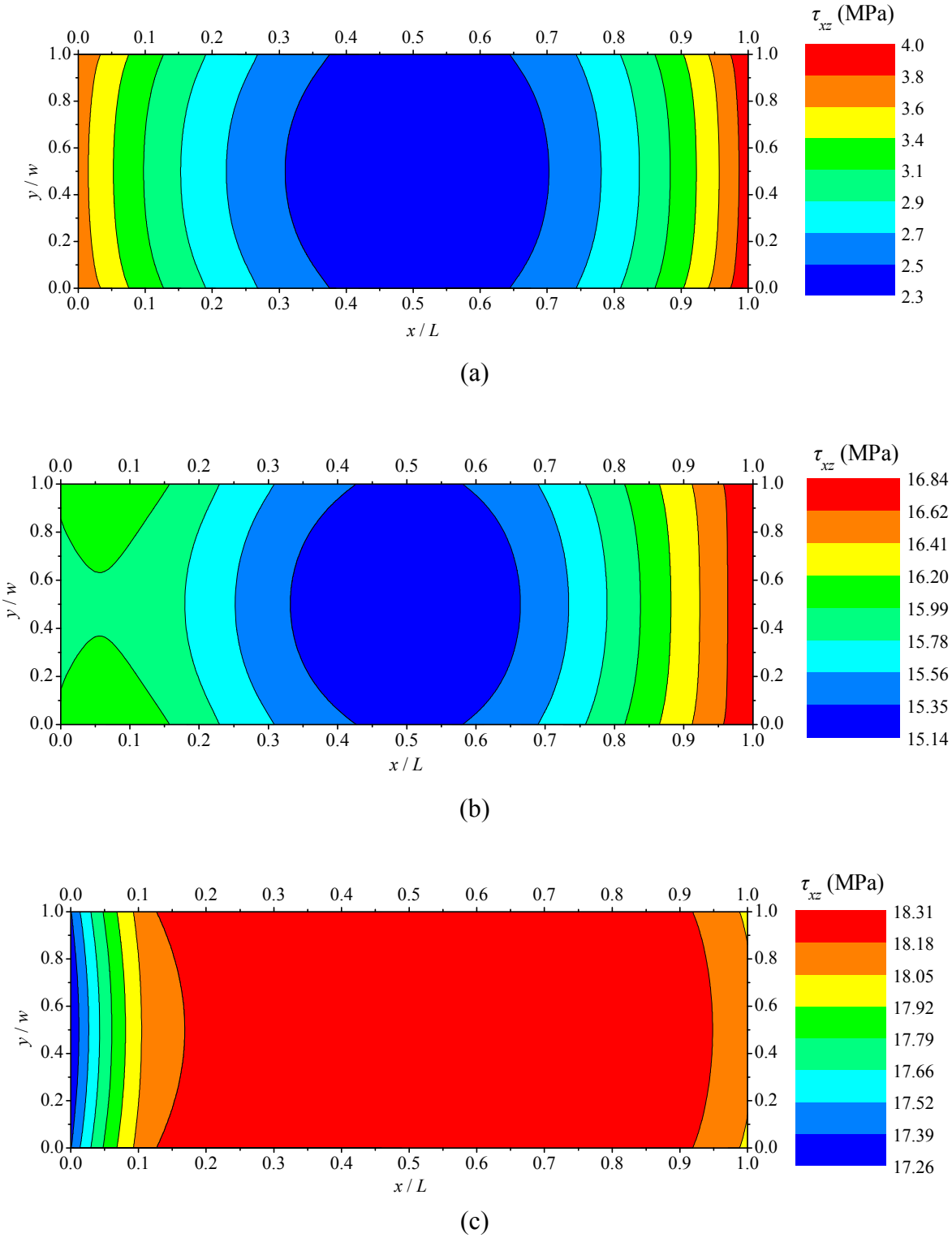

Figure 6.26: In-plane shear stresses τ_{xz} distributions over the adhesive area of the 3D DSJ model for applied displacement u equal to 0.01 mm (a), 0.07 mm (b) and 0.11 mm (c).

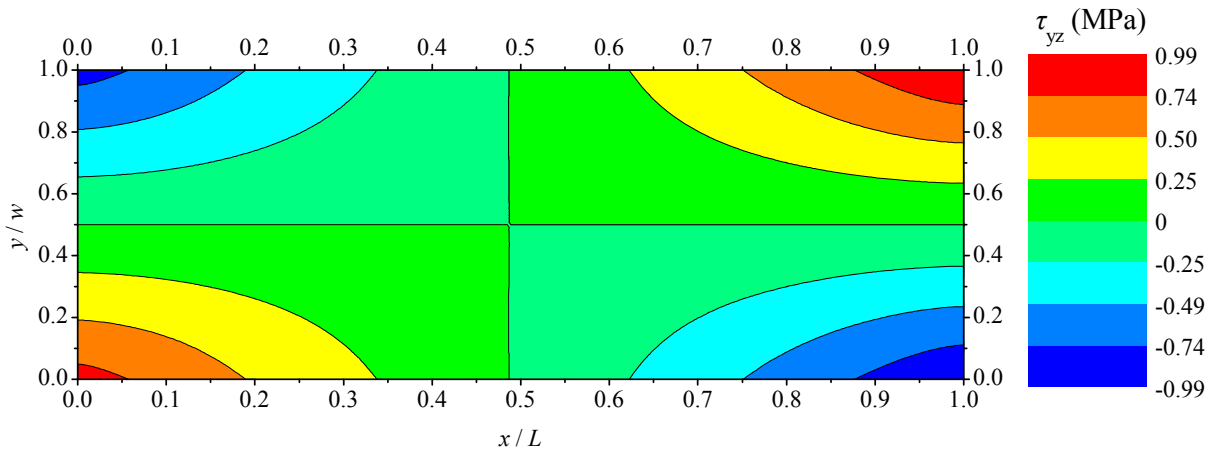

Figure 6.27: Out-of-plane shear stresses shear stresses τ_{yz} distributions over the adhesive area of the 3D DSJ model for applied displacement u equal to 0.11 mm.

6.3 Development of a Single Lap Joint subjected to Eccentric Loading

6.3.1 Description of work

According to section 6.2.4, it has been concluded that uni-axial testing of the single lap and double strap joints stresses the adhesive layer mostly in Mode I (peel stresses) and Mode II (in-plane shear stresses), in a way that the contribution of Mode III (out-of-plane shear stresses) is of insignificant importance. For this purpose, a new to the literature experiment has been designed and carried out, which is based on a simple Single Lap Joint subjected to Eccentric Loading (SLJ-EL). This test considers a common Single Lap Joint configuration which is eccentrically loaded as shown in Figure 6.28.

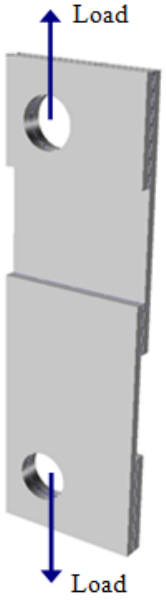

Figure 6.28: Schematic representation of the SLJ-EL adhesive joint used for the mixed-mode (Mode I, II and III) loading and fracture of the adhesive layer.

The basic concept that lays behind this configuration is that the in-plane co-axial eccentric tensile loads, lead the adhesive layer to develop normal stresses, in-plane and out-of-plane shear stresses which correspond to Mode I, II and III loading and fracture. From the early stages of loading the entire adhesive layer is subjected to mixed mode conditions which evolves in a progressive manner together with the increase of the exerted load, as will be shown in the numerical analysis part of this section.

6.3.2 Geometry and Materials

In order to design the geometrical configuration and derive the dimensions of the SLJ-EL specimen, which will be further fabricated and tested, two basic constrains have been taken under consideration. The first one aims at maintaining an elastic stress-state in both substrates involved during the entire loading history of the specimen. The second constraint aims at achieving a mode mixity ratio between Mode II and Mode III not lower to 0.5. As shown later on, the mode mixities vary over the adhesive bond area. As far as the material selection is concerned, a mild steel (St37) and a relatively stiff epoxy (Araldite 2015) have been chosen for the substrates and adhesive, respectively. Considering the above, a parametric numerical analysis has yielded the geometry and dimensions of the fabricated specimens depicted in Figure 6.29.

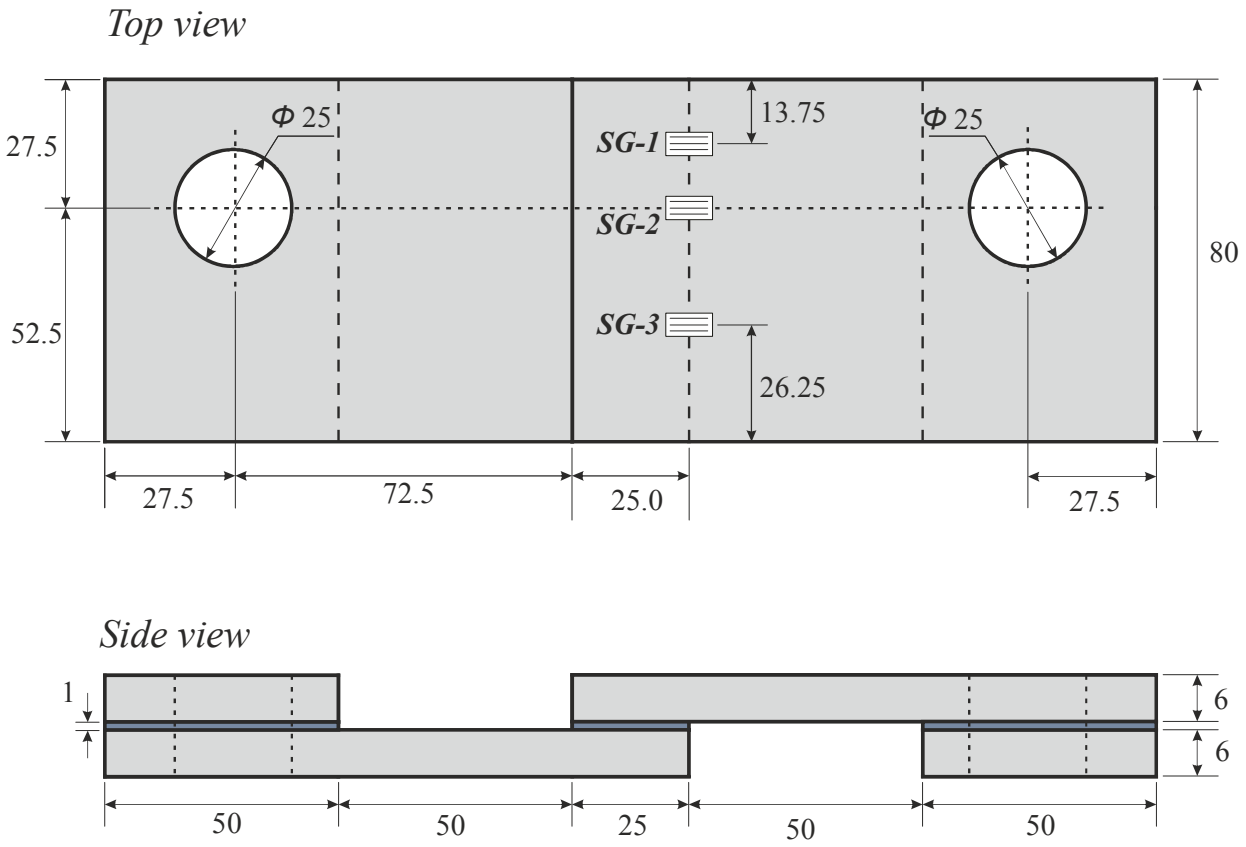

Figure 6.29: Geometry with nominal dimensions of the fabricated SLJ-EL specimens.

The tabs shown in this figure, especially in the side view, are made from the same material as the main substrates of the SLJ-EL and are adhesively bonded on the metal substrates, in order to keep the loading path between the testing machine and the specimen's geometry co-axial. Metallic pins were inserted in the holes of each specimen, which let the specimen to freely rotate at these two constrain points.

6.3.3 Fabrication procedure

All bonding surfaces have been mechanically treated with the use of the common in the shipbuilding industry Sa2½ near-white grit blast cleaning (approx. 2.5 mm grit size), according to the Swedish standards. This procedure yielded an average surface roughness Ra of the metallic bonding areas equal to 4.92 μm (CoV = 2.3%).

At the end of the surface preparation procedure, the specimens were cleaned with solvent (acetone) and then were let to dry, prior to the application of the adhesive material. First, the tabs were adhesively bonded on the main metal substrates and cured under ambient lab conditions (20°C). Then, the adhesive material was spread on the remaining bonded surfaces with the use of a spatula and then these were attached together as shown in Figure 6.30. The polypropylene spacers were utilized in order to achieve the nominal dimensions and alignment during the bonding process.

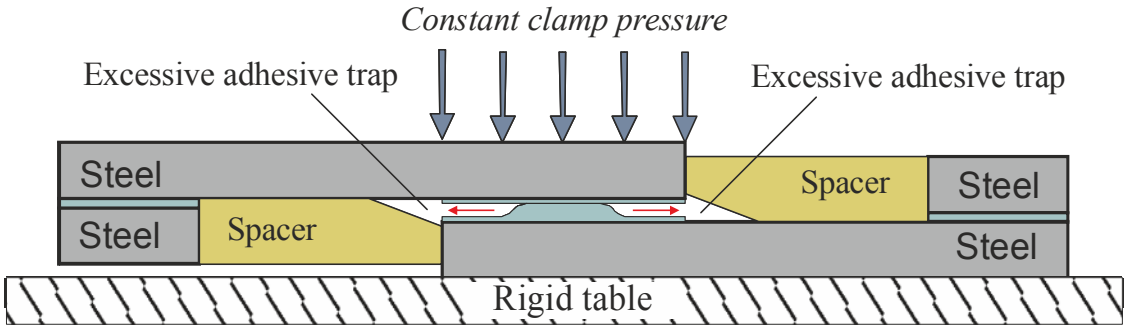

Figure 6.30: Configuration utilized for the fabrication of the SLJ-EL specimens.

The thickness of the adhesive layer was 1 mm and provisions (short tough steel wires) had been taken during fabrication to keep this value constant for all specimens. The adhesive was applied over large steel plates from which the actual specimens will be finally subtracted, in order to achieve exactly same joints. After the application of the adhesive material, constant pressure was applied over the overlap area with the aid of clamps. The system was placed in an oven, one hour after the application of the clamps, at 70°C for 45 min. After the completion of the curing process, the specimens were cut from the "mother" plate together with their corresponding loading holes, with the use of waterjet. Three specimens were finally fabricated and tested.

6.3.4 Testing procedure

The objective of the tests was to provide experimental measurements of the fabricated specimens loaded in tension for comparison with the finite element analysis results with the use of the proposed 3D mixed-mode EPZ model (see section 5.4). Additionally, the simulation of the experimental tests aim at investigating the potential of the proposed SLJ-EL geometry for testing a thin adhesive layer loaded under mixed-mode conditions. Three SLJ-EL specimens were tested under a tensile loading using a MTS hydraulic testing machine at room temperature under displacement control with a rate of 0.25 mm/min. The experimental setup is shown in Figure 6.31. Three strain gage sensors have been attached on top of the overlap edge of one side of each specimen, as shown in Figure 6.29. These locations were selected so as to provide variations of the strains along the width of each specimen and will be used for comparisons with the numerical results. Both ends of each specimen were fixed in custom-made fixtures with the use of metallic pins, which let the specimens' ends to rotate freely. The pins' average real diameter was measured equal to 24.95 mm where the specimens' corresponding diameter varied within the range between 25.2 mm and 25.8 mm. Equal thickness plastic washers were utilized as spacers in-between each side of the specimen's end and the corresponding socket area of the fixture (see Figure 6.31), in order to align the specimen with the loading axis of the testing machine. During the tests the applied displacement together with the reaction forces were monitored. The experimental measurements are presented in the next section, together with the numerical ones.

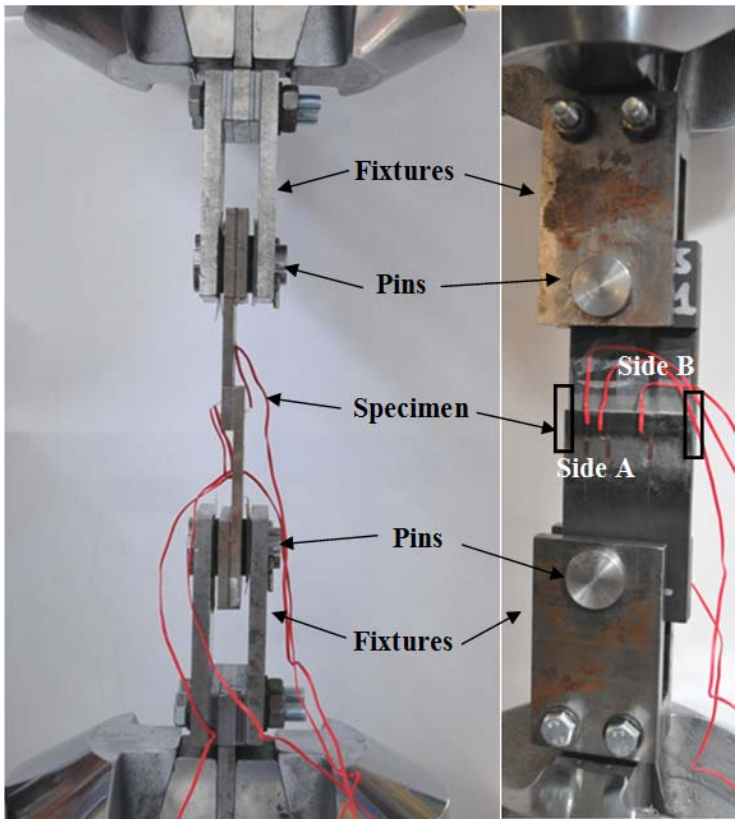

Figure 6.31: Experimental set-up of the SLJ-EL specimens.

6.3.5 Finite element modeling

This section deals with the numerical modeling of the SLJ-EL experimental tests. The geometry presented in Figure 6.29 has been considered for the construction of the finite element mesh and the corresponding boundary and loading conditions have been applied, based on the experimental set-up presented in Figure 6.31. The steel adherents and tabs have been modeled with 29904 quadratic 20-node brick elements (C3D20) available in the ABAQUS® element library. The whole adhesive layer is represented by 3D cohesive elements (see Appendix A1) and the proposed EPZ mixed-mode model (see section 5.4) has been utilized for the description of their constitutive relation. The cohesive elements utilized have constant dimensions (1.2 x 1.2) mm^2 in the entire overlap area, a value derived after a mesh density convergence analysis. For the numerical integration of the stiffness matrix and the internal force vector of the quadratic cohesive elements, a 3 x 3 Gaussian quadrature rule has been used. For reasons of simplicity and for CPU time savings the pins and its interaction with the models' holes has not been modeled. Instead, the contact surfaces of the holes' circumference have been detected and the corresponding nodes laying at these surfaces have been constrained with the use of rigid links that allow rotational degrees of freedom. The latter are not available in the formulation of the C3D20 continuum elements, but are necessary for the realistic modeling of the imposed boundary conditions (pin support – free in-plane rotation) to the specimen during the experiment. Thus, a beam-type Multi Point Constraint (MPC) has been applied at the aforementioned internal nodes of the holes (half circle) with their master node located at the geometrical center of each hole, respectively, as shown in Figure 6.32. The boundary and loading conditions are applied at the master nodes of the MPCs. The displacement control experimental loading condition is translated to tensile applied displacement to one master node ($-u_y$).

Newton-Raphson method has been utilized for the solution of the displacement control non-linear problem augmented by the line search algorithm.

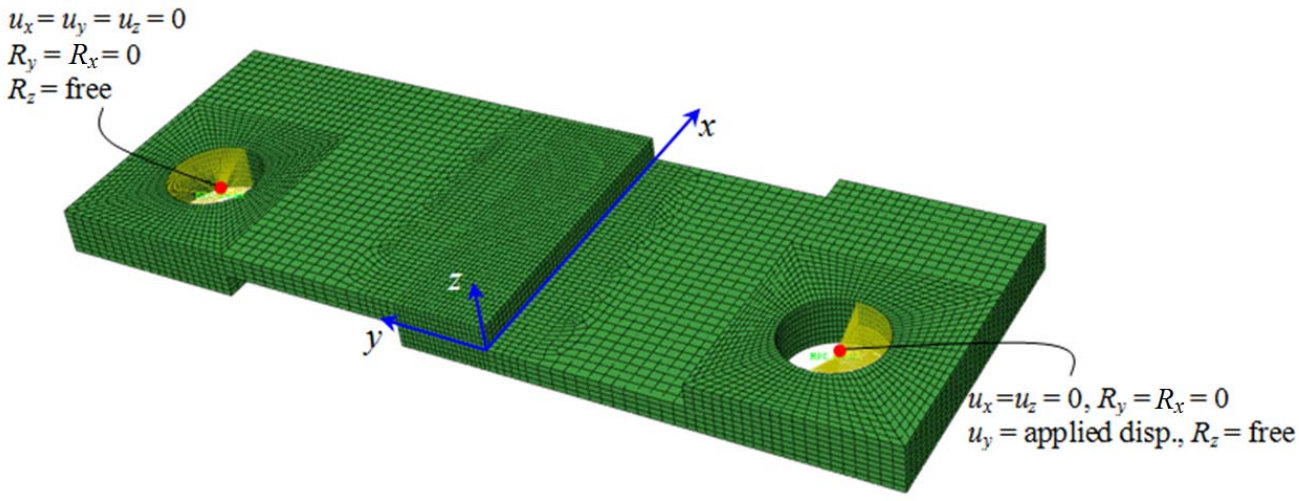

Figure 6.32: Finite element model with its corresponding boundary and loading conditions of the tested SLJ-EL specimens' geometry.

As far as the material properties is concerned, the steel adherents were modeled within their linear elastic range, having a Young modulus equal to 170 GPa (experimentally measured value) and a Poisson ratio equal to 0.3. For the description of the constitutive behaviour of cohesive elements utilized for modeling of the adhesive layer, the 3D proposed EPZ mixed-mode model is utilized. The definition of the pure mode EPZ law properties is based on the corresponding ones described in section 6.2.3.3. These properties refer to an adhesive layer of Araldite 2015 (also utilized for the fabrication of the SLJ-EL specimens) with a thickness of 0.5 mm. For fabrication reasons, in the framework of the current experimental program the adhesive layer had an actual thickness equal to 1 mm. However, according to the experimental work reported by Ji et al. (2010) and Ji et al. (2011), the parameters of the cohesive laws are affected by the thickness of the corresponding bondline, in Mode I and II loading and fracture, respectively. Specifically, the parameter significantly affected are the critical stresses $\sigma_{c,I}$ and $\sigma_{c,II}$. The authors have shown that a 1mm thick adhesive layer yields a 14.7 % percentage decrease and a 4.5 % percentage increase in the $\sigma_{c,I}$ and $\sigma_{c,II}$ magnitudes, respectively, of the corresponding magnitudes obtained from a 0.5 mm thick adhesive layer. Thus, for reasons of completeness, both cohesive law property sets (the one referring to the 0.5 mm thick adhesive and the one calculated for the 1mm thick adhesive used herein) have been utilized in the simulations of the SLJ-EL specimens. These two sets are listed in Table 6.4 and the corresponding cohesive laws are depicted in Figure 6.33.

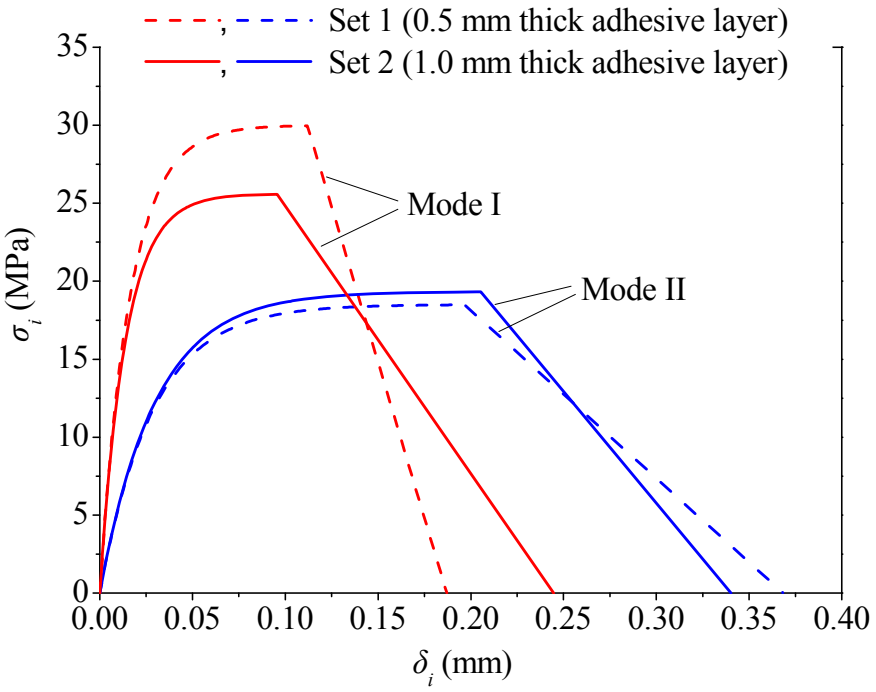

Figure 6.33: Pure mode EPZ laws utilized for the constitutive relation of the cohesive elements that model the adhesive layer.

Table 6.4: Properties of the pure mode EPZ laws utilized in simulation of the SLJ-EL tests.

magnitudes	k_I	$k_{II} = k_{III}$	$\sigma_{c,I}$	$\sigma_{c,II} = \sigma_{c,III}$	J_{Ic}	$J_{IIc} = J_{IIIc}$	e
units	N/mm^3	N/mm^3	MPa	MPa	N/mm	N/mm	%
Set 1	1850	650	30	18.5	4	4.7	0.1
Set 2	1850	650	25.6	19.33	4	4.7	0.1

6.3.6 Numerical and experimental results

The global response of the SLJ-EL configuration is presented in Figure 6.34, as experimentally measured and numerically predicted. As far as the experimental curves are concerned, these are characterized by an initial linear response followed by increasing non-linearities until the maximum force level, that is the strength of the joint. After that point, a softening behaviour (inability to carry further load) is obtained that denotes the sudden progressive failure of the adhesive layer. A very good repeatability is observed regarding their global response behaviour and regarding their maximum attained load (average strength equal to 26.36 kN with a coefficient of variance equal to 3.5%).

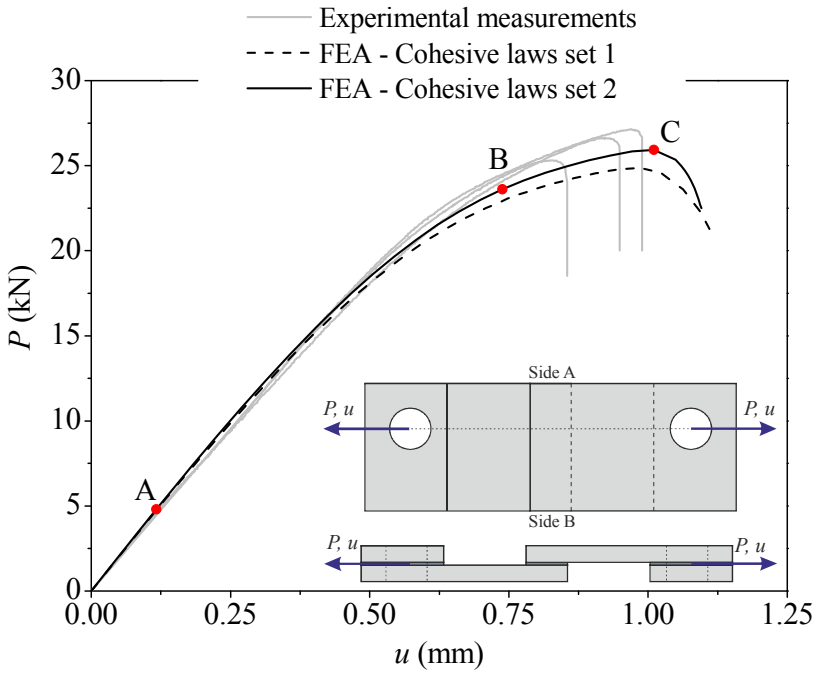

Figure 6.34: Global response of the adopted SLJ-EL configuration as experimentally measured and numerically calculated with the cohesive laws sets 1 and 2.

After the elastoplastic material response of the adhesive layer, interfacial debonding (adhesive failure) was observed in both sides A and B of all specimens as depicted in Figure 6.35.

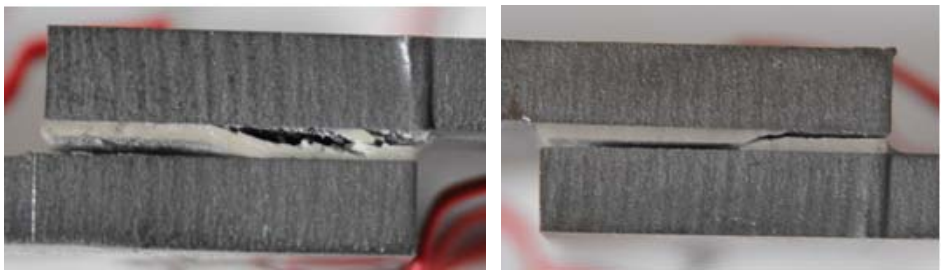

(a) (b)

Figure 6.35: Indicative fracture mode observed at the SLJ-EL side A (a) and side B (b) of Figure 6.31.

According to Figure 6.35, physical cracks initiated at the overlap edges and propagated along the steel-adhesive interface with an asymmetric manner. However, a close look of the failure surfaces, presented in Figure 6.36, denotes that the crack trajectory within the adhesive layer is oscillatory, i.e. travelling from one interface to its opposite through the adhesive material. This fact leads to the conclusion that both adhesive and cohesive failure modes are present during the fracture of the adhesive material. Accordingly, the utilization of the proposed mixed-mode model, which is developed within the framework of the Embedded Process Zone approach, is a good candidate for numerical modelling of the loading and damage behaviour of the adhesive layer utilized to form the SLJ-EL specimen.

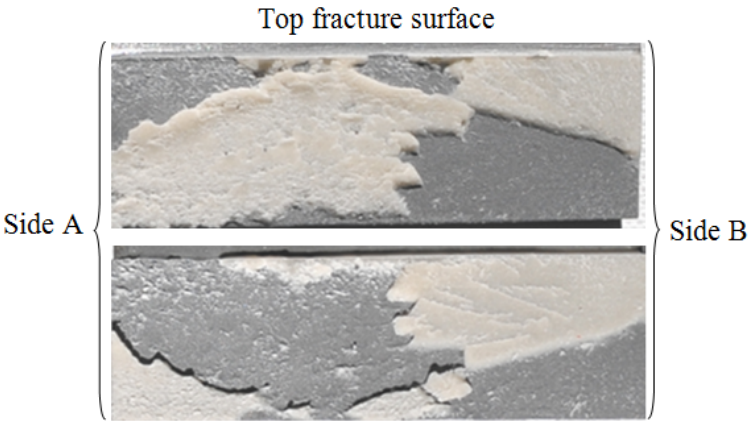

Figure 6.36: Failure surfaces of the corresponding tested SLJ-EL specimen of Figure 8.

The numerical predictions of the simulated SLJ-EL configuration is based on the finite element model of Figure 6.32 and the corresponding 2 sets of cohesive parameters listed in Table 6.4 have been utilized, respectively, for comparison reasons. The obtained results are plotted in Figure 6.34. Both curves, i.e. the dashed and continuous black lines that correspond to the cohesive law set 1 and 2, respectively, share a similar behaviour but differ in the predicted strength values. They are characterized by an initial linear response, followed by a nonlinear part

up to the strength limit, a behaviour which is close enough to the corresponding experimental measurements. However, the predicted behaviour and strength from finite element calculations with the cohesive laws set 2 (predicted strength equal to 25.91 kN, corresponding to a 2% difference from the experimental average value) yields better predictions compared to the ones obtained from the cohesive laws set 1 (predicted strength equal to 24.87 kN, corresponding to a 5.6% difference from the experimental average value). This leads to the conclusion that the procedure followed to derive the cohesive laws set 2 from the cohesive laws set 1 yields promising results.

During the tests, only elastic stresses were developed at the metal substrates of both joint types. This fact denotes that the non-linearities of the global *P-u* response are attributed to the adhesive material ductility, which is well described by the exponential function of proposed EPZ laws. Figure 6.37 presents a comparison between the experimental strains as measured from one specimen and the corresponding numerically predicted values (with the cohesive laws set 2), at the three locations of the SLJ-EL specimens as shown in Figure 6.29. Similar experimental load-strain behaviour is obtained from the two remaining specimens. The trend of the load-strain curves from all three sensors can be characterized linear, as expected, reaching maximum values just before the failure of the joint. These maximum values are well below the yield point of steel (<< 2000 με). This behaviour is justified by the fact that the steel adherents are quite stiff and, therefore, the weak point of the joint is the adhesive layer which fails first. Thus the adherents are not heavily loaded, resulting in low maximum strains. This elastic behaviour was accurately predicted by the FEA with the mixed-mode EPZ model.

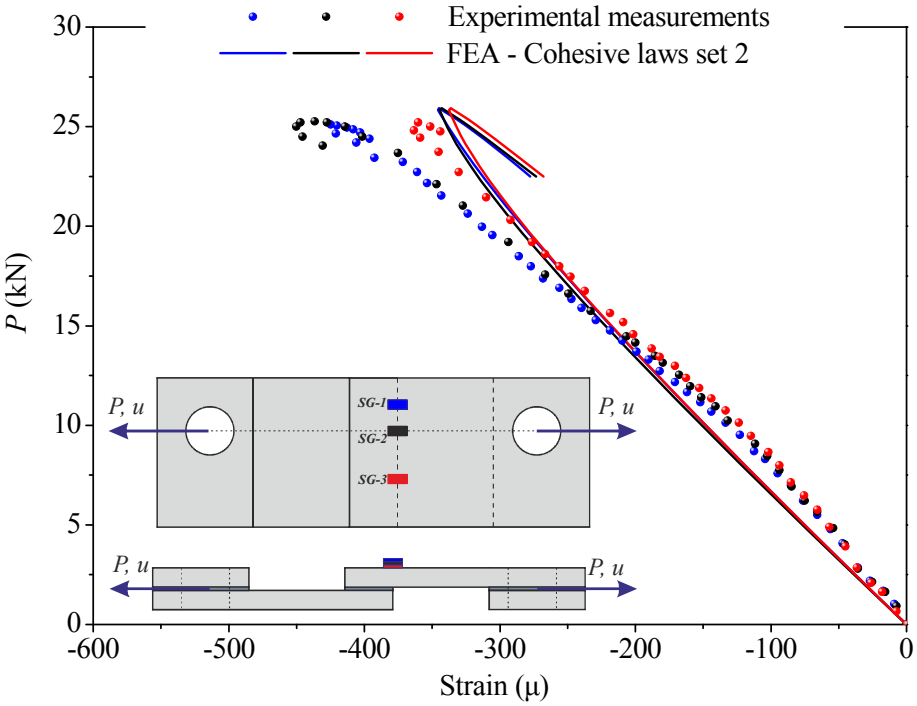

Figure 6.37: Strain measurements vs. the load of the adopted SLJ-EL configuration as experimentally measured and numerically calculated with the cohesive laws set 2.

Figure 6.38 presents the steel adherents' von Mises stresses over the deformed shape of the simulated SLJ-EL geometry as predicted during its loading history. Within the linear elastic range of the adhesive layer (point A of Figure 6.34) and prior to the creation of the fracture process zone (damage initiation and propagation) the equivalent stresses peak at the outermost edge of the load line side of the overlap area, as shown in Figure 6.38a. Additionally, the well known "bending effect" of the load eccentricity occurring at the out-of-plane (side view of Figure 6.29) is apparent at the beginning of the load application. At the force level of 23KN (point B of Figure 6.34) the von Mises stresses peak in the vicinity of the middle of the width of the overlap area, as shown in Figure 6.34b. According to this figure, the peak stresses (red contour) have decreased to 130 MPa compared to the respective ones of Figure 6.38a, being equal to 260 MPa. This fact denotes the creation and propagation of the fracture process zone developed during the loading of the adhesive layer and located ahead of the crack tip. Figure 6.38c presents the developed stresses at the maximum force level. The blue contours around the adhesive bond area, referring to stress-free areas, denote the physical creation of crack faces, i.e. the partial debonding of the adhesive joint and the redistribution of the tractions of the EPZ approach, and the resulting von Mises stresses on the metal adherents. This fact in turn, leads the peak stresses in the overlap area and in the vicinity of the crack tip to further decrease to 90 MPa.

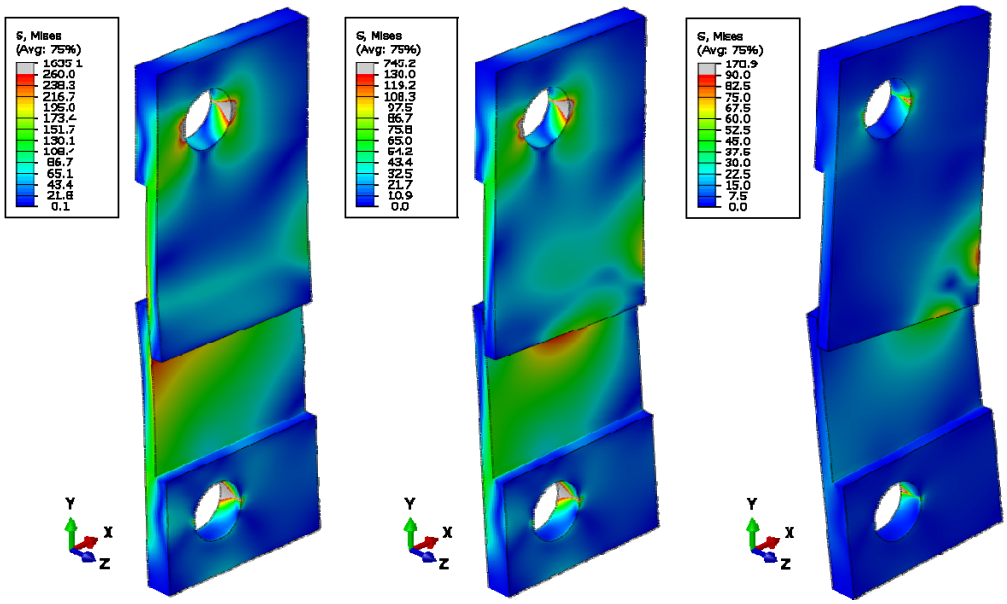

(a) (b) (c)

Figure 6.38: Deformed shapes with von Mises stress distributions of the simulated SLJ-EL specimens during the formation of the EPZ (a) and the damage propagation in the adhesive layer (b, c).

It is concluded that as the applied load increases in magnitude and the adhesive layer enters the elastic, plastic and damage region in a sequential manner, the "bending effect" of the metal adherents is being reduced. This is reasonable, since damage evolution and physical cracking of the adhesive layer, leads to a progressive decrease of the inherently induced eccentric deformation of the SLJs. This conclusion can be further justified, if one considers the

experimental and numerical load-strain behaviour at the SG-3 location (≈ 26 mm away from the load application line), as depicted in Figure 6.37, where at the maximum force level SG-3 strains are relatively lower compared to SG-1 and SG-2 strains. This fact denotes that the bending stain component has been reduced from the total strain magnitude and axial strains dominate.

Figure 6.39 shows a front view of the deformed shape of Figure 6.38c. From this figure the contribution of the out-of-plane shear stresses (referring to Mode III) in the mixed-mode loading and fracture deformation of the SLJ-EL specimen, can be clearly seen.

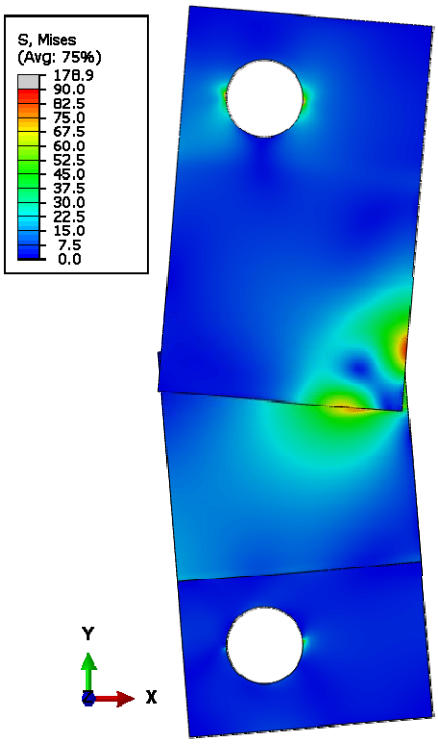

Figure 6.39: Front view of Figure 6.38 c showing the contribution of Mode III in the mixed-mode loading and fracture of the SLJ-EL geometry.

6.3.7 EPZ stress distributions on the bond area

On an effort to give some further insight to the loading and fracture process of the adhesive layer, the variation of developed peel, in-plane and out-of plane shear stresses in the embedded process is studied. Three force levels have been considered and the corresponding calculated stresses have been plotted over the adhesive layer domain with the aid of 2-dimensional graphs. These levels are denoted with the letters A, B and C on the numerical curve (calculated with the cohesive law set 2) of Figure 6.34 and refer to the linear elastic, elasto-plastic and maximum attained (strength) force level, respectively. In the following graphs the axes have been normalized to unity with respect to the nominal dimensions, that is the overlap width w (25mm) and overlap length L (80mm), and with the aid of the local coordinate system x-y-z shown in Figure 6.32. Thus, the corresponding stresses that represent the EPZ are denoted as

σ_z, σ_{yz} and σ_{xz} and correspond to the Mode I peel, Mode II in-plane and Mode III out-of-plane shear stresses, respectively.

Prior to presenting the stress field developed in the adhesive layer, it is important to see the contribution of Mode III loading and fracture to the mixed-mode response of the SLJ-EL geometrical configuration. For this purpose the absolute value of the mode mixity δ_{III}/δ_{II} (see Equation A1.24 in Appendix A1) has been plotted over the adhesive area domain, in Figure 6.40, calculated in the early stages of loading (point A in Figure 6.34). According to this figure, the mode mixity ratio increases within the area between x/L = 0.5 and x/L = 1, and peaks in the vicinity of x/L = 1, with a value of 1.5. This value denotes that the maximum contribution of Mode III is 150% higher than Mode II. This is reasonable, if one considers the eccentricity between the load-line and the outermost edge of the geometry (x/L = 1) and observing the deformed configuration of the SLJ-EL specimen in Figure 6.39.

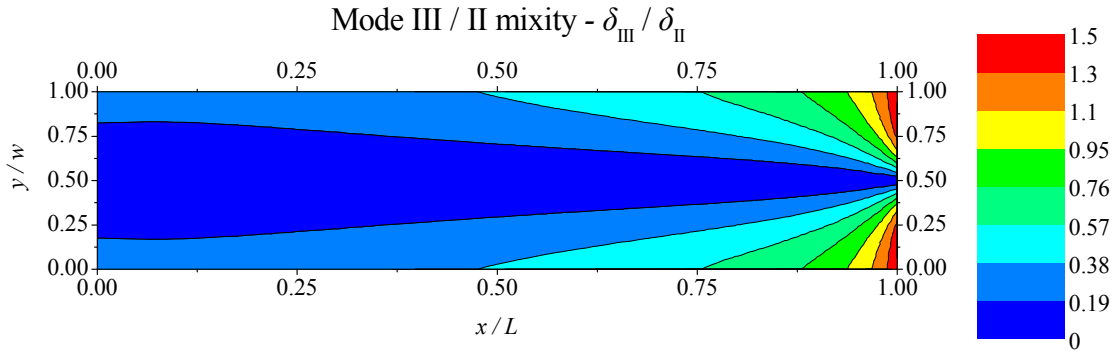

Figure 6.40: Indicative distribution of the Mode II and III separation ratio δ_{III} / δ_{II} over the bond area of the SLJ-EL adopted geometry.

Figure 6.41, Figure 6.42 and Figure 6.43 present the variation of the peel σ_z, in-plane σ_{yz} and out-of-plane σ_{xz} shear stresses over the adhesive area as evolves during the loading of the SLJ-EL configuration, respectively. As a general remark, peel, in-plane and absolute out-of-plane shear stresses are symmetrical with respect to x/L at y/w = 0.5. Within the linear elastic region (see Figure 6.41a) peel stresses are concentrated near the adhesive area edges, that is at y/w = 0 and y/w = 1, and peak in the vicinity of the loading axis. Contact stresses (negative normal tractions) are developed in most of the adhesive area (blue contours), which are assumed that do not induce damage. As the adhesive layer enters plasticity, peel stresses redistribute in a way that maximize within the range x/L = 0.25 and x/L = 0.75 and also near the edges, as shown in Figure 6.41b. Additionally, normal stresses tend to develop in a larger area within the adhesive layer, by converting their sign from negative (contact) to positive (peel). This behaviour is more intense at the maximum force level predicted by the SLJ-EL finite element modeling, according to Figure 6.41c. However, the maximum peel stresses are lower than the corresponding ones of Figure 6.41b, i.e. 7.4 MPa compared to 10 MPa. This is the result of the variable mode-mixity within the embedded process zone, obtained during the loading history of the SLJ-EL model and causes softening of some material points in a sequential manner.

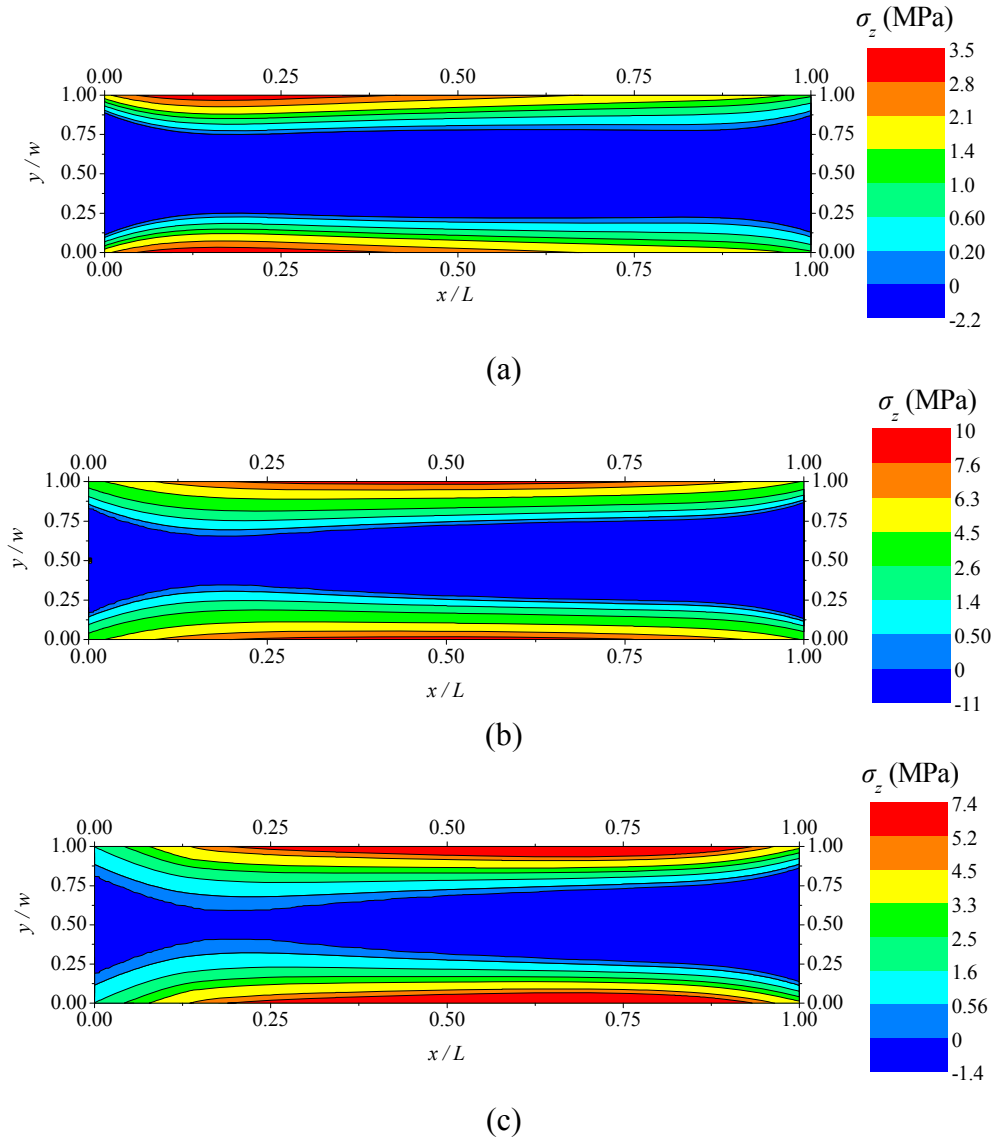

Figure 6.41: Peel stresses σ_z developed over the bond area corresponding to point A (a), B (b) and C (c) of the global response of the SLJ-EL configuration (see Figure 6.34).

The linear elastic in-plane shear stresses σ_{yz} have developed in the entire adhesive domain and increase in magnitude from the outermost edge (x/L = 1) to its opposite (x/L = 0) approaching the loading axis, as shown in Figure 6.42a. The maxims concentrate at the corner edges, which in fact are stress concentration points where damage initiates. Within the advanced non-linear region of the global response curve of the SLJ-EL geometry (point B in Figure 6.34), nearly the half of the adhesive layer has entered plasticity, denoted with the red contour region in Figure 6.42b. At that force level, unloading continued by change in sign of the σ_{yz} stresses is calculated, in the region of the adhesive layer between $x/L \approx 0.94$ and $x/L = 1$. This negative σ_{yz} stress area has extended at the maximum force level of the SLJ-EL model, according to Figure 6.42c. This behaviour is reasonable, if one considers the effect of the Mode III to the deformed

shape (scissoring of the adherents) of the SLJ-EL model presented in Figure 6.39. Also, a stress softening is observed at the vicinity of the edge near the loading axis (x/L = 0), as shown in Figure 6.42c.

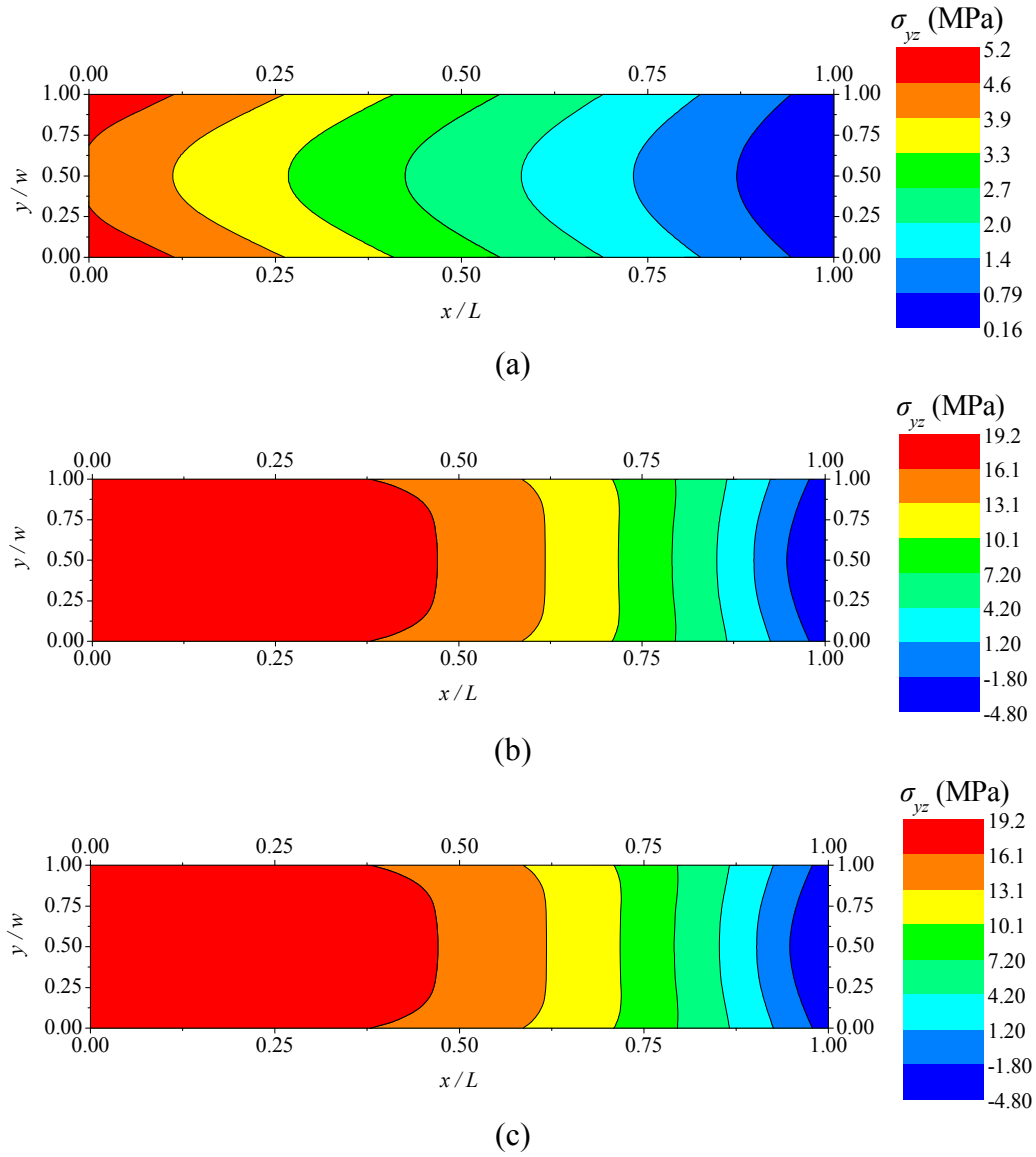

Figure 6.42: In-plane shear stresses σ_{yz} developed over the bond area corresponding to point A (a), B (b) and C (c) of the global response of the SLJ-EL configuration (see Figure 6.34).

The variation of the out-of-plane shear stresses is characterized antisymmetrical in all load levels (see Figure 6.43). Within the linear elastic response, the stress distribution of the corresponding out-of-plane shear stresses σ_{xz} is presented in Figure 6.43a. According to this figure, σ_{xz} stresses peak in absolute value at the two corner edges of the adhesive layer at x/L = 0 and decrease as approaching the opposite edges at x/L = 1. As soon as the adhesive material enters plasticity (see Figure 6.42b) and its ability to carry higher stresses decreases, the σ_{xz} stress field redistributes (see Figure 6.43b) with an opposite pattern of that of Figure 6.43a. The scissoring of the adherents of the SLJ-EL geometry becomes more intensive and now the

maxims of σ_{xz} stresses concentrate in the other left hand side half and at $y/w = 0$ and $y/w = 1$. This behaviour follows up to the maximum predicted force level, as shown in Figure 6.38c.

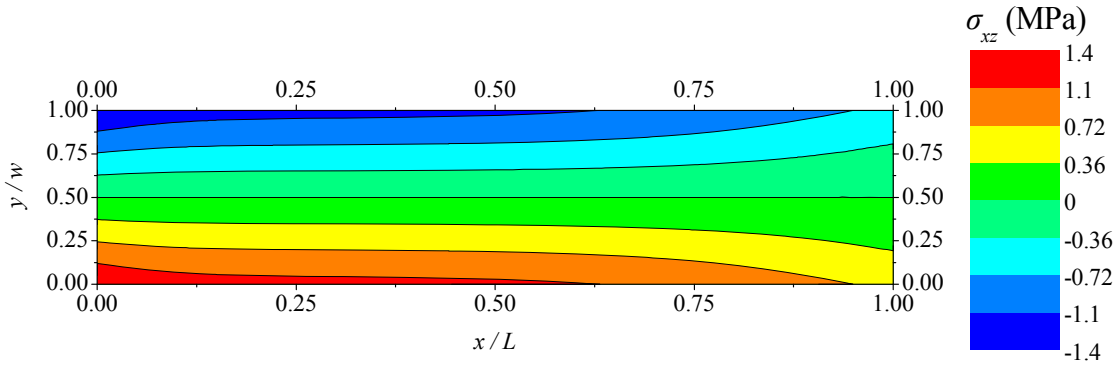

(a)

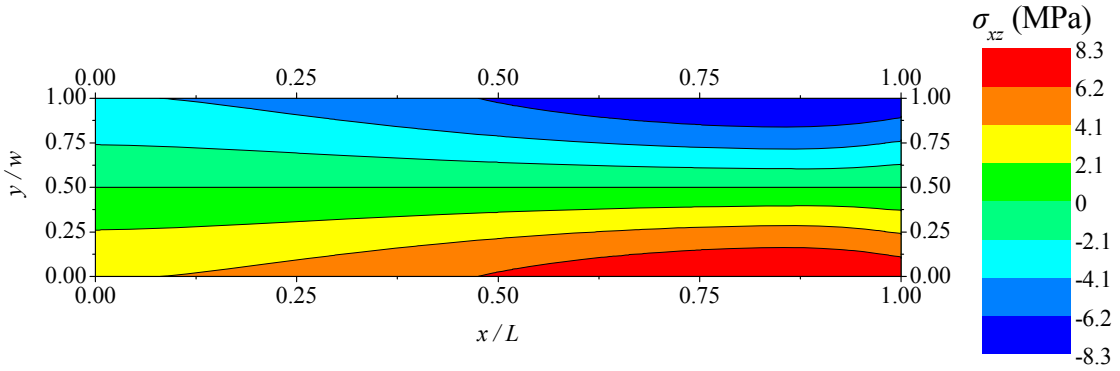

(b)

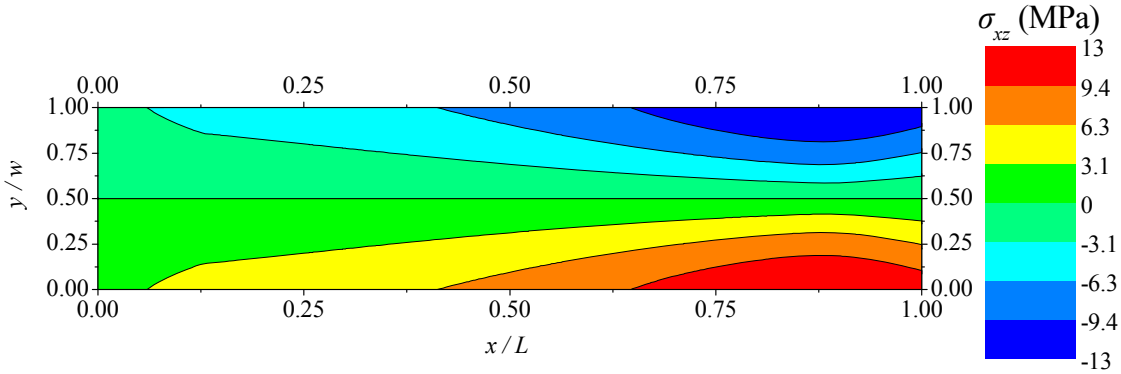

(c)

Figure 6.43: Out-of-plane shear stresses σ_{xz} developed over the bond area corresponding to point A (a), B (b) and C (c) of the global response of the SLJ-EL configuration (see Figure 6.34).

6.4 Conclusions

Experimental tests were initially performed on single-lap and double-strap joints and the corresponding measurements were compared with numerical results obtained from the developed 2D and 3D mixed-mode EPZ models, for validation purposes, as described in Chapter 5. The traction – separation laws were incorporated in the developed mixed-mode models and were

implemented into interface elements that were used to model the adhesive layer bondline, in a 2D and 3D finite element space, respectively. The numerical results are in very good accordance with the respective experimental ones, both for the load-displacement and for the load-strains curves. The proposed models predicted accurately the elastoplastic response and strength of both types of joints considered, by utilizing in each analysis the same pure mode laws.

Additionally, the existing in the literature trapezoidal law, which is adequate for modeling ductile adhesives, has been used for the FEA of the tested joints and comparisons are given. Comparisons are also provided with the corresponding FE results obtained from the PRP (Park-Paulino-Roesler) model. The shape of the PRP cohesive laws is controlled by two shape parameters (α and β) that can be adjusted so as to represent brittle, quasi-brittle and ductile material softening behaviours. For the sake of the current work, two cases regarding the selection of these parameters have been considered; brittle ($\alpha = \beta = 2$) and ductile ($\alpha = \beta = 1.1$) behaviour.

The trapezoidal law captures accurately the linear elastic region and strength but does not capture accurately the nonlinear elastoplastic region of the tested joints. For the adhesive joint cases considered where thick steel substrates and a ductile adhesive material are involved, the trapezoidal law predicts higher loads for a given value of applied displacement when compared to the corresponding results obtained from the proposed law and the experimental measurements. This difference becomes higher for values of load approaching the strength of the joints. This outcome is important when designing a structural part that includes an adhesive joint. In such a case, the proposed law predicts the global response and the stress distributions, on this part with higher accuracy than the trapezoidal law.

On the other hand, both the proposed and the PRP model (especially the brittle case with $\alpha = \beta = 2$) predict with great accuracy the elastic and plastic softening behaviour of both test cases up to the experimental maximum load. Unexpectedly, the brittle PRP cohesive laws yield more promising results compared to the ductile PRP cohesive laws. However both PRP laws predict a gradual damage behaviour after the maximum load in both joints, which is inconsistent with the rapid one experimentally registered. The proposed EPZ and the trapezoidal model capture this rapid progressive damage response.

For the definition of each law in pure Mode i (i = I, II) four parameters are necessary, that is, the initial stiffness (k_i), the critical stress ($\sigma_{c,i}$), its corresponding separation ($\delta_{0,i}$) and the critical separation ($\delta_{c,i}$) or the fracture toughness (J_{ic}). The critical stress and the fracture toughness have to be experimentally measured, whereas the initial stiffness can be evaluated easily from the elastic properties of the adhesive material provided by the manufacturer. An analytic formula has been derived for the calculation of the physical parameter $\delta_{0,i}$ through a specific numerical parameter (error e). A sensitivity study towards the effect of this parameter to the FEA results has shown that, in the case of a ductile adhesive like the one studied here, accurate predictions of the strength and conservative predictions of the corresponding displacement at failure are obtained, when considering a value of the error e equal to 1% or less. Considering the above, it can be concluded that the proposed EPZ laws can be referred as two-

parameter laws when designing towards the strength of an adhesive joint with a ductile adhesive material. However, when designing towards the maximum attained displacement, the proposed laws are three-parameter laws.

The constitutive model presented here provides an alternative capability for the simulation and design of structures with bonded components which involve a ductile adhesive material. Comparisons with the PRP model, which couples the separate fracture modes explicitly through the PRP potential validates the effectiveness of the proposed mixed mode formulation which is based on damage and fracture criteria together with the equivalent separation and the mode mixity parameter for coupling the separate fracture modes.

According to the aforementioned numerical results, it has been concluded that uni-axial testing of the single lap and double strap joints, stresses the adhesive layer mostly in Mode I (peel stresses) and Mode II (in-plane shear stresses), in a way that the contribution of Mode III (out-of-plane shear stresses) is of insignificant importance. For this purpose, a new to the literature experiment has been designed, which is based on a simple Single Lap Joint subjected to Eccentric Loading (SLJ-EL). This test considers a common Single Lap Joint configuration which is eccentrically loaded. The basic concept that lays behind this configuration is that the in-plane co-axial tensile loads, lead the adhesive layer to develop normal stresses, in-plane and out-of-plane shear stresses which correspond to Mode I, II and III loading and fracture. These tests were designed such that the metal substrates will not enter plasticity and the adhesive will be achieving a mode mixity ratio between Mode II and Mode III not lower to 0.5. The experiments were simulated in a 3-dimensional finite element space and the 3D developed mixed-mode model has been utilized for the adhesive layer. The numerical results are in very good agreement with the corresponding experimental measurements, within the linear and non-linear region and attained strength, yielding a difference of 2%. It has been concluded from a mode-mixity graph (δ_{III}/δ_{II}) that in the early stages of loading the contribution of Mode III is 150% higher than that of Mode II. Additionally, following the linear elastic response of the adhesive material, the adhesive layer laying at the vicinity of the loading axis, enters plasticity in a progressive manner until the creation of physical cracking.

This page has been intentionally left blank

7. Experimental and numerical investigation of composite-to-metal adhesive joints

7.1 Description of work

Having validated the proposed EPZ laws and mixed-mode model with experiments obtained from steel-to-steel adhesive joints (see Chapter 6), this chapter is focused on validating the proposed numerical laws with experiments from composite-to-steel adhesive joints. This chapter is divided in two main sections.

The first section (7.2) presents an experimental parametric study of adhesively bonded Single Lap Joint (SLJ) geometries between relatively thick dissimilar adherents. The primary objective of this study is to investigate the effect of various parameters, i.e. adherents' thicknesses (two different stiffness ratios, 0.175 and 0.35), adhesive thickness (0.5 and 0.8 mm) and overlap length (25 and 75 mm), on the failure load and failure mode of joints with dissimilar materials. For this purpose, mild steel and carbon fiber reinforced polymer (CFRP) laminates have been considered as the structural adherent materials. Seven SLJ cases have been considered for fabrication and experimental testing. The SLJ specimens were tested under a uni-axial tensile quasi-static displacement. Three strain gages were attached to specific locations on each SLJ specimen, aiming at giving some local insight to the strain variations during loading. The applied displacement, the reaction force and the strains were monitored during the tests. The tests where then numerically modeled in a 3D space within ABAQUS® commercial finite element software and the adhesive layer's material response was simulated with the proposed mixed-mode model.

The next section (7.3) is focused on the numerical implementation of experimentally measured cohesive laws which describe a ductile adhesive material utilized for bonding similar or dissimilar structural materials. The main aim is to provide and validate all necessary amendments that must be considered in order to obtain a Traction-Separation law that can be used as the constitutive relation of cohesive elements for the simulation of adhesive joints. Thus, typical experimental cohesive laws from steel-to-CFRP adhesive joints (same materials as in section 7.2), reported in the Diploma Thesis of Andrianakis (2011), have been considered for

numerical implementation according to the proposed EPZ laws. The steel-to-CFRP adhesive joints were tested under the Double Cantilever Beam loaded with Uneven Bending Moments (DCB-UBM) experimental configuration. The manufacturing of the specimens was performed at the Shipbuilding Technology Laboratory at the National Technical University of Athens, whereas the tests were carried out at the Risø National Laboratory for Sustainable Energy, Materials Research Division, Technical University of Denmark.

The measured cohesive laws were first converted to numerical constitutive relations according to the proposed EPZ laws and additionally, for reasons of comparison, to the already known triangular shaped cohesive laws (available model in ANSYS and ABAQUS® finite element commercial software). Then, these were utilized for the numerical simulation of the experimental tests of section 7.2and comparative results are provided.

7.2 Single Lap Joints

7.2.1 Experimental program

Initially, two CFRP composite laminated panels were manufactured which differ in the number of the constituent reinforcing layers utilized, that is 15 and 22, hence achieving two different thicknesses. The fabrics were made from 200 g/m^2 unidirectional carbon fibers (CST 200 supplied by SGL Group) and the polymer system utilized was an epoxy resin LH 160 with the 135-136 hardener, both provided by HAVEL Composites. The UD fabrics were initially impregnated with the epoxy/hardener matrix system by the hand lay-up method and afterwards the plates were cured at 25 ^{o}C for 48 hours under constant 0.6 bar pressure with the aid of vacuum bagging.

After curing, two pairs of plates with dimensions (200 x 200) mm and (200x150) mm, respectively, were cut out from the 22 layers panel. One pair of plates and a single plate with dimensions (200 x 200) mm and (200x150) mm were also cut out from the 15 layer panel. As for the tabs which are necessary to fabricate the SLJ geometry, four and three rectangular plates, have been subtracted from the 22 and 15 layers panels, respectively. All cuts were made with the use of the waterjet technique with a cutting tolerance of ±0.2 mm.

Additionally, for the metallic substrates, plates from mild steel with the corresponding dimensions of the CFRP subtracted plates have been utilized. The structural adhesive material Araldite 2015 provided by Huntsman Container Corporation Ltd., that is a two-part and relatively stiff epoxy adhesive material, has been utilized as the joining material of the metallic and CFRP substrates.

All substrates were first degreased with acetone before the application of the specific surface preparation procedure. The bonding areas of the CFRP plates were polished using first a coarse sandpaper (100), followed by a finer one (200). For the treatment of the corresponding bonding areas of the metallic plates, the common in the shipbuilding industry Sa2½ near-white

grit blast cleaning was applied (approx. 2.5 mm grit size), according to the Swedish standards. This procedure yielded an average surface roughness Ra of the metallic bonding areas equal to 4.15 μm.

Initially, each metallic plate was bonded with its corresponding metallic tab plate and provisions have been taken (short tough steel wires) in order to maintain a constant adhesive thickness. After the completeness of the curing process of the steel tabs, each CFRP substrate-tab system was adhesively bonded with its corresponding steel substrate - tab system, as shown in Figure 7.1.

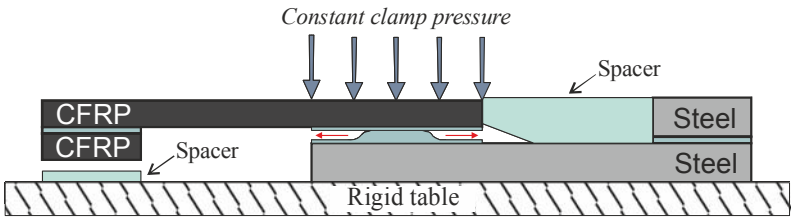

Figure 7.1: Configuration utilized for the fabrication of the dissimilar SLJ adhesive joints (polyurethane was used for the spacers).

After the assembly, the specimens were cured in an oven under a uniform pressure loading. According to the adhesive material manufacturer, curing procedure consisted of heating the specimens in 70°C for 45 minutes, followed by a slow cooling to ambient temperature. The specimens were left in ambient temperature for 48 hours before performing the tests. After the completion of the curing process, the specimens were cut with the use of waterjet. Seven cases have been considered that differ in the overlap length (25 or 75 mm), in the adhesive thickness (nominal 0.5 or 0.8 mm) and in the stiffness ratio (0.175 or 0.35). Figure 7.2 shows a schematic view of the considered SLJ cases and Table 1 lists the corresponding dimensions of each case. Three specimens were fabricated and tested from each SLJ case, resulting in total 21 specimens.

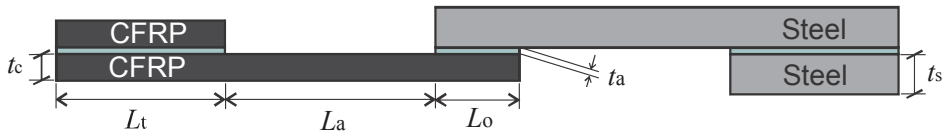

Figure 7.2: Schematic representation of the fabricated SLJ specimens.

Table 7.1: SLJ cases considered in the parametric study (magnitude *w* is the width of the joints).

Case	t_c (mm)	t_s (mm)	L_t (mm)	L_a (mm)	L_o (mm)	t_a (mm)	*w* (mm)	*SR*
SLJ-1	7.98	8	40	75	75	0.52	23.76	0.21
SLJ-2	8.60	8	40	75	75	0.89	24.00	0.22
SLJ-3	9.56	5	40	75	75	0.51	23.93	0.39
SLJ-4	9.29	5	40	75	75	0.84	23.89	0.38
SLJ-5	9.99	5	40	75	25	0.51	23.83	0.41
SLJ-6	9.99	8	40	75	25	0.85	23.99	0.26
SLJ-7	8.12	8	40	75	25	0.50	24.04	0.21

Figure 7.3 depicts a side view of a 75 mm long overlap area of respective SLJ coupons. It can be clearly seen that the adhesive layer has a uniform thickness along the overlap length.

Figure 7.3: Side view of a typical SLJ with 75 mm overlap length.

All specimens were loaded by a uniaxial static tensile displacement, applied with a speed of 0.1 mm/min by an MTS hydraulic testing machine. Three 5 mm length strain gage sensors (SG-1, SG-2 and SG-3) were placed on each SLJ specimen, at the locations shown in Figure 7.4. Their aim was to monitor strains at these three locations for reasons of comparison with the respective numerical results. During the tests the applied displacement together with the reaction forces were monitored. Figure 7.5 shows a typical SLJ-4 specimen under experimental conditions.

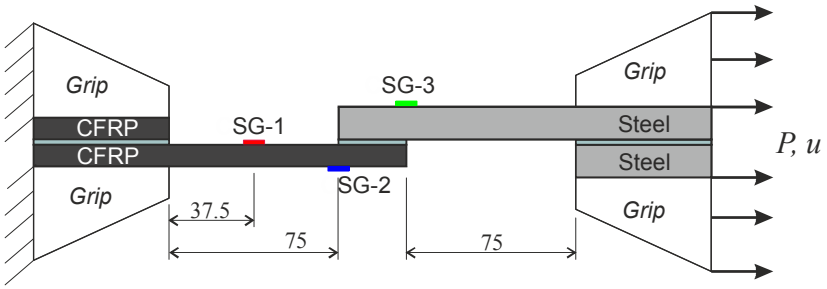

Figure 7.4: Experimental set-up of the SLJ specimens.

Figure 7.5: A typical CFRP-to-Steel SLJ with 75mm overlap length under experimental conditions.

7.2.2 Numerical modeling

The actual average dimensions listed in Table 7.1 of the SLJ geometries shown in Figure 7.2 have been considered for the finite element analysis. Thus, seven models have been constructed in a 3-dimensional space according to the mesh and loading and boundary conditions shown in Figure 6.6 and described in section 6.2.3.2. As far as the CFRP and steel adherents are concerned, quadratic 20-node brick elements (C3D20) available in the ABAQUS® element library have been utilized. The whole adhesive layer is represented by plane interface elements, described in Appendix A1, (placed between adjacent continuum elements in the overlap areas) and the proposed EPZ laws or mixed-mode model have been utilized for the description of their constitutive relation. The cohesive elements utilized have constant dimensions (0.5 x 0.5) mm^2 in the entire overlap areas. For the numerical integration of the stiffness matrix and the internal force vector, a 3 x 3 Gaussian quadrature rule has been used. The Newton-Raphson method has been utilized for the solution of the displacement control non-linear problem augmented by the line search algorithm.

Table 7.2: Orthotropic elastic properties of the CFRP adherents (Andrianakis, 2011).

E_1 (MPa)	E_2 (MPa)	E_3 (MPa)	v_{12}	v_{13}	v_{23}	G_{12} (MPa)	G_{13} (MPa)	G_{23} (MPa)
35000	3000	3000	0.35	0.3	0.3	2000	1500	1500

As far as the material properties is concerned, the CFRP adherents were modeled as linear orthotropic with the properties listed in Table 7.2. On the other hand, the steel adherents were modeled as linear elastic – perfectly plastic materials (bi-linear model) based on the Von Mises plasticity model. The Young modulus has been taken equal to 170 GPa (experimentally measured magnitude), Poisson ratio equal to 0.3 and the Yield stress limit equal to 180 MPa. For the description of the constitutive behaviour of cohesive elements utilized for modeling of the adhesive layer, the 3D proposed EPZ mixed-mode model is utilized. The definition of the pure mode EPZ law properties is based on the corresponding ones described in section 6.2.3.3. According to the manufacturer of the adhesive material the shear strength of the adhesive $\sigma_{c,II}$ varies together with the substrates utilized for the creation of the adhesive bond. The manufacturer provides the shear strength measured from adhesively bonded SLJ geometries from similar materials, including CFRP-to-CFRP. Additionally, he states that when analyzing adhesive joints with dissimilar materials, as the SLJ cases adopted herein, the selection of the $\sigma_{c,II}$ magnitude must be based on the corresponding lower value measured from SLJ with similar adherents; e.g. for an adhesive layer with 0.5 mm thickness, the $\sigma_{c,II}$ magnitude equals to 18.5 MPa and 14.25 MPa, for steel-to-steel and CFRP-to-CFRP substrates, respectively. Thus, in our case for the 0.5 mm thick adhesive layer the $\sigma_{c,II}$ magnitude has been taken equal to 14.25 MPa. The remaining parameters have been taken equal to the respective ones listed in Table 6.1 which correspond to steel-to-steel adhesive joints.

The aforementioned parameters refer to an adhesive layer with a thickness of 0.5 mm. In the framework of the current parametric analysis, an additional adhesive thickness has been considered equal to 0.85 mm. However, as reported in section 6.3.5, according to the experimental work reported by Ji et al. (2010) and Ji et al. (2011), the parameters of the cohesive laws are affected by the thickness of the corresponding bondline, in Mode I and II loading and fracture, respectively. Specifically, the parameter significantly affected are the critical stresses $\sigma_{c,I}$ and $\sigma_{c,II}$. The authors have shown that a 1 mm thick adhesive layer yields a 14.7 % percentage decrease and a 4.5 % percentage increase in the $\sigma_{c,I}$ and $\sigma_{c,II}$ magnitudes, respectively, of the corresponding magnitudes obtained from a 0.5 mm thick adhesive layer. Table 7.3 presents the corresponding parameters utilized for the definition of the pure mode EPZ laws of the 3D interface elements for the simulation of the seven SLJ cases. Set 1 corresponds to cases SLJ-1, SLJ-3, SLJ-5 and SLJ-7 whereas Set 2 corresponds to cases SLJ-2, SLJ-4 and SLJ-6. Parameter *e* has been taken equal to 0.1 % as concluded from previous investigations in Chapter 6.

Table 7.3: Properties of the pure mode EPZ laws utilized in simulation of the CFRP-to-steel SLJ tests.

Magnitude	k_I	$k_{II} = k_{III}$	$\sigma_{c,I}$	$\sigma_{c,II} = \sigma_{c,III}$	J_{Ic}	$J_{IIc} = J_{IIIc}$	e
units	N/mm^3	N/mm^3	MPa	MPa	N/mm	N/mm	%
Set 1	3700	1300	30	14.25	4	4.7	0.1
Set 2	2176	765	25.6	15	4	4.7	0.1

7.2.3 Numerical and Experimental results

7.2.3.1 Cases with long overlap length: Cases SLJ-1 to SLJ-4

In order to draw confident conclusions regarding the parametric study and the effect of the corresponding parameters (adhesive thickness, overlap length and stiffness ratio), a comparison between the experimental and numerical results in terms of the measured and calculated global response and strength (maximum attained force), is presented. Thus, Figure 7.6 presents the strengths from all seven cases considered (see Table 7.1 and Figure 7.2) as experimentally measured and numerically evaluated.

To begin with, a relatively increased deviation from the average value of the experimental strengths is obtained regarding the SLJ cases with 75 mm overlap length compared to the SLJ cases with 25 mm overlap length, resulting to a maximum coefficient of variation (CoV) equal to 5.7% and 1.4%, respectively. According to Figure 7.6, the selection of either the adhesive thickness (0.5 mm and 0.85 mm) or the stiffness ratio (0.175 and 0.35) to the strength of each joint's case has a small effect the corresponding obtained average strength. On the other hand, as expected, there is a significant effect of the overlap length on the strength of the joints, regardless the selected adhesive thickness and stiffness ratio.

In particular, a 70% increase of the adhesive thickness results to a maximum 5% increase of the strength of the corresponding SLJ cases with 25 mm overlap length. The same conclusion is drawn out for the effect of the stiffness ratio on the strength of the joints, where an increase of 100% results in a 5% maximum increase of the strength. However, the joints with three times longer overlap length yield a maximum 100% increase in their strength, with respect to the joints with the short overlap lengths, i.e. 75mm and 25 mm, respectively.

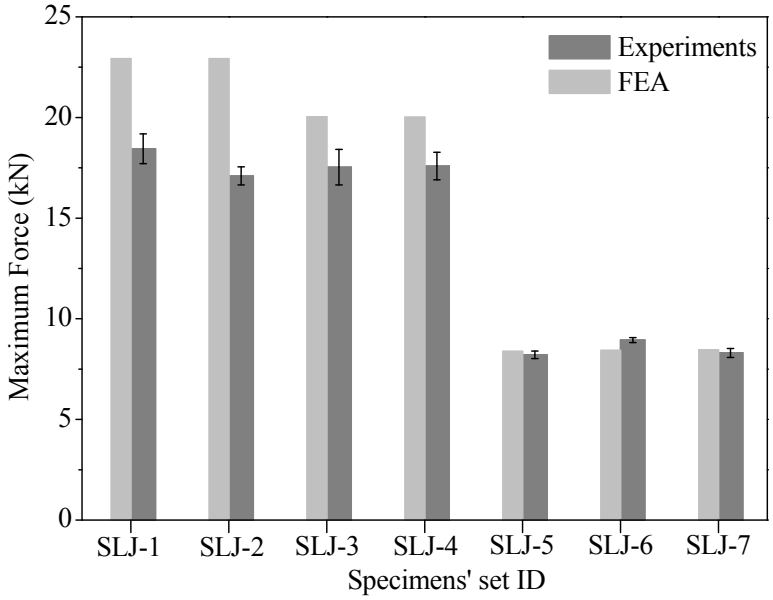

Figure 7.6: Collected experimental and numerical strengths for all considered SLJ cases.

Figure 7.7 and Figure 7.8 present a comparison between the experimentally measured and numerically evaluated global response in terms of the reaction force – applied displacement and reaction force – strains, for the SLJ-1 and SLJ-2 cases, respectively. According to the experimental measurements shown in Figure 7.7 and Figure 7.8, a very good repeatability has been obtained. In both cases, the P - u relations are globally characterized by a linear behaviour up to the maximum attained load, where further increase in the applied displacement lead to the decay of the force and the subsequent failure of the joints. In fact these two cases differ only in the adhesive thickness utilized to fabricate the SLJ geometries, that is 0.5 mm and 0.89 mm for the SLJ-1 and SLJ-2 case, respectively. The developed strains at the three measurement locations follow a linear pattern (see Figure 7.7b and Figure 7.8b), which denotes that they remain within the linear elastic region of either the CFRP or the steel substrates.

It is noteworthy, that at the force level of 15 kN for the SLJ-1 case and 12.5 kN for the SLJ-2 case, a change in the slope of the P- Strain relation has been recorded in the SG-3 location, as shown in Figure 7.7b and Figure 7.8b. This inflexion point is consistent with global $P - u$ relation, where at the same force level (15 kN for SLJ-1 case and 12.5 for SLJ-2 case), the non-linear region is starting and continues up to the strength of each joint. These changes in the slopes are attributed to the damage initiation and propagation occurring within the adhesive layer.

As far as the finite element results are concerned, the experimental behaviour in either *P* - *u* or *P* - Strains has been accurately predicted, in both SLJ-1 and SLJ-2 cases. However, as aforementioned, the proposed mixed-mode model fails to capture the experimental average strength and its corresponding displacement at failure, yielding to a difference of 15% and 17% for the SLJ-1 and SLJ-2 case, respectively. A very good prediction of the strains has been obtained particularly at the SG-1 and SG-3 measurement locations. However a slight deviation of the FEA predictions is obtained at the SG-2 location, as depicted in Figure 7.7b and Figure 7.8b.

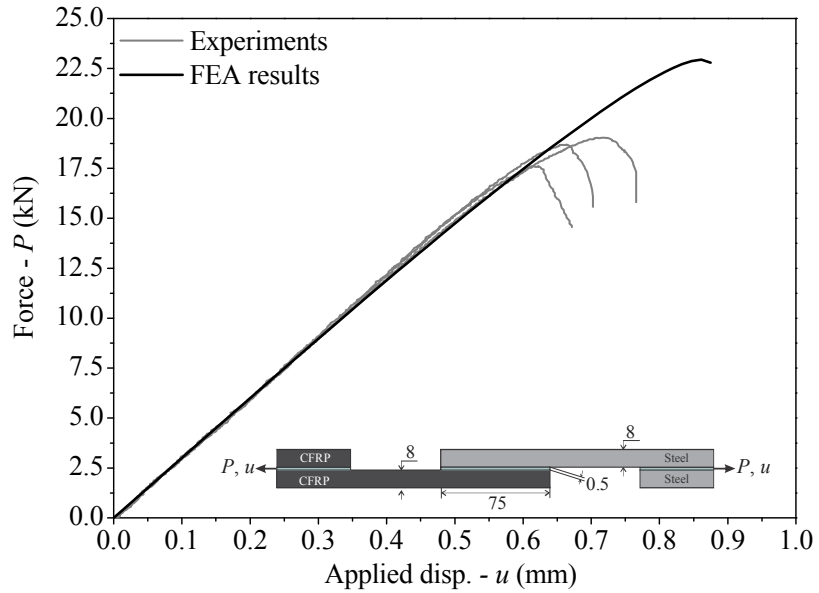

(a)

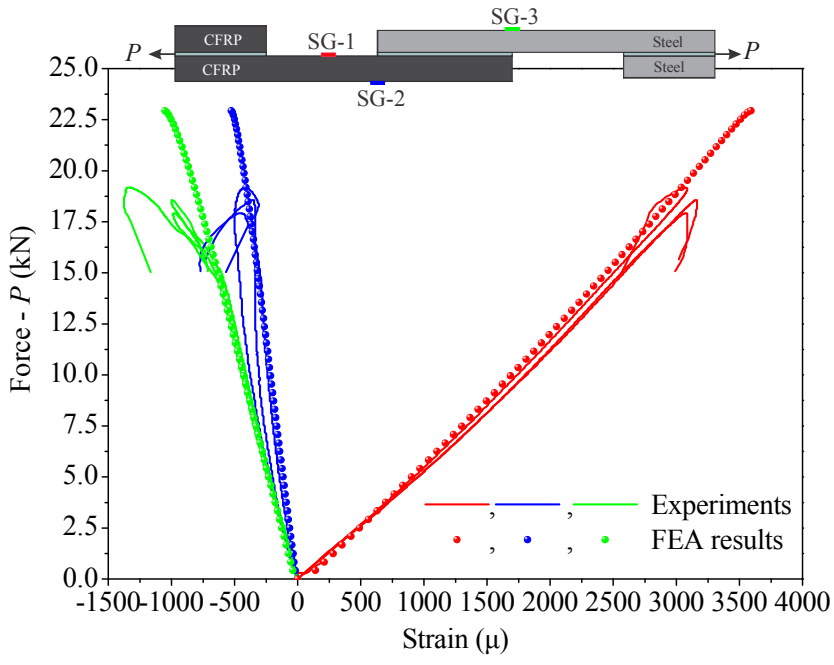

(b)

Figure 7.7: Global response of the SLJ-1 case in terms of the force – displacement (a) and force –strains (b) as experimentally registered and numerically evaluated.

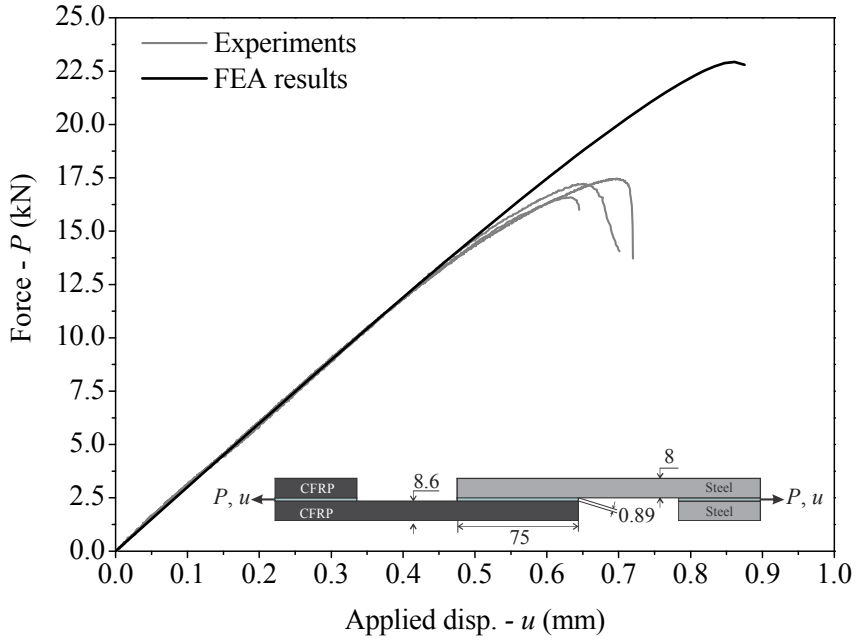

(a)

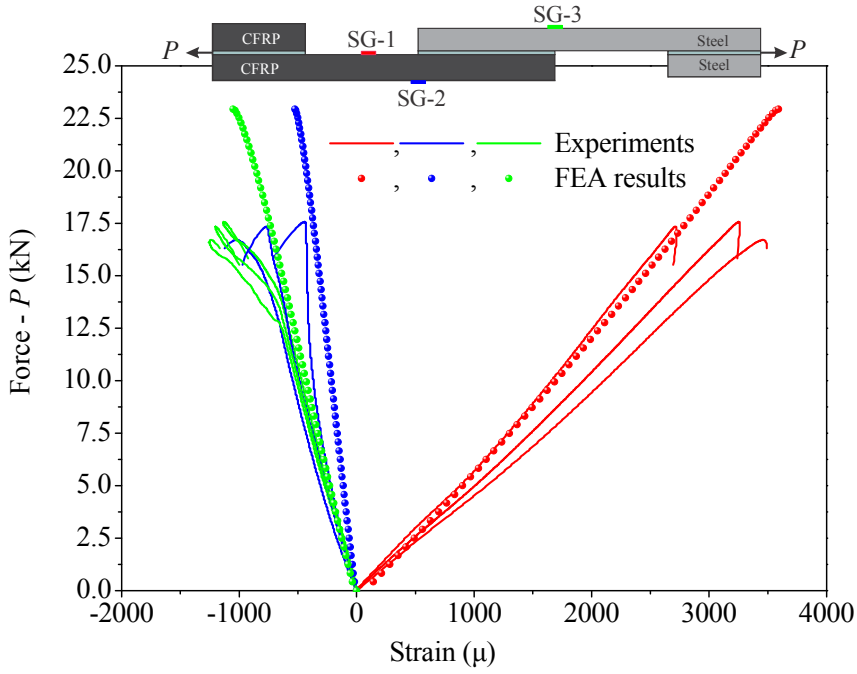

(b)

Figure 7.8: Global response of the SLJ-2 case in terms of the force – displacement (a) and force – strains (b) as experimentally registered and numerically evaluated.

Figure 7.9 presents the variation of the principal stresses at the maximum attained force level of the deformed model of SLJ-1 and SLJ-2 cases. The top substrate is the steel one, whereas the bottom substrate is the CFRP one.

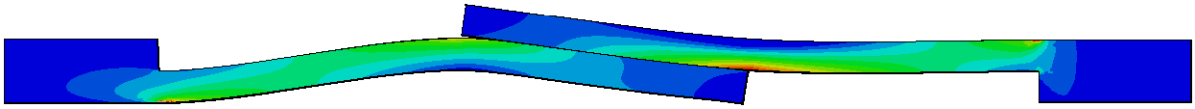

Figure 7.9: Qualitative variation of principal stresses over the SLJ domain of SLJ-1 and SLJ-2 cases.

According to the calculated deformed shape of the SLJ-1,2 models, the CFRP substrate, which is more compliant than the steel substrate, follows the well known eccentric behaviour of a single lap joint in a way that leads the adhesive layer to develop high peel and in-plane shear stresses at the right and the left hand side edges of the bondline (cohesive zone – fictitious crack), respectively. Further insight can be given by examining the developed stresses over the adhesive area as calculated with the proposed EPZ mixed-mode model. Figure 7.11, Figure 7.12 and Figure 7.13 present the peel (Mode I), in-plane (Mode II) and out-of-plane (Mode III) shear stresses, respectively, according to the local coordinate system depicted in Figure 7.10, as calculated from the SLJ-1 model. Without any loss of significant information, stress variations of the SLJ-2 model are not provided, since they share the same behaviour with the SLJ-1 model.

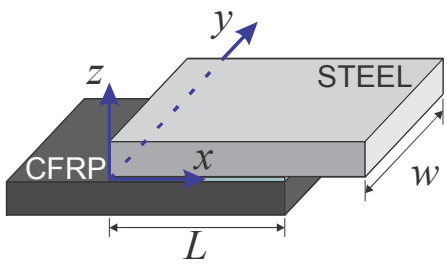

Figure 7.10: Dimensions and coordinate system of the overlap area of the SLJ configurations.

The axes of the 2D stress figures have been normalized according to the real dimensions of the overlap length and width of the model. The peel stresses plotted in Figure 7.11 are calculated at the maximum force level of the SLJ-1 model. Apart from, the symmetry with respect to the x axis at $y / w = 0.5$ that they exhibit, they peak at $x / L = 1$. This behaviour is common through the entire loading history of the SLJ model.

On the other hand, in-plane shear stresses peak at $x / L = 0$ within the linear elastic region of the adhesive material (see Figure 7.12a). As the loading increases and the adhesive layer enters plasticity the in-plane shear stresses almost reach the plateau of 14.2 MPa (see Figure 7.12b). The plastic zone then extends in that area with any further increase in the load and at the same time the adhesive material laying in the right hand side, at $x / L = 1$, contributes to the loading by developing elastic stresses. At the maximum attained force, the plasticity of the adhesive layer has extended and damage initiation and propagation is located at both adhesive edges (area of the softening behaviour of the T-S law), as shown in Figure 7.12c. However the rate and magnitude of the damage extension is much higher at $x / L = 0$; a fact that has as a consequence the deformed shape of Figure 7.9, where the cohesive zone is apparent at left hand side of the overlap area.

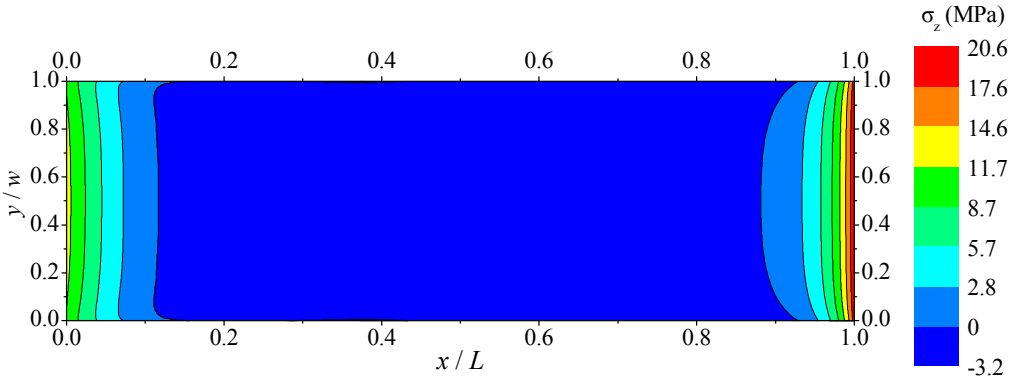

Figure 7.11: Peel stresses σ_z distribution over the adhesive area of the SLJ-1 model at the maximum attained force (u = 0.86 mm).

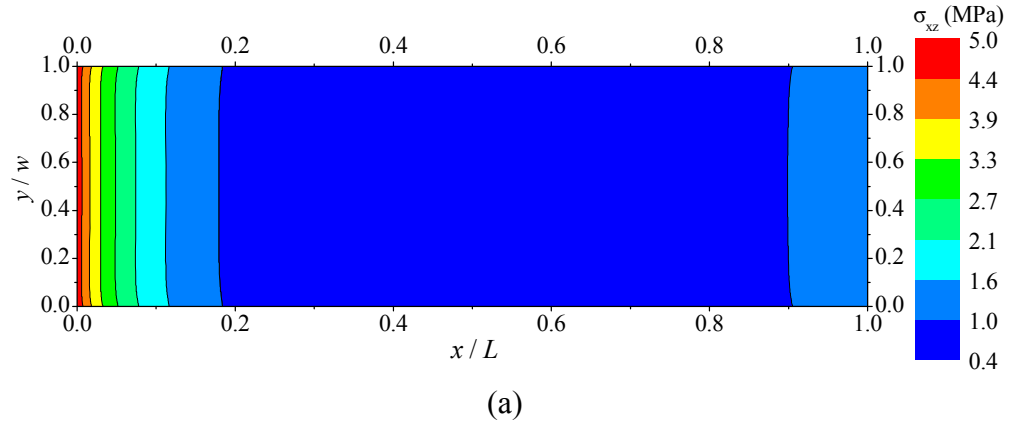

(a)

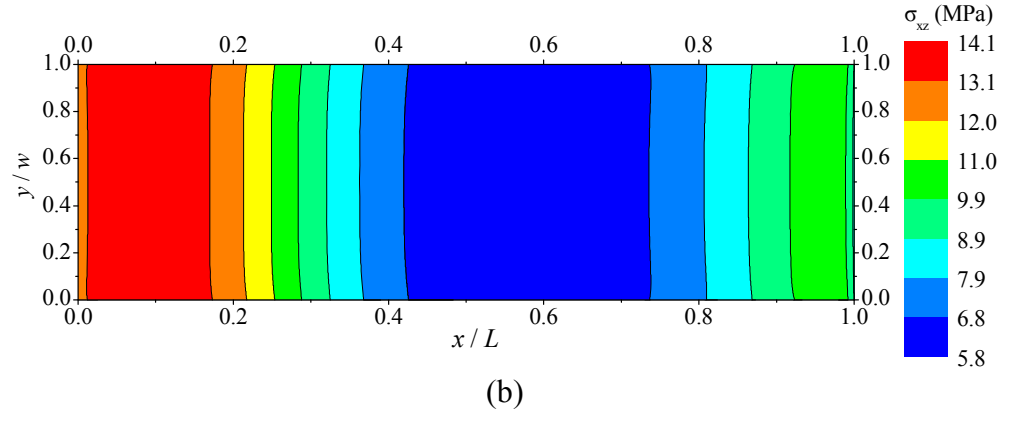

(b)

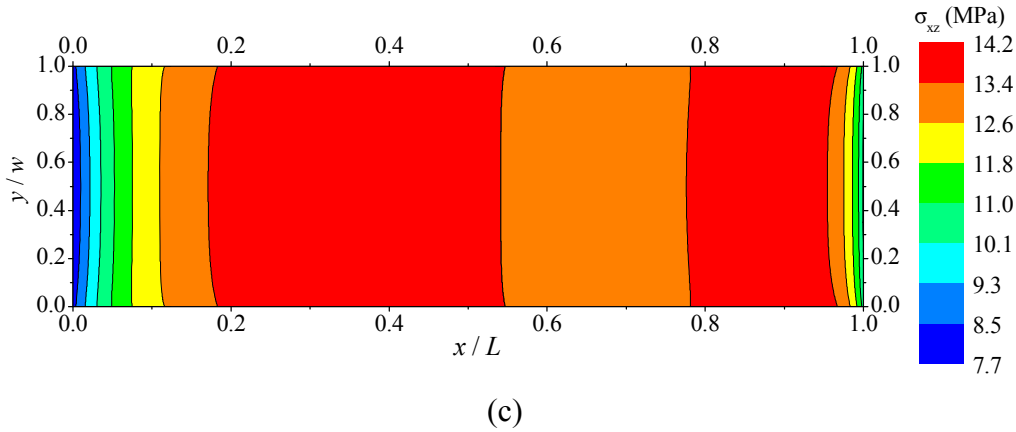

(c)

Figure 7.12: In plane shear stresses τ_{xz} distribution over the adhesive area of the SLJ-1 model for u equal to 0.1 mm (a), 0.5 mm (b) and 0.86 mm (c).

The out-of-plane shear stresses (Mode III) remain at very low levels and can be characterized linear during the entire loading history of the SLJ-1 or SLJ-2 models, as shown in Figure 13. Thus they do not contribute to the mixed-mode loading and fracture of the adhesive layer. This conclusion was expected since the problem under examination is in fact plane strain and hence, dominant fracture modes are Mode I and Mode II. They peak at the vicinity of the two corner edges of the adhesive layer, that is at $x / L = 0$ and $y / w = 0$ and 1.

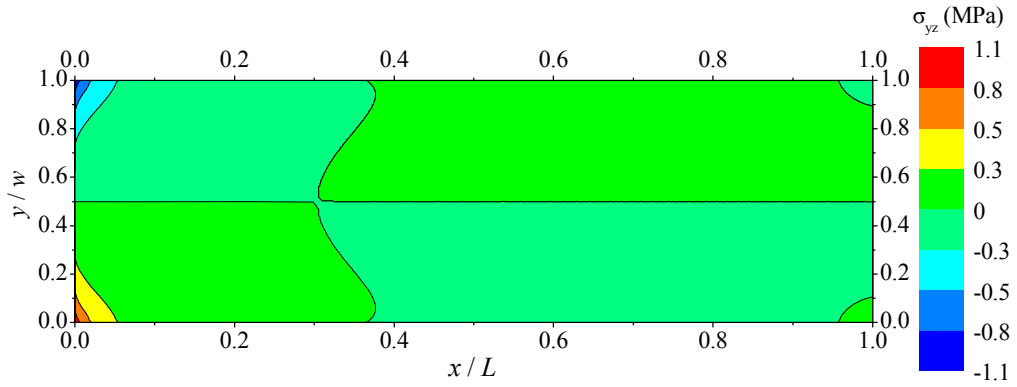

Figure 7.13: Out-of-plane shear stresses τ_{yz} distribution over the adhesive area of the SLJ-1 and SLJ-2 model at the maximum attained force (u = 0.86 mm).

Following the evaluation of the SLJ-1 and SLJ-2 cases which involve SLJ geometries with 8 mm thick steel substrates, the SLJ-3 and SLJ-4 cases are examined which involve 5 mm thick steel substrates. The corresponding results are shown in Figure 7.14 and Figure 7.15. A very good repeatability of the *P*-*u* and *P*-Strains experimental relations has been obtained.

All three respective experimental *P*-*u* curves of SLJ-3 (see Figure 7.14a) and SLJ-4 (see Figure 7.15a) case share a common behaviour, which can be divided into three regions. The first region is described by a linear behaviour bounded by the inflexion point at the force level of 13.2 kN for the SLJ-3 and 12.5 kN for the SLJ-4 case. The second region is bounded by the inflexion point and the load carrying capacity level of each joint. The third region is described by a softening behaviour, which denotes the inability of each joint to carry further load. In this region failure mechanisms are developing in the adhesive/substrate system, i.e. plasticity of the ductile adhesive, void nucleation in the adhesive, debonding at the adhesive/adherent interface, micro-cracking, etc.

Despite the overestimated prediction of the average experimental maximum loads, the FEA results predict accurately the experimental *P*-*u* behaviour in both cases, as shown in Figure 7.14a and Figure 7.15a. The same conclusions can be drawn out from the *P*-Strains relations, apart from the strain predictions at the SG-3 location of Figure 14b, where the load level of the change in the slope is underestimated with subsequent deviations in the predicted behaviour.

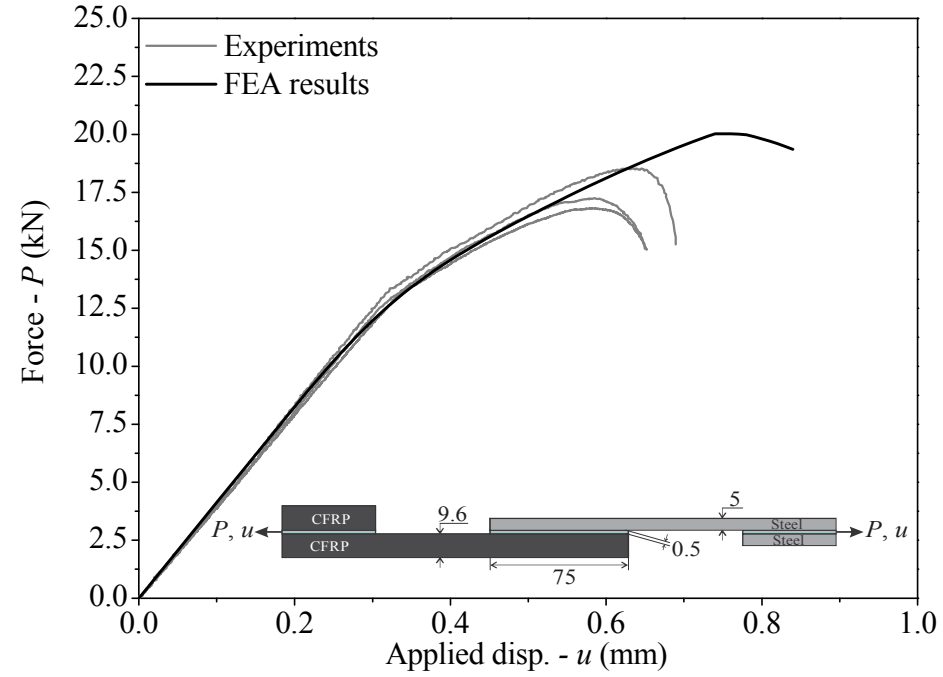

(a)

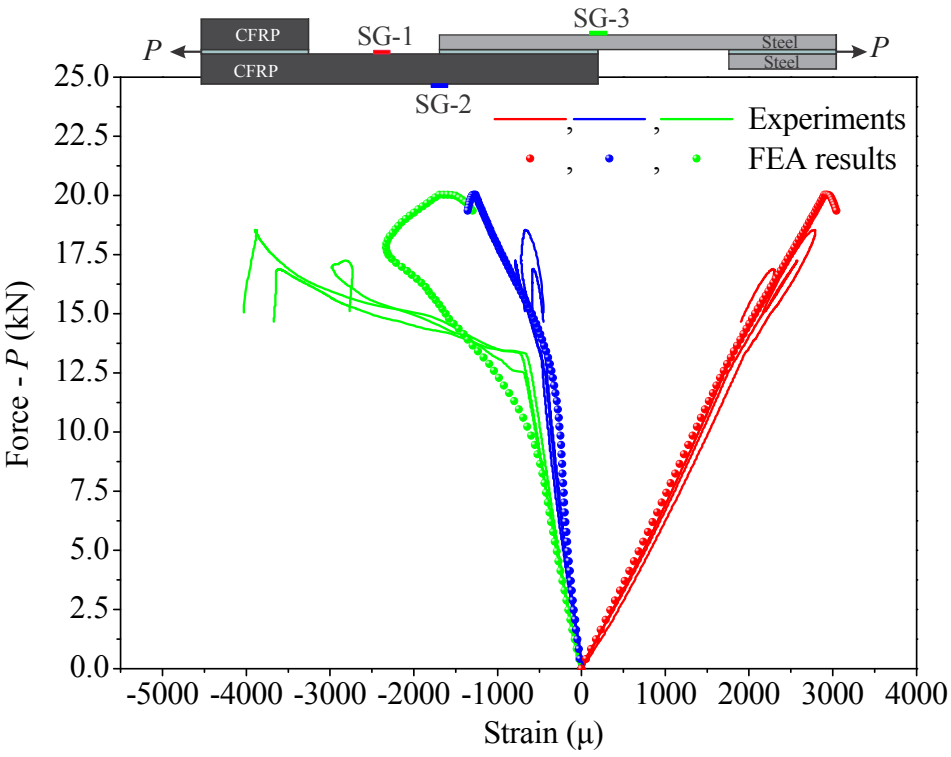

(b)

Figure 7.14: Global response of the SLJ-3 case in terms of the force – displacement (a) and force –strains (b) as experimentally registered and numerically evaluated.

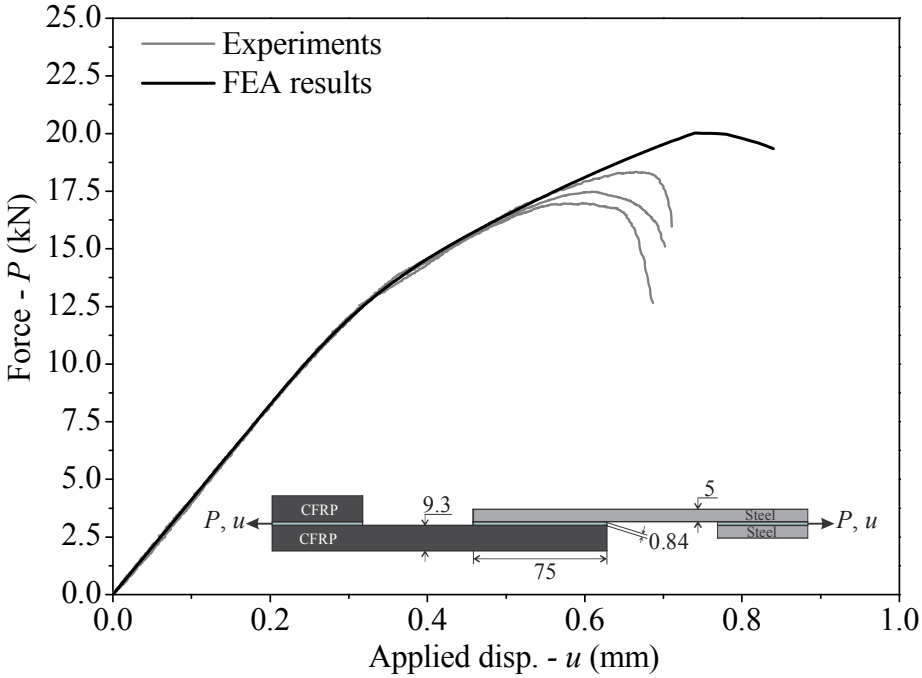

(a)

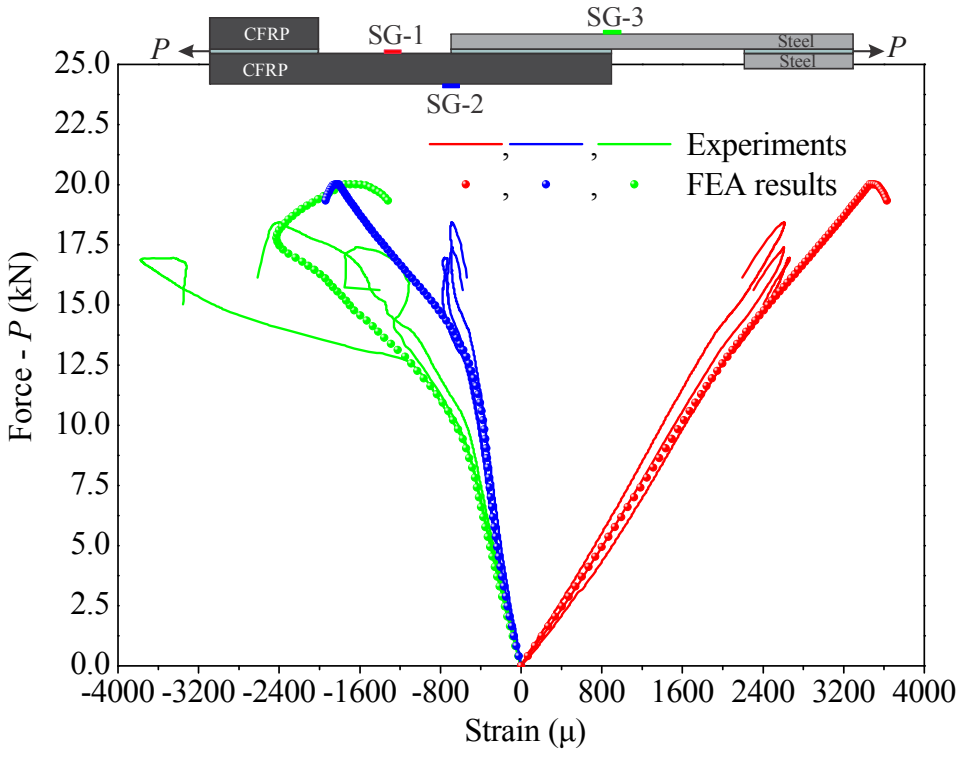

(b)

Figure 7.15: Global response of the SLJ-4 case in terms of the force – displacement (a) and force –strains (b) as experimentally registered and numerically evaluated.

The change in slope (inflexion point) and the subsequent bilinear behaviour of the *P-u* plots, are of significance importance and further examination must be given. According to the *P*-Strains relations shown in Figure 7.14b and Figure 7.15b, a change in the slope is additionally observed at the same force levels for the strains measured at the SG-3 location. In fact, this particular location refers to strain measurements on the free surface of the steel substrates at the overlap edge, as shown in Figure 7.4. This change in slope is attributed to the yield (plastic zone creation) of the steel substrate at the opposite to the SG-3 location, as experimentally observed and numerically calculated. Figure 7.16a presents a typical SLJ-3 specimen (the same occurs with the SLJ-4 specimens) after the failure of the bond, where the permanent deformation of the steel adherend can be seen with a naked eye. The developed plastic zone in the steel adherend are presented in Figure 7.16b, as numerically calculated with the use of a bi-linear (elastic perfectly plastic) material model for the ductile steel substrate.

The local yield of the steel adherend has a significant effect on the loading and fracture mode of the adhesive bond. A comparison between the experimentally captured and numerically calculated deformation in Figure 7.17 reveals at first hand the damage evolution process within the adhesive layer. The experimental observations are in good agreement with the numerical results shown in this figure. According to Figure 7.17a, an extensive damage zone (plasticity, void nucleation and micro-cracking) has been developed at the left hand side edge of the adhesive layer, whereas a smaller damage zone seems to form at the right hand side edge of the adhesive layer. This behaviour is similar to the corresponding one described previously, for the SLJ-1 and SLJ-2 cases.

(a)

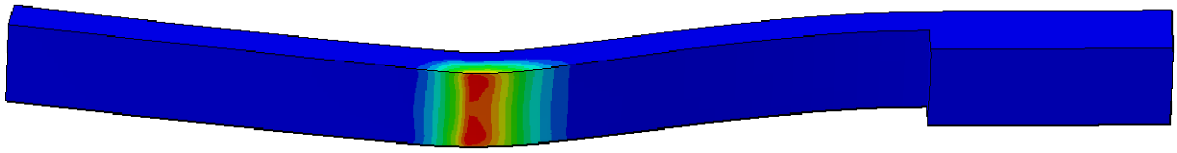

(b)

Figure 7.16: Typical failure mode of a specimen of the SLJ-3 and SLJ-4 case denoting permanent plastic deformation of the steel substrate (a) and variation of the Von Mises plastic strains over the steel adherent domain.

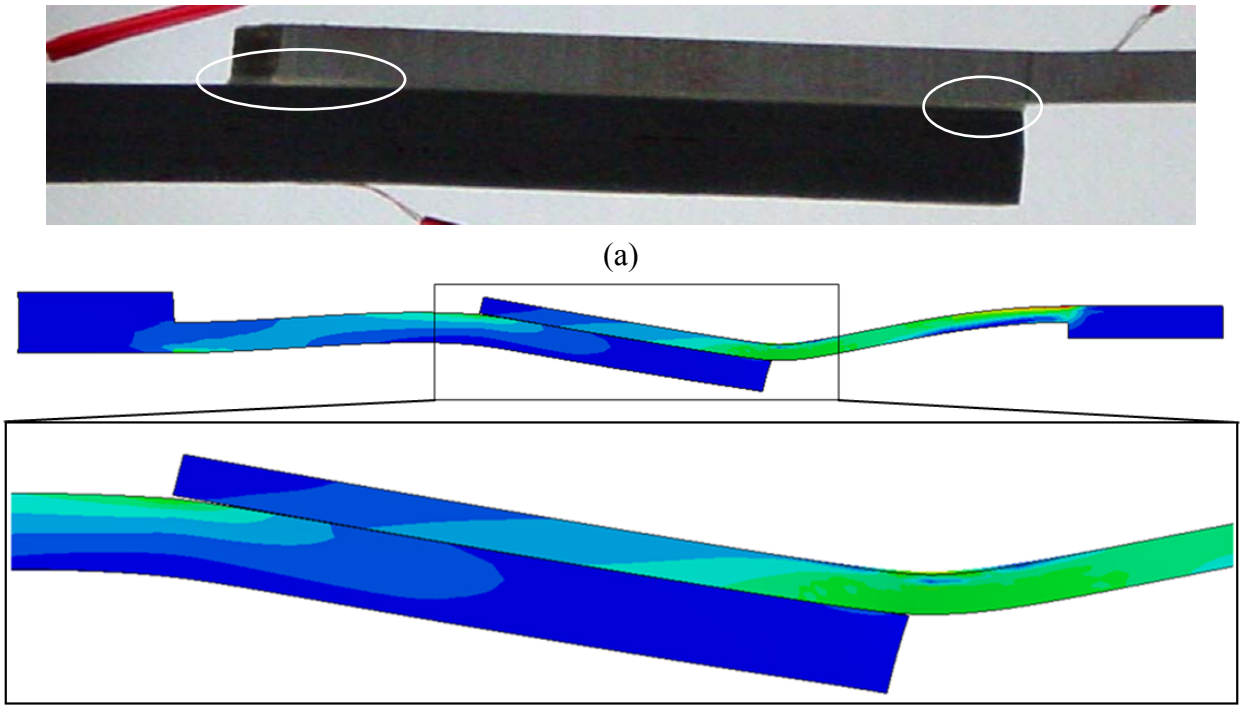

(a)

(b)

Figure 7.17: Typical deformed shape near the maximum attained force as experimentally captured (a) and numerically predicted (b).

In order to conduct confident conclusions regarding the effect of the yield zone developed in the steel adherend, the peel stress σ_z, the in-plane shear stresses σ_{xz} and the out-of-plane shear stresses σ_{yz} as these vary over the adhesive layer (see Figure 7.10) at the maximum attained force level are shown in Figure 7.18.

The peel stresses follow the same pattern to that presented in Figure 7.11 within the linear elastic region and early stages of plasticity of the adhesive layer. With further increase in the applied force and as the steel adherent enters plasticity, high peel stress concentrate in a larger area than that of Figure 7.11, as shown in Figure 7.18a. This redistribution, where the peel stresses peak in the area around $x / L = 1$ bounded within [$y / w = 0.2$, $y / w = 0.8$] and decrease in magnitude in the areas bounded within [$y / w = 0$, $y / w = 0.2$] and [$y / w = 0.8$, $y / w = 1.0$] is attributed to the subsequent redistribution of the out-of-plane shear stresses as shown in Figure 7.18c. The σ_{yz} stresses follow the pattern presented in Figure 7.13 within the linear elastic and early stages of plasticity of the adhesive layer. However, the plastic zone developed in the steel adherend leads to the shrinkage of its width at that location (see Figure 7.16), which subsequently leads the adhesive material to develop increased out-of-plane shear stresses. Thus, the contribution of the Mode III fracture mode to the failure of the SLJ-3 and SLJ-4 cases is considered important. The in-plane shear stresses follow the pattern shown in Figure 7.12a and Figure 7.12b within the linear elastic and early stages of plasticity of the adhesive layer, respectively. However, with the yield initiation of the steel adherent the in-plane shear stresses redistribute in a way that at the maximum attained load they present the variation shown in

Figure 7.18b. This behaviour is much different than the one presented in Figure 7.12c, which corresponds to SLJ-1 and SLJ-2 cases and where plasticity in the steel adherent is not present.

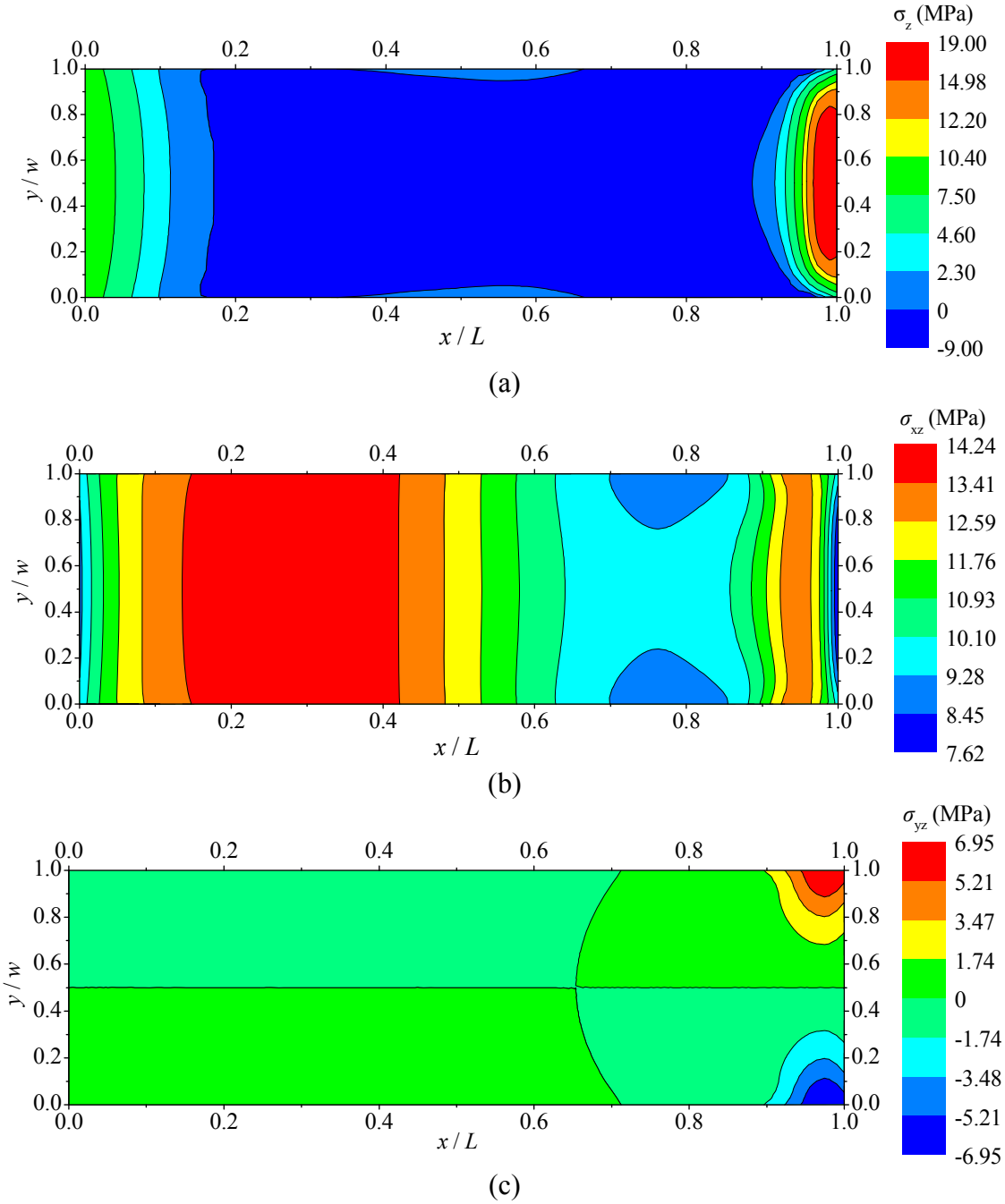

Figure 7.18: Variation of the peel stresses (a), in-plane shear stresses (b) and out-of-plane shear stresses (c) over the adhesive layer domain at the maximum attained force level as calculated with the SLJ-3 model (the same for SLJ-4 model).

7.2.3.2 Cases with short overlap length: Cases SLJ-5 to SLJ-7

Having evaluated both experimentally and numerically the behaviour of the SLJ-1,2,3 and 4 cases, which involve single lap joint geometries with 75 mm overlap length, the behaviour of the SLJ-5, 6 and 7 cases that involve 25 mm overlap length will be examined. Figure 7.19, Figure 7.20 and Figure 7.21 present a comparison between the experimental measurements and numerical results for the SLJ-5, 6 and 7 cases, respectively.

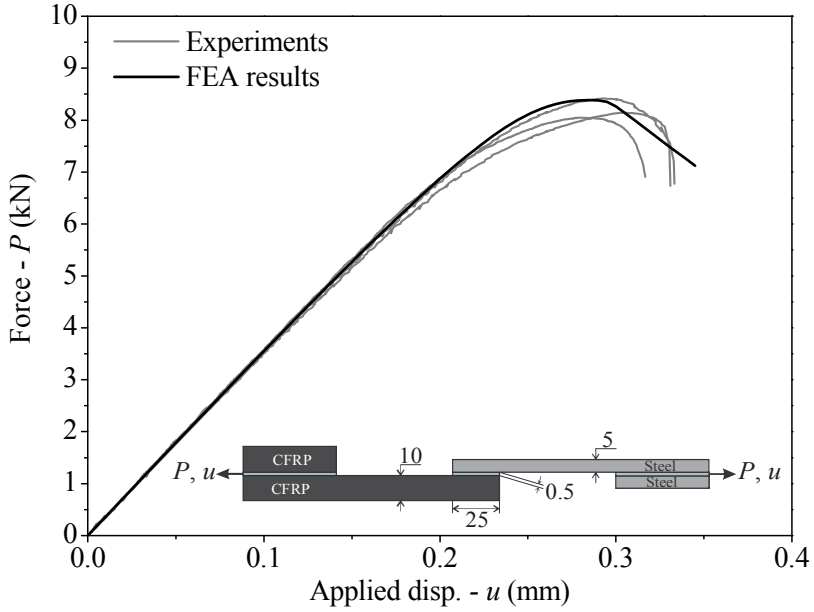

(a)

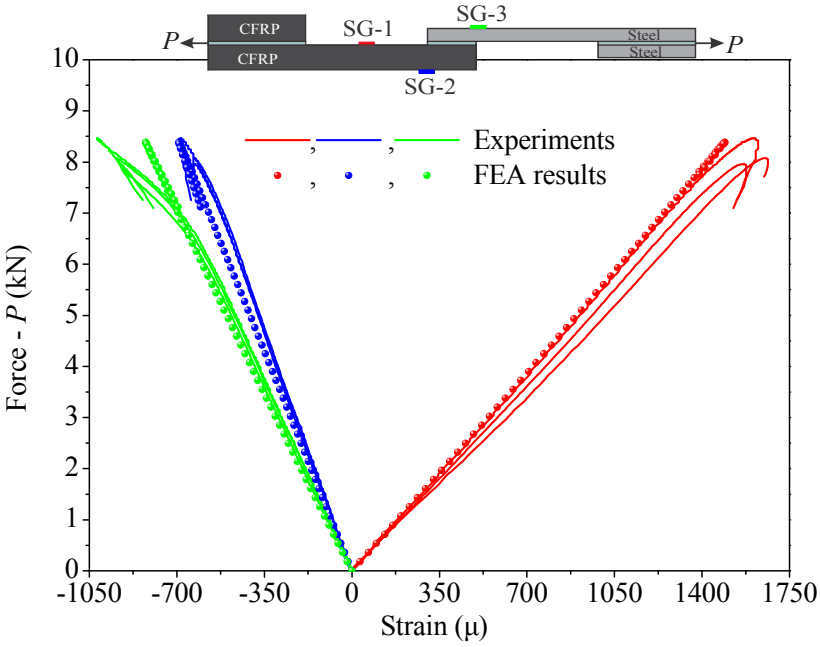

(b)

Figure 7.19: Global response of the SLJ-5 case in terms of the force – displacement (a) and force – strains (b) as experimentally registered and numerically evaluated.

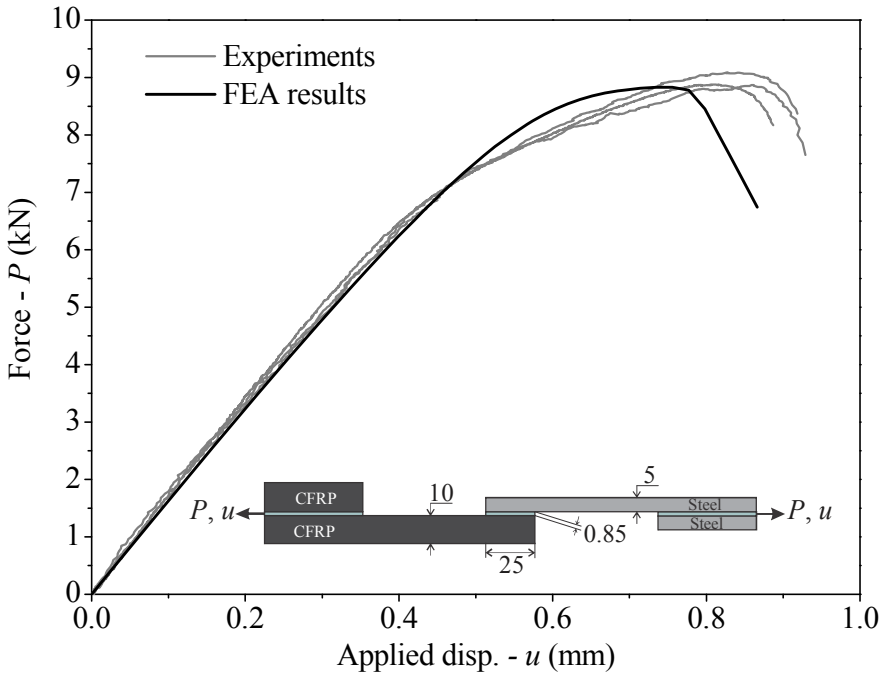

(a)

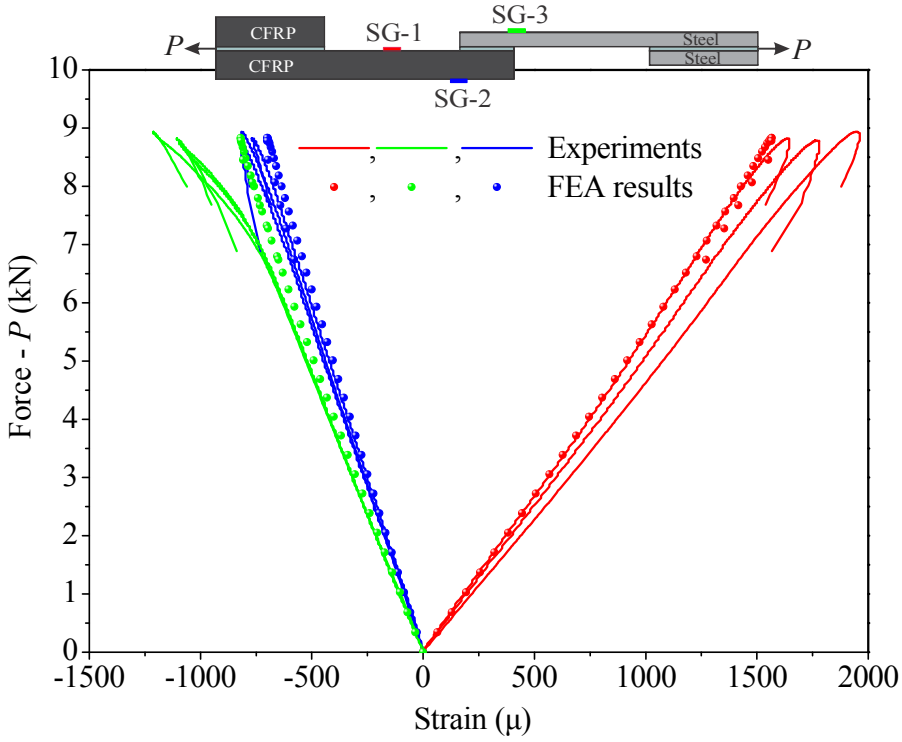

(b)

Figure 7.20: Global response of the SLJ-6 case in terms of the force – displacement (a) and force – strains (b) as experimentally registered and numerically evaluated.

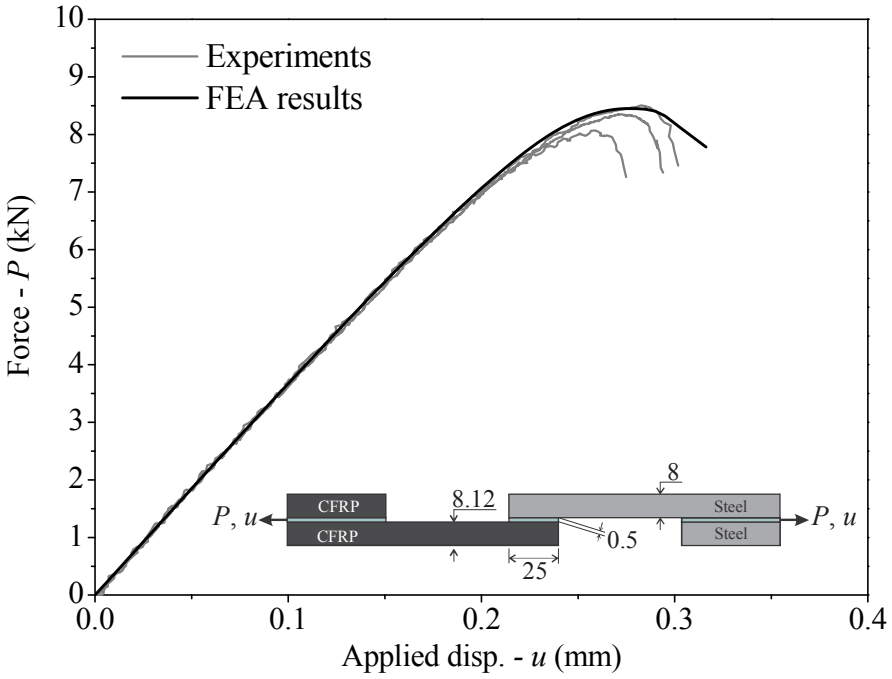

(a)

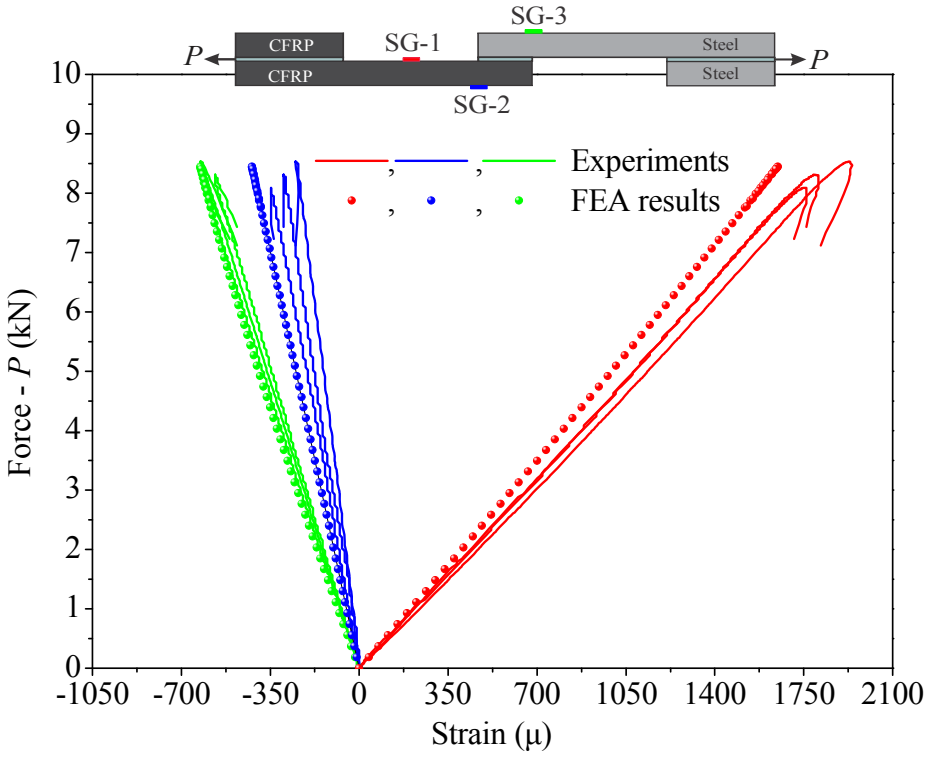

(b)

Figure 7.21: Global response of the SLJ-7 case in terms of the force – displacement (a) and force – strains (b) as experimentally registered and numerically evaluated.

According to Figure 7.19, Figure 7.20 and Figure 7.21, the experimental data are in very good agreement regarding both their behaviour and maximum joint strength. The *P-u* curves exhibit an initial linear response followed by increasing non-linearities as the adhesive layer enters plasticity. This behaviour, is more emphasized in the SLJ-6 case where the thickness of the adhesive layer is 0.85 mm compared to the respective magnitude of the SLJ-5 and SLJ-7 cases, that is 0.5 mm. This is reasonable, since thicker adhesive layers correspond to the development of larger plastic zone inside the layer, leading to increased plastic deformations and strains. As far as the FEA results are concerned, these are in great agreement with the corresponding experimental measurements, since they capture the linear and non-linear behaviour of the *P-u* plots in all three cases considered (SLJ-5, 6 and 7). A very good agreement is additionally observed between the *P*- strains experimental and numerical results.

Figure 7.22 and Figure 7.23 present the distribution of the principal stresses over the SLJ-5, 6 and SLJ-7 deformed models, respectively.

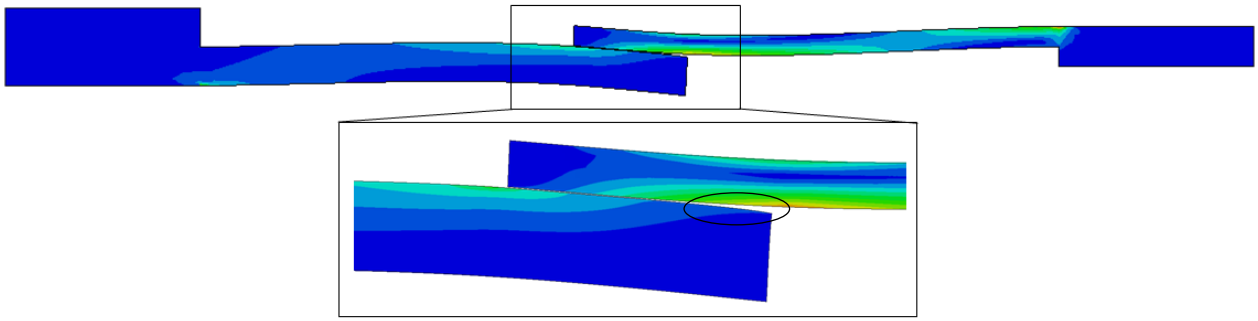

Figure 7.22: Qualitative variation of principal stresses over the SLJ domain of SLJ-5 and SLJ-6 cases.

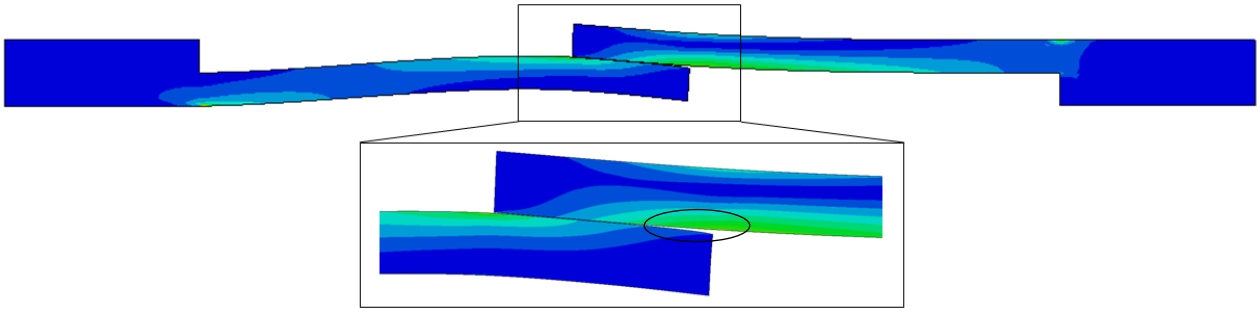

Figure 7.23: Qualitative variation of principal stresses over the SLJ domain of SLJ-7 case.

According to these figures, regardless of the stiffness ratio and the adhesive thickness, in all three cases, damage and cracking initiates at the right hand side edge of the adhesive overlap area, in under Mode I loading and fracture conditions. This statement can be further justified by examining the variation of the corresponding to Mode I peel stresses σ_z over the adhesive area, as shown in Figure 7.24. The positive peel stresses that contribute to Mode I loading and fracture develop in the areas bounded by [$x / L = 0$, $x / L = 0.25$] and [$x / L = 0.6$, $x / L = 1$], whereas in the remaining area negative contact stresses develop that denote contact conditions. The positive peel stresses peak at $x / L = 1$ with magnitude equal to 13.1 MPa. On the other hand, the in-plane shear stresses in the linear elastic region peak at the opposite edge at $x / L = 0$ (see Figure 7.25a)

and thus plasticity in the adhesive layer initiates from that point and propagates towards the remaining adhesive edge at $x / L = 1$ (see Figure 7.25b). Finally, at the maximum attained load, the in-plane shear stresses have become plastic in almost the entire adhesive area and decrease (softening) in the vicinity of the adhesive edge at $x / L = 1$, as shown in Figure 7.25c. As aforementioned, at this location peel stresses maximize and thus they become responsible for damage and fracture initiation of the adhesive layer.

The out-of-plane shear stresses σ_{yz} peak, in the entire loading history, at the two left hand side corner of the adhesive layer at the $x / L = 0$ as shown in Figure 7.26. Their magnitude remains at very low stress levels and thus σ_{yz} stresses remain in the linear elastic region, without contributing to the failure of the adhesive layer.

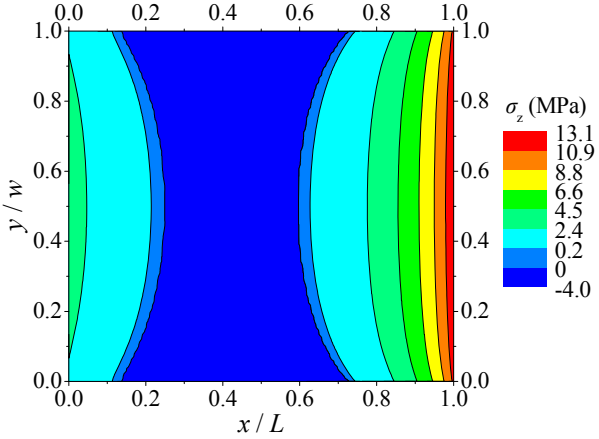

Figure 7.24: Variation of the peel stresses (over the adhesive layer domain at the maximum attained force level as calculated with the SLJ-5 model (the same for SLJ-6 and SLJ-7 model).

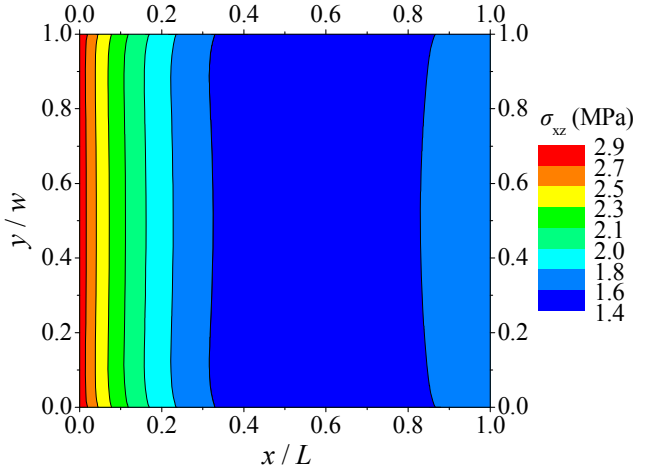

(a)

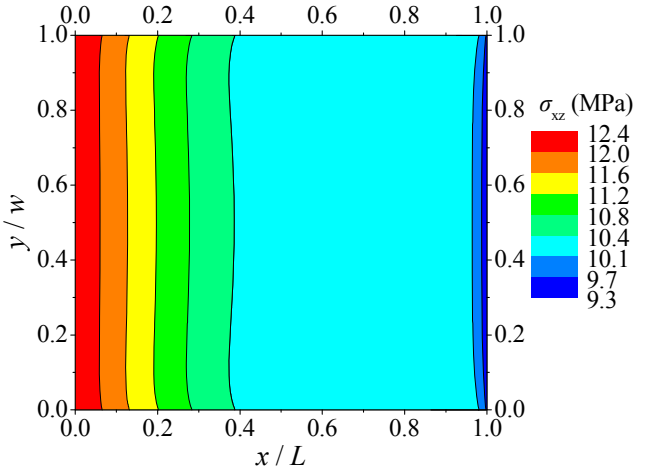

(b)

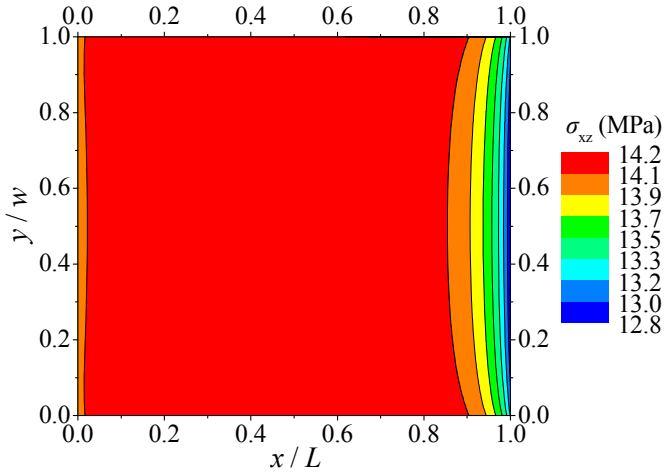

(c)

Figure 7.25: Variation of the in-plane shear stresses σ_{xz} over the adhesive layer domain at the elastic region (a), early stages of plasticity (b) and at the maximum attained force level (c) as calculated with the SLJ-5 model (the same for SLJ-6 and SLJ-7 model).

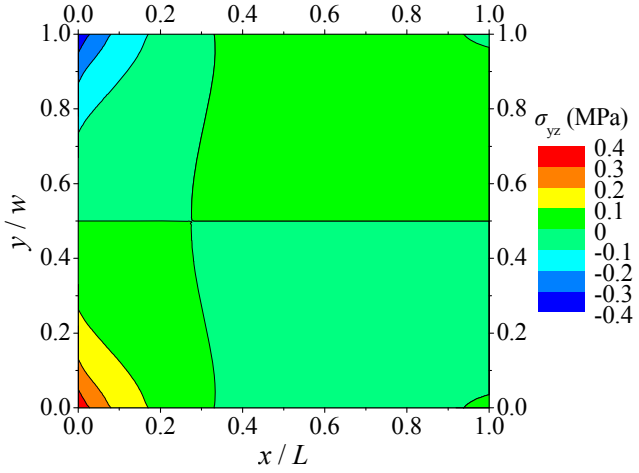

Figure 7.26: Variation of the out-of-plane shear stresses σ_{yz} over the adhesive layer domain at the maximum attained force level as calculated with the SLJ-5 model (the same for SLJ-6 and SLJ-7 model).

7.3 DCB-UBM tests

7.3.1 Experimental program

Only an overview of the experimental program of the DCB-UBM tests is given, within the framework of the current PhD thesis, since the numerical simulation of the experiments is the area of focus. Relevant detailed information is provided in the Diploma Thesis of Andrianakis (2011).

Figure 7.27 presents a schematic view of the fabricated and tested DCB-UBM specimens. The selection of the materials and their corresponding dimensions were based on their possible applications in the marine industry. The width of all specimens w had an average value equal to 30±0.2 mm. The actual adhesive thickness t_a was 1±0.05 mm. The steel and CFRP adherents had an actual thickness, t_s and t_c, equal to 5±0.2 mm and 9.5±0.5mm, respectively.

As far as the CFRP composite material is concerned, 22 layers of 200 g/m^2 and 0.4 mm thick unidirectional carbon fiber fabrics (CST200 supplied by SGL Group) were combined with an epoxy resin LH 160 with the 135-136 hardener, both provided by HAVEL Composites. The UD fabrics were initially impregnated with the epoxy/hardener matrix system by the hand lay-up method and afterwards the plates were cured at 25 ^{o}C for 48 hours under constant 0.6 bar pressure with the aid of vacuum bagging. The metal adherents, which were fabricated from mild steel, were adhesively bonded to the cured CFRP substrates with Araldite 2015 (Huntsman Container Corporation Ltd) epoxy adhesive.

Prior to the application of the adhesive material on the bonding surfaces of the adherents, a 1 mm thick PTFE sheet (equal to the adhesive thickness) was utilized for the creation of the pre-crack. The length of the PTFE sheet was selected equal to 60 mm (see Figure 7.27), a value that yields a 10 mm pre-crack defined between the crack tip and the fixture. In fact, this value

does not affect the experimental results, since the substrates are subjected to constant moments applied at the two attached metal fixtures.

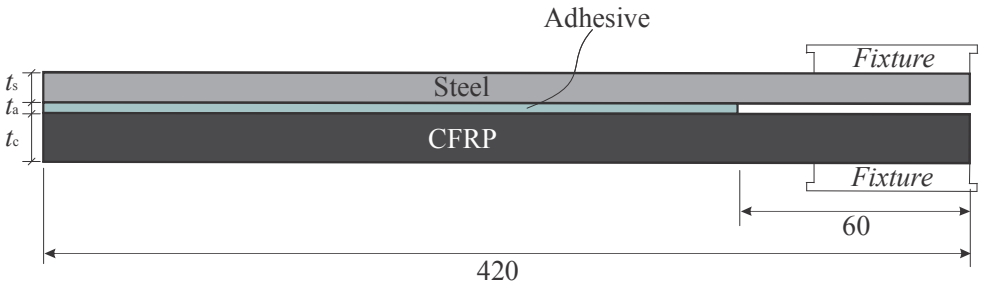

Figure 7.27: Geometrical configuration and dimensions (in mm) of the DCB-UBM specimens.

The fabricated specimens were tested under the DCB-UBM experimental configuration, as shown in Figure 7.28. As aforementioned, a special fixture was attached (bolted-bonded) at the steel and CFRP adherents (see Figure 7.27), that was used for the application of pure bending moments to the specimen by two transverse arms, using a wire/roller system at the cracked ends of the beams (see Figure 7.28a). The moment applied at each beam of the DCB specimen can be controlled through the length of the transverse arms, l_1 and l_2, resulting to a moment equal to $M_1 = Pl_1$ and $M_2 = Pl_2$, for the steel and CFRP adherend, respectively, where P is the force applied by the wire. So, by changing the lengths l_1 and l_2, different moment ratios M_1/M_2 can be obtained, enabling this way the same specimen geometry to be used for different mode mixities and eliminating the errors that could occur by changing the testing procedure in order to obtain different mode mixities. Moreover, since this set-up produces pure moments, the moment ratio throughout the length of the specimen is the same.

During the experiments, the pre-crack tip opening δ_I^* was measured for the Mode I tests and both opening δ_I^* and sliding δ_{II}^* separations were measured, for the Mode I and mixed Mode I and II loading and fracture tests, respectively. Thus, an extensometer (INSTRON 2620-602) was mounted on one side of the DCB-UBM specimens for recording the δ_I^* separation. For the mixed-mode tests, on the opposite side, two linear variable differential transducers (LVDTs) were mounted through a special set-up to keep a record of the tangential displacements δ_{II}^* at the neutral axis. The specimens were loaded using a constant displacement rate $\dot{\Delta}$ of the lower beam at 5 or 10 mm/min. Figure 2b shows a DCB-UBM specimen under testing conditions.

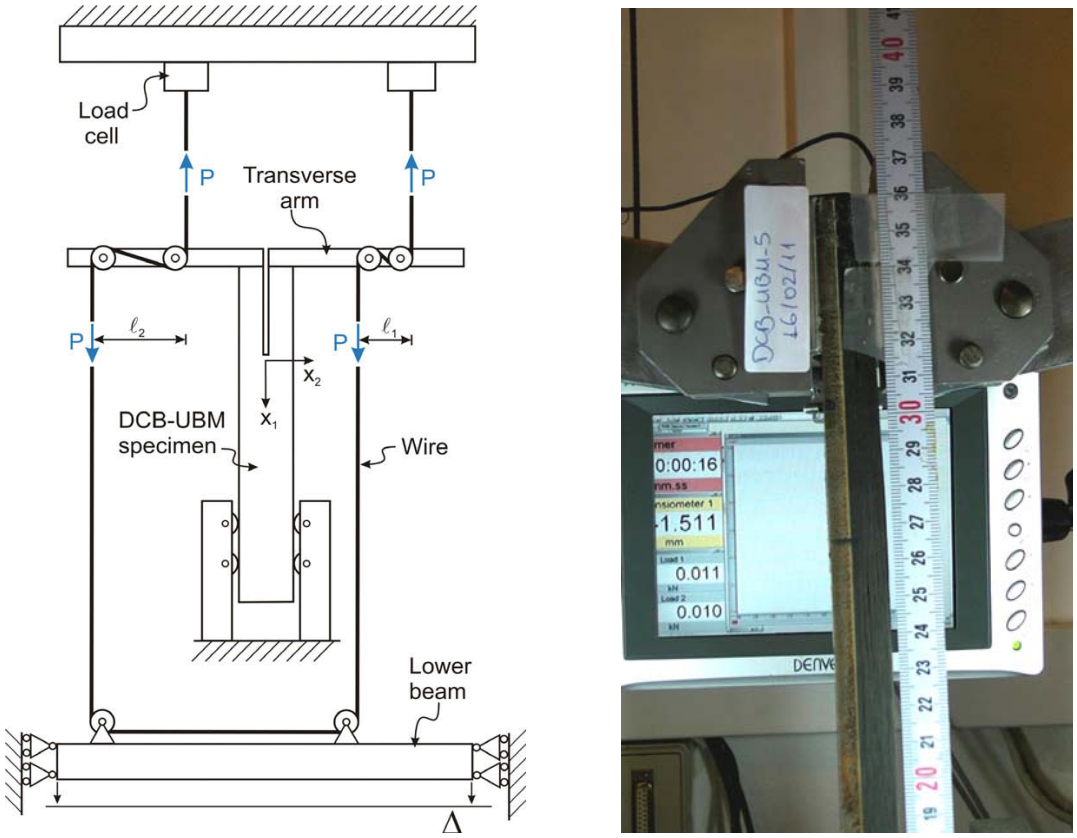

(a) (b)

Figure 7.28: Schematic view of the DCB-UBM configuration (a) and a CFRP-to-steel specimen under testing (b).

Two cases have been considered herein for testing and numerical validation, regarding the mixed-mode loading and fracture of the adhesive material. The first case (Case A) considers pure Mode I, whereas Case B considers mixed-mode (combined Mode I and II) loading and fracture of the adhesive. In order to conclude to the necessary moment ratio which must be applied to each case (Case A or B) for leading the adhesive to stress and fail under Mode I or mixed-mode conditions, preliminary finite element simulations were conducted. Thus, following the convention shown in Figure 7.29, a moment of CFRP to steel ratio equal to $M_1 / M_2 = +2$ and $M_1 / M_2 = -6$, , was obtained and utilized in the experiments for Case A and Case B, respectively.

Figure 7.29: Moment convention used in the DCB-UBM tests.

7.3.2 Post Processing of the experimental results

During the experiments the load on the wire was measured directly, through a load-cell. The normal δ_I^* and tangential δ_{II}^* separations at the pre-crack tip were determined from the

recordings of the sensor devices (extensometer and LVDTs). Figure 7.30 presents a typical applied load - normal opening relation as experimentally measured from a Case A specimen. Additionally, Figure 7.31 presents the load - normal opening and tangential sliding relations as experimentally measured from a Case B specimen. According to Figure 7.30, the load increases without any recordings of the normal opening separation, until the load level of 0.28 kN where δ_{I}^{*} begins to increase in magnitude with any further increase of the load. Prior to the load level of 0.28 kN, the applied work from the moments is dissipated for the bending of the substrates and immediately after this level, part of the work is dissipated for the formation of the Cohesive Zone (CZ) within the adhesive layer. At the load level of 0.32 kN the CZ has been fully developed and thus the load is constrained to this plateau denoting steady state fracture, with the creation of new fracture surfaces.

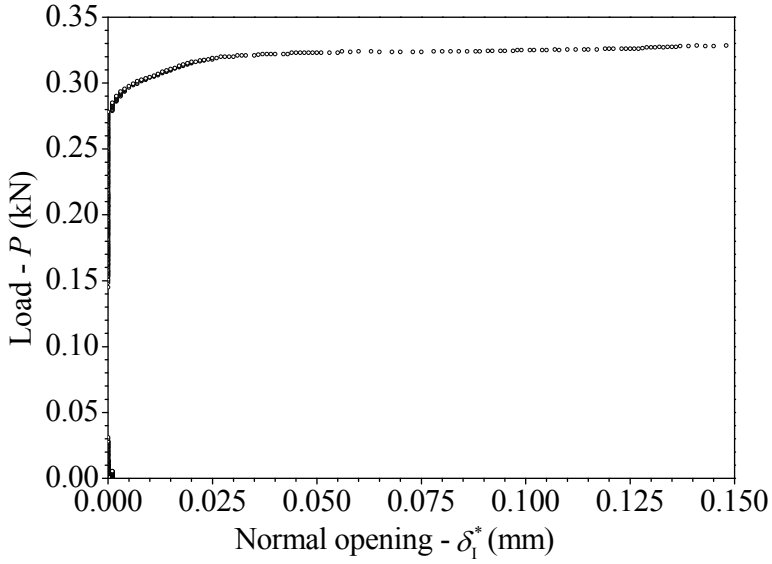

Figure 7.30: Typical global response of a Case A specimen (Mode I experiment) in terms of the applied force - normal separation.

Figure 7.31a is characterized by the same behaviour but with much lower load levels. This is reasonable, since the adhesive material is stressed under mixed-mode conditions and hence the contribution of Mode II is significant (see Figure 7.31b) to the loading and fracture response of the adhesive layer. On the other hand, the load - tangential sliding response, is somehow different, as shown in Figure 7.31b. Magnitude δ_{II}^{*} begins to increase in magnitude in the early stage of the loading history compared to magnitude δ_{I}^{*}. This is attributed to the fact that, when the thin adhesive layer is loaded under Mode II, the developed cohesive zone extends in a larger area behind the physical crack tip.

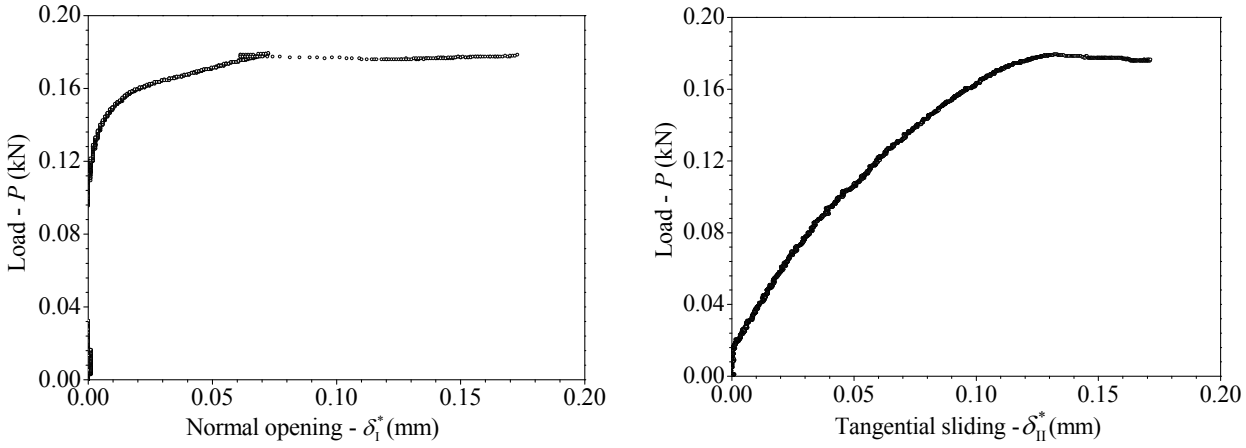

(a) (b)

Figure 7.31: Typical global response of a Case B specimen (mixed-mode experiment) in terms of the applied force - normal (a) and tangential (b) separation.

Having measured the applied load with respect to the separations ($\delta_I^*, \delta_{II}^*$), the next step is the calculation of the energy release rate J_I and J_{II}, so as to further derive the experimental cohesive laws according to the J-integral approach. This is accomplished with the use of analytical formulas in the context of linear elastic fracture mechanics, as proposed by Suo and Hutchinson (1990). According to these authors the specimen is considered as a bimaterial joint with the adhesive layer ignored. The advantage of the utilized analytical formula is that the energy release rate depends on the loading and the geometry of the DCB specimen, but not on the crack length. This fact facilitates the obtention of the release rate since the crack length is usually hard to measure.The results are based on the assumption of plane stress condition.

Figure 7.32 and Figure 7.33 present the constructed R-curves (discrete data-points) by considering the dimensions of the DCB specimens and the P - $\delta_I^*, \delta_{II}^*$ measured data of Figure 7.30 and Figure 7.31, as input parameters to the analytical formula proposed by Suo and Hutchinson (1990).

According to these figures, the behaviour of the Mode I R-curves is characterized typical. The J_I magnitude begins to increase from a certain definite level for values of δ_I^* starting from zero. This J_I level defines the well known initial fracture toughness magnitude J_{I0}, which corresponds to the energy needed for the creation of the cohesive zone and it is a constant value. From J_{I0} and forward, the behaviour of the J_I - δ_I^* relation is considered non-linear as J_I tends to stabilze at a plateau level, known as the steady state fracture toughness J_{Iss}. Magnitude J_{Iss}, from a physical point of view, corresponds to a fracture toughness level beyond which physical crack propagates with a stable manner accompanied with a full developed CZ behind the crack tip. The energy needed for the full formation of the cohesive zone $J_{Icoh.}$, is given by the subtraction of the Initial fracture toughness from the steady state fracture toughness, that is $J_{Icoh.} = J_{Iss} - J_{I0}$.

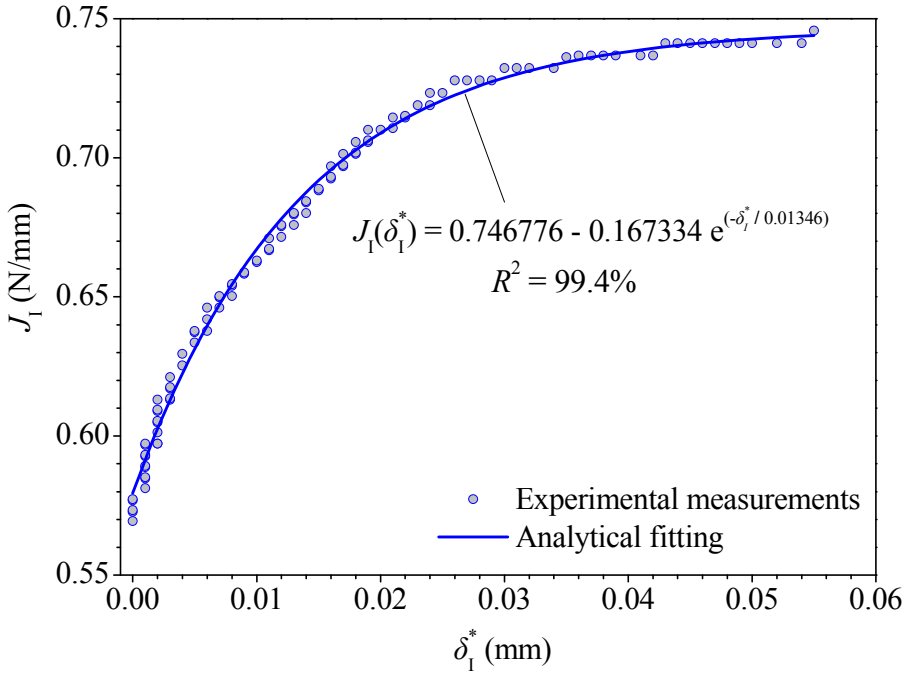

Figure 7.32: R-curve as calculated from the corresponding P - δ_I^* curve of Figure 7.30(Case A specimen).

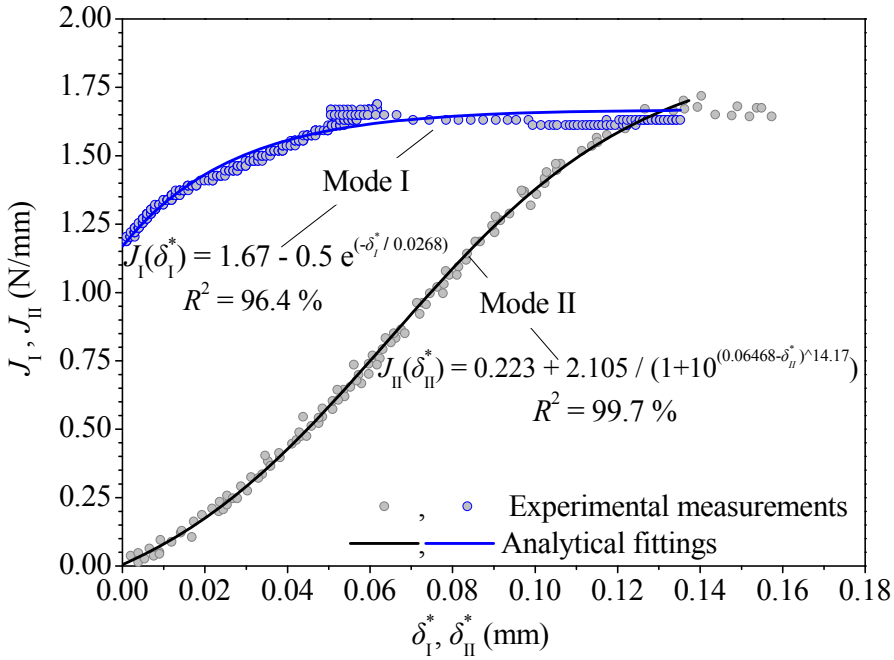

Figure 7.33: R-curves as calculated from the corresponding P - δ_I^* and P - δ_{II}^* curves of Figure 7.31 (Case B specimen).

On the other hand, the behaviour of the Mode II R-curve (J_{II} - δ_{II}^*) of the Case B specimen presented in Figure 7.33 is different. The fracture toughness J_{II} begins to increase from zero together with the recordings of the tangential sliding δ_{II}^* and tends to a plateau level, namely Steady State Fracture Toughness J_{IIss}. The Initial and cohesive fracture toughness cannot be defined explicitly.

For the calculation of the experimental cohesive laws, a differentiation must be obtain of the corresponding R-curves, presented in Figure 7.32 and Figure 7.33, with respect to δ_I^* and δ_{II}^* (if present) according to the *J*-integral approach. Thus, for avoiding errors that arise from the direct numerical differentiation of the discrete J_I - δ_I^* and J_{II} - δ_{II}^* data sets, analytical differentiation is proffered instead. Several analytical functions have been utilized for providing a best fit of the discrete data-sets, i.e. exponential, polynomial, power etc.. The final selected analytical fitting functions are presented in Figure 7.32 and Figure 7.33, accordingly. Figure 7.34 presents the obtained experimental cohesive laws from a pure Mode I (Case A) and a mixed-mode experiment (Case B), obtained after the differentiation of the analytical fitting functions shown in Figure 7.32 and Figure 7.33, respectively.

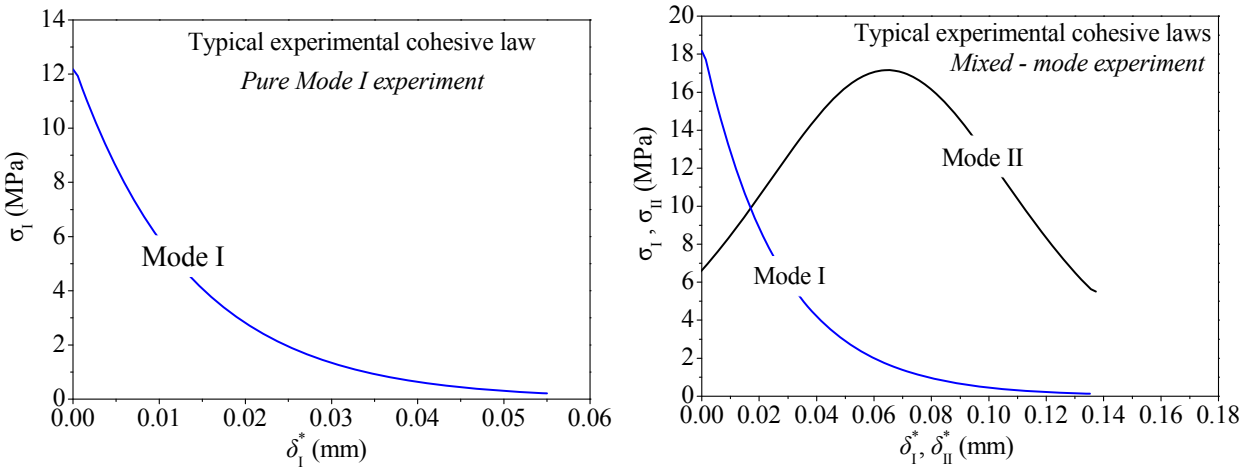

Figure 7.34: Typical experimental cohesive laws from a Case A (a) and Case B (b) experiment.

7.3.3 Numerical implementation of the experimental cohesive laws

This section aims at providing all necessary amendments that must be considered in order to utilize the obtained experimental cohesive laws in numerical simulations, according to an extrinsic triangular model and the proposed EPZ model. The triangular cohesive zone model is the one which is already built-in in most commercial FEA software (e.g. ANSYS and ABAQUS®) for the simulation of adhesive joints. However the proposed EPZ laws and mixed-mode model are more adequate, since they describe the process zone developed within a ductile adhesive material, under pure or mixed mode loading and fracture.

Let's initially consider the Mode I cohesive laws ($\sigma_I - \delta_I^*$) of Figure 7.34, as schematically shown in Figure 7.35. Regardless of the necessary amendments, i.e. the utilized shape of the numerical cohesive law, the key parameters that must be maintained constant are the characteristic fracture toughness magnitudes, i.e. J_{I0}, $J_{Icoh.}$ and J_{Iss}. As aforementioned in section 4.6, magnitude J_{I0} is a constant parameter which vanishes when differentiating the J_I - δ_I^* analytical relation to derive the corresponding cohesive law. Thus, the total area under the

$\sigma_I - \delta_I^*$ curve corresponds to the cohesive zone energy uptake $J_{Icoh.}$. According to the proposed EPZ model, the traction decreasing part is given by a linear softening function. By keeping constant the $J_{Icoh.}$ and the critical stress $\sigma_{c,I}$ magnitudes, the critical separation of the numerical softening function ($\delta_{c,i}$ - $\delta_{0,i}$) can be calculated though the area of the triangle: $J_{Icoh.} = 0.5\ \sigma_{c,I}\ (\delta_{c,i}$ - $\delta_{0,i})$.

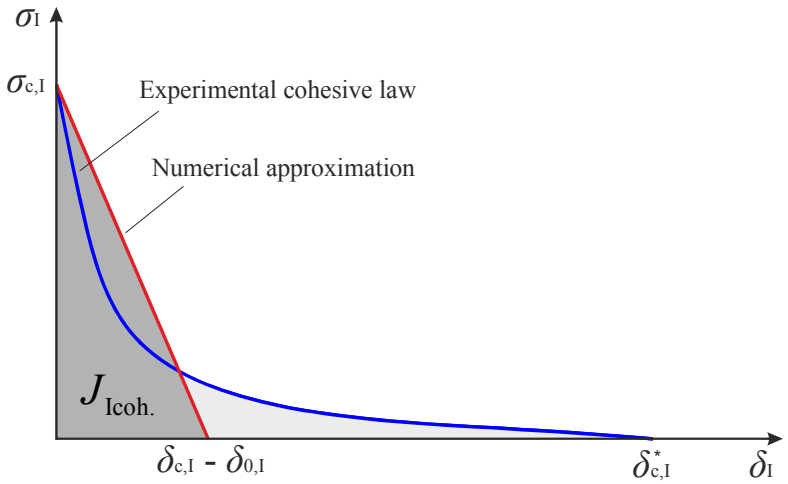

Figure 7.35: Experimental and numerical approximation of a Mode I cohesive law.

The next step is the incorporation of the initial fracture toughness parameter J_{I0} to the numerical cohesive law, which is not included in the experimental one. The proposed procedure is shown in Figure 7.36.

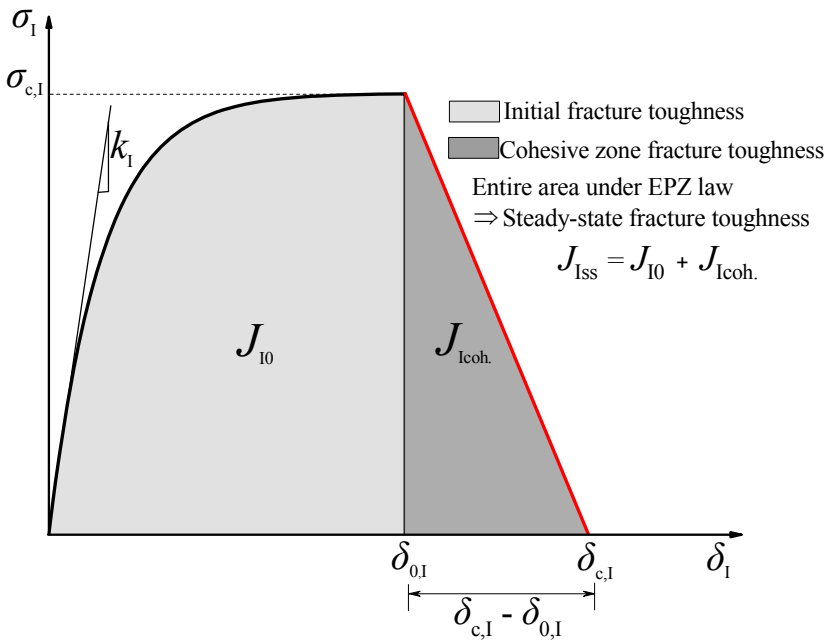

Figure 7.36: Numerical implementation of the experimental Mode I cohesive law according to the proposed EPZ law.

The aim is to equal the J_{I0} magnitude to the area under the exponential traction increase part of the proposed EPZ law, according to Equation (5.22). The initial stiffness k_I is calculated

from the ratio between the Young modulus of the adhesive material and the adhesive thickness t_a. By considering k_I, J_{I0} and $\sigma_{c,I}$, magnitude $\delta_{0,I}$ can be calculated through Equation (5.22) and additionally the error parameter e from Equation (5.4). These ammendements lead the proposed EPZ law to describe the entire process zone which is defined by magnitude J_{Iss}.

As far as the treatment of the Mode II cohesive law obtained from the mixed-mode experiment, a quite different procedure is followed. The entire area under the proposed EPZ law equals directly to the value of the measured J_{IIss} magnitude. The initial stiffness k_{II} is obtained by dividing the shear modulus of the adhesive layer to the adhesive thickness t_a. The critical stress $\sigma_{c,II}$ utilized is the one experimentally measured (see Figure 7.34b). For the calculation of the $\delta_{0,II}$ magnitude, Equation (5.4) is utilized with the error parameter e calculated from the corresponding Mode I cohesive law.

For the calculation of the extrinsic triangular laws, the procedure is more simple, since the data needed to be defined are the $\sigma_{c,i}$ and J_{iss} (i = I or II), which are directly taken from the post-processing of the experimental results.

Table 7.4: Parameters of the pure Mode I and II proposed EPZ laws.

	k_I	k_{II}	$\sigma_{c,I}$	$\sigma_{c,II}$	J_{I0}	J_{II0}	$J_{Icoh.}$	$J_{IIcoh.}$	J_{Iss}	J_{IIss}	e
	MPa/mm		MPa		N/ mm						%
Case A	3700	-	19.3	-	0.573	-	0.173	-	0.746	-	0.124
Case B	3700	1423	18.1	17.1	1.17	-	0.49	-	1.67	1.78	0.00007

7.3.4 Finite Element Modeling

In order to validate the experimental cohesive laws and the proposed numerical implementation procedure, the DCB-UBM tests have been considered for finite element modeling in a 3D space. The finite element model together with the applied boundary and loading conditions presented in Figure 7.37 are based on the average dimensions and geometry of the DCB specimen shown in Figure 7.27 and the experimental configuration shown in Figure 7.28 and Figure 7.29.

For the modeling of the steel or CFRP substrates, 20-node brick elements (C3D20) available in the ABAQUS® element library have been utilized. The adhesive layer has been totally removed and 3D cohesive elements (see Appendix A1) have been used instead for a length of 100 mm after the pre-crack tip, with dimensions equal to 0.5 x 0.5 mm^2, a value derived after a mesh density convergence analysis. For the numerical integration of the stiffness matrix and the internal force vector of the quadratic cohesive elements, a 3 x 3 Gaussian quadrature rule has been used.

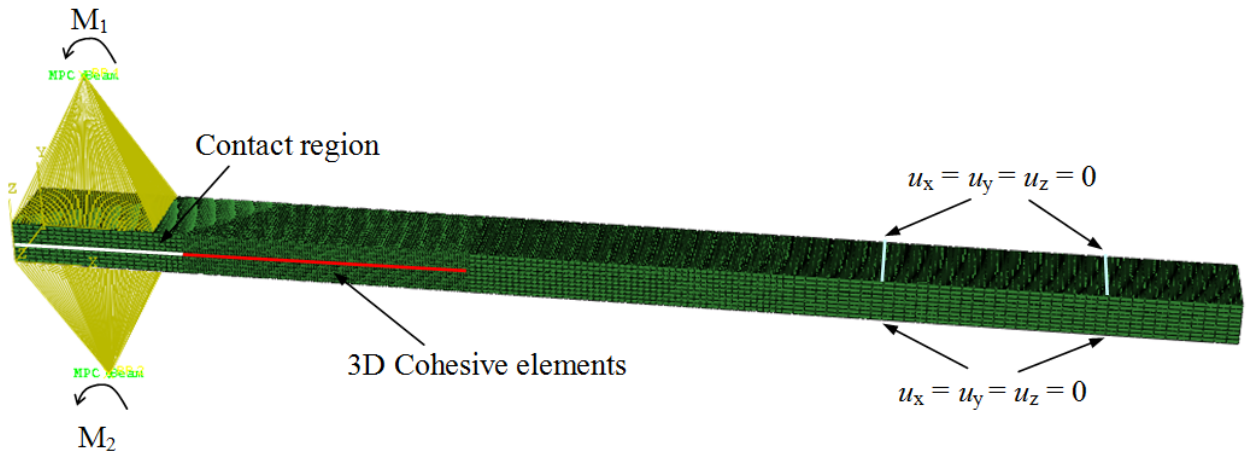

Figure 7.37: Finite element model of the DCB-UBM tests together with the imposed loading and boundary conditions.

As far as the material properties are concerned, the CFRP adherents were modeled as linear orthotropic with the properties listed in Table 7.2. The steel adherents were modeled as isotropic linear elastic. The Young modulus has been taken equal to 170 GPa and the Poisson ratio equal to 0.3. For the description of the constitutive behaviour of cohesive elements utilized for modeling of the adhesive layer, the 3D proposed EPZ laws and mixed-mode model was utilized. The definition of the pure mode EPZ law properties is based on the corresponding ones described in the previous section and listed in Table 7.4.

The degrees of freedom (dofs) of the nodes laying at the areas of the DCB model, where the aluminum parts were bonded have been tied with the use of beam elements (kinematic Multi-Point Constraint - MPC). Thus, the bending moment (M_1 and M_2) was applied at the master node of each MPC set, since corresponding rotational dofs where implicitly introduced thanks to the beam elements. The corresponding applied moments are listed in Table 7.5 for each case modeled (Case A and Case B).

The translational dofs laying at the locations where the rollers hold the specimen into position (see Figure 7.28) have been constrained. Additionally, contact elements have been placed in-between the pre-crack surfaces in order to avoid element interpenetration. This is necessary when modeling the mixed-mode Case B tests, where the moments have the same sign.

In order to account for the geometrical and material nonlinearities, the Newton-Raphson method has been utilized together with a line search algorithm. A force controlled approach was utilized for the solution of the non-linear problem.

Table 7.5: Applied loading conditions and corresponding details.

	M_1 / M_2	P	l_1	l_2	M_1	M_2
		kN	mm	mm	N mm	N mm
Case A	-2	0.4	176.5	86.5	-70600	34600
Case B	6	0.2	519	86.5	103800	17300

7.3.5 Experimental and Numerical results

Figure 7.38 and Figure 7.39 present a comparison between the experimentally measured and numerically calculated global responses of the pure Mode I (Case A) and mixed-mode (Case B) DCB-UBM configurations, respectively.

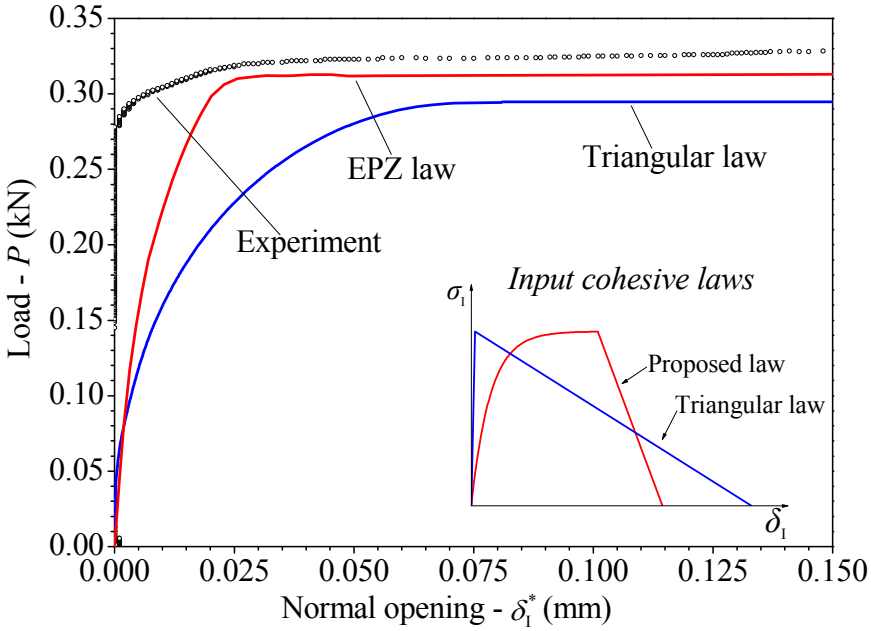

Figure 7.38: Comparison of the experimental and numerical results of the Case A specimen.

The numerical results have been calculated with the triangular extrinsic CZM and the proposed EPZ model, considering the properties listed in Table 7.4. According to the predictions of the pure Mode I test (see Figure 7.38), both types of laws share a common behaviour, described by an initial non-linear load increasing part followed by a constant load level (plateau region). The second part agrees well with the corresponding behaviour of the experimental results, compared to the first part, where deviations are apparent. However, numerical prediction with the proposed EPZ law yields a steeper load increasing part in contrast with the prediction obtained by the triangular law, which is more compliant. However, the experimental load plateau (0.32 kN) and the corresponding normal opening value δ_I^* (0.03 mm) where the load plateau is obtained, is accurately predicted (< 3% deviation) by the proposed EPZ law. The numerical prediction with the triangular law underestimates the experimental load plateau (≈ 9% deviation) and overestimates the corresponding normal opening value (≈ 40%).

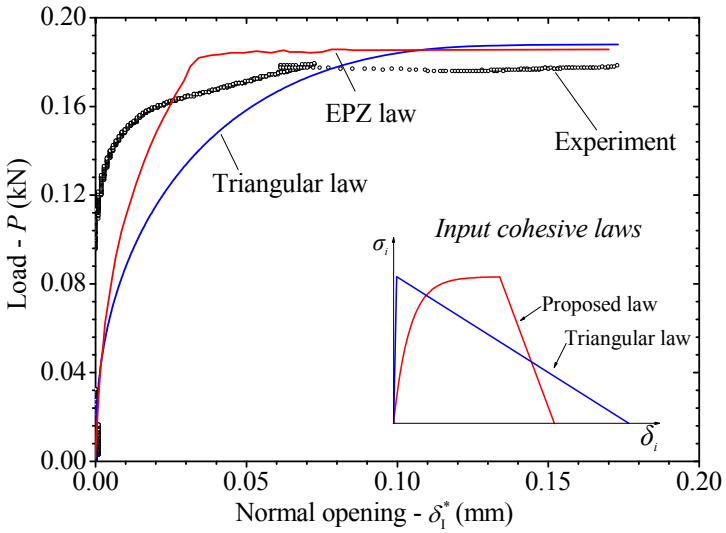

(a)

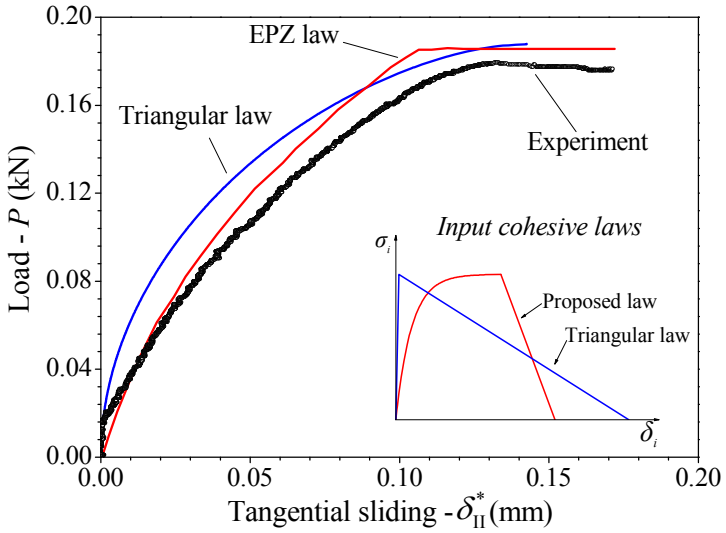

(b)

Figure 7.39: Comparison of the experimental and numerical results of the Case B specimen in terms of the load and pre-crack tip normal opening (a) and tangential sliding (b).

The numerical prediction of the mixed-mode DCB-UBM case (Case B) is presented in Figure 7.39. A similar behaviour as in Case A is obtained regarding the numerical P - δ_{I}^{*} relation. Both the triangular and the EPZ laws capture the experimental load plateau (≈ 0.18 kN) with a deviation less than 8%. However the proposed EPZ law underestimates the corresponding normal opening value δ_{I}^{*} (0.07 mm) since the load plateau is obtained with a deviation equal to 40%, in the P - δ_{I}^{*} (see Figure 7.39a). The triangular law overestimates this magnitude with a deviation equal to 38%. The numerical P - δ_{II}^{*} relation obtained with the proposed EPZ law, shown in Figure 7.39b, is in better agreement to the experimental one in the initial non-linear load increasing part, as compared to the prediction with the triangular law. However, the triangular law predicts more accurately than the EPZ law the experimental tangential sliding displacement δ_{II}^{*} (0.13 mm) where the load plateau is obtained.

7.4 Conclusions

Initially, an experimental parametric study of adhesively bonded Single Lap Joint (SLJ) geometries between relatively thick dissimilar adherents has been conducted. The experimental part involved an investigation of the effect of various parameters, i.e. adherents' thicknesses, adhesive thickness and overlap length, on the failure load and failure mode of joints with dissimilar materials. The tests where then numerically predicted in a 3D space and the adhesive layer's material response was simulated with the proposed mixed-mode model.

For the cases considered, where relatively thick substrates were utilized, there was a small effect of the adhesive thickness and the stiffness ratio to the experimental strength of the joints. On the other hand, as expected, there is a significant effect of the overlap length to the strength of the joints, regardless of the selected adhesive thickness and stiffness ratio. In particular, a 70% increase of the adhesive thickness results to a maximum 5% increase of the strength of the corresponding SLJ cases with 25 mm overlap length. The same conclusion is drawn for the effect of the stiffness ratio to the strength of the joints, where an increase of 100% results in a 5% maximum increase of the strength. However, the joints with three times longer overlap length (200% increase) yield a maximum 100% increase in their strength, than the joints with short overlap lengths, i.e. 75mm and 25 mm, respectively. In the case where a long overlap length (75mm) and a relatively thin steel adherend (5mm) was utilized, the steel entered plasticity at the vicinity of the adhesive overlap edge. Numerical simulations of the aforementioned experiments were conducted in a 3-dimensional finite element space by utilizing the developed 3D mixed-mode EPZ model. According to the numerical results, the proposed model captured accurately the global responses, in terms of force-displacement and force-strains, in all seven cases modeled. The experimental strengths of the short overlap lengths were predicted with great accuracy compared to the corresponding predictions of the cases with long overlap lengths where larger deviations were calculated.

In the following, particular focus has been given on the numerical implementation of experimentally measured cohesive laws which describe a ductile adhesive material utilized for bonding similar or dissimilar structural materials. The main aim was to provide and validate all necessary amendments that must be considered in order to obtain a Traction-Separation law that can be used as the constitutive relation of cohesive elements for the simulation of adhesive joints. Thus, typical experimental cohesive laws from steel-to-CFRP adhesive joints, derived from Double Cantilever Beam tests subjected to Uneven Bending Moments (DCB-UBM), have been considered for numerical implementation according to the proposed EPZ laws. The measured cohesive laws were first converted to numerical constitutive relations according to the proposed EPZ laws and additionally, for reasons of comparison, to the already known triangular shaped cohesive laws (available model in ANSYS and ABAQUS® finite element commercial software). Then, these were utilized for the numerical simulation of the experimental tests and comparative results are provided. The proposed laws and procedure has yield promising comparisons between the experimental and numerical results, denoting the validity of the former.

8. Numerical parametric analysis of tubular adhesive joints

8.1 Introduction

Much of the existing pipeline infrastructure is constructed from steel materials. Steel is strong, mechanically robust and relatively inexpensive. However, large sums of money are spent in trying to reduce the exposure of steel pipelines to corrosive environments. A recent study (Koch et al., 2002) indicated that in the United States alone the annual direct cost of corrosion in the gas-distribution network was $5 billion US and the corresponding corrosion cost for drinking water and sewer systems was $36 billion per year. One way to overcome this problem is to use a material with good corrosion resistance, such as fibre reinforced polymers (FRPs), instead of steel.

Various fibre reinforced composite thin walled tubular structures have been in preferential use in piping systems for the last two decades and have a wide range of applications in aerospace, marine, chemical, petroleum and other industries for transportation of various fluids. FRPs represent an attractive alternative for pipelines subjected to severe internal or external environments in onshore or offshore applications (Lees, 2006).

Most recently, composite tubes have been used in forming truss structures in space launch vehicles for weight reduction considerations. With properly developed manufacturing processes for composite pipes (such as centrifugal casting and computer controlled filament winding) within the past decade, the mechanical performance of such pipes has been dramatically improved. Ideally a pipe system would be preferred to be designed without joints, since joints could be a source of weakness and/or excess weight. However, limitations on component size imposed by manufacturing processes and the requirement of inspection, accessibility, repair and transportation/assembly necessitates some load carrying joints in most piping systems. The rule of thumb states that one joint should be installed for every four feet of composite pipe in marine applications, thus, further demanding the development of efficient composite pipe joints (Ramadan and Taheri, 2011).

Pipe joining systems can be classified into two major categories, depending on whether the joint is designed to take the full axial load due to the internal pressure (tensile resistant joints) or whether provision is made so that the system resists the axial forces away from the joints

(non-tensile resistant). Adhesive joints are widely used as tensile resistant connections for CFRP filament-wound pipe sections. These joints are typically formed using either a bell and spigot system (Single Lap Joint - SLJ) or a coupler (Single Strap Joint - SSJ) to connect two pipe sections (see Figure 8.1). It is important to note that, in the latter case, the mechanical properties of the coupler can be quite different to those of the pipe. If a thin-walled pipe section is closed and fully pressurized, then the hoop stresses will be twice the longitudinal stresses. However, there may well be cases where axial loads occur in the absence of pressure, e.g. as a result of bending, axial loads due to thermal expansion, self-weight, etc. and the performance under these conditions is also important.

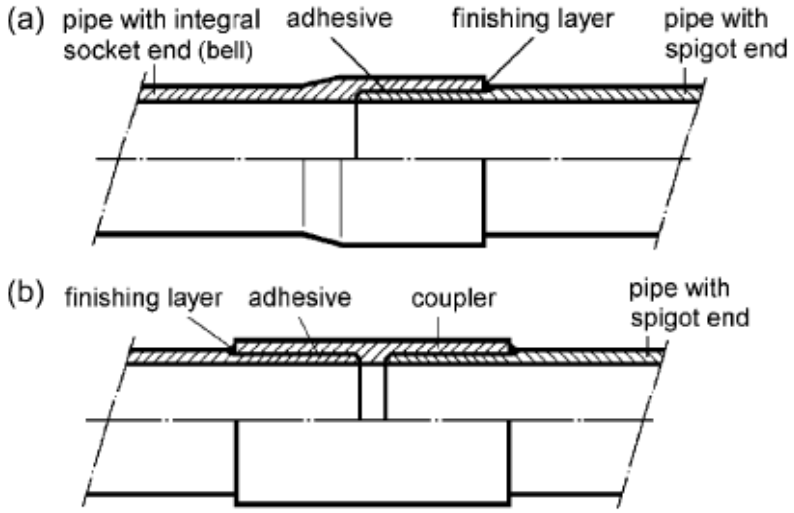

Figure 8.1: SLJ (a) and SSJ (b) popular adhesive joint connections of composite tubes used in pipeline systems (Lees, 2006).

Bonded joints between tubular members under axial tension develop relatively high stresses with steep gradients localized at the joint ends. The stress concentrations which arise from geometric discontinuities are well established facts. In the event of adhesion failure, the process begins to happen from these vulnerable and critical end-zones of the joints. Failure due to the various possible modes, such as interlaminar or intralaminar delamination, cohesion failure, adhesion failure or a combination thereof and their subsequent propagation/coalescence, cause abrupt fracture in the adhesively bonded joints. Consequently, the importance of effective adhesive bonding has been recognized in the past years and considerable amounts of analytical, finite element and experimental works have been carried out on the subject of adhesive joints. A good amount of literature dealing with the stress analysis of adhesively bonded lap joints between flat adherents is available (Anyfantis, 2009). However, literature relating to bonded thin walled tubular lap joints is very limited (Ramadan and Taheri, 2011).

One of the fundamental problems in the analysis of adhesive joints in FRP composite tubes involving stress and strain fields is to construct an appropriate mathematical model representing the physical problem and able to be solved with reasonable amount of accuracy. Fracture mechanics parameters such as SERR, *J*-integral and SIF can be used to characterize the

propagation of such failures or damages, but do not predict the joints' strength and thus Cohesive Zone Modeling (CZM) techniques are necessary that combine damage and fracture mechanics (see section 2.3.3). Although plenty articles are available for the prediction of damage initiation and propagation in adhesively bonded flat laminated FRP composites by utilizing CZM techniques, none has been devoted to the realistic 3D analysis of tubular adhesive joints. Most of the analyses so far in this direction are of two-dimensional in nature, considering flat adherents with simplified assumptions, that lack explaining the mixed mode fracture behaviour of adhesively bonded joints of laminated FRP composites under a general state of loading conditions.

Considering the lack of the applications of CZM techniques to the realistic numerical predictions of tubular adhesive joints in the literature, this chapter focuses on a parametric finite element analysis of tube-to-tube and tube-to-flange adhesive joints. For this purpose and having validated the proposed EPZ mixed-mode model with steel-to-steel and steel-to-CFRP experiments in previous chapters, this model will be used herein as the constitutive relation of 3D cohesive elements for modeling CFRP-to-CFRP tubular adhesive joints. While the particular focus is pipeline connections, the embodied principles are applicable to any adhesively bonded advanced composite tubular joint subjected to a combination of pressure and axial load or torsion moments.

8.2 Details of the parametric study

This parametric study focuses on investigating the effect of geometric and material parameters to the behaviour and strength of tubular adhesive joints used for bringing together CFRP pipes. Initially, it is essential to specify a candidate piping system where CFRP tubes will be utilized instead of the already installed steel pipes.

Various piping systems are available in ships, which are designated for the transportation of either liquids or gas and are designed according to corresponding rules and regulations. A good candidate piping system for replacement with CFRP tubes is the one that involves bilge, ballast and sea water pipes. Thus, a steel pipe has been selected that has an internal diameter of 150 mm and a wall thickness of 4.5 mm, according to the "ABS Rules for building and classing steel vessels (see Table 4 on part 4-6-2) Part 4: Vessels systems and machinery, Chapter 6: Piping systems, Section 2: Metallic piping". These steel pipes are designed to operate at a maximum 10 bar internal pressure.

According to the literature (Lees, 2006), the selected CFRP pipes to replace the corresponding aforementioned steel ones, have a wall thickness of 4mm while the internal diameter remains equal to 150 mm. In order to investigate the joining configuration of these tubes, the two adhesive joint geometries shown in Figure 8.1 have been adopted. A tube-to-flange adhesive joint has been additionally included in the numerical parametric study, due to the

interest of studying the effect of the inherent tri-material system it poses. The selected flange type and geometry is taken according to the KS JIS rules for Flanges. Since the current work is focused on providing to the literature the potential of CZM techniques and the proposed mixed-mode EPZ model for modeling tubular adhesive joints, the adopted geometries presented in Figure 8.2 refer to simplified versions of the corresponding ones presented in Figure 8.1. The value of the free length (from overlap edge to the end of the joint) is selected equal to 200 mm. This value has been derived from preliminary finite element simulations, aiming at eliminating the effect of the stress field developed at the ends of the joints, i.e. locations where boundary and axial loadings are applied.

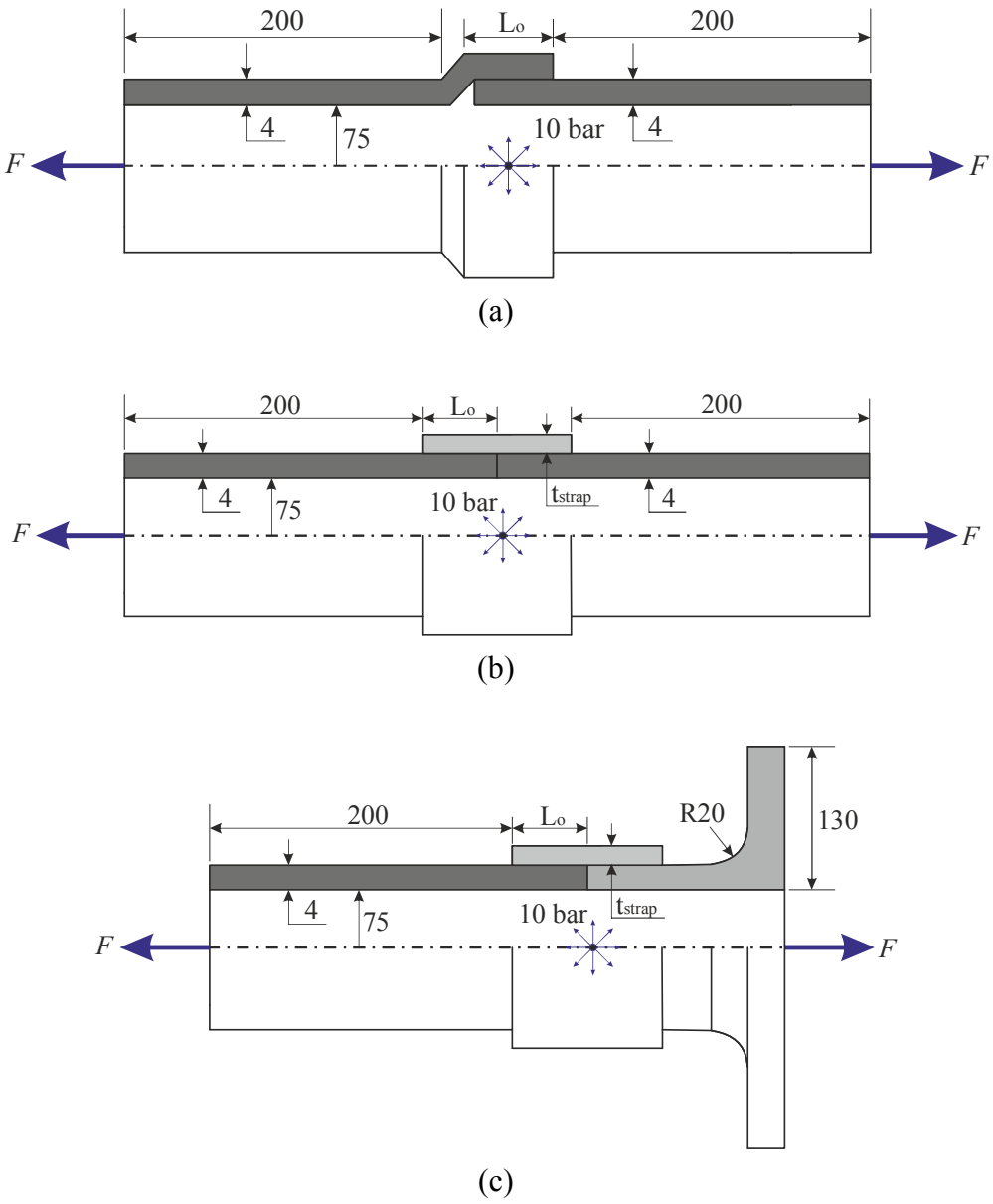

Figure 8.2: Tube-to-tube SLJ (a) and SSJ (b) geometries and tube-to-flange SSJ (c) geometry adopted in the numerical parametric study (all dimensions in mm).

The aim of the parametric study is to yield conclusions regarding the effect of various geometric and material parameters to the behaviour and strength of the adopted adhesive joint cases, subjected to combined internal pressure and axial loading. The operational pressure of 10 bar has been kept constant for all cases, while the axial strength of the joints (ultimate applied force - F_u) was calculated.

In all three adhesive joints (Figure 8.2a, b and c) six values of the overlap length L_o have been considered, as follows:

- 20 mm
- 40 mm
- 60 mm
- 80 mm
- 100 mm
- 120 mm

As far as the SLJ cases are concerned, the L_o magnitude is the unique parameter investigated. However, for the tube-to-tube and the tube-to-flange SSJ adhesive joint cases the effect of strap material and thickness t_s have been also considered in the parametric study. The two materials selected for the strap are the following:

- CFRP (the same as the tube material)
- Aluminum

and the two strap thicknesses are the following:

- 4 mm
- 8 mm.

Hence, 24 cases have been considered for the tube-to-tube and tube-to-flange SSJ geometries (6 overlap lengths x 2 materials x 2 strap thicknesses) and 6 cases for the tube-to-tube SLJ geometries.

8.3 Numerical Modeling

For the numerical simulation of the parametric cases described in the previous section, a finite element mesh has been constructed in a 3-dimensional space (see Figure 8.3) according to the dimensions shown in Figure 8.2. For modeling the CFRP tubes, strap material and flange, 20-node brick elements (C3D20) available in the ABAQUS® element library have been utilized. The adhesive layer laying at the overlap regions of the tubular adhesive joints was represented by zero-thickness 3D cohesive elements (see Appendix A1). For the numerical integration of the stiffness matrix and the internal force vector of the quadratic cohesive elements, a 3 x 3 Gaussian quadrature rule has been used. For the SSJ cases (see Figure 8.2b and Figure 8.2c), no adhesive (and hence no cohesive elements) was placed in-between the faces of the tubes or tube and

flange that come in contact, thus avoiding the creation of butt-type adhesive joints. The material properties utilized in the parametric numerical analyses are listed in Table 8.1.

Table 8.1: Material properties of the substrates and adhesive utilized in the FE parametric analyses.

T 300/934 CFRP [±45º] (Das and Pradhan; 2010)								
E_r (MPa)	E_θ (MPa)	E_z (MPa)	$\nu_{r\theta}$	ν_{rz}	$\nu_{\theta z}$	$G_{r\theta}$ (MPa)	G_{rz} (MPa)	$G_{\theta z}$ (MPa)
9600	59574	59574	0.42	0.02	0.02	7000	4500	4500
6061 Aluminum Alloy (www.matweb.com)								
E (MPa)	ν							
73000	*0.33*							
Stainless Steel (flange material)								
E (MPa)	ν							
200000	*0.33*							
Adhesive material (proposed EPZ laws parameters) - Mode II = Mode III								
k_I (N/mm)	k_{II} (N/mm)	$\sigma_{c,I}$ (MPa)	$\sigma_{c,II}$ (MPa)	J_{I0} (N/mm)	J_{II0} (N/mm)	e (%)		
1850	623	25.6	19.3	4	4.7	0.1		

A mesh sensitivity analysis has been conducted regarding the number of elements utilized through the thickness of the pipe and straps, both in the overlap area and in the free length regions. The effect of the through-thickness element divisions to the strength of the joints was investigated by selecting three corresponding values, i.e. 1, 3 and 5. The results have shown that this parameter does not affect at all the calculated strength of the joints, but only increases the CPU time with further increase of the divisions. Thus 1 element has been utilized in all cases, apart from the cases that involve thick straps (8 mm), which were modelled with two elements through their thickness. In all cases, the in-plane dimensions of the continuum and cohesive elements laying at the overlap areas was taken equal to 2 x 2 mm^2, a value derived after a mesh density convergence analysis. An element length equal to 6 mm has been utilized in the free length areas of all modeled cases, since the stress gradients at these areas area are small due to the effects of the internal pressure and axial loading.

For the simulation of the loading conditions presented in Figure 8.2, two sequential load cases have been considered. Initially a pressure of 1 MPa (10 bar) was applied on all element faces located in the internal surface of the tubes and flanges, by considering the tube and flange edges fully fixed (all dofs constrained). After the solution of this load case, the developed stress state was maintained invariant and then the second load case was applied; the axial translation constraint applied at all nodes of one of the edges was released and a prescribed axial displacement was applied, for the simulation of the axial loading (F). All dofs of the nodes at the other edge were maintained constrained. In order to account for geometrical and material

nonlinearities, the Newton-Raphson method has been utilized together with a line search algorithm. A displacement controlled approach is utilized for aiding the convergence of the non-linear solution and for avoiding numerical instability issues involved in crack growth analyses, where softening behaviour is apparent.

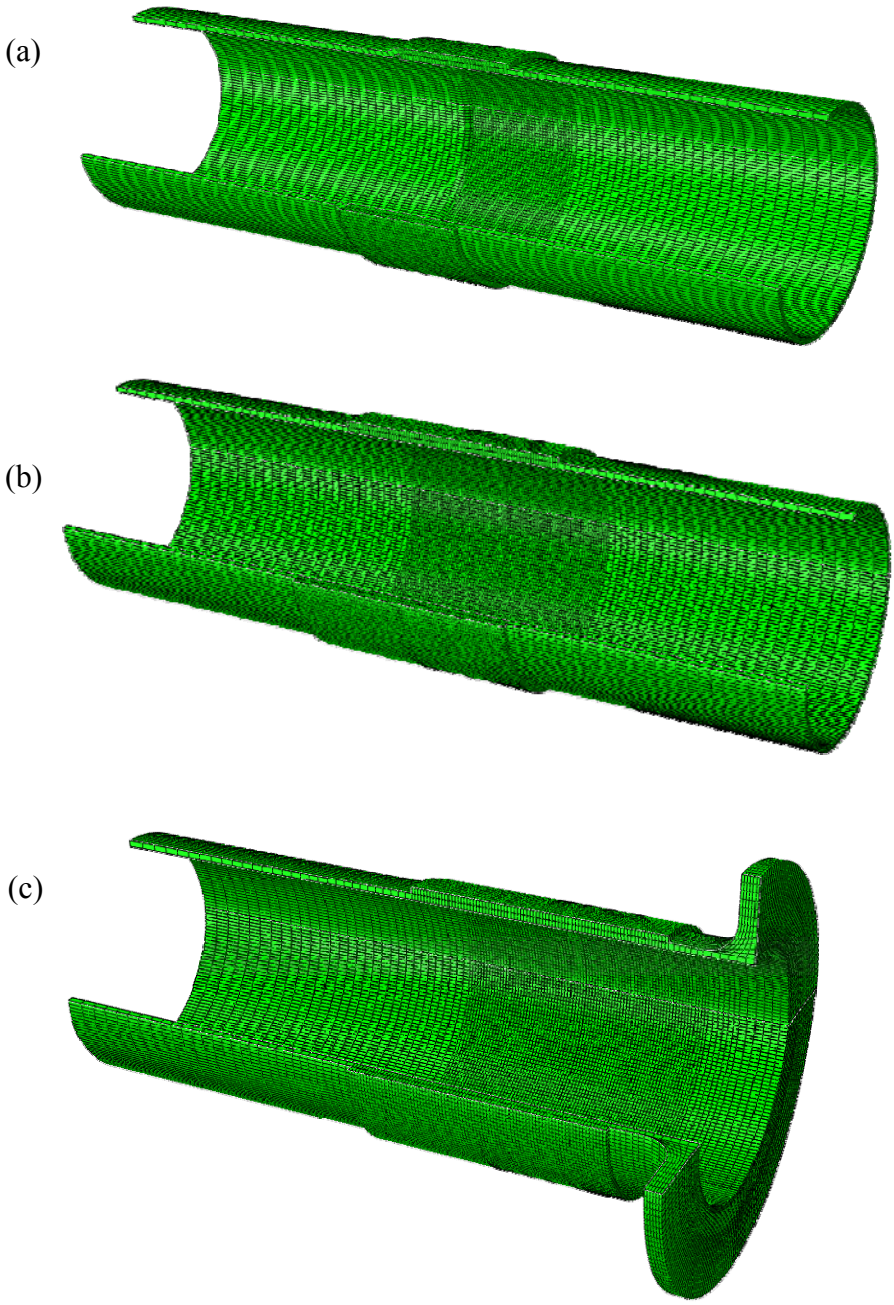

Figure 8.3: Typical finite element mesh of a tube-to-tube SLJ (a) and SSJ (b) case and of a tube-to-flange SSJ case (c).

8.4 Numerical results

8.4.1 Tube-to-tube adhesive joints

The main scope of the current parametric study is the investigation of the effect of the parameters given in detail in section 8.2 on the strength of the adopted tube-to-tube and flange-to-tube adhesive joints. Figure 8.4, presents a comparison of the maximum attained load (strength), as numerically predicted from the finite element models given in Figure 8.3, for all considered cases of the SLJ and SSJ tube-to-tube adhesive joint geometries. It must be noted that the overlap length L_o in the SSJ cases is the half length of the strap material, according to Figure 8.2.

To begin with, the strength predictions are approximately equal for all considered cases and for L_o values less than 80 mm. Regardless the case considered, the trend of the global response curve denotes a behaviour of the strength tending to a plateau as of the overlap length increases. This behaviour is obvious for L_o values higher than 100 mm and particularly for the SSJ cases that have an 8 mm thick strap. The existence of a plateau beyond which the strength of lap joints does not increase with further increase in the overlap length is a common characteristic of adhesive joints with flat adherents (Anyfantis, 2009).

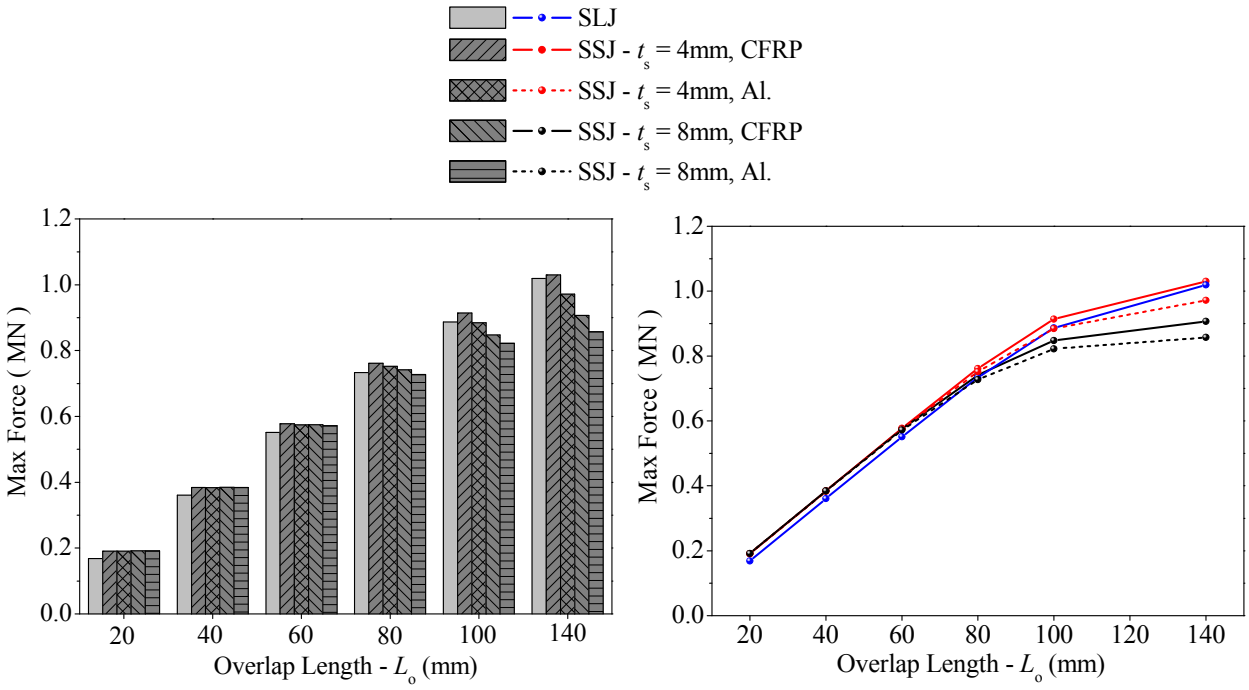

Figure 8.4: Comparison of the maximum attained forces from all tube-to-tube SLJ and SSJ cases.

According to Figure 8.4, the SLJ cases fail at the same force level as the SSJ geometries with a 4mm CFRP strap material, even if the latter configuration has an actual overlap length of $2L_o$. Thus, the SLJ configuration is preferable in design considerations, because with less adhesive material and avoiding extra strap materials, the same strength levels can be attained compared to the SSJ geometry. However, a special mould has to be manufactured for the

creation of the special socket in one of the tube's end (see Figure 8.2a). Additionally, it can be concluded that regardless the selected material for the strap (CFRP or Aluminum) of the SSJ geometries, thinner straps (4 mm) yield higher levels of strength compared to the thicker straps (8 mm), only for large L_o. On the other hand, for a given thickness, CFRP straps yield higher strength values compared to Aluminum straps, according to Figure 8.4. For a given thickness, the stiffness ratio between CFRP and Aluminum ($E_{\theta,CFRP}$ / $E_{Al.}$) is equal to 0.82. Considering the aforementioned observation, stiffer strap materials, in terms of the material properties, yield lower strength values of the tube-to-tube SSJ configurations.

Figure 8.5 presents a comparison of the global Force-Displacement responses as numerically calculated for the six different overlap lengths, for the tube-to-tube SLJ geometry and for a typical SSJ geometry. In reality, each curve begins from zero; however, for reasons of clarity, the curves have been shifted between each other by 0.4 mm.

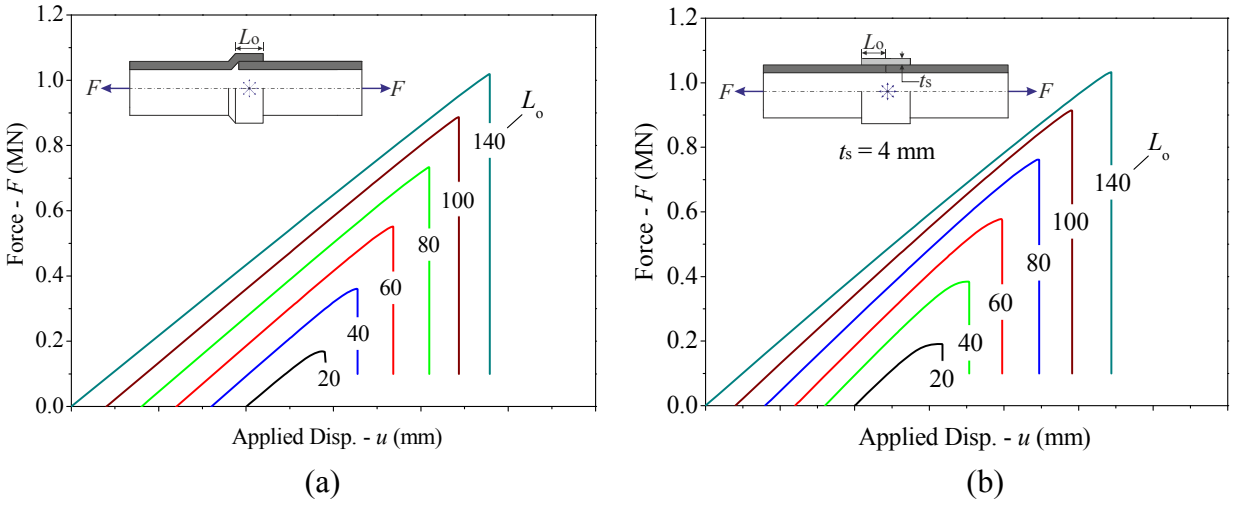

Figure 8.5: Global response of the SLJ (a) and SSJ (b) tube-to-tube cases. The numerical obtained curves have been shifted by 0.4 mm for reasons of clarity.

According to Figure 8.5, the trend of the predicted global response is characterized non-linear for small overlap lengths and turns into linear as the overlap length increases, particularly in the typical SSJ case of Figure 8.5b. This behaviour is totally attributed to the exponential traction increasing part of the proposed EPZ laws, which describes the elastoplastic region of the ductile adhesive material utilized. Thus, in the cases where a relatively small overlap length is utilized, the entire adhesive layer contributes to the stress development and subsequently enters plasticity at the same time leading to sudden failure. This behaviour is evident in Figure 8.6a and Figure 8.6b, where the red- and blue-colored stress contours correspond to the plastic material response of the adhesive layer and have developed in the entire overlap length.

On the other hand, larger overlap lengths lead the stresses to be constrained at the vicinity of the adhesive edges, as shown in Figure 8.6, in a way that they reduce in magnitude in the vicinity of the overlap's middle. Hence, plasticity is localized at the vicinity of the adhesive

edges and propagates together with the damage initiation and propagation from these points into the middle of the adhesive layer.

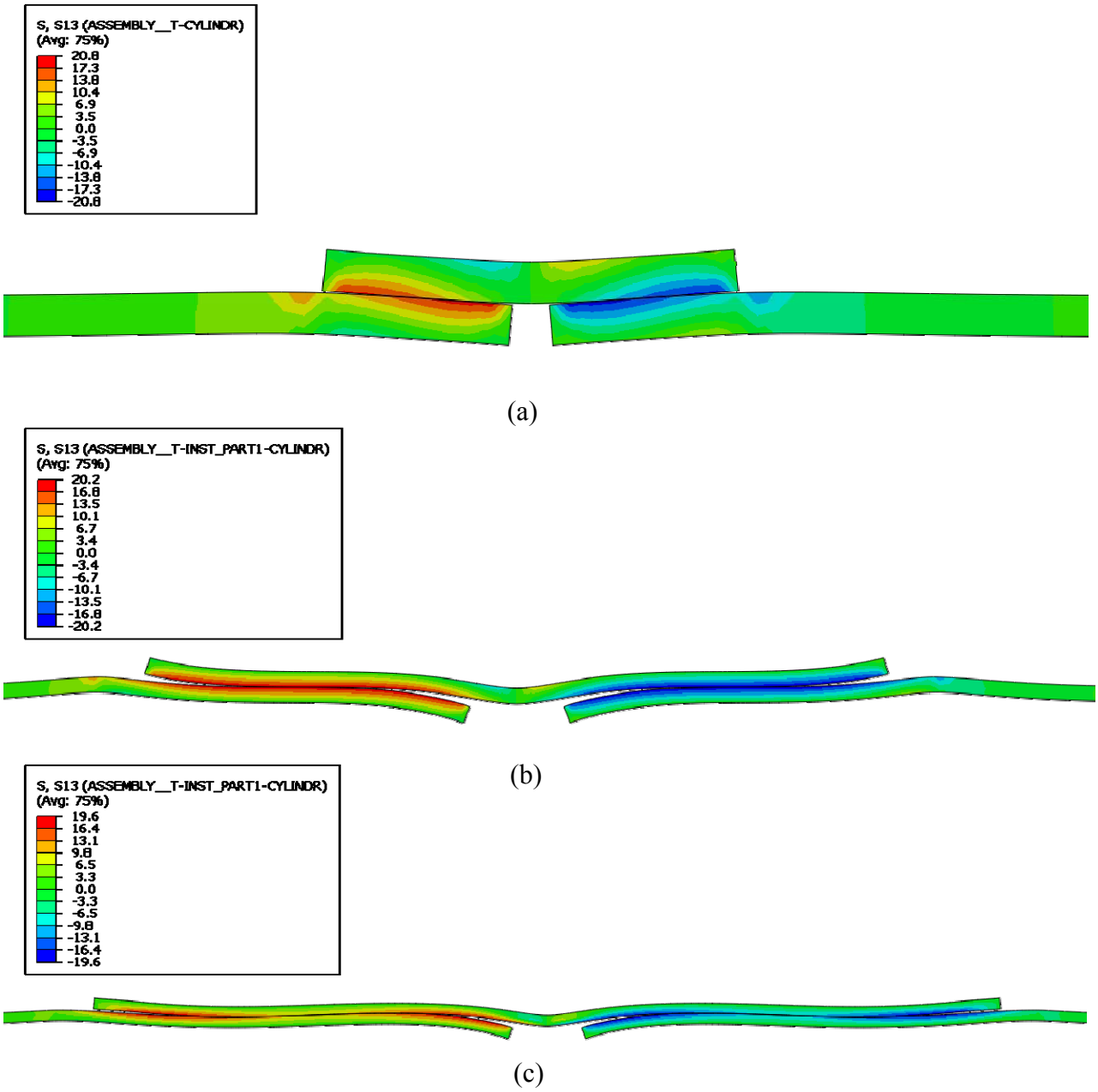

Figure 8.6: In-plane shear stress variation of the 2D axisymmetric SSJ tube-to-tube adhesive joint with L_o equal to 20, 80 and 140 mm at the maximum force level.

Figure 8.7 presents a comparison between the predicted distributions of the in-plane shear stresses of the 2D axisymmetric tube-to-tube SSJ adhesive joint with a 4 mm and 8 mm CFRP strap material. The SSJ case with the thin strap yields a 14% higher strength than the corresponding SSJ case with a thick strap. This behaviour can be justified by observing the variation shown in Figure 8.7b. The regions laying at the outer overlap edges develop plastic shear stresses whereas shear stress become plastic in much smaller regions at the middle of the

joints compared to Figure 8.7a. For this purpose, the stress concentrations developing in the middle of the overlap, lead to the premature failure of the adhesive joints.

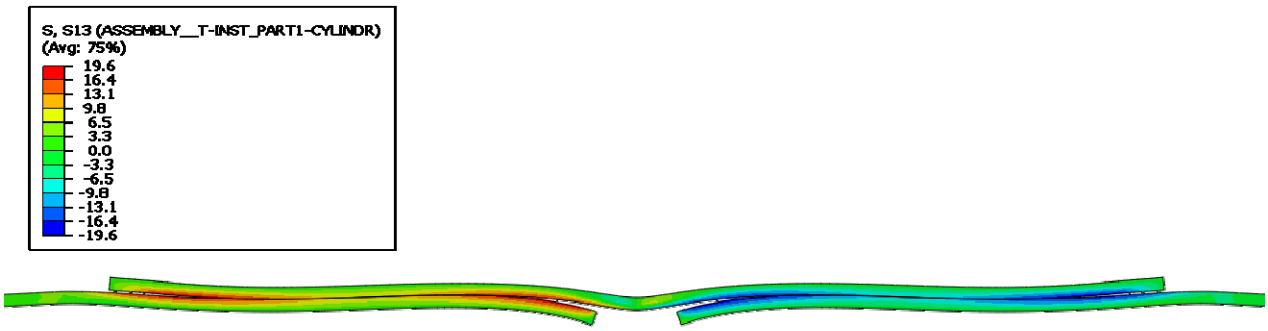

(a)

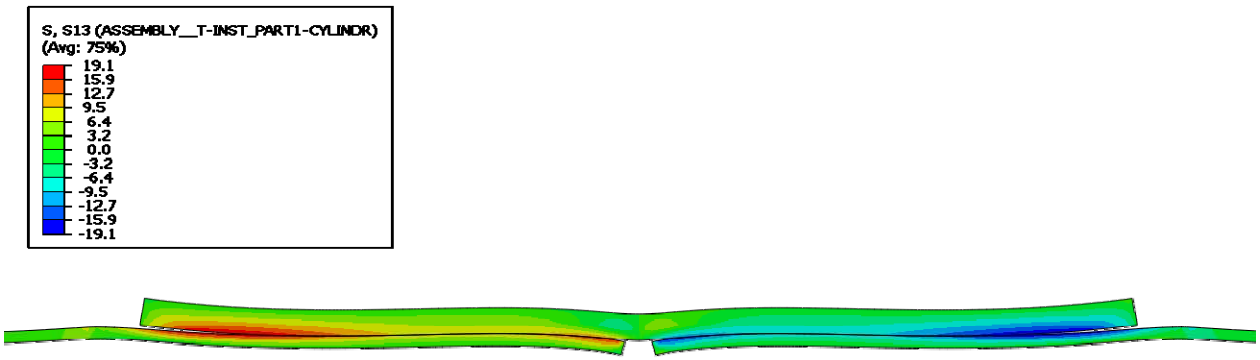

(b)

Figure 8.7: In-plane shear stress variation of the 2D axisymmetric tube-to-tube SSJ adhesive joint with L_o equal 140 mm and 4mm (a) and 8mm (b) CFRP strap at the maximum force level.

8.4.2 Tube-to-Flange adhesive joints

A similar behaviour is observed in Figure 8.8 regarding the trend of the strength-overlap length curves of the tube-to-flange SSJ cases. The predicted strengths are equal, whereas for all cases and for L_o values less than 80 mm, beyond this value, the strengths tend to reach a specific plateau level, different from case to case.

In contrast to the tube-to-tube SSJ cases (see Figure 8.4), the thin CFRP straps of the tube-to-flange SSJ cases yield the lowest strength values for L_o higher than 80 mm, as shown in Figure 8.8. This is attributed to the cooperation of the adhesive joint formed between the thin CFRP strap and the steel flange, where a small stiffness ratio equal to 0.3 arises from the steel-to-aluminum adhesive joint. The best performance, in terms of strength, is obtained by utilizing the thin Aluminum straps for tube-to- flange SSJ. Figure 8.9 presents a comparison of the global Force-Displacement responses as numerically calculated for the six different overlap lengths, for a typical SSJ geometry. As in Figure 8.5, the global response is characterized as non-linear for

small overlap lengths and turns to linear as the overlap length increases. Figure 8.10 presents the in-plane shear distribution over the axisymmetric tube-to-flange SSJ adhesive joint, at the maximum load level. This figure can be compared to the corresponding tube-to-tube SSJ case shown in Figure 8.7b, where the shear stresses peak towards the middle of the tube-to-flange SSJ case, compared to the tube-to-tube case.

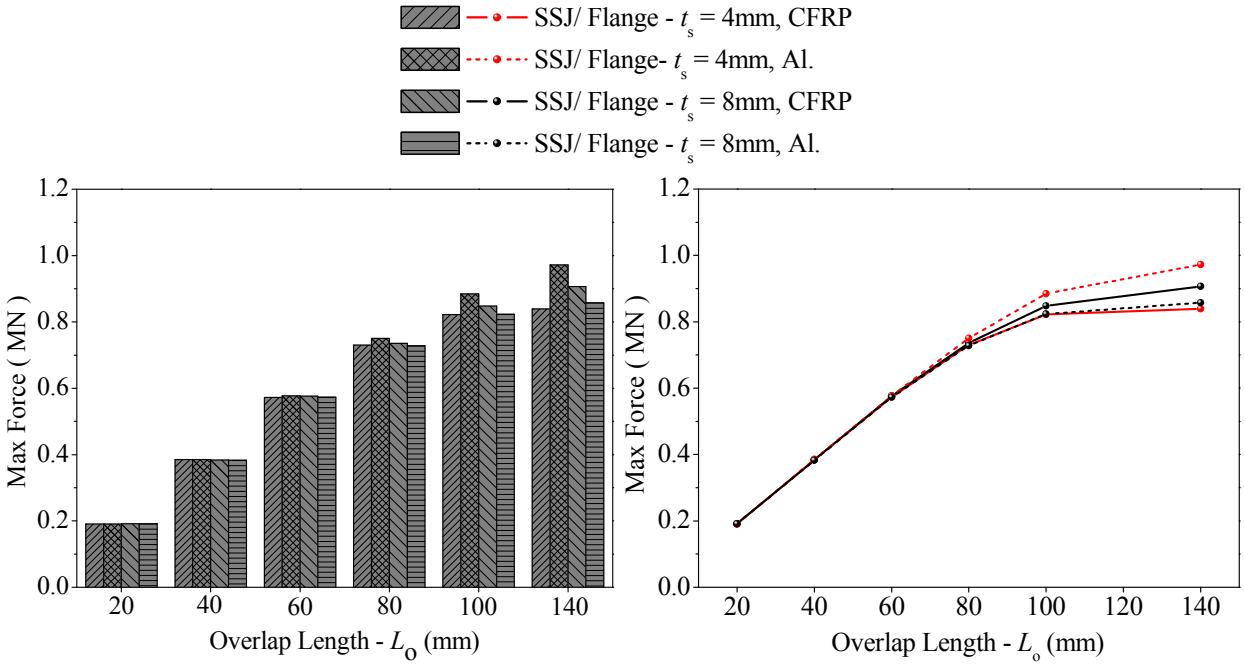

Figure 8.8: Comparison of the maximum attained forces from all tube-to-flange SSJ cases.

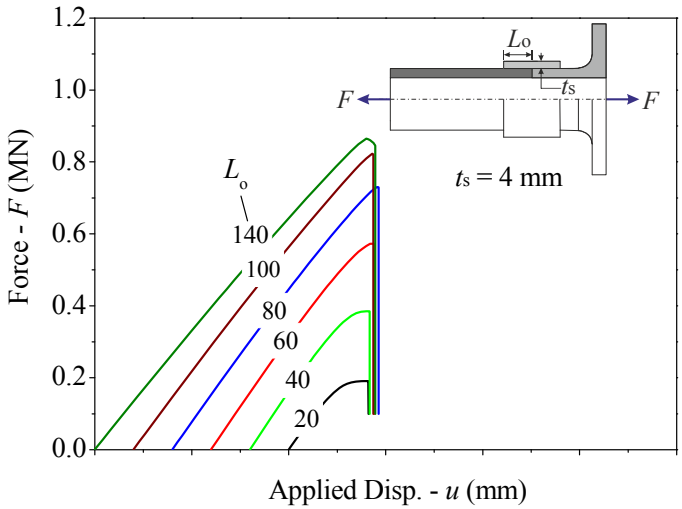

Figure 8.9: Global response of the SSJ flange-to-tube cases. The numerical obtained curves have been shifted by 0.4 mm for reasons of clarity.

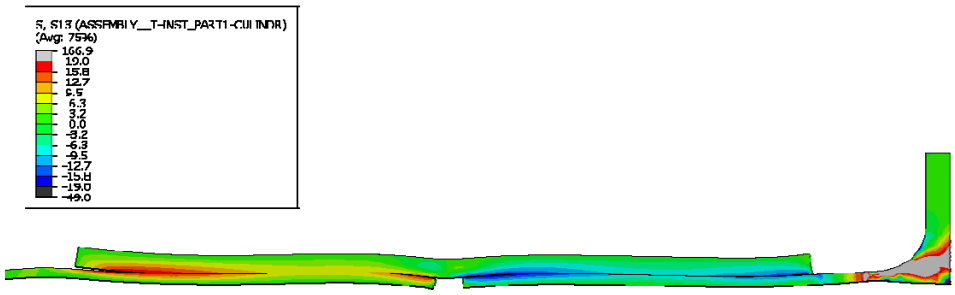

Figure 8.10: In-plane shear stress variation of the 2D axisymmetric tube-to-flange SSJ adhesive joint with L_o equal 140 mm and 8mm CFRP strap at the maximum force level.

8.5 Conclusions

An extensive numerical parametric study has been conducted involving tubular adhesive joints used for bringing together CFRP pipes. Thus, single lap and single strap geometries have been considered for tube-to-tube adhesive joints and single strap geometries for tube-to-flange joints. This parametric study focuses on investigating the effect of geometric and material parameters to the behaviour and strength of tubular adhesive joints used for bringing together CFRP pipes in marine applications.

The cases were modeled in a 3dimensional finite element space and the proposed 3D mixed-mode model has been utilized for the material response of the adhesive layer. Applying an internal pressure to all cases, the outcome from the simulations was the ultimate strength under axial loading. According to the numerical results, regardless the case considered, the trend of all global response curves denotes a behaviour of the strength to tend to a plateau with the increase of the overlap length (L_o). This behaviour is obvious for L_o values higher than 100 mm and particularly for the SSJ cases that have an 8mm thick strap. The existence of a plateau beyond which the strength of lap joints does not increase with further increase in the overlap length is a common characteristic of adhesive joints with flat adherents.

Additionally, the SLJ cases fail at the same force level as the SSJ geometries with a 4mm CFRP strap material, even if the latter configuration has an actual overlap length of $2L_o$. Thus, the SLJ configuration is preferable in design considerations, because with less adhesive material and avoiding extra strap materials the same strength levels can be attained, compared to the SSJ geometry. On the other hand, a special mould has to be manufactured for the creation of the special reception in one tube's end.

This page has been intentionally left blank

9. Conclusions and scientific novelties

The field of computational mechanics and specifically finite element methods has been well matured, by providing finite element technology capable to simulate the kinetics and kinematics which develop during the deformation of composite materials and structural adhesively bonded joints. However, there is a lack in the literature regarding constitutive models that incorporate damage and failure, in either case, which is the motivation of the current PhD thesis. For this purpose, in the present study, an effort has been made to develop new constitutive relations that predict the loading and fracture response of composite structures and adhesively bonded joints, under the framework of cohesive finite element technology together with damage and fracture mechanics.

The general conclusions and novelties are as follows:

- Development of a Progressive Failure Model within the framework of finite element procedures that can adequately predict the failure load of composite structures through the assessment of the in-plane fracture modes. The model has been utilized for the simulation of the loading and fracture response of a stiffened composite panel under compressive loads, within the buckling and post-buckling region. It has been concluded that the developed PFM is an efficient analysis and design tool in addressing the failure mechanisms that are involved composite structures.
- Development of novel traction-separation laws for modeling Mode I and Mode II delamination initiation and propagation in fibrous composite materials. A methodology is presented according to which experimentally measured fiber bridging laws are converted to numerical constitutive equations of cohesive elements based on specific proposed amendments. The constitutive relations include the effect of both zones occurring during delamination growth, i.e. fiber bridging zone and cohesive zone. These laws were utilized for modeling Double Cantilever Beam (DCB) and End Notch Flexure (ENF) composite geometries for addressing Mode I and Mode II loading and fracture, respectively. It has been concluded, that the proposed procedure and constitutive relations are adequate numerical tools for the analysis and design of composite structures that fail in delamination.
- Development of a novel traction-separation law for the finite element prediction of the mixed-mode response of a ductile adhesive layer used in adhesively bonded joints, based

on the Embedded Process Zone (EPZ) approach. The new to the literature law were initially formulated for pure Mode I, Mode II and Mode III loading fracture and then it was incorporated into a developed mixed-mode model (2D and 3D) which accounts for their coupling and interdependency. It has been concluded that the proposed EPZ mixed-mode model can be referred to as two-parameter laws when designing towards the strength of an adhesive joint with a ductile adhesive material compared to the existing three-parameter trapezoidal model. However, when designing towards the maximum attained displacement, the proposed laws are three-parameter laws. The model has been initially applied for the prediction of the response of metal-to-metal adhesive joints, that is Single Lap and Double Strap Joints. The proposed model is an adequate analysis and design tool which can predict the force-displacement response, the failure load and the developed elastic, plastic and damage stress fields, as these evolve during the loading of adhesively bonded joints.

- A new to the literature experimental test has been designed and carried out, based on a Single Lap Joint subjected to Eccentric tensile Loading (SLJ-EL). This test has been used for the validation of the aforementioned 3D EPZ mixed-mode model, since the adhesive layer fails under the contribution of all three fracture modes (Mode I, Mode II and Mode III) in a progressive manner, during the loading of the specimen.
- New to the literature experimental tests have been conducted that involve adhesively bonded thick CFRP and steel adherents under the Single Lap Joint (SLJ) geometrical configuration, within the framework of a parametric study. It has been concluded that only the overlap length has a significant effect on the joints' strength compared to the adhesive's thickness and the joint stiffness ratio. The proposed EPZ 3D mixed-model has been applied for the simulation of the experiments, concluding to promising results.
- A new procedure is proposed for converting experimental cohesive laws obtained from Double Cantilever Beam tests subjected to Unbalanced Bending Moments (DCB-UBM), to numerical traction-separation laws, according to the novel EPZ laws. This procedure provides all necessary amendments that must be taken under consideration when utilizing experimental laws to numerical simulations. The procedure has been validated with pure and mixed-mode tests and it has been concluded that it yields very promising results.
- New to the literature predictions of tubular adhesive joints are presented which involve cohesive zone modeling in a 3-dimensional space with the use of the proposed 3D EPZ mixed-mode model. The potential of the proposed model has been shown through a wide numerical parametric analysis of tubular adhesive joints.

In conclusion, the present PhD thesis provides advanced numerical tools that can be further integrated in a more general Finite Element code for the prediction of the failure response of structures that involve composite materials and adhesive joints. Thus, damage and failure

occurring either within composite materials or within the adhesive layer of the joined members could be numerically captured and, consequently, the maximum allowable loading conditions of a structure can be accurately predicted.

References

Adams, R.D., Harris, J.A., 1984. Strength prediction of bonded single lap joints by nonlinear finite element methods. International Journal of Adhesion and Adhesives 4: 65- 78.

Adams, R.D., Comyn, J., Wake, W.C., 1997. Structural adhesive joints in engineering. London, Chapman & Hall.

Adams, R.D., Harris, J.A., 1987. The influence of local geometry on the strength of adhesive joints. International Journal of Adhesion and Adhesives 7: 69-80.

Alfano, G., Crisfield, M.A., 2001. Finite element interface models for the delamination analysis of laminated composites: mechanical and computational issues. International Journal of Numerical Methods in Engineering 50:1701-1736.

Alfano, M., Furgiuele, F., Leonardi, L., Maletta, C., Paulino, G.H., 2007. Fracture analysis of adhesive joints using intrinsic cohesive zone model. Key Eng Mater 348:13–16.

Alfano, M., Furgiuele, F., Leonardi, L., Maletta, C., Paulino, G.H., 2009. Mode I fracture of adhesive joints using tailored cohesive zone models. International Journal of Fracture 157:193–204.

Allix, O., Corigliano, A., 1996. Modeling and simulation of crack propagation in mixed-modes interlaminar fracture specimens. International Journal of Fracture 77: 111-140.

Andersson, T., Stigh, U., 2004. The stress-elongation relation for an adhesive layer loaded in modus I using equilibrium of energetic forces. International Journal of Solids and Structures. 41: 413-434.

Andrianakis, A., 2011. Experimental and numerical study of a steel-to-composite adhesive joint under bending moments. Diploma Thesis, School of Naval Architecture and Marine Engineering, National Technical University of Athens, in Greek.

Anyfantis, K., 2009. Adhesive bonding of dissimilar materials: Literature review. Technical report No. STL-279-F-09, Shipbuilding Technology Laboratory, National Technical University of Athens.

Anyfantis, K.N. and Tsouvalis, N.G. 2010. Characterization of Fiber Bridging in Mode II Fracture Growth of Laminated Composite Materials, Applied Mechanics and Materials, Vols. 24-25, Trans Tech Publications, Switzerland.

Anyfantis, K.N., Tsouvalis, N.G., 2009. The effect of surface preparation on the effect of double strap adhesive joints with thick steel adherents. 2nd International Conference on Marine Structures - Analysis and Design of Marine Structures, Lisbon, Portugal, March 2009.

Anyfantis, K.N., Tsouvalis, N.G., 2011a. Post Buckling Progressive Failure Analysis of Composite Laminated Stiffened Panels. *Applied Composite Materials*, published on line.

Anyfantis, N.K., Tsouvalis, N.G., 2011b. Experimental and numerical investigation of Mode II fracture in fibrous reinforced composites. Journal of Reinforced Platics and Composites 30, 473-487.

Anyfantis, K.N., Tsouvalis, N.G., 2012a. A novel traction-separation law for the prediction of the mixed mode response of ductile adhesive joints. International Journal of Solids and Structures. 49: 213-226.

Anyfantis, K.N., Tsouvalis, N.G., 2012b. A 3D ductile constitutive mixed-mode model of cohesive elements for the finite element analysis of adhesive joints. Journal of Adhesion Science and Technology, accepted for publication.

Ashcroft, I., 2011. Fatigue Load Conditions, in Handbook of Adhesion Technology, ed. by L.M.F. da Silva, A Ochsner, R.D. Adams (Springer, Heidelberg, 2011).

ASTM D5528-01, 2007. Standard test method for Mode I interlaminar fracture toughness of unidirectional fiber-reinforced polymer matrix composites: In annual book of ASTM standards: Volume 15.03.

Baker, A.A., 1988. Crack patching: experimental studies, practical applications. In: Baker AA, Jones R, editors. Bonded repair of aircraft structures. Dordrecht: Martinus Nijho Publishers, (Chapter 6).

Baker, R.M, Hart, F., 1957. Analysis of bonded joints in vehicular structures. Journal of AIAA 11, 1650-1654.

Balle, F., Wagner, G., Eifler D., 2009. Ultrasonic metal welding of aluminium sheets to carbon fibre reinforced thermoplastic composites. Advanced Engineering Materials 11, 1-2.

Banea, M.D., da Silva, L.F.M., Campilho, R.D.S.G., 2010. Temperature dependence of the fracture toughness of adhesively bonded joints. Journal of Adhesion Science and Technology 24: 2011-2026.

Barret, J.D., Foschi, R.O., 1997. Use of standardized sequences of flight-by-flight load spectra in fatigue testing of structural aircraft components. Engineering Fracture Mechanics 9, 371-378.

Berry, J.P., 1983. Determination of fracture surface energies by the cleavage technique, Journal of Applied Physics 34, 62.

Bishopp, J., 2005. Handbook of Adhesives and Sealants. McGRAW Hill Inc.

Blackman, B.R.K., Brunne, A.J., Williams, J.G., 2006. Mode II fracture testing of composites: a new look at an old problem. Engineering Fracture Mechanics 73, 2443-2455.

Broek, D., 1986. Elementary Fracture Mechanics. 4th edition, Martinus Nijhoff, Dordrecht, The Netherlands.

Burkholder, G.L., Kwon, Y.W., Pollak, R.D., 2011. Effect of carbon nanotube reinforcement on fracture strength of composite adhesive joints. Journal of Material Science 46, 3370–3377.

Camanho, P.P., Matthews, F.L., 1999. A progressive damage model for mechanically fastened joints in composites laminates. Journal of Composite Materials 33, 2248-2280.

Campilho, R.D.S.G., 2009, Repair of composite and wood structures. Ph.D. Dissertation, Engineering Faculty of Porto University.

Campilho, R.D.S.G., Banea, M.D., Pinto, AM.G., da Silva, L.F.M., de Lesus, A.M.P., 2011a. Strength prediction of single- and double-lap joints by standard and extended finite element modelling. International Journal of Adhesion and Adhesives 31: 363 372.

Campilho, R.D.S.G., Pinto, AM.G., Banea, M.D., da Silva, L.F.M., 2011b. Optimization study of hybrid spot welded-bonded single-lap joints. International Journal of Adhesion and Adhesives.

Campilho, R.D.S.G., Banea, M.D., Chaves, F.J.P., da Silva, L.F.M., 2011c. Modelling of single-lap joints using cohesive zones models: effect of the cohesive parameters on the output of the simulations. Journal of Adhesion.

Campilho, R.D.S.G., Banea, M.D., Chaves, F.J.P., da Silva, L.F.M., 2011d. Extended Finite Element Method for fracture characterization of adhesive joints in pure mode I. Computational Material Science 50: 1543- 1549.

Campilho, R.D.S.G., de Moura, M.F.S.F., Ramantani, D.A. Morais, J.J.L., Barreto, A.M.J.P., Domingues, J.J.M.S,2010. Adhesively-bonded repair proposal for wood members damaged by horizontal shear using carbon-epoxy patches. Journal of Adhesion 86: 649-670.

Campilho, R.D.S.G., de Moura, M.F.S.F., Domingues, J.J.M.S., 2005. Modelling single and double-lap repairs on composite materials. Composites Science and Technology 65: 1948- 1958.

Campilho, R.D.S.G., de Moura, M.F.S.F., Domingues, J.J.M.S., 2007. Stress and failure analyses of scarf repaired CFRP laminates using a cohesive damage model. Journal of Adhesion Science and Technology 21: 855- 970.

Campilho, R.D.S.G., de Moura, M.F.S.F., Domingues, J.J.M.S., 2008a. Using a cohesive damage model to predict the tensile behaviour of CFRP single-strap repairs. International Journal of Solids and Structures 45: 1497- 1512.

Campilho, R.D.S.G., de Moura, M.F.S.F., Domingues, J.J.M.S.,Morais, J.J.L., 2008b. Computational modelling of the residual strength of repaired composite laminates using a cohesive damage model. Journal of Adhesion Science and Technology 22, 1565- 1591.

Campilho, R.D.S.G., de Moura, M.F.S.F., Domingues, J.J.M.S., 2009a. Numerical prediction on the tensile residual strength of repaired CFRP under different geometric changes. International Journal of Adhesion and Adhesives 29: 195- 205.

Campilho, R.D.S.G., de Moura, M.F.S.F., Pinto, A.M.G., Morais, J.J.L., Domingues, J.J.M.S, 2009b. Modelling the ten sile fracture behaviour of CFRP scarf repairs. Composites Part B 40: 149- 157.

Campilho, R.D.S.G., de Moura, M.F.S.F., Ramantani, D.A. Morais, J.J.L., Domingues, J.J.M.S, 2009c. Tensile behaviour of three-dimensional carbon-epoxy adhesively bonded single- and doublestrap repairs. International Journal of Adhesion and Adhesives 29: 678-686.

Cao, J., Grenesdt, L., 2003. Test of a redesigned glass-fiber reinforced vinylester to steel joint for use between a naval GRP superstructure and a steel hull. Composite Structures 60, 439-445.

Cao, J., Grenesdt, L., 2004. Design and testing of joints for composite sandwich/steel hybridic ship hulls. Composites: Part A 35, 1091 – 1105.

Carberger, T., Stigh, U., 2010. Influence of layer thickness on cohesive properties of an epoxy-based adhesive-an experimental study. Journal of Adhesion 86: 814-833.

Carlsson, L.A., Gillespie, J.W., Pipes, R.B., 1986. On the Analysis and Design of the End Notched Flexure (ENF) Specimen for Mode II Testing. Journal of Composite Materials 20, 594-604.

Cavallini, G., Davi, G., Milazzo, A., 2006. Boundary element modeling and analysis of adhesive bonded structural joints. Electronic Journal of Boundary Elements 4: 31-48.

Chandra, N., Li, H., Shet, C., Ghonem, R., 2002. Some issues in the application of cohesive zone models for metal-ceramic interfaces. International Journal of Solids and Structures 39: 2827-2855.

Charalambides, M., Kinloch, A.I., Wang, Y., Williams, J.G., 1992. On the analysis of mixed mode failure. International Journal of Fracture 54, 269- 291.

Chen, D., Cheng, S., 1983. An analysis of adhesive-bonded single lap joints. Journal of Applied Mechanics 50, 109-115.

Chen, J., 2002, Predicting progressive delamination of stiffened fibre-composite panel and by decohesion models. Journal of Thermoplastic Composite Materials 15: 429-441.

Cheuk, P.T., Tong, L., Rider, A.N., Wang, J., 2005. Analysis of energy release rate for fatigue cracked metal-to-metal double-lap shear joints. International Journal of Adhesion and Adhesives 25: 181- 191.

Choupani, N., 2008. Interfacial mixed-mode fracture characterization of adhesively bonded joints. International Journal of Adhesion and Adhesives 28: 267-282.

Clarke, J.D., Mcgregor, I.J., 1993. Ultimate tensile stress over a zone: a new failure criterion for adhesive joints. Journal of Adhesion 42: 227- 245.

Clifford, S.M., Manger, C.I.C.,Clyne, T.W., 2002. Characterization of a glass fibre reinforced vinylester to steel joint for use between naval GRP superstructure and a steel hull. Composite Structures 57, 59-66.

Crocombe, A. D., Adams, R. D., 1981. Influence of the spew fillet and other parameters on the stress distributions in the single-lap joint. Journal of Adhesion 13: 141-155.

Crocombe, A.D., 1989. Global yielding as a failure criteria for bonded joints. International Journal of Adhesion and Adhesives 9: 145- 153.

da Silva, L.F.M., Adams, R.D., 2007. Techniques to reduce the peel stresses in adhesive joints with composites. International Journal of Adhesion & Adhesives 27: 227-235.

da Silva, L.F.M., Critchlow, G.W., Figueiredo, M.A.V., 2008. Parametric study of adhesively bonded single lap joints by the Taguchi method. Journal of Adhesion Science and Technology 22: 1477-1494.

da Silva, L.F.M., Carbas, R.I.C., Critchlow, G.W., Figueiredo, M.A.V., Brown, K., 2009a. Effect of material, geometry, surface treatment and environment on the shear strength of single lap joints. International Journal of Adhesion and Adhesives 29: 32.

da Silva, L.F.M., das Neves, P.J.C., Adams, R.D., Spelt, J.K., 2009b. Analytical models of adhesively bonded joints- Part I: literature survey. International Journal of Adhesion and Adhesives 29: 319- 330.

da Silva, L.F.M., das Neves, P.J.C., Adams, R.D., Wang, A., Spelt, J.K., 2009c. Analytical models of adhesively bonded joints- part II: comparative study. International Journal of Adhesion and Adhesives 29: 331 – 341.

da Silva, L.F.M., Öchsner, A., Adams, R.D. (eds.), 2011. Handbook of Adhesion Technology. Springer, Heidelberg.

Dance, B.G.I., Kellar, E.J.C., 2004. Workpiece Structure Modification. International Patent Publication Number WO 2004/028731 A1.

De Bruyne, N. A., 1944. The strength of glued joints. Aircraft Engineering 16: 115-118.

de Moura M.F.S.F., Oliveira J.M.Q., Morais J.J.L., Xavier J., 2009, Mixed-mode I/II wood fracture characterization using the mixed-mode bending test, Engineering Fracture Mechanics 77: 144-152.

de Moura, M.F.S.F., de Morais, A.B., 2008. Equivalent crack based analyses of ENF and ELS tests. Engineering Fracture Mechanics 75, 2584-2596.

Deng, J., Lee, M., 2008. Effect of plate end and adhesive spew geometries on stresses in retrofitted beams bonded with a CFRP plate. Composites: Part B 39, 731-739.

Dillard, D.A., Singh, H.K., Pohlit, D.J., 2009. Observations of decreased fracture toughness for mixed mode fracture testing of adhesively bonded joints. Journal of Adhesion Science and Technology 23: 515- 1530.

Dow Chemical Company, 2012. Information on: http://www.dow.com, last visited at January 2012.

Duan, K., Hu, X., Mai, Y.W., 2004. Substrate constraint and adhesive thickness effects on fracture toughness of adhesive joints. Journal of Adhesion Science and Technology 18: 39- 53.

Dugdale, D.S., 1960. Yielding of steel sheets containing slits. Journal of the Mechanics and Physics of Solids 8: 100-104.

Dvorak, G., Zhang, J., Canyurt, O., 2001. Adhesive tongue-and-groove joints for thick composite laminates. Composites Science and Technology 61, 1123–1142.

ESDU, 1979.Engineering Sciences Data Unit, Inelastic shear stresses and strains in adhesive bonding lap joints loaded in tension or shear (Computer Program). Engineering Sciences Data Item Number 79016.

Falzon, G.B., Hitchings, D., 2003. Capturing mode-switching in postbuckling composite panels using a modified explicit procedure. Composite Structures 60, 447 – 453.

Falzon, G.B., Stevens, A.K., Davies, O.G., 2000. Postbuckling behaviour of a blade-stiffened composite panel loaded in uniaxial compression. Composites Part A: Applied Science and Manufacturing 31, 459-468.

Faulkner, S. D. , Kwon, Y. W., Bartlett, S., Rasmussen, E. A., 2009. Study of composite joint strength with carbon nanotube reinforcement. Journal of Material Science 44, 2858–2864.

Frostig, Y., Thomsen, T.O., Mortensen, H., 1999. Analysis of adhesive-bonded joints, square-end, and spew-fillet- high-order theory approach. Journal of Engineering Mechanics 125, 1298-1307.

Goland, M., Reissner, E., 1944. The stresses in cemented joints. Journal of Applied Mechanics 11: 17-27.

Goyal, V.K, Johnson, E.R., Goyal, V.K., 2008. Predictive strength-fracture model of composite bonded joints. Composite Structures 82: 434–446.

Grabovac, I., Whittaker, D., 2009. Application of bonded composites in the repair of ships structures - A 15-year service experience. Composites Part A 40, 1381-1398.

Greenwood, L. 1969. The Strength of a Lap Joint, in Aspects of Adhesion-5, ed. by D. Alner (University of London Press, London, 1969).

Harris, F.A., Beevers, A., 1999. The effects of grit-blasting on surface properties for adhesion. International Journal of Adhesion & Adhesives 19, 445-452.

Hart-Smith, LJ., (1973). Adhesive-bonded double-lap joints. NASA CR-112235, National Aeronautics and Space Administration.

Hashemi, S., Kinloch, A.J., Williams, J.G., 1990. The analysis of interlaminar fracture in uniaxial fibrepolymer composites. Proceedings of the Royal Society A427, 173-199.

Hashemi, S., Kinloch, AJ., Williams, J.G., 1989. Corrections needed in double cantilever beam tests for assessing the interlaminar failure of fibre composites. Journal of Materials Science Letters 8: 125-129.

Hashin, Z., 1980. Failure criteria for unidectional fiber composites. Journal of Applied Mechanics 47, 329 - 334.

Hentinen, M., Hildebrand, M., Visuri, M., 1997. Adhesively bonded joints between FRP sandwich and metal, VTT, Technical Research Center of Finland, available on-line.

Hinton, M., Kaddour, A., Soden, P., 2002. A comparison of the predictive capabilities of current failure theories for composite laminates, judged against experimental evidence. Composites Science and Technology 62, 1725–1797.

Hsiao, K-T, Alms, J., Advani, S.G., 2003. Use of epoxy/multiwalled carbon nanotubes as adhesives to join graphite fibre reinforced polymer composites. Nanotechnology 14, 791–793.

Hutchinson, J.W. 1968. Singular behavior at the end of a tensile crack in a hardening material. Journal of the Mechanics and Physics of Solids 16: 13-31.

Ikegami, K., Takeshita T., Matsuo, K., Sugibayashi, T., 1990. Strength of adhesively bonded scarf joints between glass fibre-reinforced plastics and metals. International Journal of Adhesion and Adhesives 10, 385-400.

Irwin, R.G., Kies, A.J., 1954. Critical energy rate analysis of fracture. Welding Journal Research Supplement 33, 193-198.

ISO 15024:2001, 2001. Fibre-reinforced plastic composites: Determination of mode I interlaminar fracture toughness, GIC, for unidirectionally reinforced materials.

Jalali, S.J., Taheri, F., 1998. An analytical solution for cross-ply laminates under cylindrical bending based on through-the-thickness inextensibility, Part I: Static loading. International Journal of Solids Structures 35, 1559–1574.

Jensen, F.M., 2008. Ultimate strength of a large wind turbine blade. Risø-PhD-34(EN).

Ji, G., Ouyang, Z., Li, G., 2011, Effects of bondline thickness on Mode-II interfacial laws of bonded laminated composite plate, International Journal of Fracture 168:197–207.

Ji, G., Ouyang, Z., Li, G., Ibekwe, S., Pang, S.S., 2010. Effects of adhesive thickness on global and local Mode-I interfacial fracture of bonded joints. International Journal of Solids and Structures 47: 2445- 2458.

John, S.J., Kinloch, A.I., Matthews, F.L., 1991. Measuring and predicting the durability of bonded fibre/ epoxy composite joints. Composites 22: 121-127.

Kafkalidis, M.S., Thouless, M.D., 2002. The effects of geometry and material properties on the fracture of single lap-shear joints. International Journal of Solids and Structures 39: 4367 – 4383.

Katsiropoulos C.V., Chamos, A.N., Tserpes, K.I., Pantelakis, S.G., 2011. Fracture toughness and shear behavior of composite bonded joints based on a novel aerospace adhesive. Composites Part B: Engineering, article in press.

Khalili, S. M. R., Shiravi, M., Nooramin A.S., 2010. Mechanical behaviour of notched plate repaired with polymer composite and smart patches – experimental study. Journal of reinforced plastics and composites 29, 3021.

Kinloch, A.J., 1987. Adhesion and Adhesives: Science and Technology (Chapman & Hall, London,1987)

Kinloch, A.J., Shaw, S.I., 1981. The fTacture resistance of a toughened epoxy adhesive. Journal of Adhesion 12: 59- 77.

Koch, G.H., Brongers, M.P.H., Thompson, N.G., Virmani, Y.P., Virmani, J.H.,2002. Corrosion costs and preventive strategies in the United States. Office of Infrastructure Research and Development, Report FHWA-RD-01-156.

Kubair, D., Geubelle, P., 2003. Comparative analysis of extrinsic and intrinsic cohesive models of dynamic fracture International Journal of Solids and Structures 40, 3853.

Labeas, G., Belesis, S., Stamatelos, D., 2008. Interaction of damage failure and post-buckling behaviour of composite plates with cut-outs by progressive damage modeling. Composites Part B: Engineering 39, 304-315.

Ladeveze, P., Allix, O., Deu, J., Leveque, D., 2000. A mesomodel for localisation and damage computation in laminates. Computer Methods in Applied Mechanics and Engineering 183, 105–122.

Laurin, F., Carrere, N., Maire, F.J., 2007. Laminated composite structures subjected to compressive loading: A material and structural analysis. Composite Structures 80, 172-182.

Lee, J.D., 1982. Three-dimensional finite element analysis of damage accumulation in composite laminate. Computers & Structures 15, 335 – 350.

Lee, S.J., Lee, D.G., 1992. Development of a failure model for the adhesively bonded tubular single lap joint. Journal of Adhesion 40: 1-14.

Lees, A.W., 1986. Bonding Composites. International Journal of Adhesion & Adhesives 4 , 591-602.

Lees, J.M., 2006. Behaviour of GFRP adhesive pipe joints subjected to pressure and axial loadings, Composites: Part A 37:1171–1179.

Leffler, K., Alfredsson, K.S., Stigh, U., 2007. Shear behaviour of adhesive layers. International Journal of Solids and Structures 44: 530-45.

Lim, A. S., Melrose Z.R. , Thostenson E.T., Chou, T.W., 2011. Damage sensing of adhesively-bonded hybrid composite/steel joints using carbon nanotubes. Composites Science and Technology 71, 1183-1189.

Liu, X., Wang, G., 2007. Progressive failure analysis of bonded composite repairs. Composite Structures 81: 331-340.

Lopes, S.C., Camanho, P.P., Gurdal, Z., Tatting, B.F., 2007. Progressive failure analysis of two-placed, variable-stiffness composite panels. International Journal of Solids and Structures 44, 8493-8516.

Luo, Q., Tong, L., 2007. Fully-coupled nonlinear analysis of single lap adhesive joints. International Journal of Solids and Structures 44, 2349–2370.

Magalhães, A.G., de Moura, M.F.S.F., Gonçalves, J.P.M., 2005. Evaluation of stress concentration effects in single-lap bonded joints oflaminate composite materials. International Journal of Adhesion and Adhesives 25: 313- 319.

Martin, R.H., Davidson, B.D., 1999. Mode II fracture toughness evaluation using four point bend, end notched flexure test. Plastics, Rubbers and Composites 28, 401-406.

Melogranaa, D.J., Grenestedt L.J., Maroun L.J., 2003. Adhesive tongue-and-groove joints between thin carbon fiber laminates and steel. Composites: Part A 34, 119–124.

Möller, F. , Thomy, C. , Vollertsen F., Schiebel , P., Hoffmeister C., Herrmann, A. S., 2010. Novel method for joining CFRP to aluminum. Physics Procedia 5, 37-45.

Morais, B.A., Pereira, B.A., Teixeira, P.J., Cavaleiro, N.C., 2007. Strength of epoxy adhesive bonded stainless-steel joints. International Journal of Adhesion and Adhesives 27, 679-686.

Mortensen, F., Thomsen, O.T., 2002. Analysis of adhesive bonded joints: a unified approach. Composite Science and Technology 62, 1011–1031.

Mouring, E.S., 1999. Buckling and postbuckling of composite ship panels stiffened with perform frames. Ocean Engineering 26, 793-803.

Naik, N.G., Gopalakrishnan, S., Ganguli, R., 2008. Design optimization of composites using genetic algorithms and failure mechanism based failure criterion. Composite Structures 83, 354-367.

Needleman, A., 1987. A Continuum Model for Void Nucleation by Inclusion Debonding. Journal of Applied Mechanics: Transactions of the ASME 54- 525.

O'Brien, E.P., Ward, T.E., Guo, S., Dillard, D.A., 2003. Strain energy release rates of a pressure sensitive adhesive measured by the shaft-loaded blister test. Journal of Adhesion 79: 69-97.

Öchsner, A., 2011. Special Numerical Techniques, in Handbook of Adhesion Technology, ed. by L.M.F.da Silva, A. Ochsner, RD. Adams (Springer, Heidelberg, 2011).

Ojalvo, I.U., Eidinoff, H.L., 1978. Bond thickness effects upon stresses in in single-lap adhesive joints. Journal of the American Institute of Aeronautics and Astronautics 16, 204-211.

Oplinger, D.W., 1994. Effects of adherend deflection on single lap joints. International Journal of Solids and Structures 31, 2565–2587.

Orifici, A.C., Thomson, S.R., Degenhardt, R., Kling, A., Rohwer, K., Bayandor, J., 2008a. Degradation investigation in a postbuckling composite stiffened fuselage panel. Composite Structures 82, 217-224.

Orifici, C.A., Shah, A.S., Herszberg, I., Kotler, A., Weller, T., 2008b. Failure analysis in postbuckled composite T-sections. Composite Structures 86, 146-153.

Oterkus, E., Barut, A., Madenci, E., Smeltzer, S.S., Ambur, R.D., 2006. Bonded lap joints of composite laminates with tapered edges. International Journal of Solids and Structures 43, 1459-1489.

Padhi, G.S., Shenoi, R.A., Moy, S.S.J., Hawkins, G.L., 1998. Progressive failure and ultimate collapse of laminated composite plates in bending. Composite Structures 40, 277-291.

Panigrahi, S.K., Pradhan, B., 2007. Three dimensional failure analysis and damage propagation behaviour of adhesively bonded single lap joints in laminated FRP composites. Journal of Reinforced Plastics and Composites 26: 183-201.

Park, K., Paulino, G.H., Roesler, J.R., 2009, A unified potential-based cohesive model of mixed-mode fracture. Journal of Mechanics and Physics of Solids 57: 891-908.

Pires, I., Quintino, L., Durodola, J.F., Beevers, A., 2003. Performance of bi-adhesive bonded aluminium lap joints. International Journal of Adhesion & Adhesives 23, 215-223.

Puck, A., Schurmann. H., 1998. Failure analysis of frp laminates by means of physically based phenomenological models. Composites Science and Technology 58, 1045–1067.

Radaman, A. E., Farid T., 2011. Influence of adherend's delamination on the response of single lap and socket tubular adhesively bonded joints subjected to torsion, Composite Structures 93: 1765–1774

Raju, I.S., Sistla, R., Krishnamurthy, T., 1996. Fracture mechanics analyses for skin-stiffener debonding. Engineering Fracture Mechanics 54, 371-385.

Rice, J.R., Rosengren, G.F., 1968. Plane strain deformation near a crack tip in a powerlaw hardening material. Journal of the Mechanics and Physics of Solids 16: 1-12.

Rose, L.F.R., 1988. Theoretical analysis of crack patching. In: Baker AA, Jones R, editors. Bonded repair of aircraft structures. Dordrecht: Martinus Nijho Publishers, (Chapter 5).

Russell, A.J., Street, K.N., 1985. Moisture and Temperature Effects on the Mixed Mode Delamination Fracture of Unidirectional Graphite/Epoxy. In: W.S. Johnson, Editor, Delamination and Debonding of Materials (3rd edn), STP 876, ASTM, Philadelphia, 349–370.

Salgado, N.K., Aliabadi, M.H., 1998. The boundary element analysis of cracked stiffened sheets reinforced by adhesively bonded patches. Journal of Numerical Methods in Engineering 42: 195- 217.

Sato, C., Ikegami, K., 1992. Tensile Strength of Single Lap Joint and Scarf Joint between CFRP and Carbon Steel. Journal of Adhesion 39, 29-41.

Schuecker, C., Davidson, B.D., 2000. Effect of friction on the perceived mode II delamination toughness from three- and four- point bend end-notched flexure tests. Composite structure, theory and practice ASTM STP 1383, 334–44.

Shahid, M., Hashim, A.S., 2002. Effect of surface roughness on the strength of cleavage joints. International Journal of Adhesion and Adhesives 22, 235-244.

Shahin, K., Taheri, F., 2008. The strain energy release rates in adhesively bonded balanced and unbalanced specimens and lap joints. International Journal of Solids and Structures 45: 6284-6300.

Shenoi, R.A., Wellicome, J.F., 1993a. Composite Materials in Marine Engineering, Volume 2: Practical Considerations, Cambridge University Press, Great Britain.

Shenoi, R.A., Wellicome, J.F., 1993b. Composites Materials in Maritime Structures. Cambridge University, Vol. 1.

Smith, C.M., 1990. In: Design of Marine Structures in Composite Materials. Elsevier Applied Science, Oxford.

Song, S.H., Paulino, G.H., Buttlar, W.G., 2006. A bilinear cohesive zone model tailored for fracture of asphalt concrete considering viscoelastic bulk material. Engineering Fracture Mechanics 73: 2829-2848.

Sørensen, B.F., Jacobsen, T.K., 2003. Determination of cohesive laws by the J integral approach. Engineering Fracture Mechanics 70: 1841- 1858.

Sørensen, B.F., Jacobsen, T.K., 2009. Characterizing delamination of fibre composites by mixed mode cohesive laws. Composites Science and Technology 69, 445-456.

Sørensen, B.F., Jørgensen, K., Jacobsen, T.K., Østergaard, R.C., 2006. DCB-specimen loaded with uneven bending moments. International Journal of Fracture 141:159–72.

Sørensen, B.F., Kirkegaard, P., 2006. Determination of mixed mode cohesive laws. Eng. Fract. Mech. 73, 2642–2661.

Sorensen, L., Botsis, J., Gmür, T., Cugnoni, J., 2007. Delamination detection and characterisation of bridging tractions using long FBG optical sensors. Composites: Part A 38, 2087-2096.

Sorensen, L., Botsis, J., Gmür, T., Humbert, L., 2008. Bridging tractions in mode I delamination: Measurements and simulations. Composites Science and Technology 68, 2350-2358.

Stevens, K.A., Ricci, R., Davies, G., 1995. Buckling and postbuckling of composite structures. Composites 26, 189-199.

Sun, W., Yang, C., 2004. Fracture analysis of adhesive-bonded single-lap composite joints, International SAMPE Technical Conference 3931-3942.

Suo, Z., Bao, G., Fan, B., 1992. Delamination R-curve phenomena due to damage. Journal of Mechanics and Physics of Solids 40, 1–16.

Suo, Z, Hutchinson, J.W.,1990. Interface crack between two elastic layers. International Journal of Fracture 43: 1-18.

Szekrényes, A., Uj, J., 2005. Advanced beam model for fiber-bridging in unidirectional composite double-cantilever beam specimens. Engineering Fracture Mechanics 72, 2686–2702.

Tamuzs, V., Tarasovs, S., Vilks, U., 2001. Progressive delamination and fiber bridging modeling in double cantilever beam composite specimens. Engineering Fracture Mechanics 68, 513–525.

Tong, L., Steven, G.P., 1999. Analysis and design of structural bonded joints. Boston: Kluwer Academic Publishers.

Tsai, M.Y., Oplinger, D.W., Morton, J., 1998. An improved theoretical solutions for adhesive lap joints. International Journal of Solids and Structures 35, 1163–1185.

Tsai, S.W., Wu, E.M., 1971. A general theory of strength for anisotropic materials. Journal of Composite Materials 5, 58 - 80.

Tsouvalis, N.G., Anyfantis, K.N., 2010. Numerical Prediction of the Response of Metal-to-Metal Adhesive Joints with Ductile Adhesives. In Proceedings of the BSSM Conference on Advances in Experimental Mechanics 2010, Liverpool, September 2010, also in Applied Mechanics and Materials, Vols. 24-25: 189-194.

Tsouvalis, N.G., Anyfantis, K.N., 2012. Determination of the Fracture Process Zone under Mode I Fracture in Glass Fiber Composites. Journal of Composite Materials 46: 27-41.

Tsouvalis, N.G., Karatzas, V.A., 2011. An investigation of the tensile strength of a composite-to-metal adhesive joint. Applied Composite Materials 18, 149-163.

Turon, A., Costa, J., Camanho, P.P., Davila, C.G., 2007. Simulation of delamination in composites under high-cycle fatigue. Composites Part A 38: 2270—2282.

Tvergaard, V., Hutchinson, J.W., 1992. The relation between crack growth resistance and fracture process parameters in elastic-plastic solids. Journal of the Mechanics and Physics of Solids 40: 1377- 1397.

Tvergaard, V., Hutchinson, J.W., 1993. The influence of plasticity on the mixed-mode interface toughness. Journal of the Mechanics and Physics of Solids 41: 1119- 1135.

Ucsnik, S., Scheerer, M., Zaremba, S., Pahr, D.H., 2010. Experimental investigation of a novel hybrid metal-composite joining technology. Composites Part A 41: 369-374.

Vable, M., 2008. Stress analysis of bonded joints by boundary element method, in Modeling of Adhesively Bonded Joints, ed. by L.F.M. da Silva, A. Ochsner (Springer, Heidelberg, 2008).

Volkersen, O., 1938. Die Niektraftverteiling in Zugbeanspruchten mit Konstanten Laschenquerschritten. Luftfahrtforschung 15, 41-47.

Wang, H., Vu-Khanh, T., Le, V.N., 1995. Effects of Large Deflection on Mode II Fracture Test of Composite Materials. Journal of Composite Materials 29, 833-849.

Wang, Y., Williams, J.G., 1992. Corrections for mode II fracture toughness specimens of composites materials. Composites Science and Technology 43, 251-256.

Williams, J.G., 1989. End corrections for orthotropic DCB specimens. Composite Science and Technology 35, 367–376.

Williams, M.L., 1959. The stresses around a fault or crack in dissimilar media. Bulletin of the seismological Society of America 49: 199- 204.

Xiao, X., Foss, P.H., Schroeder, J.A., 2004. Stiffness prediction of the double lap shear joint. Part1:Analytical solution. International Journal of Adhesion and Adhesives 24: 229–237.

Yan, Z.M., You, M., Yi, X.S., Zheng X.L., Li Z., 2007. A numerical study of parallel slot in adherend on the stress distribution in adhesively bonded aluminum single lap joint. International Journal of Adhesion & Adhesives 27, 687–695.

Yang, C., Huang, H., Tomblin, J.S., Sun, W., 2004. Elastic–plastic model of adhesive-bonded single-lap composite joints. Journal of Composite Materials 38, 293–309.

Yang, Q.D., Thouless, M.D., Ward, S.W. 2001. Elastic-plastic mode-II fracture of adhesive joints. International Journal of Solids and Structures 38: 3251-62.

Yang, Q.D., Thouless, M.D., 2001. Mixed – mode fracture analyses of plastically – deforming adhesive joints. International Journal of Fracture 110: 175-187.

Yang, Q.D., Thouless, M.D., 2001. Mixed-mode fracture analyses of plastically deforming adhesive joints. International Journal of Fracture 110: 175- 187.

Yang, Q.D., Thouless, M.D., Ward, S.M., 1999. Numerical simulations of adhesively-bonded beams failing with extensive plastic deformation. Journal of the Mechanics and Physics of Solids 47: 1337- 1353.

Yang, Q.D., Thouless, M.D., Ward, S.M., 2000. Analysis of the symmetrical 90° peel test with extensive plastic deformation. Journal of Adhesion 72: 115- 132.

Zeng, Q., Sun, C.T., 2001. Novel design of bonded lap joint. Journal of AIAA 39, 1991-1996.

Zhang, Y., Vassilopoulos, P. A. Keller, T., 2010. Mode I and II fracture behaviour of adhesively-bonded pultruted composite joints. Engineering Fracture Mechanics 77: 128-43.

Zhao, X., Adams, R.D., da Silva, L.F.M., 2011. Single lap joints with rounded adherend comers: experimental results and strength prediction. Journal of Adhesion Science and Technology 25: 837- 856.

Zou, G.P., Shahin, K., Taheri, F., 2004. An analytical solution for the analysis of symmetric composite adhesively bonded joints. Composite Structures 65, 499–510.

List of PhD Publications

Journal papers relevant to the PhD work

1. Anyfantis K.N. and Tsouvalis N.G., "Post Buckling Progressive Failure Analysis of Composite Laminated Stiffened Panels", *Applied Composite Materials*, published on line (2011) (http://dx.doi.org/10.1007/s10443-011-9191-1).

2. Tsouvalis N.G. and Anyfantis K.N., "Determination of the Fracture Process Zone under Mode I Fracture in Glass Fiber Composites", *Journal of Composite Materials*, 46(1), pp. 27-41, 2012, (http://dx.doi.org/10.1177/0021998311401934).

3. Anyfantis K.N. and Tsouvalis N.G., "Experimental and numerical investigation of Mode II fracture in fibrous reinforced composites", *Journal of Reinforced Plastics and Composites*, 30 (6), pp. 473-487, 2011, (http://dx.doi.org/10.1177/0731684410397682).

4. Hashim, S.A., Nisar, J.A., Tsouvalis, N., Anyfantis, K., Moore, P., Chirica, I., Berggreen, C., Orsolini, A., Quispitupa, A., McGeorge, D., Hayman, B., Boyd, S., Misirlis, K., Downes, J., Dow, R. and Juin, E., "Fabrication, Testing and Analysis of Steel/Composite DLS Adhesive Joints", *Ships and Offshore Structures*, 6 (1&2), pp. 115-126, 2011, (http://dx.doi.org/10.1080/17445302.2010.522019),

5. Anyfantis K.N. and Tsouvalis N.G., "A novel traction-separation law for the prediction of the mixed mode response of ductile adhesive joints", *International Journal of Solids and Structures*, 49 (1), pp. 213-226, 2012, (http://dx.doi.org/10.1016/j.ijsolstr.2011.10.001).

6. Anyfantis K.N. and Tsouvalis N.G., "A 3D ductile constitutive mixed-mode model of cohesive elements for the finite element analysis of adhesive joints", *Journal of Adhesion Science and Technology*, accepted for publication (2012).

Reviewed conference papers

1. Anyfantis K.N. and Tsouvalis N.G., "The effect of surface preparation on the effect of double strap adhesive joints with thick steel adherents", *2nd International Conference on Marine Structures - Analysis and Design of Marine Structures*, Lisbon, Portugal, March 2009.

2. Tsouvalis, N.G. and Anyfantis, K.N., "Numerical Prediction of the Response of Metal-to-Metal Adhesive Joints with Ductile Adhesives", in Proceedings of the *BSSM Conference on Advances in Experimental Mechanics 2010*, Liverpool, September 2010, also in Applied Mechanics and Materials, Vols. 24-25 (2010) p 189-194, (http://dx.doi.org/10.4028/www.scientific.net/AMM.24-25.189).

3. Anyfantis, K.N. and Tsouvalis, N.G., "Characterization of Fiber Bridging in Mode II Fracture Growth of Laminated Composite Materials", in Proceedings of the *BSSM Conference on*

Advances in Experimental Mechanics 2010, Liverpool, September 2010, also in Applied Mechanics and Materials, Vols. 24-25 (2010) p 245-250, (http://dx.doi.org/10.4028/www.scientific.net/AMM.24-25.245).

4. Anyfantis K.N. and Tsouvalis N.G., "Experimental parametric study of single-lap adhesive joints between dissimilar materials", *European Conference of Composite Materials -ECCM15*, June 2012, abstract accepted.

Conference papers

1. Hashim S., Berggreen C., Tsouvalis N., McGeorge D., Chirica I., Boyd S., Moore P., Juin E., Nisar J., Anyfantis K. and Misirlis K., " Design and analysis of DLS steel/composite thick-adherend adhesive joints", *17th International Conference on Composite Materials, ICCM-17***,** Edinburgh, UK, July 2009.

Reports

1. Anyfantis K., "Adhesive Bonding of Dissimilar Materials: Literature Survey", Report No. STL-279-F-09, Shipbuilding Technology Laboratory, NTUA, February 2009.
2. Anyfantis K., "A novel traction-separation law for the numerical prediction of the elasto-plastic response and debonding of adhesive joints with ductile adhesives", Report No. STL-310-F-10-R1, Shipbuilding Technology Laboratory, NTUA, January 2011.
3. Anyfantis K., "Ανάπτυξη 3-διάστατων καταστατικών νόμων για την ανάλυση συνδέσμων με όλκιμα κολλητικά μέσα με την μέθοδο των Πεπερασμένων Στοιχείων", Report No. STL-318-F-11, Shipbuilding Technology Laboratory, NTUA, October 2011.

Planned future publications

1. Experimental and numerical investigation of the contribution of the Mode I, II and III loading and fracture to the failure of adhesive joints bonded with ductile adhesive materials (work described in section 6.3).

2. Experimental and numerical parametric study of single-lap adhesive joints between dissimilar materials (work described in section 7.2).

3. Experimental and numerical investigation of the mixed-mode response of steel-to-composite specimens tested under the DCB-UBM configuration (work described in section 7.3).

4. Numerical parametric analysis of tubular adhesive joints subjected to internal pressure and axial loading (work described in chapter 8).

Appendix A

Formulation of the 3D and 2D interface element

Cohesive Zone Modeling (CZM) techniques have been adopted for the simulation of the crack initiation and propagation process in cohesive or interfacial failure problems or delamination of laminated composite materials, developing under pure or mixed mode loading and fracture conditions. As it has been shown in section 2.3.3, under the framework of Finite Element Analysis procedures, CZM techniques are based on the incorporation of interface (or cohesive) elements in-between the adjacent faces of continuum elements that lay on the plane (or path) were the fracture process will take place.

The main focus of the current PhD thesis is based on providing to the literature cohesive laws that adequately predict the loading and fracture behaviour of the modeled system (adhesive joint or composite itself). Since, ABAQUS® does not provide the ability to the user to program his own cohesive laws, it is essential to develop and program an interface element formulation so as to implement the developed cohesive laws (constitutive relation of the developed cohesive elements). Thus for the needs of the current PhD thesis a 2D and a 3D cohesive element have been developed, which formulation is given in Appendix A1 and A2, respectively.

Appendix A1: Formulation of the 3D interface element

The 3-Dimensional interface finite element consists of two quadratic plane elements (initially co-planar), which describe the mechanics and kinematics in a three dimensional Cartesian space of the cohesive zone to be modeled. The two constituent planar elements connect the adjacent faces of two 3D continuum elements. Each plane element consists of 8 nodes and thus the cohesive element has 16 nodes in total. The 3D cohesive element can be connected with 20-node 3D volumetric continuum elements, as shown in Figure A1.1. The two constitutive planes of the 3D interface element are located in the same position (coincident nodes – zero thickness), in the initial undeformed state and separate as a consequence of the deformation of the connected volumetric continuum elements.

Figure A1.2 presents the parent 3-D interface finite element together with the global coordinate system (x-y-z) and the respective local curvilinear coordinate system (ξ-η). In this figure, the presented node numbering follows the connectivity convention of ABAQUS®. The relative displacements (separations), which result from the displacements of the two constituent planes of the interface element, will be transformed according to an orthogonal triad unit vector system lying on the reference plane. This triad allows the transformation to a normal and two tangential separations, which in turn yield tractions in the corresponding directions, through the constitutive relation that describes the cohesive zone being modeled.

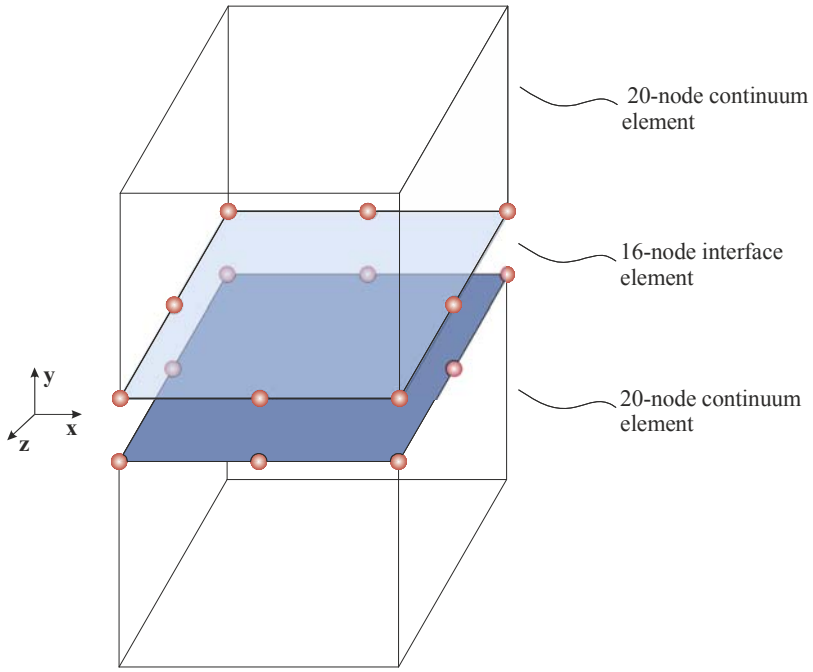

Figure A1.1: Connectivity of the 16-node 3D interface finite element with 20-node volumetric continuum elements.

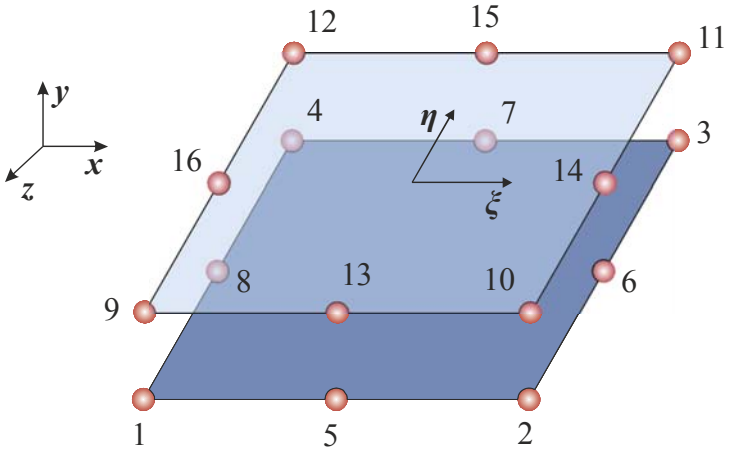

Figure A1.2: 3D interface finite element.

Each node of the developed interface element has three degrees of freedom (dof's), one translation in each direction of the global coordinate system (u_x, u_y, u_z). Thus, the total nodal dofs of the 3D cohesive element are 48 (3x16). The vector containing the nodal dofs is given by:

$$u_N = \left\{ u_x^1 \quad u_y^1 \quad u_z^1 \quad u_x^2 \quad u_y^2 \quad u_z^2 \quad .... \quad u_x^{16} \quad u_y^{16} \quad u_z^{16} \right\}^T = \left\{ \begin{array}{c|c} \{u_N^{bottom}\}_{1x24} & \{u_N^{top}\}_{1x24} \end{array} \right\}^T \tag{A1.1}$$

The difference of the nodal displacements of the top and bottom plane that defines the relative displacements is calculated by:

$$\Delta u_{\mathrm{N}} = \left\{ u_{\mathrm{N}}^{\mathrm{top}} - u_{\mathrm{N}}^{\mathrm{bottom}} \right\} \tag{A1.2}$$

The top plane is defined by nodes 9 - 16 whereas the bottom plane is defined by nodes 1 - 8, by following the convention of Figure A1.2. Equation A1.2 can be rewritten in a programming environment as follows:

$$\overset{24\,\mathrm{x}\,1}{\left\{ \Delta u_{\mathrm{N}} \right\}} = \overset{24\,\mathrm{x}\,48}{\left[\Phi \right]} \left\{ \begin{matrix} u_{\mathrm{N}}^{\mathrm{bottom}} \\ u_{\mathrm{N}}^{\mathrm{top}} \end{matrix} \right\} = \left[\begin{array}{c|c} \overset{24\,\mathrm{x}\,24}{\left[-\mathrm{I} \right]} & \overset{24\,\mathrm{x}\,24}{\left[\mathrm{I} \right]} \end{array} \right] \left\{ \begin{matrix} u_{\mathrm{N}}^{\mathrm{bottom}} \\ u_{\mathrm{N}}^{\mathrm{top}} \end{matrix} \right\} \tag{A1.3}$$

Matrix [Φ] consists of two square unite matrices with 24 x 24 dimensions, sequentially placed. For the interpolation of the nodal relative displacements within the reference surface of the cohesive element (see Figure A1.3), quadratic polynomials have been utilized with respect to the local coordinate system (ξ, η). Let $N_i(\xi, \eta)$ be the shape functions that correspond to a node pair, as listed in Table A1.1, where ξ and η are within the range of [-1,1].

Table A1.1: Node pairs that share the same shape functions.

	Node Pairs	
i	Node 1	Node 2
1	1	9
2	2	10
3	3	11
4	4	12
5	5	13
6	6	14
7	7	15
8	8	16

Each shape function gives 1 to its corresponding node pair and 0 to the remaining nodes. The shape functions utilized for the 3D cohesive element are given by the following equations:

$$N_1(\xi,\eta) = \frac{1}{4}(1-\xi)(1-\eta) - \frac{1}{2}(N_5 + N_8) \tag{A1.4a}$$

$$N_2(\xi,\eta) = \frac{1}{4}(1+\xi)(1-\eta) - \frac{1}{2}(N_5 + N_6) \tag{A1.4b}$$

$$N_3(\xi,\eta) = \frac{1}{4}(1+\xi)(1+\eta) - \frac{1}{2}(N_6 + N_7) \tag{A1.4c}$$

$$N_4(\xi,\eta)=\frac{1}{4}(1-\xi)(1+\eta)-\frac{1}{2}(N_7+N_8) \tag{A1.4d}$$

$$N_5(\xi,\eta)=\frac{1}{2}(1-\xi^2)(1-\eta) \tag{A1.4e}$$

$$N_6(\xi,\eta)=\frac{1}{2}(1+\xi)(1-\eta^2) \tag{A1.4f}$$

$$N_7(\xi,\eta)=\frac{1}{2}(1-\xi^2)(1+\eta) \tag{A1.4g}$$

$$N_8(\xi,\eta)=\frac{1}{2}(1-\xi)(1-\eta^2) \tag{A1.4h}$$

By utilizing the preceding shape functions, the relative displacements can be rewritten within the reference plane of the cohesive element, in a continuous form, considering the discrete nodal values:

$$\Delta u(\xi,\eta)=\begin{Bmatrix}\Delta u_{\mathrm{x}}(\xi,\eta)\\ \Delta u_{\mathrm{y}}(\xi,\eta)\\ \Delta u_{\mathrm{z}}(\xi,\eta)\end{Bmatrix}=H(\xi,\eta)\,\Delta u_{\mathrm{N}} \tag{A1.5}$$

where vector Δu is of dimensions 3x1 whereas matrix $H(\xi, \eta)$ is of dimensions 3x48 and is defined in the following way:

$$H(\xi,\eta)=\left[\mathrm{N}_1(\xi,\eta)\mathrm{I}_{3x3}\middle|\mathrm{N}_2(\xi,\eta)\mathrm{I}_{3x3}\right| \quad .... \quad \left|\mathrm{N}_8(\xi,\eta)\mathrm{I}_{3x3}\right] \tag{A1.6}$$

By combining Equation A1.3 with Equation A1.5 matrix B is obtained with dimensions 3x48, which connects vector Δu with the nodal dof's vector u_{N}:

$$\Delta u(\xi,\eta)=\mathrm{B}u_{\mathrm{N}}=\mathrm{H}(\xi,\eta)\Phi\,u_{\mathrm{N}} \tag{A1.7}$$

A reference plane is defined that lays on the middle in-between the top and bottom planes of the 3D cohesive element, as shown in Figure A1.3.

The coordinates of the reference plane are defined as the average of the coordinates of the top and bottom plane:

$$x_{\mathrm{N}}^{\mathrm{R}}=\frac{1}{2}\left(x_{\mathrm{N}}^{\mathrm{top}}-x_{\mathrm{N}}^{\mathrm{bottom}}\right) \tag{A1.8}$$

where x_N^{top} and x_N^{bottom} are the coordinates of the top and bottom surface, respectively, at a given location as calculated during the non-linear solution of the equations of equilibrium. Thus, for the calculation of x_N^{top} and x_N^{bottom} the corresponding coordinates of the nodes (see Figure A1.4) at the undeformed state X_N^{top} and X_N^{bottom} are being summed with the respective displacements, calculated at a given step of the non-linear analysis.

$$x_N^{bottom} = X_N^{bottom} + u_N^{bottom} \tag{A1.9a}$$

$$x_N^{top} = X_N^{top} + u_N^{top} \tag{A1.9b}$$

As shown in Figure A1.3, an orthogonal triad is defined on the reference plane, which consists of two tangential unit vectors t_1 και t_2 and one normal to the t_n. For the calculation of these vectors a continuous description of the coordinates of the reference plane is essential.

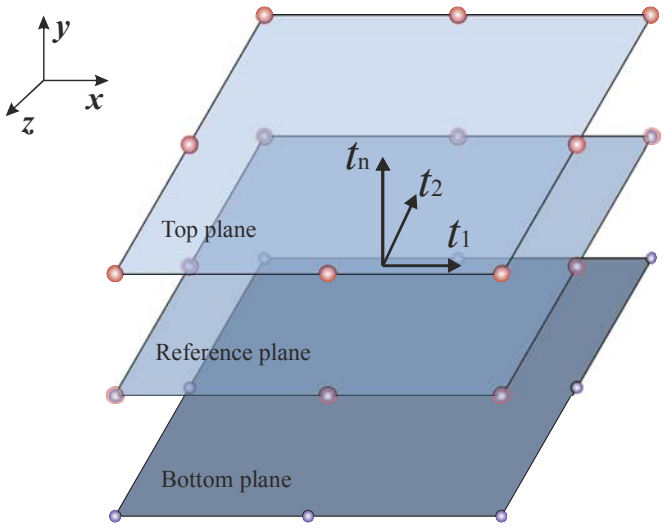

Figure A1.3: The three planes that define the 3D interface element.

Thus the coordinates of all material points laying on the reference plane (see Figure A1.4) are being calculated by utilizing the matrix containing the shape functions, as follows:

$$x^R = H(\xi,\eta)\, x_N^R \tag{A1.10}$$

By this way the unit vectors being parallel to ξ and η axis are being defined, respectively:

$$v_{\xi} = \frac{\partial x^{\mathrm{R}}}{\partial \xi} \frac{1}{\left\| \frac{\partial x^{\mathrm{R}}}{\partial \xi} \right\|} \tag{A1.11a}$$

$$v_{\eta} = \frac{\partial x^{\mathrm{R}}}{\partial \eta} \frac{1}{\left\| \frac{\partial x^{\mathrm{R}}}{\partial \eta} \right\|} \tag{A1.11b}$$

For the calculation of the partial derivatives $\frac{\partial x^{\mathrm{R}}}{\partial \xi}$ and $\frac{\partial x^{\mathrm{R}}}{\partial \eta}$, Equation (A1.10) is inserted in Equation (A1.11).

$$\frac{\partial x^{\mathrm{R}}}{\partial \xi} = \frac{\partial}{\partial \xi}\left(\mathrm{H}(\xi,\eta)\, x_{\mathrm{N}}^{\mathrm{R}}\right) = x_{\mathrm{N}}^{\mathrm{R}} \frac{\partial \mathrm{H}(\xi,\eta)}{\partial \xi} \tag{A1.12a}$$

$$\frac{\partial x^{\mathrm{R}}}{\partial \eta} = \frac{\partial}{\partial \eta}\left(\mathrm{H}(\xi,\eta)\, x_{\mathrm{N}}^{\mathrm{R}}\right) = x_{\mathrm{N}}^{\mathrm{R}} \frac{\partial \mathrm{H}(\xi,\eta)}{\partial \eta} \tag{A1.12b}$$

where $\frac{\partial \mathrm{H}(\xi,\eta)}{\partial \xi}$ and $\frac{\partial \mathrm{H}(\xi,\eta)}{\partial \eta}$ is the first partial derivative of the shape functions (Equation A1.4) with respect to ξ given as follows:

$$N_{1,\xi}(\xi,\eta) = -\frac{1}{4}(1-\eta) - \frac{1}{2}\left(N_{5,\xi} + N_{8,\xi}\right) \tag{A1.13a}$$

$$N_{2,\xi}(\xi,\eta) = \frac{1}{4}(1-\eta) - \frac{1}{2}\left(N_{5,\xi} + N_{6,\xi}\right) \tag{A1.13b}$$

$$N_{3,\xi}(\xi,\eta) = \frac{1}{4}(1+\eta) - \frac{1}{2}\left(N_{6,\xi} + N_{7,\xi}\right) \tag{A1.13c}$$

$$N_{4,\xi}(\xi,\eta) = -\frac{1}{4}(1+\eta) - \frac{1}{2}\left(N_{7,\xi} + N_{8,\xi}\right) \tag{A1.13d}$$

$$N_{5,\xi}(\xi,\eta) = -\xi(1-\eta) \tag{A1.13e}$$

$$N_{6,\xi}(\xi,\eta) = \frac{1}{2}\left(1-\eta^2\right) \tag{A1.13f}$$

$$N_{7,\xi}(\xi,\eta) = -\xi\left(1+\eta\right) \tag{A1.13g}$$

$$N_{8,\xi}(\xi,\eta) = -\frac{1}{2}\left(1-\eta^2\right) \tag{A1.13h}$$

and with respect to η given as follows:

$$N_{1,\eta}(\xi,\eta) = -\frac{1}{4}\left(1-\xi\right) - \frac{1}{2}\left(N_{5,\eta} + N_{8,\eta}\right) \tag{A1.14a}$$

$$N_{2,\eta}(\xi,\eta) = \frac{1}{4}\left(1+\xi\right) - \frac{1}{2}\left(N_{5,\eta} + N_{6,\eta}\right) \tag{A1.14b}$$

$$N_{3,\eta}(\xi,\eta) = \frac{1}{4}\left(1+\xi\right) - \frac{1}{2}\left(N_{6,\eta} + N_{7,\eta}\right) \tag{A1.14c}$$

$$N_{4,\eta}(\xi,\eta) = \frac{1}{4}\left(1-\xi\right) - \frac{1}{2}\left(N_{7,\eta} + N_{8,\eta}\right) \tag{A1.14d}$$

$$N_{5,\eta}(\xi,\eta) = -\frac{1}{2}\left(1-\xi^2\right) \tag{A1.14e}$$

$$N_{6,\eta}(\xi,\eta) = -\eta\left(1+\xi\right) \tag{A1.14f}$$

$$N_{7,\eta}(\xi,\eta) = \frac{1}{2}\left(1-\xi^2\right) \tag{A1.14g}$$

$$N_{8,\eta}(\xi,\eta) = -\eta\left(1-\xi\right) \tag{A1.14h}$$

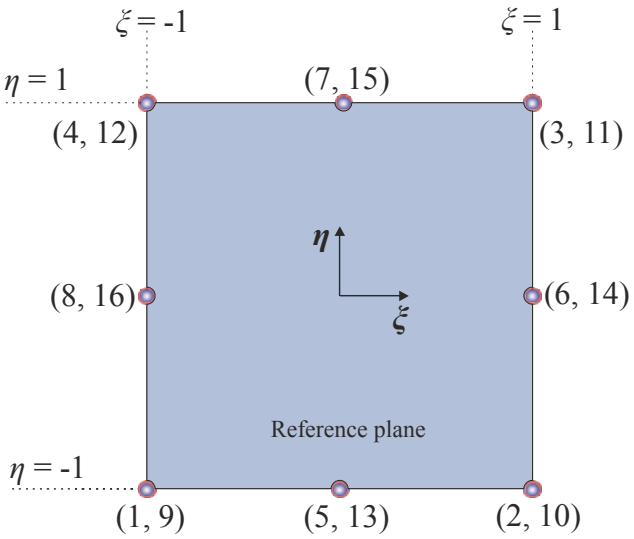

Figure A1.4: Reference plane of the 16-node 3D interface element.

The normal unit vector t_n (see Figure A1.3) equals to the cross product of the coplanar orthogonal unit vectors v_ξ and v_η. Thus, the local normal unit vector expressed in the curvilinear system of the reference plane is equal to:

$$t_n = v_\xi \times v_\eta = \left(\frac{\partial x^R}{\partial \xi} \times \frac{\partial x^R}{\partial \eta} \right) \frac{1}{\left\| \frac{\partial x^R}{\partial \xi} \times \frac{\partial x^R}{\partial \eta} \right\|} \tag{A1.15}$$

the coordinates of which are calculated as follows:

$$t_n^1 = \frac{y_\xi \cdot z_\eta - z_\xi \cdot y_\eta}{|J|} \tag{A1.16a}$$

$$t_n^2 = \frac{z_\xi \cdot x_\eta - x_\xi \cdot z_\eta}{|J|} \tag{A1.16b}$$

$$t_n^3 = \frac{x_\xi \cdot y_\eta - y_\xi \cdot x_\eta}{|J|} \tag{A1.16c}$$

where x_ξ, y_ξ, z_ξ and x_η, y_η, z_η is the first partial derivative of the coordinates of each point laying on the reference plane with respect to ξ and η, respectively. The magnitude of the vector t_n equals to the Jacobian determinant of the transformation matrix and its calculation is given by the following equation:

$$|J| = \left\| \frac{\partial x^{\mathrm{R}}}{\partial \xi} \times \frac{\partial x^{\mathrm{R}}}{\partial \eta} \right\| = \sqrt{\left(y_\xi \cdot z_\eta - z_\xi \cdot y_\eta \right)^2 + \left(z_\xi \cdot x_\eta - x_\xi \cdot z_\eta \right)^2 + \left(x_\xi \cdot y_\eta - y_\xi \cdot x_\eta \right)^2} \tag{A1.17}$$

The unit tangential vector t_1 is taken equal and parallel to v_ξ:

$$t_1 = \frac{\partial x^{\mathrm{R}}}{\partial \xi} \frac{1}{\left\| \frac{\partial x^{\mathrm{R}}}{\partial \xi} \right\|} \tag{A1.18}$$

and its corresponding components are given by the following equation:

$$t_1^1 = \frac{x_\xi}{|J_1|} \tag{A1.19a}$$

$$t_1^2 = \frac{y_\xi}{|J_1|} \tag{A1.19b}$$

$$t_1^3 = \frac{z_\xi}{|J_1|} \tag{A1.19c}$$

The magnitude of vector t_1 equals to:

$$|J_1| = \left\| \frac{\partial x^{\mathrm{R}}}{\partial \xi} \right\| = \sqrt{x_\xi + y_\xi + z_\xi} \tag{A1.20}$$

Aiming at constructing an orthogonal basis t_1 - t_2 - t_{n} the unit vector t_2 is given by the cross product of the unit vectors t_1 - t_{n}.

$$t_2 = t_1 \times t_{\mathrm{n}} \tag{A1.21}$$

with components

$$t_2^1 = t_{\mathrm{n}}^2 t_1^3 - t_{\mathrm{n}}^3 t_1^2 \tag{A1.22a}$$

$$t_2^2 = t_{\mathrm{n}}^3 t_1^1 - t_{\mathrm{n}}^1 t_1^3 \tag{A1.22b}$$

$$t_2^3 = t_{\mathrm{n}}^1 t_1^2 - t_{\mathrm{n}}^2 t_1^1 \tag{A1.22c}$$

At this point, the rotational matrix Θ, which consists of the three orthogonal unit vectors t_1 - t_2 - t_n, can be defined:

$$\Theta = \begin{bmatrix} t_1^1 & t_2^1 & t_n^1 \\ t_1^2 & t_2^2 & t_n^2 \\ t_1^3 & t_2^3 & t_n^3 \end{bmatrix} \tag{A1.23}$$

The relative displacements given by Equation (A1.7) and expressed with respect to the *x*-*y*-*z* coordinate system can be transformed with the use of the rotational matrix Θ, with respect to the orthogonal triad t_1 - t_2 - t_n.

$$\Delta u_{1-2-n}(\xi,\eta) = \Theta^T \Delta u(\xi,\eta) \tag{A1.24}$$

and in matrix form:

$$\begin{Bmatrix} \delta_{III} \\ \delta_{II} \\ \delta_{I} \end{Bmatrix} = \begin{bmatrix} t_1^1 & t_1^2 & t_1^3 \\ t_2^1 & t_2^2 & t_2^3 \\ t_n^1 & t_n^2 & t_n^3 \end{bmatrix} \begin{Bmatrix} \Delta u_x \\ \Delta u_y \\ \Delta u_z \end{Bmatrix} \tag{A1.25}$$

Having calculated the local coordinate system with respect to the global coordinate system, the internal force vector and the stiffness matrix of the 3D cohesive element may be calculated. Taking under consideration the large displacement and rotation theory and neglecting inertial and field forces the expression of the virtual work for a body with volume *V* with several interfaces S_{coh}, is given as follows:

$$\int_V \sigma \nabla^S \delta u \, dV + \int_{S_{coh}} \delta \Delta u_{1-2-n}^T t_{coh} \, dS_{coh} = \int_{S_{ext}} \delta u^T t_{ext} \, dS_{ext} \tag{A1.26}$$

where σ is the Cauchy stress tensor, u is the displacement field, Δu are the relative displacements per node pair and t_{ext} and t_{coh} are the tractions applying to the internal and external surfaces of the cohesive element at a given deformation state. Thus, the nodal internal forces form a 48 x 1 vector f_N^{el} which is defined as follows:

$$f_N^{el} = \int_{-1}^{1}\int_{-1}^{1} B^T \Theta^T t_{loc} |J| \, d\xi \, d\eta \tag{A1.27}$$

The traction vector t_{loc} contains the three stresses (loading and fracture in Mode I, II and III) that develop within the cohesive element and expressed by the constitutive relation of the interface with respect to the relative displacements $\Delta u_{1-2-\text{n}} = \{\delta_{\text{III}} \quad \delta_{\text{II}} \quad \delta_{\text{I}}\}$.

$$t_{\text{loc}} = \begin{Bmatrix} \sigma_{\text{III}} \\ \sigma_{\text{II}} \\ \sigma_{\text{I}} \end{Bmatrix} = f\left(\{\delta_{\text{III}} \quad \delta_{\text{II}} \quad \delta_{\text{I}}\}\right) \tag{A1.28}$$

The tangent stiffness matrix K^{el} of the 3D 16-node interface element has dimensions 48 x 48 and defined according to ABAQUS® sign convention as:

$$\text{K}^{\text{el}} = -\frac{\partial f_{\text{N}}^{\text{el}}}{\partial d_{\text{N}}} = -\int_{\text{el}} B^{\text{T}} \frac{\partial t_{\text{loc}}}{\partial \Delta u} B \, \text{dS}_{\text{el}} \tag{A1.29}$$

which concludes to the following equation:

$$\text{K}^{\text{el}} = -\int_{-1}^{1}\int_{-1}^{1} B^{\text{T}} \Theta^{\text{T}} C_{\text{loc}} \Theta B \left|J\right| \text{d}\xi \text{d}\eta \tag{A1.30}$$

where C_{loc} is the 3 x 3 tangent stiffness matrix of the constitutive relation of the cohesive zone being modeled,

$$C_{\text{loc}} = \frac{\partial t_{\text{loc}}}{\partial \Delta u_{1-2-n}} \tag{A1.31}$$

and in matrix form:

$$C_{\text{loc}} = \begin{bmatrix} C_{\text{III}} & 0 & 0 \\ 0 & C_{\text{II}} & 0 \\ 0 & 0 & C_{\text{I}} \end{bmatrix} \tag{A1.32}$$

The out of the diagonal terms lead to coupling between the respective loading and fracture modes. In general, these are assumed equal to zero, since coupling and interdependency of the pure modes is established within the formulation of the constitutive model utilized.

For the calculation of the f_{N}^{el} and K^{el} magnitudes, given by Equation (A1.27) and (A1.30), respectively, a numerical integration procedure is utilized based on the Gauss scheme, which is given by the following relation:

$$\mathrm{I}=\int_{-1}^{1}\int_{-1}^{1} f(\xi,\eta)\mathrm{d}\xi\mathrm{d}\eta \cong \sum_{i=1}^{m}\sum_{j=1}^{n} W_i W_j f(\xi_i,\eta_j) \tag{A1.33}$$

where m and n are the Gauss points along ξ and η axes, magnitudes W_i and W_j are the Gauss weights at the corresponding integration point (i, j). In general, equal number of integration points is utilized along each axis, so a (m x m) scheme is produced. In the current work, a 3 x 3 Gauss point scheme has been utilized. Figure A1.5 and Table A1.2 present the locations with their corresponding weights according to Gauss numerical procedure, which were utilized for the integration of the global force vector and stiffness matrix of the developed interface element.

Table A1.2: Gauss quadrature numerical integration considering 9 points (3x3).

Gauss point	i	ξ_i	W_i	j	η_j	W_j
1	1	$-\sqrt{0.6}$	0.55555555555	1	$\sqrt{0.6}$	0.55555555555
2	2	0	0.88888888888	1	$\sqrt{0.6}$	0.55555555555
3	3	$\sqrt{0.6}$	0.55555555555	1	$\sqrt{0.6}$	0.55555555555
4	1	$-\sqrt{0.6}$	0.55555555555	2	0	0.88888888888
5	2	0	0.88888888888	2	0	0.88888888888
6	3	$\sqrt{0.6}$	0.55555555555	2	0	0.88888888888
7	1	$-\sqrt{0.6}$	0.55555555555	3	$-\sqrt{0.6}$	0.55555555555
8	2	0	0.88888888888	3	$-\sqrt{0.6}$	0.55555555555
9	3	$\sqrt{0.6}$	0.55555555555	3	$-\sqrt{0.6}$	0.55555555555

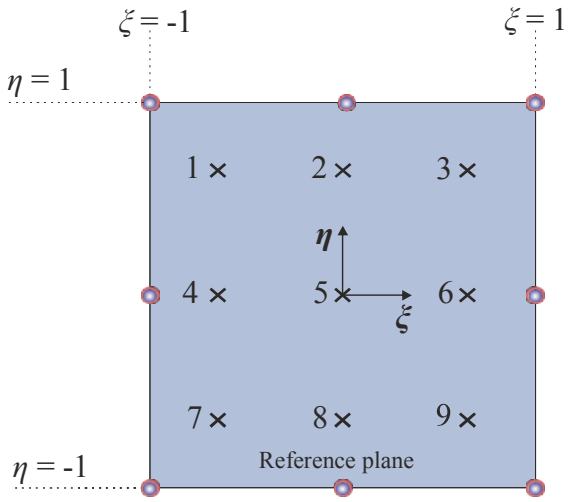

Figure A1.5: Location of the 9 Gauss points laying on the reference plane of the 3D interface element.

Appendix A2: Formulation of the 2D interface element

The 2-Dimensional interface finite element consists of two quadratic line elements (initially co-planar), which describe the mechanics and kinematics in a two dimensional Cartesian space of the cohesive zone to be modeled. The two constituent line elements connect the adjacent faces of two 2D continuum elements. Each plane element consists of 3 nodes and thus the cohesive element has 6 nodes in total. The 2D cohesive element can be connected with 8-node 2D plane continuum elements, as shown in Figure A2.1. The two constitutive lines of the 2D interface element are located in the same position (coincident nodes – zero thickness), in the initial undeformed state and separate as a consequence of the deformation of the connected plane continuum elements.

Figure A2.2 presents the parent 3-D interface finite element together with the global coordinate system (x-y-z) and the respective local curvilinear coordinate system (ξ-η). In this figure, the presented node numbering follows the connectivity convention of ABAQUS®. The relative displacements (separations), which result from the displacements of the two constituent lines of the interface element, will be transformed according to an orthogonal triad unit vector system lying on the reference line. This triad allows the transformation to a normal and two tangential separations, which in turn yield tractions in the corresponding directions, through the constitutive relation that describes the cohesive zone being modeled.

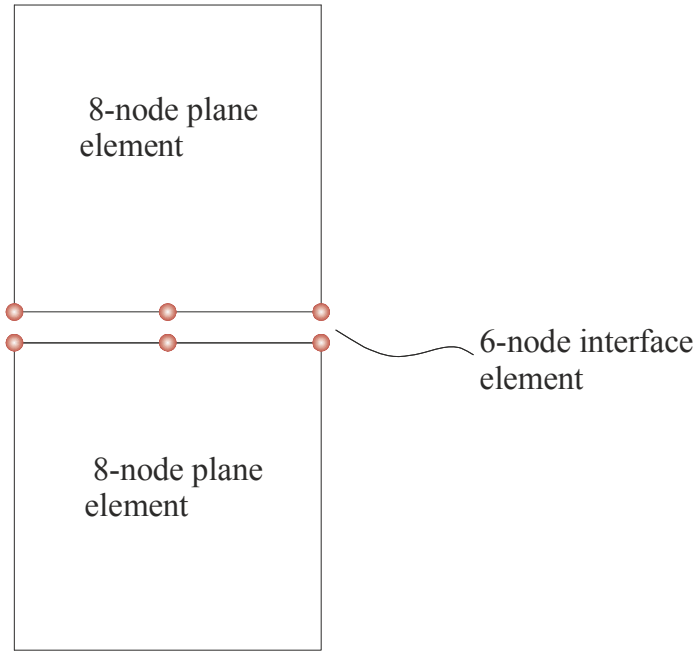

Figure A2.1: Connectivity of the 16-node 3D interface finite element with 20-node volumetric continuum elements.

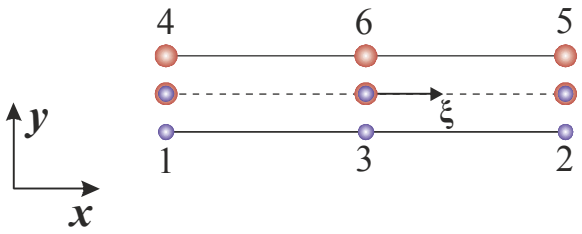

Figure A2.2: 2D interface finite element.

Each node of the developed interface element has two degrees of freedom (dof's), one translation in each direction of the global coordinate system (u_x, u_y). Thus, the total nodal dof's of the 2D interface element are 12 (2x6). The vector containing the nodal dofs is given by:

$$u_N = \left\{ u_x^1 \quad u_y^1 \quad u_x^2 \quad u_y^2 \quad .... \quad u_x^6 \quad u_y^6 \right\} = \left\{ \left\{ u_N^{bottom} \right\}^{1x6} \middle| \left\{ u_N^{top} \right\}^{1x6} \right\}^T \tag{A2.1}$$

The difference of the nodal displacements of the top and bottom line that defines the relative displacements are given by Equation (A1.2). The top line is defined by nodes 4 - 6 whereas the bottom plane is defined by nodes 1 - 3, by following the convention of Figure A2.2. Equation A1.2 can be rewritten in a programming environment as follows:

$$\left\{ \Delta u_N \right\}^{6x1} = \left[\Phi \right]^{6x12} \begin{Bmatrix} u_N^{bottom} \\ u_N^{top} \end{Bmatrix} = \left[\left[-I \right]^{6x6} \middle| \left[I \right]^{6x6} \right] \begin{Bmatrix} u_N^{bottom} \\ u_N^{top} \end{Bmatrix} \tag{A2.2}$$

Matrix [Φ] consists of two square unite matrices with 6 x 6 dimensions, sequentially placed. For the interpolation of the nodal relative displacements within the reference surface of the cohesive element (see Figure A2.3), quadratic polynomials have been utilized with respect to the local coordinate system ξ. Let $N_i(\xi)$ be the shape functions that correspond to a node pair, as listed in Table A2. 1, where ξ and η are within the range of [-1,1].

Table A2. 1: Node pairs that share the same shape functions.

	Node Pairs	
i	Node 1	Node 2
1	1	4
2	2	5
3	3	6

Each shape function gives 1 to its corresponding node pair and 0 to the remaining nodes. The shape functions utilized for the 2D cohesive element are given by the following equations:

$$N_1(\xi)=\frac{1}{2}\left(-\xi+\xi^2\right) \tag{A2.3a}$$

$$N_2(\xi)=\frac{1}{2}\left(\xi+\xi^2\right) \tag{A2.3b}$$

$$N_3(\xi)=1-\xi^2 \tag{A2.3c}$$

By utilizing the preceding shape functions, the relative displacements can be rewritten within the reference line of the cohesive element, in a continuous form, considering the discrete nodal values:

$$\Delta u\left(\xi\right)=\begin{Bmatrix}\Delta u_{\mathrm{x}}\left(\xi\right)\\ \Delta u_{\mathrm{y}}\left(\xi\right)\end{Bmatrix}=H\left(\xi\right)\Delta u_{\mathrm{N}} \tag{A2.4}$$

where the vector Δu is of dimensions 2x1 whereas matrix H (ξ, η) is of dimensions 2x12 and defined by the following way:

$$H\left(\xi\right)=\left[\mathrm{N}_1\left(\xi\right)\mathrm{I}_{2\mathrm{x}2}\middle|\mathrm{N}_2\left(\xi\right)\mathrm{I}_{2\mathrm{x}2}\middle|\mathrm{N}_3\left(\xi\right)\mathrm{I}_{2\mathrm{x}2}\right] \tag{A2.5}$$

By combining Equation A2.3 with Equation A2.5 matrix B is obtained with dimensions 2x12, which connects vector Δu with the nodal dof's vector u_{N}:

$$\Delta u\left(\xi\right)=\mathrm{B}u_{\mathrm{N}}=\mathrm{H}\left(\xi\right)\Phi u_{\mathrm{N}} \tag{A2.6}$$

A reference line is defined that lays on the middle in-between the top and bottom lines of the 2D cohesive element, as shown in Figure A2.3.

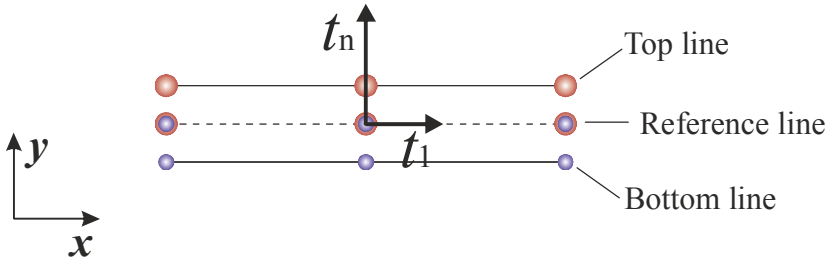

Figure A2.3: The three lines that define the 2D interface element.

The coordinates of the reference line $x_{\mathrm{N}}^{\mathrm{R}}$ are defined as the average of the coordinates of the top $x_{\mathrm{N}}^{\mathrm{top}}$ and bottom $x_{\mathrm{N}}^{\mathrm{bottom}}$ line as shown in Equation A1.8. Again, for the calculation of

x_N^{top} and x_N^{bottom} the corresponding coordinates of the nodes (see Figure A2.4) at the undeformed state X_N^{top} and X_N^{bottom} are being summed with the respective displacements, calculated at a given step of the non-linear analysis (see Equation A1.9).

As shown in Figure A2.3, an orthogonal basis is defined on the reference line, which consists of a tangential unit vector t_1 and a normal to the tangential, t_n. For the calculation of these vectors a continuous description of the coordinates of the reference plane is essential.

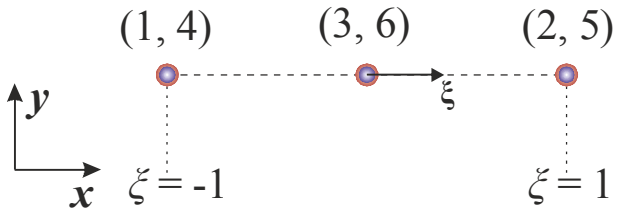

Figure A2.4: Reference plane of the 16-node 3D interface element.

Thus the coordinates of all material points lying on the reference plane are being calculated by utilizing the matrix containing the shape functions, as follows:

$$x^R = \mathrm{H}(\xi)\, x_N^R \tag{A2.7}$$

The unit tangential vector t_1 is taken equal and parallel to v_ξ:

$$t_1 = v_\xi = \frac{\partial x^R}{\partial \xi} \frac{1}{\left\| \frac{\partial x^R}{\partial \xi} \right\|} \tag{A2.8}$$

For the calculation of the partial derivative $\frac{\partial x^R}{\partial \xi}$, Equation (A2.7) is inserted in Equation (A2.8).

$$\frac{\partial x^R}{\partial \xi} = \frac{\partial}{\partial \xi}\left(\mathrm{H}(\xi)\, x_N^R\right) = x_N^R \frac{\partial \mathrm{H}(\xi)}{\partial \xi} \tag{A2.9}$$

where $\frac{\partial \mathrm{H}(\xi)}{\partial \xi}$ is the first partial derivative of the shape functions (Equation A2.3) with respect to ξ given as follows:

$$N_{1,\xi}(\xi) = -\frac{1}{2} + \xi \tag{A2.10a}$$

$$N_{2,\xi}(\xi) = \frac{1}{2} + \xi \tag{A2.10b}$$

$$N_{3,\xi}(\xi) = -2\xi \tag{A2.10c}$$

At this point the corresponding components of the tangential vector t_1 can be written as:

$$t_1^1 = \frac{x_\xi}{|J|} \tag{A2.11a}$$

$$t_1^2 = \frac{y_\xi}{|J|} \tag{A2.11b}$$

where x_ξ and y_ξ are the first partial derivatives of the coordinates of each point laying on the reference line with respect to ξ.

The normal unit vector t_n (see Figure A2.3) is now defined as:

$$t_n = \left(-y_\xi, x_\xi\right) \frac{1}{\left\| \frac{\partial x^R}{\partial \xi} \right\|} \tag{A2.12}$$

and its corresponding components are given by the following equations:

$$t_n^1 = -\frac{y_\xi}{|J|} \tag{A2.13a}$$

$$t_1^2 = \frac{x_\xi}{|J|} \tag{A2.13b}$$

The magnitude of vectors t_1 and t_n equal to the Jacobian determinant of the rotational matrix and its calculation is given by the following equation:

$$|J| = \left\| \frac{\partial x^R}{\partial \xi} \right\| = \sqrt{x_\xi^2 + y_\xi^2} \tag{A2.14}$$

At this point, the rotational matrix Θ, which consists of the two orthogonal unit vectors t_2 - t_n, can be defined:

$$\Theta = \begin{bmatrix} t_1^1 & t_2^1 \\ t_1^2 & t_2^2 \end{bmatrix} \tag{A2.15}$$

The relative displacements given by Equation (A2.6) and expressed with respect to the *x*-*y* coordinate system can be transformed with the use of the rotational matrix Θ, with respect to the orthogonal triad t_1 - t_n.

$$\Delta u_{1-n}(\xi) = \Theta^T \Delta u(\xi) \tag{A2.16}$$

and in matrix form:

$$\begin{Bmatrix} \delta_{II} \\ \delta_I \end{Bmatrix} = \begin{bmatrix} t_1^1 & t_1^2 \\ t_n^1 & t_n^2 \end{bmatrix} \begin{Bmatrix} \Delta u_x \\ \Delta u_y \end{Bmatrix} \tag{A2.17}$$

Having calculated the local coordinate system with respect to the global coordinate system, the internal force vector and the stiffness matrix of the 2D interface element may be calculated. Taking under consideration the large displacement and rotation theory and neglecting inertial and field forces the expression of the virtual work for a body with volume *V* with several interfaces S_{coh}, is given as follows:

$$\int_V \sigma \nabla^S \delta u \, dV + \int_{S_{coh}} \delta \Delta u_{1-2-n}^T t_{coh} \, dS_{coh} = \int_{S_{ext}} \delta u^T t_{ext} \, dS_{ext} \tag{A2.18}$$

where σ is the Cauchy stress tensor, u is the displacement field, Δu are the relative displacements per node pair and t_{ext} and t_{coh} are the tractions applying to the internal and external surfaces of the cohesive element at a given deformation state. Thus, the nodal internal forces form a 12 x 1 vector f_N^{el} which is defined as follows:

$$f_N^{el} = w \int_{-1}^{1} B^T \Theta^T t_{loc} |J| \, d\xi \tag{A2.19}$$

The traction vector t_{loc} contains the three stresses (loading and fracture in Mode I and II) that develop within the cohesive element and expressed by the constitutive relation of the interface with respect to the relative displacements $\Delta u_{1-n} = \{\delta_{II} \quad \delta_I\}$.

$$t_{loc} = \begin{Bmatrix} \sigma_{II} \\ \sigma_I \end{Bmatrix} = f\left(\{\delta_{II} \quad \delta_I\}\right) \tag{A2.20}$$

The tangent stiffness matrix K^{el} of the 2D 6-node interface element has dimensions 12 x 12 and defined according to ABAQUS® sign convention as:

$$\mathrm{K}^{\mathrm{el}} = -\frac{\partial f_{\mathrm{N}}^{\mathrm{el}}}{\partial d_{\mathrm{N}}} = -\int_{\mathrm{el}} B^{\mathrm{T}} \frac{\partial t_{\mathrm{loc}}}{\partial \Delta u} B \, \mathrm{dS}_{\mathrm{el}} \tag{A2.21}$$

which concludes to the following equation:

$$\mathrm{K}^{\mathrm{el}} = -w \int_{-1}^{1} B^{\mathrm{T}} \Theta^{\mathrm{T}} C_{\mathrm{loc}} \Theta B \left| J \right| \mathrm{d}\xi \tag{A2.22}$$

where C_{loc} is the 2 x 2 tangent stiffness matrix of the constitutive relation of the cohesive zone being modeled,

$$C_{\mathrm{loc}} = \frac{\partial t_{\mathrm{loc}}}{\partial \Delta u_{1-n}} \tag{A2.23}$$

and in matrix form:

$$C_{\mathrm{loc}} = \begin{bmatrix} C_{\mathrm{II}} & 0 \\ 0 & C_{\mathrm{I}} \end{bmatrix} \tag{A2.24}$$

The out of the diagonal terms lead to coupling between the respective loading and fracture modes. In general, these are assumed equal to zero, since coupling and interdependency of the pure modes is established within the formulation of the constitutive model utilized.

For the calculation of the $f_{\mathrm{N}}^{\mathrm{el}}$ and K^{el} magnitudes, given by Equation (A1.27) and (A1.30), respectively, a numerical integration procedure is utilized based on the Gauss scheme, which is given by the following relation:

$$\mathrm{I} = \int_{-1}^{1} f\left(\xi\right) \mathrm{d}\xi \cong \sum_{i=1}^{m} W_i f\left(\xi_i\right) \tag{A2.25}$$

where m are the Gauss points along ξ axis, magnitudes W_i are the Gauss weights at the corresponding integration point i. In the current work, a 3 Gauss point scheme has been utilized. Figure A2. 5 and Table A2. 2 present the locations with their corresponding weights according to Gauss numerical procedure, which were utilized for the integration of the global force vector and stiffness matrix of the developed interface element.

Table A2. 2: Gauss quadrature numerical integration considering 3 points.

Gauss point	i	ξ_i	W_i
1	1	$-\sqrt{0.6}$	0.55555555555
2	2	0	0.88888888888
3	3	$\sqrt{0.6}$	0.55555555555

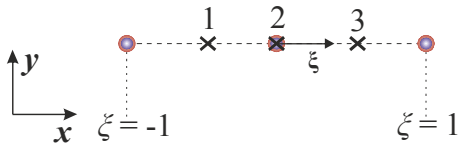

Figure A2. 5: Location of the 3 Gauss points laying on the reference line of the 2D interface element.